UNIVERSITY OF OKLAHOMA

GRADUATE COLLEGE

MOLECULAR BEAM EPITAXIAL GROWTH OF INTERBAND CASCADE STRUCTURES WITH ADVANCES IN INAS- AND GASB-BASED INTERBAND CASCADE LASERS

A DISSERTATION

SUBMITTED TO THE GRADUATE FACULTY

in partial fulfillment of the requirements for the

Degree of

DOCTOR OF PHILOSOPHY

By

JEREMY MASSENGALE
Norman, Oklahoma
2023

Downloaded from SHAREOK. Persistent Handle URL: https://hdl.handle.net/11244/337500

MOLECULAR BEAM EPITAXIAL GROWTH OF INTERBAND CASCADE STRUCTURES WITH ADVANCES IN INAS- AND GASB-BASED INTERBAND CASCADE LASERS

A DISSERTATION APPROVED FOR THE
HOMER L. DODGE DEPARTMENT OF PHYSICS AND ASTRONOMY

BY THE COMMITTEE CONSISTING OF

Dr. Michael Santos, Chair

Dr. Rui Yang, Co-Chair

Dr. Ian Sellers

Dr. Bruno Uchoa

Dr. Alberto Marino

© Copyright by JEREMY MASSENGALE 2023
All Rights Reserved.

Dedicated to the memory of my grandmother, Mary. Without her undying love and support, my educational journey would not have been possible. And to my wife, Lucia, who has supported me unconditionally in the pursuit of this endeavor.

Acknowledgements

The research presented in this dissertation was supported in part by NSF under Grant ECCS-1931193 and Oklahoma Center for the Advancement of Science and Technology (OCAST) under Award AR21-024.

First and foremost, I want to thank my advisers Dr. Michael Santos and Dr. Rui Yang for offering me the opportunity to be a part of this research group, and for allowing me to branch out and become involved with many aspects of the various projects we have worked on together. Dr. Yang, your love of this research is inspiring, and has motivated me to reach for greater heights than I would have otherwise. I want to thank you for all of the time you spent teaching me ICL characterization techniques, instilling in me the notion to question the things that we do and the results that we achieve, and for always having time to provide me with near immediate feedback, whether it be in regards to my long winded emails, or to simply chat about measurements, techniques, or results. Your attention to detail and meticulous work ethic has guided, shaped, and informed my own research process, and for that I will be forever grateful.

Dr. Santos, thank you for the many long talks about MBE growth and material characterization that we had over the years, while at times we may have even confused ourselves, I think we had a lot of insights and laughs along the way. I also want to thank you for the time we spent together talking about life, work, and their balance, as well as about career outlook. Thank you for allowing me to guide some parts of this dissertation and supporting me in my own free ranging

endeavors.

Also, I would like to thank my committee members, Dr. Ian Sellers, Dr. Bruno Uchoa, and Dr. Alberto Marino, all of which I have either had the opportunity to take courses with or spend time in journal club with. Thanks to each of you for sharing your knowledge with me and for guiding me along this journey.

I want to thank Dr. Hao Ye for beginning my MBE growth training when I first joined the group. I want to offer my most sincere thanks to Dr. Lu Li, who mainly trained me in MBE and material characterization techniques, and who was partly responsible for some of the early growth presented in this dissertation. Even after leaving OU, he has always made himself available to discuss things with me, especially once I began working on ICL fabrication, and for that I am eternally grateful. I would also like to thank Dr. Tetsuya Mishima for growing some of the GaSb-based ICLs presented in this dissertation and our collaborators Dr. John Klem and Mr. Samuel Hawkins of Sandia National Laboratories for growing the InAs-based ICLs presented in this dissertation.

I offer thanks to Dr. Preston Larson, who helped with the AFM and SEM characterization presented in this dissertation, and to Dr. Gang Yang and Dr. Binbin Weng, for their help with fabrication over the last few years.

I thank our former group members Dr. Yuchao Jiang for allowing me to use his band structure and waveguide simulation programs, which were invaluable in my learning of ICL characterization, as well as Dr. S.M. Shazzad Rassel for taking the time to chat with me about various aspects of those simulation programs. I

also want to thank our former group members with whom I shared some overlap with: Dr. Lin Lei, Dr. Hossein Lotfi, Dr. Wenxiang Huang, Dr. Yuzhe Lin, and Mr. Jonathan-David Francois. I extend thanks to our current group member Mr. Yixuan Shen, who has helped with some of the fabrication and device testing reported in this dissertation.

I would like to thank the many friends I met during my time in the program at OU, and while there are too many to mention here, I would like to especially thank Dr. Lance McDowell for our many discussions about life, loved ones, research, and the future. I would be remiss if I did not also mention the friends I made when I first joined this program. Dr. Hamidreza "Mahyar" Esmaielpour, Dr. Matthew Holtfrerich, and Dr. Zhonghe Liu. Those first two years that we shared in that office debating each other about our homework, sharing stories of the places we came from, and discussing our hopes and dreams for the future were an enriching part of my life. Those early days in the program could be so stressful, yet I think they represent an amazing time in our lives, and I will forever look back fondly on the moments we shared together.

To my parents and siblings, thank you for supporting me in my decision to leave home and pursue this endeavor. For understanding all those times I was not home for the holidays, when I could not call or text back right away, and for loving me all the same. I want to especially thank my father, Greg. My whole life you have unconditionally supported me and helped me to reach for the stars. Thank you for always taking pride in me and for always making sure I felt loved.

Lastly, I want to thank my wife, Lucia. You have loved me and supported me everyday since I met you. You have offered me guidance, perspective, and hope in times when I felt most lost. You have unselfishly cared for me and have been so understanding. With your amazing talents you helped me edit and create some of the very images in this dissertation. While this may close one chapter of our lives, it also heralds the begging of the next, and I am excited to see where that journey may take us!

Table of Contents

Acknowledgements **i**

List of Tables **xi**

List of Figures **xxi**

Abstract **xxii**

1 Introduction **1**
1.1 Infrared Radiation and Applications 1
1.2 Laser Development and Fundamentals 4
1.2.1 A Brief History of Laser Development 4
1.2.2 Laser Fundamentals 6
1.3 MIR Semiconductor Lasers 8
1.4 III-V Materials 8
1.4.1 Quantum Well Configurations 10
1.4.2 Band Alignment 15
1.5 Cascade Lasers 17
1.6 The Interband Cascade Laser 19
1.6.1 From Origin to Room Temperature Operation 19
1.6.2 Recent Progress in ICL Performance 24
1.7 Dissertation Introduction 27

2 Molecular Beam Epitaxial Growth **30**
2.1 Principles of MBE Growth 30
2.1.1 Reflection High Energy Electron Diffraction 33
2.1.2 Determining Growth Rates using RHEED 35
2.1.3 Growth Rate Calibration on the GENxplor 37
2.2 Strain in MBE Grown Structures 40
2.2.1 Mathematical Definition of Strain 43
2.3 Strain Balance Methods 45
2.3.1 Derivation and Extension of the Zero Stress Method 46
2.3.2 Relating Zero-Stress to Measured Results 50
2.4 Experimental MBE Setup 53
2.4.1 MBE Cell Configuration 53
2.4.2 Achieving UHV Conditions 55
2.4.3 Temperature Monitoring During Active Growth 58
2.5 Summary of MBE Growth 59

3 Material Characterization **61**
3.1 Measuring the Doping Concentration 61
3.1.1 The Hall Effect 61
3.1.2 The van der Pauw Technique 63
3.1.3 Conducting Hall Measurements 64
3.1.4 Doping Calibration Studies on the GENxplor 65

3.2 Differential-Interference-Contrast Microscopy . . . 68
3.3 X-ray Diffraction . . . 72
3.3.1 The Reciprocal Lattice and Crystal Diffraction . . . 73
3.3.2 Analyzing XRD Spectra . . . 77
3.3.3 Identification of Peaks in XRD Results . . . 80
3.3.4 Experimental Procedure for XRD Scans . . . 82
3.4 Other Material Characterization Tools . . . 85

4 Growth Studies of IC Structures 87
4.1 $InAs_xSb_{1-x}$ Alloy Calibration . . . 88
4.1.1 Critical Thickness Criteria . . . 88
4.1.2 Initial Alloy Calibration Efforts . . . 91
4.1.3 Revised InAsSb Alloy Calibration . . . 93
4.1.4 First Attempt at GaSb-based ICL Growth . . . 97
4.2 Optimizing the InAs/AlSb SL . . . 100
4.3 Optimizing the GaSb Buffer Layer . . . 107
4.3.1 Experimental Setup and Substrate Preparation . . . 108
4.3.2 Material Characterization of GaSb Buffer Layers . . . 111
4.4 Growth Studies for ICTPVs . . . 112
4.4.1 A Brief Review of ICTPV Operating Principles . . . 112
4.4.2 Interface control via Sb-soaking in ICTPVs . . . 113
4.4.3 Graded Doping Profiles in the Absorber of an ICTPV . . . 117
4.5 The Resonant Cavity Enhanced ICTPV . . . 121
4.5.1 Details of the Distributed Bragg Reflector . . . 122
4.5.2 $AlAs_xSb_{1-x}$ Alloy Calibration . . . 124
4.5.3 Growth and Testing of the DBR . . . 127

5 Device Fabrication and Characterization 132
5.1 Fabrication and Characterization Introduction . . . 132
5.2 Device Fabrication . . . 132
5.3 ICL Performance Characterization . . . 135
5.3.1 ICL Emission Spectrum . . . 135
5.3.2 ICL IVL Characteristics . . . 143
5.4 Pulsed IVL Measurements . . . 146
5.4.1 Pulsed IVL Experimental Setup . . . 147
5.4.2 Pulsed IVL Calibration . . . 150
5.4.3 Pulsed Duty Cycle Deviation . . . 154
5.4.4 Direct Calculation of the Pulse Delay . . . 155
5.5 Summary of Device Characterization . . . 156

6 InAs-based Interband Cascade Lasers 158
6.1 InAs-based ICLs for Long Wavelength Operation . . . 160
6.1.1 Advanced Waveguide Design . . . 163
6.1.2 Active Region Innovation . . . 165
6.1.3 Band Edge Diagrams . . . 167
6.2 InAs-based ICL Design and Material Characterization . . . 169
6.3 Initial InAs-based ICL Results . . . 174

6.3.1 EB7289 Results . . . 175
6.3.2 EB7342 Results . . . 178
6.4 Revised InAs-based ICL Design . . . 181
6.4.1 Growth Characterization of Recent InAs-based ICLs . . . 184
6.5 Recent InAs-based ICL Device Results . . . 186
6.5.1 EB7541 and EB7547 Results . . . 187
6.5.2 EB7541 and EB7547 Summary . . . 192
6.5.3 EB7523 and EB7539 Results . . . 193
6.6 Further Discussion and Analysis . . . 196
6.7 Summary of Long Wavelength InAs-based ICLs . . . 199

7 GaSb-based Interband Cascade Lasers 201
7.1 Early GaSb-based ICLs with Advanced Waveguides . . . 202
7.1.1 Growth Characteristics of Y061L and Y062L . . . 203
7.1.2 Performance Characterization of Y061L and Y062L . . . 204
7.2 GaSb-based ICLs for shorter Mid-wavelength Operation . . . 207
7.2.1 Design of Y082L and Y083L . . . 207
7.2.2 Growth Characteristics of Y082L and Y083L . . . 209
7.3 Initial Results for GaSb-based ICLs Operating Between 3.3-3.4 μm . . . 216
7.3.1 Y082L Results . . . 216
7.3.2 Y083L Results . . . 220
7.3.3 Comparison of Y082/83L to Y061/62L . . . 224
7.4 Follow Up Study of GaSb-based ICLs Y086L and Y087L . . . 226
7.4.1 Growth Characteristics of Y086L and Y087L . . . 226
7.4.2 Growth Impact on the Potential Operation for Y086L and Y087L 228
7.4.3 Performance Results of Y086L . . . 230
7.4.4 Performance Results of Y087L . . . 235
7.4.5 Discussion and Comparison between Y082L, Y086L, and Y087L 238

8 Conclusion and Future Directions 242
8.1 Dissertation Summary . . . 242
8.2 Future Research Endeavors . . . 247

REFERENCES 249

A List of Publications 263

List of Tables

2.1 The various parameters of the GR calibration conducted in the Spring of 2020. The source material cell temperatures are reported as measured from the thermocouple. 39

3.1 The various parameters of the doping calibration conducted in the Spring of 2020. Dopant cell temperatures are reported as measured from the thermocouple. 70

4.1 MBE Growth Parameters for the initial InAsSb composition + doping calibration in the Fall of 2016. In the table, the valve values are in units of Mil (1 mil = 25.4 μm) and the Flux values have the units of (Torr). . 92

4.2 MBE Growth Parameters for the later InAsSb composition calibration in the Spring of 2017. In the table, the Sb fraction is calculated assuming the alloy is strained to the substrate. The MBE system was down for a period of several weeks between M141 and M164, and thus the growth calibration changed and needed to be redone. The values of h_c are calculated based on Eq. 4.3 using the Sb fractions determined from the measured XRD data. 96

4.3 MBE Growth Parameters for the GaSb buffer layer growth study. All structures were grown with a V_{Sb}/III_{Ga} of about 2.5. All flux values reported have the unit of Torr. The Sb flux during heating/cooling (h/c) times varied by about 50% overall. 110

4.4 Extracted material characterization details from XRD measurements of some of the early ICTPV devices. The DA 0th order peak to substrate spacing is presented in units of arcseconds. Also shown is the perpendicular mismatch and the out-of-plane strain type. 114

4.5 MBE growth parameters for a series of early AlAsSb alloy growth studies. The Sb and As valve open values are given in mils (1 mil = 25.4 μm) and the fluxes are listed in units of Torr. The alloy compositions are extracted from the measured XRD patterns and are assumed to be the strained compositions. 125

5.1 Experimentally determined neutral density filter attenuation factors over time. 152

List of Figures

1.1 Depiction of the electromagnetic spectrum. The blown up portion shows the sub-division of the infrared part of the spectrum into its three regions. 2
1.2 Selected simulated absorbance spectra for a number of fingerprint molecules using the websim SpectraPlot, which uses the HITRAN 2012 and HITEMP 2010 databases. 3
1.3 Depiction of a 4-level system, with E_2 being the metastable state where population inversion occurs. Excited electrons in this state couple to the background electric field, which is the catalyst for generating stimulated emission. 7
1.4 Depiction of the cavity modes of a Fabry-Perot style cavity, with the free spectral range (FSR) showing the mode spacing. 8
1.5 Qualitative depiction of the convolution of the Fabry-Perot cavity modes with that of the optical gain profile, resulting in the emission spectrum of a laser. 9
1.6 Energy bandgap (left axis) and wavelength of emission (right axis) with lattice constant for the various III-V semiconductors. 10
1.7 Depiction of a parallel MQW configuration. 11
1.8 Qualitative depiction of an $Al_xGa_{1-x}As/GaAs/Al_xGa_{1-x}As$ heterostructure showing the difference between interband and intersubband transitions. 13
1.9 Depiction of a series MQW configuration which shows two different transition types. Pictured on the left is a series QW based on interband transitions with unipolar barriers (such as the case for an ICL), while the right shows a series QW based on intersubband transitions. 14
1.10 Position of the conduction and valence-band edges for a variety of semiconductors, taken from Grundmann. 16
1.11 Qualitative depiction of the various types of band alignment in MQW structures. 17
1.12 Qualitative band diagram of what would later become the ICL. 21
1.13 Qualitative band diagram of the ICL proposed by Meyer and Yang, which included the use of a single hole injector form from a layer of $Ga_{0.7}In_{0.3}Sb$. 22
1.14 Qualitative band diagram of the ICL with the W-shaped active region consisting of $InAs/Ga_{0.7}In_{0.3}Sb/InAs$ encased with AlSb barriers. 23
1.15 Qualitative band diagram of the modern ICL with typical features including the W-QW active region, the GaInSb hole injector, and the heavily Si-doped and also thinned electron injector. 26

2.1 Qualitative schematic of an MBE chamber showing various components used for growth.[1] 32
2.2 Qualitative diagram of the RHEED image formation process showing the beam interaction with the crystal surface and the subsequent diffraction pattern on the phosphorus (RHEED) screen. 34
2.3 The evolution of a rough to smooth surface (left to right) as determined from the RHEED pattern during growth. 35

2.4 Depiction of the evolution of the growth surface of a single monolayer of material and the corresponding intensity variation (taken from In GR calibrations in 2018) of the central diffraction peak measure by RHEED. 36
2.5 Plot of the GR in monolayers (ML) per second and the beam flux as a function of the temperature of the Ga effusion cell for the GaAs GR study in spring of 2020. 40
2.6 Plot of the GR and the beam flux as a function of function of the temperature of the Al effusion cell for the AlAs GR study in spring of 2020. 41
2.7 Plot of the GR and the beam flux as a function of the temperature of the In effusion cell for the InAs GR study in spring of 2020. 42
2.8 Depiction of biaxial tensile strain occurring in an epilayer with a lattice constant that is smaller than the substrate lattice constant. 43
2.9 Depiction of biaxial compressive strain occurring in an epilayer with a lattice constant that is larger than the substrate lattice constant. 44
2.10 Deformation of a square (**a**). (**b**) Pure hydrostatic deformation ($\epsilon_{xx} = \epsilon_{yy} = 0.2, \epsilon_{xy} = 0$), (**c**) pure shear deformation ($\epsilon_{xx} = \epsilon_{yy} = 0, \epsilon_{xy} = 0.2$), and (**d**) mixed deformation ($\epsilon_{xx} = \epsilon_{yy} = 0.1, \epsilon_{xy} = 0.1$)[2] 45
2.11 The Veeco GENxplor system used for the growth of many of the structures reported in this dissertation. Several components are labeled: (a) The substrate rotation motor, (b) the cryopump, (c) the growth chamber, (d) the RHEED camera and screen enclosed by a black cloth, (e) the shutters for each cell placed circularly around the system, (f) the various effusion cells placed circularly around the system as well as their cooling water supply (blue) and return (red) lines. Not pictured is the RHEED gun, which is on the other side of the MBE system. 54
2.12 (a) The dry vacuum pump used to pump down the system to about 10^{-3} Torr as well as to pump down the load/lock (entry/exit) chamber (b). The buffer chamber (c) is placed between (b) and the growth chamber (d). A transfer arm (e) can be used to move the sample in between (c) and (d) before and after growth. 57

3.1 Qualitative depiction of the Hall Effect with a magnetic field oriented out of the surface. 62
3.2 Depiction of the geometry of the Hall samples measured in this dissertation. The typical size of the samples ranged from 5×5 mm to 10×10 mm. Indium metal is used for the contact and high purity gold is used for the leads. . 64
3.3 Plot of the natural log of the n-doped (Si) carrier concentration in InAs as a function of the inverse of the Si cell temperature. A recent calibration in Feb. 2020 (blue) is plotted against a previous calibration from April 2017 (black) showing the high degree of consistency over time. 67
3.4 Plot of the natural log of the n-doped (Te) carrier concentration in GaSb as a function of the inverse of the GaTe cell temperature. A recent calibration in Feb. 2020 (blue) is plotted against a previous calibration from May 2017 (red) showing a slight difference at higher cell temperature due to the slightly different GRs used during calibration. 68

3.5 Plot of the natural log of the p-doped (Be) carrier concentration in GaSb as a function of the inverse of the Be cell temperature. Several calibration studies are shown between 2017 and 2020 related to contact annealing. . 69
3.6 Example of typical oval hillock defects under 40X magnification in Y065V, an ICTPV structure taken in Nov. 2018. 71
3.7 Example of a surface defect count showing about 45 defects in the traced out area on the surface of an ICTPV structure (Y072V) taken at 10X magnification in April 2019. 72
3.8 Depiction of several lattice planes in a cubic lattice.[3] 75
3.9 Depiction of the geometry of scattering in a crystal.[3] 76
3.10 Depiction of Bragg diffraction from two planes of atoms in a crystal. The extra distance traveled by the wave striking the lower plane is 2dsin(θ).[3] 77
3.11 Example of a measured (004) XRD spectrum for an ICL (Y082L-blue) compared to the simulated XRD spectra (red) based on the ideal device design. The x-axis is ω relative to the peak for the GaSb substrate, which $\theta = 30.36°$. Generally, these plots are then centered to the known substrate position. 79
3.12 A top-down view of the XRD setup. The top image (a) shows the home state of the stage, where a sample is placed directly between the x-ray source and the detector. The bottom (b) shows the position of the stage after moving to the Bragg angle of the substrate to perform signal calibration. The angle ω is formed between the sample and the x-ray beam, while θ is formed between the incident beam and the diffracted beam. The last angle, ψ is a tilt of the sample holder which rotates the sample with respect to the beam horizontal as depicted in (a). 85

4.1 The bending of a grown-in threading dislocation to create a length of misfit dislocation at the interface between an epilayer and the substrate.[4] 89
4.2 Plot of the mismatch percent as a function of the critical thickness of an epilayer based on Eq. 4.3. Several different $InAs_{0.91}Sb_{0.089}$ layer thicknesses and their associated mismatch values are referenced. 91
4.3 Normalized XRD pattern for several calibration structures grown on GaAs (M052/53/54) as well as one (M055) grown on a GaSb substrate. The position of both the GaAs and GaSb substrate peaks are set to 0 arcsec in order to demonstrate the relative separation of the InAsSb alloy peaks grown on the two difference substrates. The relaxed InAsSb peak can be seen clearly, centered at roughly -10000 arcsec for the test structures grown on GaAs, while that grown on the GaSb substrate is much closer, indicating a strained system. 94
4.4 Arrhenius plot of the doping concentration as a function of 1/T according to Hall measurements. The wafer names also show the extracted alloy composition values from the XRD patterns. 95
4.5 XRD pattern for M055, an InAsSb alloy calibration wafer grown on GaSb. For this thin epilayer, the Pendellosung fringes may be observed to the left and right of the substrate/alloy peaks. 97

4.6 XRD pattern for several InAsSb alloy calibration wafers grown on GaSb. The key describes several MBE growth parameter adjustments such as the substrate temperature, the As/Sb ratio, and the extracted alloy composition from the measured XRD. 98
4.7 XRD pattern of wafer M189 (blue), a 1.2 μm thick InAsSb layer grown on a 500 nm GaSb buffer. Also shown is the simulated XRD pattern (red) of $InAs_{0.911}Sb_{0.089}$ on GaSb. 99
4.8 DIC surface image of M189 taken under 40X magnification, which exhibits few defects and a very smooth background. 100
4.9 Measured (blue) and simulated (red) XRD patterns for Y039L, which shows significant deviations due to reduced crystalline quality. This is confirmed with DIC imaging, which shows a very rough and heavy defect surface. 101
4.10 DIC imaging under 40 × magnification for Y040LED (left) and Y041LED (right). Both structures have quite smooth surfaces, with few defects. . 102
4.11 Measured (blue) and simulated (red) XRD patterns for both Y040/41LED. It may be observed that the FWHM of the SL peaks arising from the cascade region of the LED are very narrow, indicating good material quality. Furthermore, most of the SL peaks also align with the intended design, indicating good strain-balancing. 103
4.12 Measured (blue) and simulated (red) XRD patterns for a 180 period InAs/AlSb SL test structure (M191). The SL peak FWHM is very broad, indicating poor material quality which likely stems from non-ideal MBE growth conditions. 104
4.13 The measured AFM imaging of a 5×5 μm square of the surface of M190 and M191. This measurement shows that the RMS surface roughness of the InAs/AlSb structure is nearly 5× larger than for the thicker InAsSb layer. 104
4.14 Measured XRD pattern (blue) for M220, a 180 period InAs/AlSb (26.5/23.5 Å) SL compared to the simulated XRD pattern (red). The FWHM of the various XRD peaks for M220 are quite narrow, indicating good material quality, however all peaks are shifted to higher angular position with respect to that observed in the simulation. 105
4.15 Measured XRD pattern (blue) for M220, a 180 period InAs/AlSb (26.5/23.5 Å) SL compared to a plot of the simulated XRD pattern (red) as well as several other simulations using a variety of different interface combinations. 106
4.16 Measured XRD patterns (blue, orange, green, purple) for several InAs/AlSb SL structures with variable Sb soak times in order to reduce the strain-balance issues associated with a rough interface. These are compared with a simulation (red) which has an atomically abrupt interface. 108
4.17 DIC imaging of the worst (M372, left) and best (M373, right) wafers from the GaSb buffer layer growth study under 40× magnification. 111
4.18 Schematic illustration of a multistage ICTPV cell under forward bias. The green arrows indicate the ideal transport path for electrons, while the gold arrows indicate the ideal transport path for holes. 113

4.19 Measured XRD patterns (blue, orange, green, purple) for several InAs/AlSb SL structures with variable Sb soak times in order to reduce the strain-balance issues associated with a rough interface. These are compared with a simulation (red) which has an atomically abrupt interface. 116
4.20 Depiction of a single cascade stage with N layers of doped absorbers (DAs). The overall DA sequence begins with a known starting p-doping level, corresponding to a known starting Be cell temperature. At the completion of the Nth layer, a known ending p-doping level should be achieved, corresponding to a known Be cell temperature. This will occur over a timer interval Δt that is known based on the GR of the materials. 119
4.21 MBE growth parameters for Y065V (top) and Y066V (bottom) including the total growth time for the DA in each cascade stage, the ΔT of the Be cell needed in each DA period, and the associated Be cell ramp rate to achieve the graded doping profile. 120
4.22 MBE growth parameters for Y074V, as an example, which includes the total growth time for the DA in each cascade stage, the ΔT of the Be cell needed in each DA period, and the associated Be cell ramp rate to achieve the graded doping profile. 120
4.23 Plot of the reflectance of a GaSb/$AlAs_{0.08}Sb_{0.92}$ DBR as a function of the number of periods (m) based on Eq. 4.6 with index values for GaSb and AlAsSb at a target wavelength of 4 μm. A target reflectance greater than 95% can be achieved with 10 periods. 123
4.24 Measured XRD pattern for M375, the first growth of the AlAsSb alloy for the DBR mirror. The FWHM of the peaks are rather broad due to the reduced material quality associated with the incorrect alloy composition. 125
4.25 Measured XRD patterns for a series of AlAsSb alloys grown on GaSb. The overall As valve opening was adjusted only slightly, ranging between 21-22.2 mils, corresponding to a total valve exploration range of only 1.2 mils (29.4 μm). 126
4.26 Plot of the As valve settings as a function of the measured As composition for several grown wafers. A power fit was used to predict the ideal valve setting to achieve an 8% As composition. 128
4.27 Schematic diagram of the intended DBR structure for the RCE ICTPV. 129
4.28 DIC image of the surface of M381 (left) which shows only a slight amount of background surface roughness. Measured XRD pattern (blue) compared with a simulation (red) for M381. Qualitatively it is seen that there is a SL period variation based on the placements of the harmonic peaks relative to the simulation. 129
4.29 Measured (solid) and simulated (dashed) reflectance spectra for three GaSb/$AlAs_{0.08}Sb_{0.92}$ DBR mirrors with ten periods. 130

5.1 Schematic diagram of the BA (left) and NR (right) fabrication process. 134
5.2 Each ICL is connected by at least two Au wires to the contact pads of the ceramic package so that burnout from large injection currents may be prevented. The inset shows the final configuration of the ICLs ready for measurement. 135

5.3 A semiconductor laser with a thin active layer. The emitted beam forms an elliptical pattern, where the divergence in the "fast axis" direction is more pronounced than in the "slow axis" direction.[2] 136
5.4 A comparison of the spectral response and sensitivity of the various internal detectors for the FTIR using the internal infrared source. . . . 138
5.5 The spectral response of a type-I GaSb-based ICL operating at 80 K, with a threshold current of 9.5 mA and a wavelength of 2.82 μm. The laser ridge width is 100 μm, while the cavity length is 1.5 mm. 139
5.6 Example showing the wavelength tunability with temperature for a type-I ICL operating with an 80 K emission wavelength of 2.82 μm in cw mode, which redshifts to 3.19 μm at room temperature in pulsed mode, resulting in a tuning of 1.69 nm/K. 140
5.7 An example IVL result showing the typical IV characteristics for an ICL, albeit with a large V_{th}, on the left. On the right is the IL result, which lists the I_{th}, maximum output power, and thermal rollover of the ICL. . 145
5.8 Experimental setup diagram for IVL measurements in pulsed mode. . . 148
5.9 Experimental setup for IVL measurements in pulsed mode showing the alignment of the two lenses needed to guide the beam into the MCT detector. 149
5.10 Filter attenuation factor between the 100x and 10x filters showing the 10x filter data beginning to saturate, which dramatically decreases the attenuation factor. 150
5.11 Theoretical depiction of a square pulse shape for the signal being measured by the lock-in amplifier.[5] 151
5.12 Spectral transmission for a CaF2 cryostat window (left) and a ZnSe cryostat window (right)[Data courtesy of ThorLabs]. 153
5.13 Pulsed IVL curve for EB7289BA1-1A taken with two different current sources and on two different dates. 155
5.14 Oscilloscope comparison under the same injection current for EB7289BA1-1A using the Avtech source (left) and the ILX LDP-3811 (right), which shows a significant pulse delay or "turn-on" time for the Avtech. 156
5.15 Measured IL curve under pulsed operation for EB7523BA3-2F using the Avtech and ILX current sources and different scaling methods. 157

6.1 Qualitative band diagram of the modern ICL with typical features including the W-QW active region, the GaInSb hole injector, and the heavily Si-doped and also thinned electron injector. 159
6.2 Qualitative depiction of the general layer structure for the ICL, where a different waveguide is typically used, depending on the type of ICL grown (GaSb-based or InAs-based). 161
6.3 Simulated optical modal profile and refractive index for two hypothetical waveguides for InAs-based ICLs with similar layer thicknesses. The first waveguide (blue) is composed of the n^+-InAs plasmon cladding and undoped InAs SCL, while the second (red) also incorporates an intermediate SL cladding formed of a thin InAs/AlSb SL. 165

6.4 Calculated optical modal profile and refractive index of the waveguide for EB7289 at 80 K with an emission wavelength λ measured from the pulsed spectra of 10.5 μm. 170
6.5 Illustrated band edge diagram of one cascade stage and the layer sequence for EB7342, which includes $InAs_{0.5}P_{0.5}$ barriers in the QW active region. 172
6.6 Measured (blue) and simulated (red) XRD patterns for EB7289 (left) and EB7342 (right), which demonstrates good crystalline quality. 173
6.7 Illustration of the BA fabricated wafers for EB7289 and EB7342. 174
6.8 SEM images taken at (a) 100,000×, (b) 10,000×, and (c) 50,000× magnifications for several laser bars after fabrication showing various measurements performed on the IC structures with the SEM software. 175
6.9 Threshold current density (J_{th}) as a function of temperature (T) for several devices made from the first ICL wafer. The inset depicts the pulsed lasing spectrum for device EB7289BA1-1A at various temperatures. 176
6.10 Current–voltage- and output power characteristics for EB7289BA1-1A in cw mode, where arrows indicate threshold at various temperatures. The inset shows the cw emission spectra between 80 and 107 K. 177
6.11 Pulsed output power as a function of the injection current at several temperatures for EB7289BA1-1A. 178
6.12 J_{th} as a function of T for several devices from the EB7342. The right inset shows the pulsed lasing spectrum for EB7342BA1-3E, while the left inset shows a zoomed in view depicting the blue shift of 4 nm with increasing T near the maximum operating temperature. 179
6.13 Pulsed current–voltage- and output power characteristics at several temperatures for EB7342BA1-3F. The inset is its lasing spectrum at 120 K. 181
6.14 Calculated optical modal profile and refractive index of the waveguide for EB7541 at 80 K with an emission wavelength λ measured from the pulsed spectra of 10.2 μm. Also shown are estimated optical parameters of the waveguide based on the simulation results. 183
6.15 Calculated optical parameters of the four 20-stage InAs-based ICLs in this study, with the 80 K emission wavelength λ measured from the pulsed spectra. 183
6.16 Measured XRD pattern (blue, top) compared to the simulated pattern (red, bottom) for ICL wafer EB7541. 185
6.17 Threshold current density (Jth) as a function of temperature for several devices made from the four InAs ICL wafers. 187
6.18 CW results for the current-voltage-power (IVL) characteristics (a) for EB7541BA3-3H along with the cw emission spectrum (b) between 80 K and 123 K. 189
6.19 Pulsed current–voltage–power (IVL) characteristics for EB7541BA3-3H with the lasing spectrum (inset) at 150 K and 155 K. 190
6.20 Current–voltage–power (IVL) characteristics for EB7547BA3-2A in cw mode. The inset shows the cw lasing spectrum between 80 K and 102 K. 191
6.21 Pulsed current–voltage–power (IVL) characteristics for EB7547BA3-2A with the lasing spectrum (inset) at 120 K and 137 K. 192

6.22 Current–voltage–power (IVL) characteristics for EB7523BA3-2F in cw mode. The inset shows the cw emission spectrum between 80 K and 90 K. 194
6.23 Pulsed results for the current–voltage–power (IVL) characteristics (a) for EB7523BA3-2F along with the pulsed emission spectrum (b) between 80 K and 160 K. 195
6.24 Current–voltage–power (IVL) characteristics for EB7539BA2-2D in cw mode. The inset shows the cw emission spectrum between 80 K and 85 K. 196
6.25 Current–voltage–power (IVL) characteristics for EB7539BA2-2A in pulsed mode. The inset shows the pulsed emission spectrum between 120 K and 150 K. 197
6.26 Several estimated device parameters based on measured results in pulsed mode at 80 K and their respective waveguide simulations. 199

7.1 Schematic drawing of the GaSb-based ICL design.[6] 203
7.2 DIC images of Y061L (left) and Y062L (right) under 40× magnification. Both wafers have a similar average surface defect density as shown, where the background surface is slightly rougher for Y061L. 204
7.3 XRD patterns for Y061L (blue), Y062L (red), and the simulated pattern (red) according to the intended design. 205
7.4 Qualitative band diagram of Y082L, a GaSb-based ICL with much thinner InAs layers in the W-QW active region in order to support shorter wavelength operation between 3.3 and 3.4 μm at RT. 208
7.5 The calculated optical modal profile and refractive index for (a) Y082L and (b) Y083L. Listed in the plots are the optical confinement factor (Γ), the internal loss due to free-carrier absorption (α_i), the threshold gain (g_{th}), and the effective refractive index (n_{eff}). 209
7.6 The experimentally measured XRD pattern (blue) along with the simulated pattern (red) for Y082L, which is representative of both ICL wafers grown. 211
7.7 Simulated XRD pattern for a 1.7 μm thick $InAs_{0.91}Sb_{0.09}$ alloy on a GaSb substrate. 213
7.8 Measured XRD pattern (blue) for Y082L along with the simulated XRD pattern (red) of a 1.7 μm thick $InAs_{0.91}Sb_{0.09}$ alloy on a GaSb substrate. The inset shows a zoomed in view in the vicinity of the substrate peak, which allows for the identification of the alloy peak from the measured XRD data, and the subsequent determination of the alloy composition. . 214
7.9 The J_{th} and V_{th} results as a function of temperature for two representative devices from ICL wafer Y082L with different laser ridge widths in both cw and pulsed modes. Included are the calculated R_{th} and T_o values. . 217
7.10 CW IVL characteristics for Y082LBA1-3F (a) and Y082LBA1-3H (b) from 80 K to their maximum operating temperatures of 240 K and 225 K, respectively. Also shown are the extracted external quantum efficiency values (EQE). 218
7.11 Normalized spectra under pulsed excitation for (a) Y082LBA1-3F and (b) Y082LBA1-3H. Shown in the plot are the threshold current, threshold current density, threshold voltage, and emission wavelength at each temperature step. 219

7.12 The J_{th} and V_{th} as a function of temperature for two representative devices from ICL wafer Y083L with different laser ridge widths in both cw and pulsed modes. Included are the calculated R_{th} and T_o values. . 221
7.13 CW IVL characteristics for (a) Y083LBA1-3G and (b) Y083LBA1-3E from 80 K to their maximum operating temperatures of 228 K and 210 K, respectively. Also shown are the extracted external quantum efficiency values (EQE). 222
7.14 Normalized spectra under pulsed excitation for (a) Y083LBA1-3G and (b) Y083LBA1-3E. Shown in the plot are the threshold current, threshold current density, threshold voltage, and emission wavelength at each temperature step. 223
7.15 DIC images of Y086L (left) and Y087L (right) under 40× magnification. Both wafers have a similar average surface defect density as shown, which is slightly smaller than previous GaSb-based ICLs. However, the background surface roughness in both of these new ICL wafers is larger than previous ICLs. 228
7.16 The experimentally measured XRD pattern (blue) along with the simulated pattern (red) for Y086L, which is representative of both ICL wafers grown. 229
7.17 The calculated optical modal profile and refractive index for Y082L (red) and Y086L (blue) based on the intended operating wavelength, but with the structure thicknesses modified by the measured XRD results. 231
7.18 Normalized spectra under cw excitation for (left) Y086LBA1-2A/B and (right) Y086LBA1-2C. Shown in the plot are the threshold current, threshold current density, threshold voltage, and emission wavelength at each temperature step. 232
7.19 CW IVL characteristics for (a) Y086LBA1-2B and (b) Y086LBA1-2D from 80 K to their maximum operating temperatures of 260 K and 250 K, respectively. Also shown are the extracted external quantum efficiency values (EQE). 232
7.20 The J_{th} and V_{th} as a function of temperature for devices from ICL wafers Y082L, Y086L, and Y087L with different laser ridge widths in both cw (solid) and pulsed (dashed) modes. 233
7.21 Normalized spectra under pulsed excitation for (a) Y086LBA1-1H and (b) Y086LBA1-1F. Shown in the plot are the threshold current, threshold current density, threshold voltage, and emission wavelength at each temperature step. 234
7.22 Normalized spectra under cw excitation for (a) Y087LBA1-1H and (b) Y087LBA1-1F. Shown in the plot are the threshold current, threshold current density, threshold voltage, and emission wavelength at each temperature step. 236
7.23 CW IVL characteristics for (a) Y087LBA1-1H and (b) Y087LBA1-1F from 80 K to 250 K, respectively. Beyond 250 K, no appreciable output power was detected in cw mode. Also shown are the extracted external quantum efficiency values (EQE). 237

7.24 Normalized spectra under pulsed excitation for (a) Y087LBA1-1H and (b) Y087LBA1-1F. Shown in the plot are the threshold current, threshold current density, threshold voltage, and emission wavelength at each temperature step. 238

Abstract

Interband cascade lasers (ICLs) based on the type-II quantum well (QW) active region have attracted much interest over the years, in large part due to their low power consumption. Their operation hinges on two key features; interband transitions in type-II quantum wells and a cascade configuration which enhances the gain, per current density. The cascade configuration forms an energy staircase where an injected electron recombines with a hole within the active region of a single cascade stage to generate a photon, and is then quickly swept into the next cascade stage, where the same process may occur. In this way, each injected electron may generate a photon for every cascade stage it travels through, allowing for quantum efficiencies that exceed the conventional limit of unity.

The overall ICL structure is built from a combination of multiple superlattice (SL) heterostructures, forming as many as hundreds of individual layers, with some of the layers having sub-nanometer thicknesses. Therefore, the growth of these devices requires atomic layer precision in thickness control in order to achieve an overall strain-balanced system where defects are minimized, leading to superior crystalline quality and acceptable device performance. Molecular beam epitaxy is a crystal growth technique that is ideal for this endeavor, with growth of IC related structures spanning a range of III-V materials including InAs, GaSb, AlSb, and their related alloys on both InAs and GaSb substrates.

A variety of MBE optimization and calibration efforts are presented, which tackle some of the most important SL and alloy structures in the ICL. Methodologies are developed to achieve nearly lattice-matched alloys with ideal composition parameters and minimal surface defects, characterized by differential interference contrast microscopy (DIC) and x-ray diffraction (XRD). Also, new growth techniques are developed and employed to achieve superior crystalline quality in SL

systems, which led to nearly an order of magnitude reduction in the perpendicular mismatch between measurable SL structures and the substrate, and was implemented in GaSb-based ICLs to achieve the first ever growth of these structures on the GENxplor system in our group.

While GaSb-based ICLs have demonstrated efficient room temperature (RT) operation in the 3-6 μm range, extending the operating wavelength of these ICLs presents several challenges including the reduced thermal conductivity of the optical cladding layers and the diminished electron-hole wavefunction overlap in the type-II QW, which arises due to the increased InAs QW width needed to support long wavelength emission. To alleviate the former concern, an advanced waveguide that was originally developed for InAs-based ICLs operating at 4.6 μm[7] was employed in InAs-based ICLs designed to emit beyond 10 μm. The advanced waveguide may enhance the device performance by reducing the free-carrier loss and improving the optical confinement in the cascade active region. Broad area (BA) devices made from InAs-based ICL wafers with this design feature showed operation in cw mode up to 10.9 μm at 80 K with output powers of up to 32 mW/facet, the largest output power among interband lasers at this wavelength, and up to 11.5 µm at 137 K in pulsed mode, the longest emission wavelength achieved for the standard W-QW active region ICL.

To address the issue of the diminished electron-hole wavefunction overlap at longer wavelengths, $InAs_{0.5}P_{0.5}$ barriers are introduced, in addition to the standard AlSb barrier, in the W-QW active region, which have a lower valence band edge than the traditional AlSb barrier used. Based on the relevant perspective on band edge positions in type-II heterostructures[8], a barrier material with As or P containing compounds lowers the electronic state in the InAs QW. This allows the InAs well width to be reduced, or at least not increased as much, in devices designed to operate at longer wavelengths, which preserves a more substantial

wavefunction overlap with the GaInSb hole well. The first implementation of this design yielded ICLs operating in pulsed mode up to 120 K beyond 13.2 μm, which is the longest wavelength ever achieved among III-V interband lasers and validated the prediction that such barrier layers could enhance the long wavelength emission.[8] ICLs with revised designs utilizing the advanced waveguide and the $InAs_{0.5}P_{0.5}$ barriers exhibited cw operation beyond 12.4 μm, which is the first demonstration of a BA ICL operating in cw mode at such a long wavelength, and up to 150 K, beyond 13 μm in pulsed mode. CW output powers beyond 12 mW/facet were measured, comparable with and even higher than previous ICLs without $InAs_{0.5}P_{0.5}$ barriers operating at much shorter wavelengths (<10 μm).[9]

The advanced waveguide was also investigated in GaSb-based ICLs tailored to emit near 3.3 and 3.4 μm at RT. The implementation of this feature resulted in cw operation of BA ICLs up to 260 K and pulsed operation up to 390 K, with RT threshold current densities as low as 151 A/cm^2, akin to other GaSb-based ICLs using the conventional waveguide at similar wavelengths.[10] Furthermore, the characteristic temperature (T_o) of some of these ICLs was nearly 60 K at RT, which is the highest among RT ICLs with similar lasing wavelengths, indicating the potential for the advanced waveguide in GaSb-based ICLs designed to emit at shorter wavelengths.

Chapter 1

Introduction

Today, much of our life is dominated by technological innovations developed over the last 100 years, during the so-called information revolution, which is sometimes referred to as the scientific and technical revolution, or the post-industrial society. At the heart of it all is the merging of science with society in fundamental ways that shape our lives, from scientific discovery to economic productivity to pleasure and relaxation. Intrinsic to this are technologies which have arisen from the development of our most successful physical theory: quantum mechanics. An important branch of these quantum technologies are those that in some way exploit or utilize infrared radiation for practical purposes to enrich our lives.

1.1 Infrared Radiation and Applications

Infrared radiation is the portion of the electromagnetic spectrum which ranges from approximately 0.7μm to 1 mm, just longer than visible light, but shorter than microwave radiation as shown in Fig. 1.1. Generally, this region is sub-divided into several smaller bands, and at times these sub-divisions may have varying degrees of nomenclature, for the purposes of this dissertation that of Choi will be adopted[11]. These sub-divisions include the near-infrared (NIR) from 0.7 μm–2 μm, the mid-infrared (MIR) from 2 μm–20 μm, and the far-infrared (FIR) from 20 μm–1000 μm.

There exist a multitude of practical applications by harnessing either the generation or absorption of light within this bandwidth. For example, the NIR part of the spectrum is widely used for long distance communication utilizing fiber optics[12], while the FIR region is suited for thermal imaging, useful for

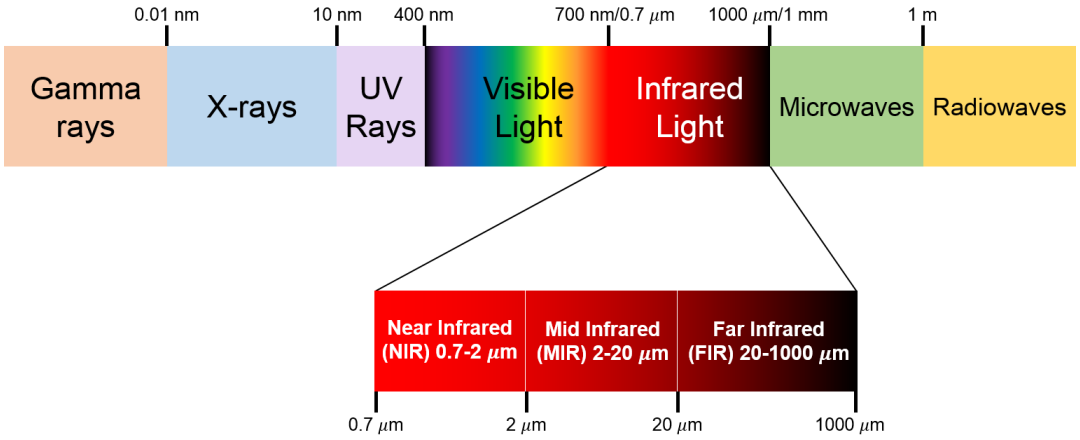

Figure 1.1: Depiction of the electromagnetic spectrum. The blown up portion shows the sub-division of the infrared part of the spectrum into its three regions.

applications such as night-vision detection and medical imaging. Also, in the NIR and shorter wavelengths in the MIR portion of the spectrum, thermophotovoltaic devices can be used to capture radiation from a heat source, generally in the temperature range of 1000-2000 K[13, 14] and convert it into usable electricity. In the MIR, lasers may be used in military applications such as for stand-off detection[15, 16], jamming heat-seeking missiles[17], and other security and defense measures[18]. They may also be used in other areas such as industrial process control[19] and free space optical communication[20, 21]. Perhaps the most notable and important application in the MIR is the sensing and detection of various gas and chemical species. Such molecules, which readily absorb light in this region, are often referred to as "fingerprint" molecules. Their absorption of light in the MIR is associated with their rotovibrational modes, which include stretching, vibration, and rotation under infrared illumination. These molecules include those associated with greenhouse effects, natural gas, manufacturing processes, and which may constitute indicators of life on a planet. Examples of such molecules include methane (CH_4), ethane (C_2H_6), carbon monoxide (CO), carbon dioxide (CO_2), sulfur dioxide (SO_2), formaldehyde (CH_2O), hydrochloric acid (HCl), among

others, whose simulated absorption spectra in the MIR are shown in Fig. 1.2[22]. Detection of the various species of gas molecules typically requires cw emission in a single spectral mode, though output power as low as 1 mW is sufficient as opposed to the militaristic applications which need not have high spectral precision, but do require large output power. By detecting some of these base molecular compounds, more complex structures in an environment may be inferred, as well as the conditions and/or causes of the generation of such molecules within an environment.

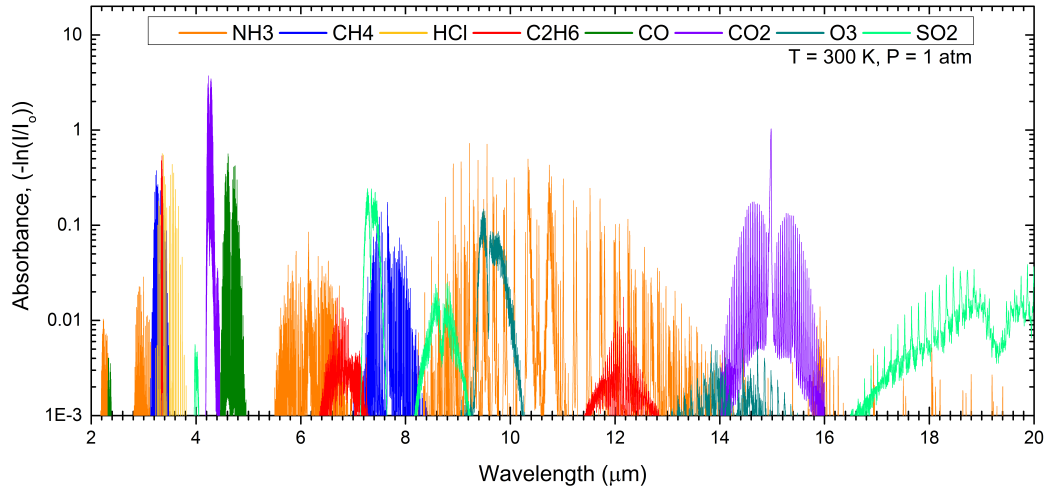

Figure 1.2: Selected simulated absorbance spectra for a number of fingerprint molecules using the websim SpectraPlot, which uses the HITRAN 2012 and HITEMP 2010 databases.

For example, a single-mode distributed feedback (DFB) interband cascade laser (ICL) operating at 3.27 μm was deployed for CH_4 detection on Mars. The ICL device is part of the tunable laser spectrometer (TLS) of the Sample Analysis at Mars (SAM) instrument package, which is housed on the Curiosity rover as part of the NASA Mars Science Laboratory (MSL) mission, which arrived on August 6, 2012. Detection of atmospheric CH_4 at a mean value of 0.69 $\pm$ 0.25 parts per billion by volume (ppbv), with episodically elevated levels of 7.2 $\pm$ 2.1 ppbv produced by an unknown source, was discovered and published in 2015[23]. The

multitude of potential applications in the infrared has beckoned the development of device technologies which can rise to meet the growing needs of modern society, especially over the last 50 years.

1.2 Laser Development and Fundamentals

Today, there exist many types of laser technologies. From high power, destructive devices aimed with military applications in mind, to portable low power technologies such as the hand held laser pointer. The following section is meant to showcase the humble beginnings of the laser to the modern, rapid development of various laser technologies.

1.2.1 A Brief History of Laser Development

The beginning of the laser can trace its roots all the way back to 1917 and the concepts of spontaneous and stimulated emission, forming part of the fundamental basis for the laser, that was first put forth by Albert Einstein[24]. It was decades later when the first practical technology was developed, that of the maser, which is the microwave analog to the laser, by Charles Townes at Columbia University. First Townes developed the working theory in 1951, and shortly thereafter, in 1953, he and his team developed the first experimental maser, using a stream of energized ammonia (NH_3) molecules to produce the amplification of microwaves at around 24 GHz[25]. Later in 1958 Townes and Schawlow extended the theory of the maser to visible and infrared light, now named the laser [26]. The first laser to ever be experimentally realized though, was by Theodore Maiman at Hughes Research Laboratories in 1960, based on the pink ruby crystal[27]. Just a couple of years later in 1962, the first working semiconductor laser diode, based on GaAs p-n junctions, was developed by Robert Hall at GE Research Laboratory, which

operated in pulsed mode at 77 K and with a very large (by modern standards) threshold current density (J_{th}) of 8500 A/cm^2[28]. Following several years of rapid development of a variety of lasers by various research groups, including the CO_2 laser(1964), Nd:YAG laser(1964), Dye laser (1966), and Excimer laser(1970), the first room temperature (RT) semiconductor laser operating in continuous-wave (cw) mode was demonstrated by Hayashi and Panish at Bell Laboratory[29]. They used a GaAs-$Al_xGa_{1-x}As$ double heterostructure design, where the smaller bandgap GaAs is placed between the layers of $Al_xGa_{1-x}As$, which act as the cladding (or waveguide) for the device. Their design significantly reduced the J_{th} of the Fabry-Perot style diode to a mere 1600 A/cm^2.

The next couple of decades would see further refinements made to semiconductor lasers, with other novel devices such as the free electron laser (1977) and the X-ray laser (1980) coming into existence. However, the experimental demonstration of the first cascade laser, the quantum cascade laser (QCL), operating in pulsed mode at 125 K and at 4.3 μm by Faist et. al. in 1994[30] dramatically shifted the landscape of MIR semiconductor laser devices. Later that year, the concept of the interband cascade laser (ICL) was proposed by Rui Q. Yang at the 7th International Conference on Superlattices, Microstructures, and Microdevcies and later published in 1995[31, 32]. These cascade-based devices, whose operation hinges on the cascaded emission of photons, have become the standard for efficient and coherent semiconductor sources offering cw operation at ambient temperatures over much of the infrared spectral range of the aforementioned applications. To better understand these devices, the following sections present a review of basic laser concepts and the quantum well (QW) configurations that paved the way for these semiconductor device technologies.

1.2.2 Laser Fundamentals

The name itself is an acronym, standing for **L**ight **A**mplification by the **S**timulated **E**mission of **R**adiation, and which reflects the physical processes involved in the device. Laser light has several important properties which differs from other forms of light. First, the light from a laser exhibits a high degree of spatial coherence. This feature allows the light to be focused into a small spot size. Additionally, this means that the light is highly directional, allowing the emitted radiation to remain mostly collimated after passing through an aperture over long distances. In addition to the high spatial coherence, laser emission is also nearly monochromatic, indicating its high degree of temporal coherence. Central to the development of the laser is the resonant cavity and the active (or gain) medium. The cavity acts as an optical resonator, allowing for the enhancement of the electric field produced within the gain medium. The gain medium, allowing for the amplification of the electric field, must be a type of material that has an excited state that is metastable, meaning the electrons which transition there, remain in the excited state for a long enough time such that over small time scales, there will exist a greater number of electrons in the excited state than in the ground state (for a 2-level system). Such a scenario is referred to as a population inversion and is required for the generation of laser light. The photon energy, and hence the emission wavelength, of the process is characteristic of the energy difference between these two states. Generally speaking, a gain medium may typically consist of a 4-level system where the 2nd excited state acts as the metastable state for population inversion as depicted in Fig.1.3.

The typical, and most simple cavity type is the so-called Fabry-Perot cavity which is comprised of two mirrors separated by some distance L, known as the cavity length, that are partially transmitting. The small portion of the optical wave

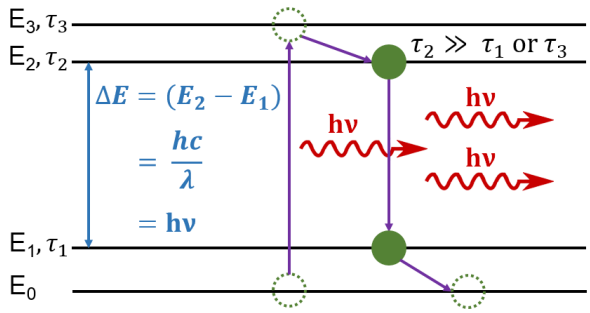

Figure 1.3: Depiction of a 4-level system, with E_2 being the metastable state where population inversion occurs. Excited electrons in this state couple to the background electric field, which is the catalyst for generating stimulated emission.

that is transmitted through the mirrored ends of the cavity form the laser beam. These mirrors allow for the optical wave to be bounced back and forth, where if the gain sufficiently overlaps, creates an optical feedback condition. The optical gain profile is typically characterized by a Gaussian profile. The electrons in the excited state couple to this field and are enticed to transition to the ground state together, giving rise to stimulated emission. The stimulated emission continues to undergo multiple round trip reflections, giving rise to constructive interference within the cavity leading to cavity modes with a characteristic mode spacing called the free spectral range (FSR) as shown in 1.4.

The FSR is related the gain medium and the resonant cavity by,

$$\Delta\nu_{FSR} = \frac{c}{2Ln_g} \tag{1.1}$$

where c is the speed of light in vacuum, L is the cavity length as previously mentioned, and n_g is the group index of refraction of the gain medium. The lasing emission profile is a convolution of the Gaussian gain profile and the cavity modes as shown in Fig. 1.5.

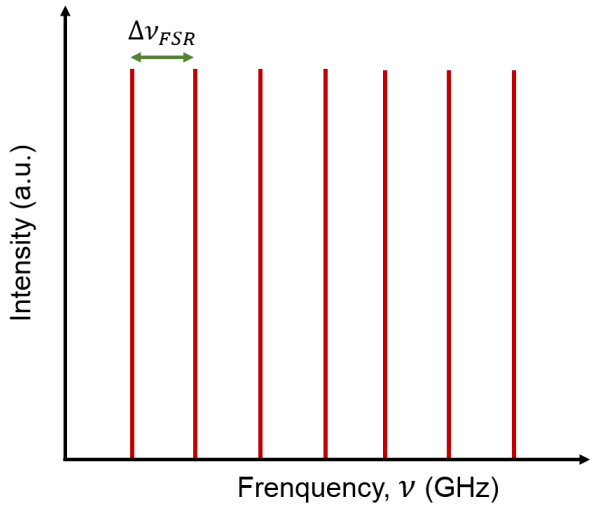

Figure 1.4: Depiction of the cavity modes of a Fabry-Perot style cavity, with the free spectral range (FSR) showing the mode spacing.

1.3 MIR Semiconductor Lasers

The rapid development of semiconductor device technology over the last few decades also extends to that of the laser. Here the hypothetical atomic energy levels as depicted in Fig.1.3 are instead replaced by the conduction and valence bands formed from the use of appropriate materials arranged to form various types of quantum well configurations, also known as heterostructures. The following sections detail these specifics and discuss how to make use of these arrangements to form the QCL and ICL, respectively.

1.4 III-V Materials

One of the principle workhorses of the modern semiconductor laser technology is that of an active region based on the family of III-V materials as shown in Fig. 1.6[33]. These materials consist of those found in group III and V of the periodic table, which include: Al, Ga, In, N, P, As, and Sb and their related binary and alloy compounds, and are particularly well suited to optoelectronic applications in the

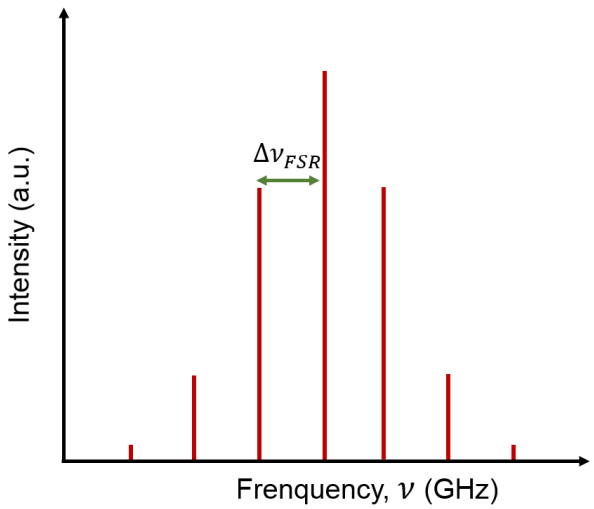

Figure 1.5: Qualitative depiction of the convolution of the Fabry-Perot cavity modes with that of the optical gain profile, resulting in the emission spectrum of a laser.

infrared. In the figure, direct bandgap transitions are shown by solid curves while indirect transitions are shown by dashed curves. Lines connecting two different binary materials refer to their ternary/quaternary compounds. The most well established and mature III-V material system is that of GaAs, used in many applications from solar cells, to infrared detectors, to lasers, with other material systems seeing increased development for practical applications such as InP, used in various optoelectronic devices[34] and GaN, making headway in the development of high intensity blue light emitting diodes (LEDs)[35, 36]. The 6.1 Å family is a subset of the III-V material system which consists of those materials whose binary lattice constants are close to 6.1 Å, such as InAs, GaSb, and AlSb, which are well suited to quantum well engineering through MBE growth as will be discussed in more detail in Chapter 2. These materials have a broad span of bandgaps, ranging from 0.36 to 2.2 eV at room temperature as well as different types of band-edge alignments that may be exploited for a variety of practical devices such as high electron mobility transistors[37], resonant tunneling diodes[38, 39], infrared

lasers[32, 40], and infrared photodetectors[41]. The following sections detail some key aspects of QWs made from the 6.1 Å family of materials.

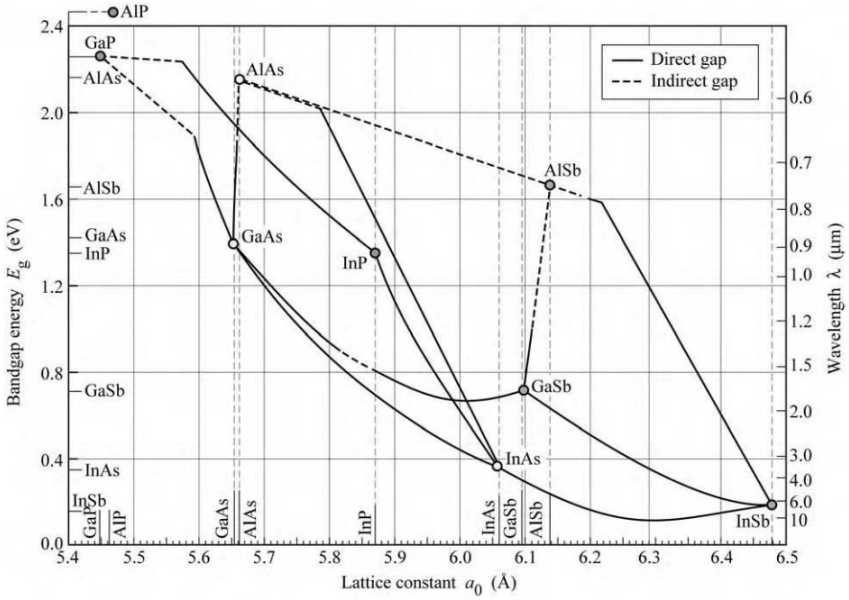

Figure 1.6: Energy bandgap (left axis) and wavelength of emission (right axis) with lattice constant for the various III-V semiconductors.

1.4.1 Quantum Well Configurations

For a semiconductor laser, multiple quantum wells (MQW) must be used in order to create an active region that has sufficient gain to support efficient lasing. From an equivalent circuit perspective, there are two ideal configurations which may be used to create the active region. In the first type, which have traditionally been used for the so-called bipolar p-n junction lasers, a parallel configuration may be used where the quasi-Fermi level for the carriers between each stage is maintained at the same level as shown in Fig. 1.7. Here the electrons and holes are injected into the conduction and valence bands of the QW stack, where they become evenly distributed amongst the N number of QW's in the MQW system. As electron-hole-recombination takes place, a photon emission field is generated within the active region, which supports stimulated emission. As a parallel configuration,

the total J_{th} required to generate lasing comes directly from the equivalent circuit perspective,

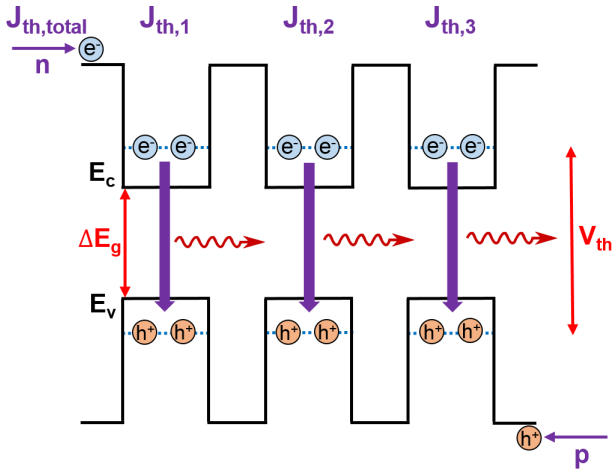

Figure 1.7: Depiction of a parallel MQW configuration.

$$J_{th,total} = J_{th,1} + J_{th,2} + J_{th,3} + ...J_{th,N} \rightarrow N \cdot J_{th,m} \tag{1.2}$$

where $J_{th,m}$ is the threshold current required to activate lasing in a single QW in this configuration. The threshold voltage (V_{th}) of the laser is related to the bandgap plus some small quantity arising from internal losses within the system[42] as,

$$V_{th} = \frac{E_g + \Delta E}{q} \tag{1.3}$$

The power consumed by a semiconductor laser in this parallel QW configuration may be expressed as,

$$P_{th,total} = P_{th,N-QW} + P_{th,device} \tag{1.4}$$

where $P_{th,N-QW}$ is the power consumed by the total active region of the N-stack series of QWs and $P_{th,device}$ is related to the total electrical resistance of the device

as a whole (sometimes referred to as the parasitic resistance). These terms may be written as,

$$\begin{aligned} P_{th,N-QW} &= V_{th} \cdot I_{th,total} = NV_{th}I_{th,m} \\ P_{th,device} &= I_{th,total}^2 \cdot R_{device} = N^2 I_{th,m}^2 R_{device} \end{aligned} \tag{1.5}$$

Therefore, Eq. 1.4 may be rewritten as,

$$P_{th,total} = P_{th,N-QW} + P_{th,device} \rightarrow NV_{th}I_{th,m} + N^2 I_{th,m}^2 R_{device} \tag{1.6}$$

As can be seen above, the parallel configuration results in a two carrier process involving both electrons and holes where the threshold current required for lasing scales linearly with the number of active quantum wells (QW), which may result in large threshold currents in devices with many QWs, while the power consumed by the device scales quadratically with the number of QWs. However, the tradeoff for such a configuration is a low threshold voltage.

The second QW configuration is the series configuration, which is typically used for quantum cascade-based lasers. In this configuration, there are two types of transitions which may occur, as opposed to the single transition type of the parallel QW, which are called interband and intersubband transitions. Fundamentally different, interband transitions are the same as those seen in the parallel QW, where the transition occurs between the conduction band and the valence band, involving two carrier types; electrons and holes. Counter to this is the intersubband transition in which the conduction band electron transitions from one subband to another within the conduction band, resulting in a single carrier process. A qualitative example of this is shown in Fig. 1.8 for an $Al_xGa_{1-x}As/GaAs/Al_xGa_{1-x}As$ heterostructure. In the series configuration, an electric field initiates forward bias and the bands bend, which results in a tunneling effect whereby each injected

electron transitions into each successive QW after generating a photon, leading to a high quantum efficiency (greater than 1 in the ideal case). Generally speaking, the quantum efficiency of the laser is the ratio between the number of photons produced to the number of electrons injected. This energy staircase effect is often referred to as the cascade effect[43], a depiction of which may be seen in Fig. 1.9 for both the interband and intersubband transition type.

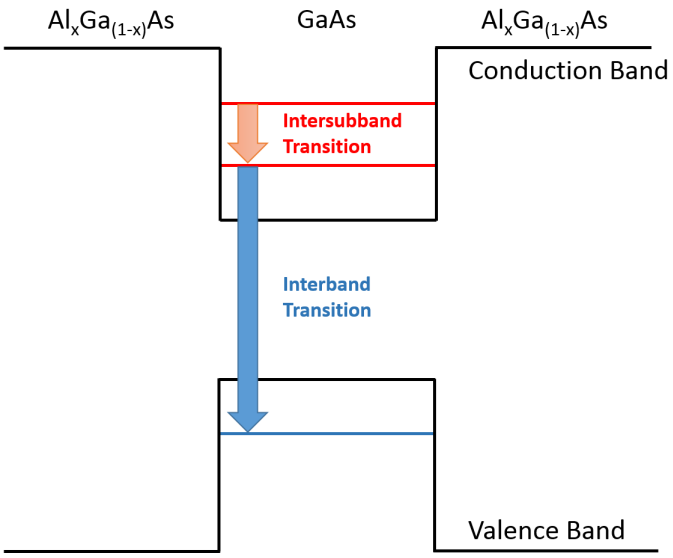

Figure 1.8: Qualitative depiction of an $Al_xGa_{1-x}As/GaAs/Al_xGa_{1-x}As$ heterostructure showing the difference between interband and intersubband transitions.

The emission from an intersubband transition is determined by the thickness/composition of the QW based on the energy separation between the subbands. Since the subband energy separation is small, typically wider band gap materials are required to create such QWs. Meanwhile, the interband transition emission is controlled by both the well width/composition and the semiconductor bandgap energy, giving an additional degree of freedom to the device designer.

Much like the parallel configuration, the total J_{th}, V_{th}, and subsequent P_{th} may be determined,

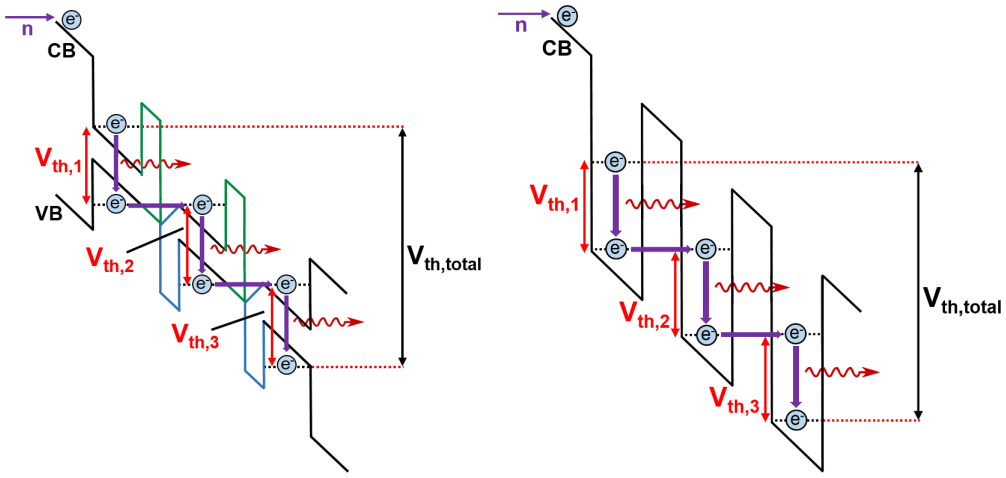

Figure 1.9: Depiction of a series MQW configuration which shows two different transition types. Pictured on the left is a series QW based on interband transitions with unipolar barriers (such as the case for an ICL), while the right shows a series QW based on intersubband transitions.

$$\begin{aligned} J_{th} &= J_{th,m} \\ V_{th,total} &= V_{th,1} + V_{th,2} + V_{th,3} + ...V_{th,N} \rightarrow N \cdot \frac{E_g + \Delta E}{q} \\ P_{th,total} &= NV_{th}I_{th,m} + I_{th,m}^2 R_{device} \end{aligned} \tag{1.7}$$

where in this configuration the same current flows through each QW, which gives rise to a threshold current which does not scale when the number of stages is increased! However, due to the cascade process multiple voltage drops are required in order to properly align the various QWs. In this case, as shown above, the total threshold voltage is the sum of each voltage drop along the N-stack series of QWs, which gives rise to a threshold voltage which scales linearly with the number of stages.

The parallel configuration requires higher current and lower voltage than the series configuration and also has a larger series resistance, subsequently generating more heat. Because of the nature in which current is injected into the parallel QW, there exists a non-uniformity in the carrier distribution which leads to higher

absorption loss. These issues are alleviated in the series configuration, since each QW in the stack has the same current, and hence a uniform carrier distribution[42]. Because of these differences in the threshold current and voltage, the resulting total power consumed by the series device in Eq. 1.7 compared with that of the parallel configuration in Eq. 1.6 indicates that the series configuration is more ideal for a lower power consumption device, especially when the number of cascade stages are increased. From a technological point of view, this is a preferred outcome for any type of portable device, which may rely on battery or solar power for its operation.

1.4.2 Band Alignment

In a QW, semiconductor materials with different bandgaps are combined to form heterostructures where the relative position of the conduction and valence band edges of the constituent materials lead to different types of QW band alignments due to their differing electron affinities. In order for the heterostructure formed to have the desired QW configuration, the type of band alignment is crucial for proper manipulation of carriers within the device. Typical band alignments include the type-I, type-II staggered, and type-II broken-gap alignments, which arise from materials common in the design of semiconductor devices. Fig. 1.10 depicts the position of the conduction and valence-band edges for a variety of semiconductors[2]. Of particular note is the central region, which comprises the various III-V based binary materials used heterostructure design for optoelectronic devices.

A qualitative representation of the various band alignments is shown in Fig. 1.11. In a type-1 band alignment, both the conduction and valence band edge of one material lay within the conduction and valence band edges of the second material, examples of which may include material combinations such as $Al_xGa_{1-x}As$/GaAs or AlSb/GaSb QWs. Here the electrons and holes are confined in the same layer,

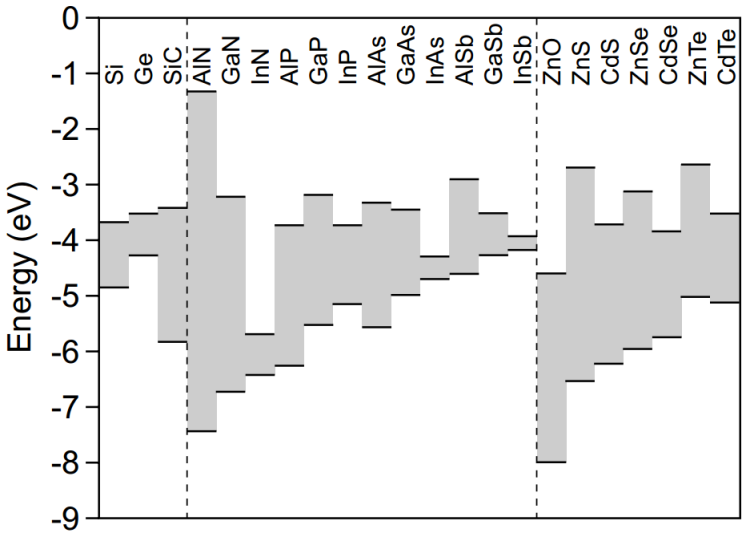

Figure 1.10: Position of the conduction and valence-band edges for a variety of semiconductors, taken from Grundmann.

where the wavefunction overlap is close to 100%, giving rise to spatially direct transitions. In the type-II staggered band alignment, the conduction band edge of one material lies below that of the other material. Also, the valence band edge of the same material lies below that of the other material as well. Examples of a type-II staggered band alignment include heterostructures formed from AlSb/InAs QWs. Lastly, the type-II broken-gap alignment consists of a material whose conduction band edge lies below the valence band edge of the other material. The broken gap alignment plays a crucial role in the active region of ICLs, and includes heterostructures such as GaSb/InAs and $Ga_xIn_{1-x}Sb$/InAs QWs. In both of the type-II band alignments, the electrons and holes are confined within adjacent material layers, leading to election-hole wavefunction overlaps that are less than 100%, with spatially indirect transitions. The tradeoff is that the energy gap can be somewhat smaller than that of the constituent bandgaps of the materials forming the heterostructure, which can be more advantageous for the design of tailored emission wavelengths in ICLs.

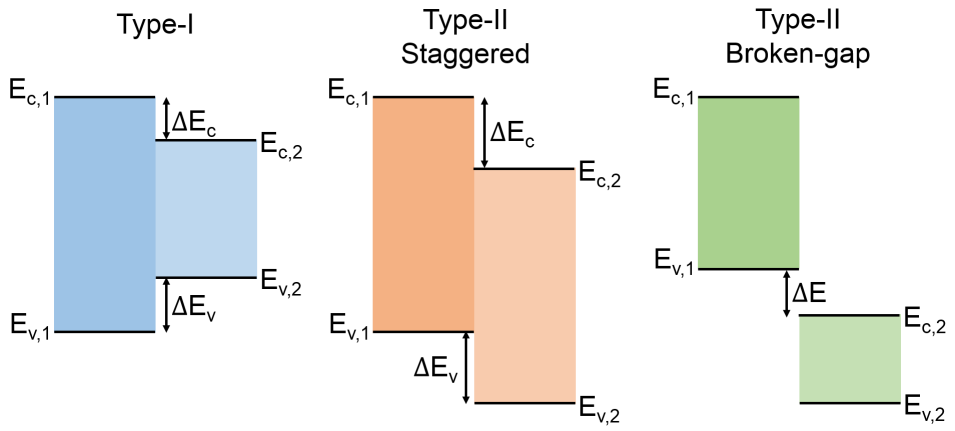

Figure 1.11: Qualitative depiction of the various types of band alignment in MQW structures.

1.5 Cascade Lasers

In the years leading up to the early 2000s, III-V-based MQW diode lasers utilizing the type-I band alignment were thought to be the preferred method to achieving a practical IR source which could operate at room temperature (RT)[17]. However, lasers based on this configuration operated typically in the NIR and low end of the MIR, and in order to be usable among a broader range of the IR spectrum for potential applications, their wavelengths would have to be extended further into the MIR. The thought at the time was to increase the strain in the Sb containing layers. One such approach used compressively strained $InAs_{0.935}Sb_{0.065}$ QWs with tensilely strained $In_{0.15}Al_{0.85}As_{0.9}Sb_{0.1}$ barriers to achieve emission between 3.2 and 3.55 μm with pulsed operation up to 225 K and cw operation up to 175 K.[44]. More recently, another group achieved cw emission of 3.15 μm at 290 K with a more significant output power of 220 mW[45] using an asymmetric separate confinement heterostructure approach. Here the QW active region was formed of an AlGaInAsSb/GaInAsSb/AlGaInAsSb heterostructure, along with an AlGaAsSb separate confinement layer and AlSb/InAs hole stopper, the latter two in place

to suppress carrier recombination outside of the active region in order to improve the internal efficiency of the device. Since such lasers rely on transitions between energy bands across the parallel QW configuration, the population inversion is broadly distributed across the wells leading to a gain spectrum that is relatively broad as well. Also, the longest emission wavelength to date for MQW diode lasers in cw mode at RT is 3.44 μm[46, 47], indicating the fundamental physical limitations of the type-1 MQW diode technology toward extending their operating wavelengths into the longer MIR region.

Parallel to development on the type-1 MQW systems, significant progress has been made on quantum cascade-based lasers utilizing QWs and superlattices (SL) in the series configuration over the last couple of decades. Inspired by the seminal work of Esaki and Tsu on superlattices (SLs) in 1970[48] and the initial proposal on the possibility of amplifying electromagnetic waves in a SL by Kazarinov and Suris in 1972[49], Faist et. al. first published their pioneering work on the design and demonstration of a unipolar semiconductor injection laser, which they called the quantum cascade laser (QCL) in 1994[30]. The QCL was the first realized quantum cascade-based laser, which made use of intersubband transitions across multiple QWs connected in series. The significance was that the emission wavelength of the laser could be entirely determined by the energy separation of the subbands levels as governed by the quantum confinement in the heterostructure, which could allow tailoring of the emission wavelength over a broad range that could exceed the type-1 MQW diode laser capability. Also unlike the MQW diode laser, which generated a photon for every injected electron and hole, the QCL was capable of generating a photon for each cascade period every injected electron passed through, significantly improving the quantum efficiency of the device. The first QCL operated at 90 K with an emission wavelength of 4.26 μm, a V_{th} of 8 V, a J_{th} of 11 kA/cm^2, and a peak output power of 8.5 mW/facet. In the intervening years

since the first demonstration of the QCL, much work has gone into improving its performance and is beyond the scope of this dissertation, though some practical knowledge pertaining to QCLs is relevant when comparing to ICLs, and thus will be presented. More recently, an updated QCL with better wall plug efficiency (WPE) of nearly 30% in pulsed mode and 22% in cw mode was published (2020) by F. Wang out of the Razeghi group[50]. The laser had an emission wavelength of 4.9 μm with a cw output power of 5.6 W at RT. The J_{th} of the 45-stage QCL was 1.3 kA/cm^2 at its maximum WPE.

The QCL has undergone tremendous improvements since its original conception and implementation, but there exist several drawbacks to this device technology. Perhaps most important is the short carrier lifetime, which is on the order of $\approx$ 1 picosecond (ps), whereas the typical radiative transition time is on the order of 1 nanosecond (ns). This leads to significant optical phonon scattering within the QCL, which forces the device to require very large threshold current densities ($\approx$ 1 kA/cm^2 or more) to support lasing. Also, at least 30-40 cascade stages are required to provide sufficient gain in order to generate the lasing action, and so typically large threshold voltages ($\approx$ 10 V or more) are needed. These factors may limit possible applications for QCLs, especially those more suited to portable, lower power applications.

1.6 The Interband Cascade Laser

1.6.1 From Origin to Room Temperature Operation

In parallel with the development of the QCL was the ICL, which has several advantages. Because interband transitions are used instead of intersubband transitions, the fast optical phonon relaxation channel is eliminated from the active region, greatly increasing the carrier lifetime and allowing for a significant reduction

in the J_{th} required for lasing. For the ICL, the principle non-radiative transition affecting the device is due to Auger recombination, which occurs approximately three orders of magnitude slower than the phonon scattering in QCLs. Fewer cascade stages are also required, which led to a reduction in the V_{th} needed to provide sufficient gain. In fact, the first indication of the ICL was discussed at a conference by Rui Yang the same year the QCL was published (1994) and was later published in 1995[32]. The new concept was on the efficient extraction of electrons from the lower lasing subband by using a so-called leaky QW based on interwell photon-assisted interband tunneling, which would allow the electron or hole wavefunction to leak through more easily, thus reducing the lifetimes of the lower energy states. This could be accomplished because of the type-II broken gap alignment that exists between InAs and GaSb, and which allows for a strong coupling between the conduction band in InAs and the valence band in GaSb, forming a semimetallic interface. The overall structure consisted of an InAs/GaSb active region, which could include a thin barrier layer of AlSb between. Following this, an electron injection region was implemented to sweep the electron from one InAs/GaSb active region, into the next set of InAs/GaSb active regions. This combination of the active region and the electron injector form the cascade period of the ICL as shown in Fig. 1.12.

Just a year later, Meyer[51], with Yang et al., coined the term ICL for this style of device when they proposed the addition of the so-called "electron blocker" to improve the performance of the ICL. A key feature in the proposed improvement of the type-II ICL was the addition of a layer of $Ga_{0.7}In_{0.3}Sb$ between the InAs and AlSb in the active region. This added an extra hole well to act as a hole injector for holes traveling in the opposite direction as electrons, and which could prevent leakage from the electron active region, a qualitative depiction of which is shown in Fig. 1.13. A year later (1997) the first experimentally working ICL was realized

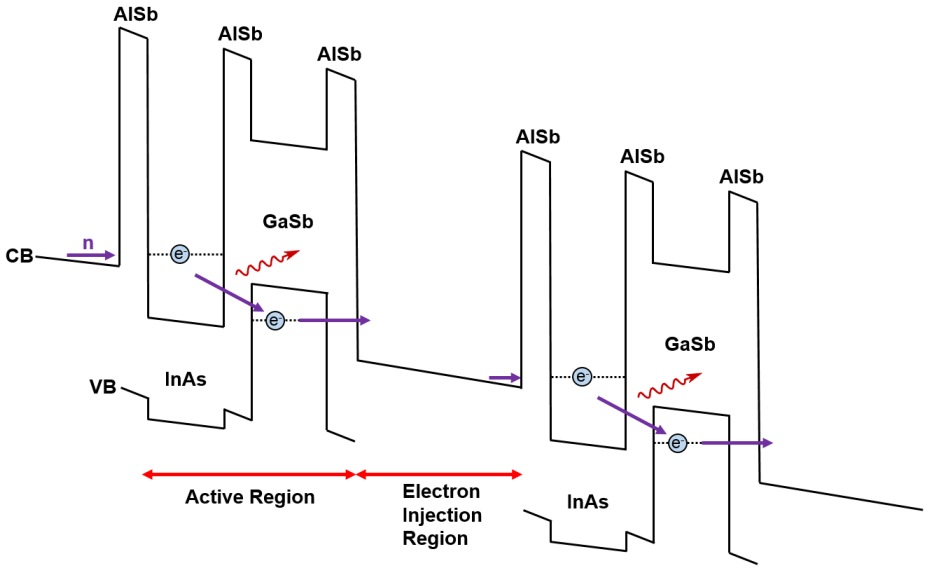

Figure 1.12: Qualitative band diagram of what would later become the ICL.

by Lin and Yang[52] of a 20-stage device operating up to 170 K in pulsed mode at 3.8 μm with a large J_{th} of several kA/cm^2. Later that same year saw further refinements in the design and production of the ICL with two groups publishing improved performance results. In one case, a 23-stage device with a maximum operating temperature of 170 K in pulsed mode was presented by Yang[53], which used a similar design to that of Fig. 1.13. At 80 K, this device exhibited a peak output power of 0.5 mW/facet with an external quantum efficiency (EQE) of 131% operating at 3.9 μm.

A theoretical investigation of MIR VCSELs by Vurgaftman and Meyer[54] showed that introducing a second InAs well after the GaInSb well, forming a "W-shaped" QW, could enhance the optical gain by increasing the electron-hole wavefunction overlap considerably, which then leads to a greater electron-hole recombination rate that may reduce the injection current required for lasing. An example of this design is shown in Fig. 1.14. Later the first sets of ICLs which incorporated the W-QW, along with 22 cascade stages, were produced. These ICLs exhibited lasing up to 225 K in pulsed mode at 3 μm with a peak output power

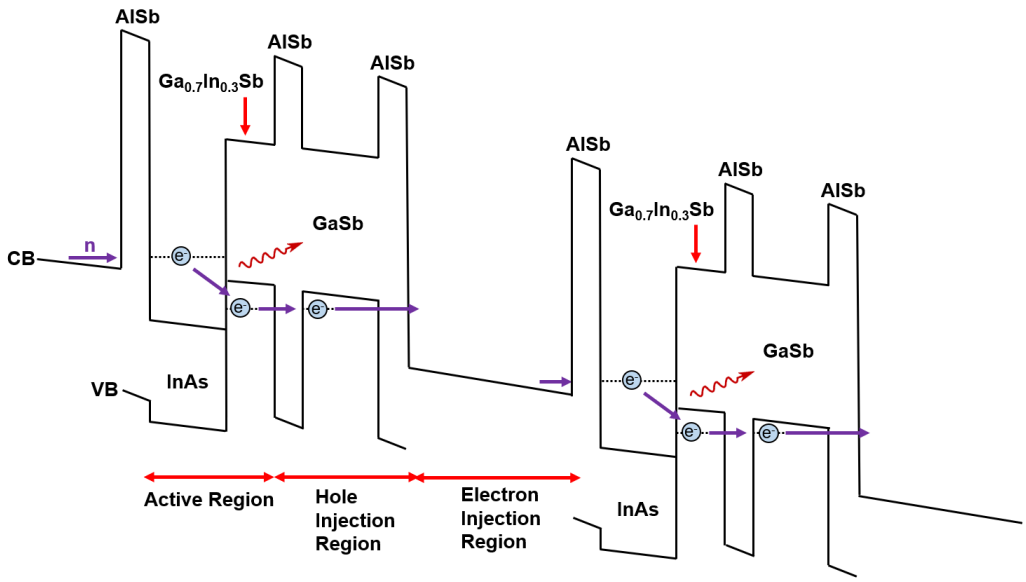

Figure 1.13: Qualitative band diagram of the ICL proposed by Meyer and Yang, which included the use of a single hole injector form from a layer of $Ga_{0.7}In_{0.3}Sb$.

of 430 mW and 532 mW, respectively, at 100 K. The first ICL had an EQE of 130%[55], while the second had an EQE of 160%[56]. The threshold current density was also significantly reduced thanks to these design changes, with a measured J_{th} = 170 A/cm^2 at 80 K for the second device. Since 2004 the W-QW, or "W" ICL, active region has become the standard for ICL design amongst the various research groups working on this laser.

By 2002, RT operation had been achieved by Yang et. al., operating out of Maxion Technologies and the Army Research Laboratory (ARL)[57, 58]. The design consisted of an 18-stage ICL based on the W-QW configuration. The ICL was able to operate up to 300 K in pulsed mode (with a low duty cycle of $<$ 1%) and 150 K in cw mode. The emission wavelength at the maximum pulsed temperature was 3.51 μm with a J_{th} of 6.9 kA/cm^2, while at 80 K threshold current densities as low as 13.2 A/cm^2 and a wall plug efficiency of 17% were observed. By 2003/2004, Yang et. al, working out of NASA's Jet Propulsion Laboratory (JPL) had significantly reduced the RT pulsed lasing J_{th} to $\approx$ 1 kA/cm^2 with

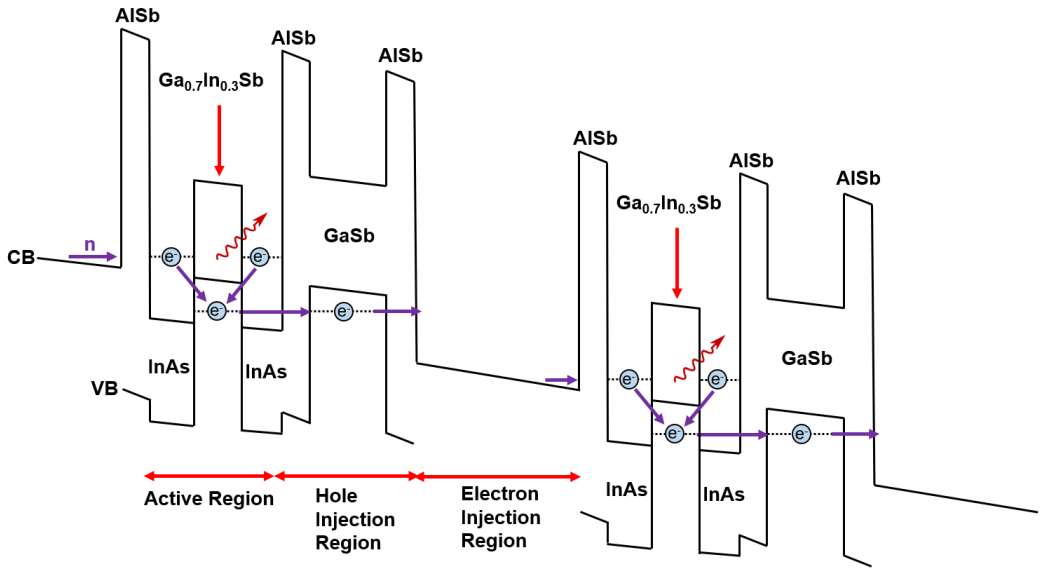

Figure 1.14: Qualitative band diagram of the ICL with the W-shaped active region consisting of InAs/$Ga_{0.7}In_{0.3}Sb$/InAs encased with AlSb barriers.

an emission wavelength as large as 4.1 μm[59] as well as above RT operation at 325 K in pulsed mode and up to 200 K operation in cw mode[60]. Continued improvement saw ICLs operating at RT with $J_{th} = 630$ A/cm^2 and at 237 K in cw mode, with a wall plug efficiency of 26%[61]. Next, a 12-stage ICL was fabricated with a thick layer of Au deposited on the top metal contact in order to enhance its thermal dissipation. The ICL was able to operate in cw mode up to 264 K with an emission wavelength of 3.3 μm[62], which represented a significant milestone as that operating temperature was accessible by a thermoelectric cooler, which is necessary for any practical application.

While the road toward cw RT operation was long, it was not without discovery and innovation. In 2008, the first reported ICL operating in cw mode was published by Kim and Meyer out of NRL[63]. The design involved a 5-stage ICL where the principal modifications called for reduced doping in the cladding layers in order to suppress internal optical losses as well as the introduction of lightly doped GaSb layers around the active region, forming the so-called separate confinement layer

(SCL). The SCL helps to increase the optical confinement factor due to the large refractive index contrast between it and the active region (roughly 3.8 for GaSb and 3.5 for the active region), and thus enhancing the gain of the ICL, according to

$$g_{th} = \frac{\alpha_i + \alpha_m}{\Gamma} \tag{1.8}$$

where α_i represents the optical internal losses due to various factors but does not include carrier losses such as Auger recombination, α_m represents the mirror losses, and Γ is the optical confinement factor, which serves to characterize the confinement/spreading of the optical wave within the active region of the ICL. These changes allowed for fewer cascade stages to be employed, since the increased gain was sufficient to generate lasing. The best ICL from those tested was a 9.2 μm wide ridge, which could operate up to 319 K in cw mode with an emission wavelength of 3.75 μm. At 300 K the emission wavelength was 3.7 μm, $J_{th} \approx 750$ A/cm^2, and had a total output power of 10.5 mW, with back facet coating.

1.6.2 Recent Progress in ICL Performance

From 2010 to 2015 numerous efforts by various research groups took place to enhance the performance of ICLs through a number of lines of inquiry, including design modifications/optimizations, refined growth/fabrication techniques, and the use of different material systems. Performance targeted improvements include those such as, reduced threshold current densities, higher operating temperatures, and better wall plug efficiency, to name a few. In 2010, a group from the University of Wurzburg published results on shortening the length of the electron injector region[64]. The proposal called for reducing the length by approximately 16% in order to increase the intensity of the optical mode within the active region of the

ICL by roughly 10-15%, which increased the device gain. This had a secondary benefit as it reduced the number of interfaces, which can impact the strain of the device, and consequently lowered the complexity of the MBE growth. While the device did not achieve new results for metrics such as emission wavelength, operating temperature, or output power, it did exhibit a J_{th} of roughly half that of a reference device without the changes to the electron injector.

In 2011, a critical flaw in the design of previous ICLs was discovered and published by Vurgaftman et. al.[65], which pointed out that there existed a significant imbalance between the densities of electrons and holes in the active wells and that by heavily n-type doping the electron injectors, the threshold current density could be significantly reduced. To better understand this feature, consider the band structure of the modern ICL as depicted in Fig. 1.15. Unlike the conventional diode laser or the QCL, the ICL generates both electrons and holes internally, in each cascade stage. Their source can be thought of as originating from the region between the hole injector and the electron injector, which forms a semimetalliac interface (under applied bias) where the valence band edge of GaSb lies above that of the conduction band edge of InAs by approximately 0.2 eV. Because of this, electron states in the InAs QW and hole states in the GaSb QW are allowed to become populated in thermal quasi-equilibrium. This external electric field used to shift the bands and begin the cascade process sweeps these carriers away from this interface, with the holes flowing to the left and the electrons flowing to the right. Since these carriers are constantly being swept away from the interface, in order to remain in a quasi-equilibrium, an equal number of carriers must be continuously generated at this location.

The imbalance in the carrier densities occurs because, previously, the internally generated carriers far exceeded the moderate n-doping of the electron injectors.

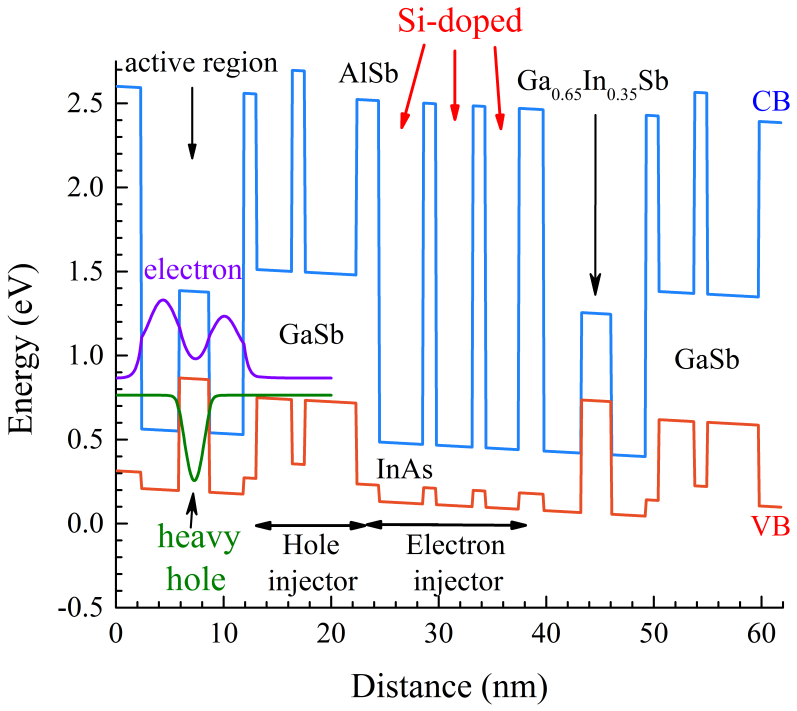

Figure 1.15: Qualitative band diagram of the modern ICL with typical features including the W-QW active region, the GaInSb hole injector, and the heavily Si-doped and also thinned electron injector.

During calculations, they found that the injected electrons mainly tended to localize within the electron injectors, whereas most of the injected holes would transfer to the $Ga_{0.7}In_{0.3}Sb$ hole well. Therefore, the population of carriers within the QW active region was heavily skewed towards holes, creating a significant imbalance. By increasing the electron doping concentration within the electron injectors by over an order of magnitude (5×10^{18} cm^{-3}), there may be a rebalancing of the carrier distributions where the electron and hole populations within the QW active region may become more comparable. Devices tested with this change in mind exhibited improved CW and pulsed performance and operated at higher temperatures, with J_{th} as low as 167 A/cm^2, V_{th} as low as 2.1 V, and cw output powers as large as 158 mW, three times larger than previously reported at the time. This carrier rebalancing feature has also become a core component of modern ICL design.

1.7 Dissertation Introduction

The work presented in this dissertation falls into two main categories: 1) Material growth and material characterization techniques for IC structures and 2) Fabrication and testing of InAs-based and GaSb-based ICLs with structural changes towards enhancing their performance in the long wavelength and mid wavelength portion of the MIR. Toward that goal, Chapter 2 focuses on a discussion of molecular beam epitaxy (MBE), which is the primary tool used to grow the interband cascade structures reported here. This technique is invaluable because it allows for the creation of high-quality heterostructures, which is mandatory for complicated devices such as the interband cascade laser. Topics addressed include the principles of MBE growth, strain and strain-balance methods in MBE grown structures, and the experimental setup, called the GENxplor, used to grow many of the IC structures reported here.

Structural characterization of the grown materials goes hand-in-hand with refining the growth to achieve high crystalline quality results, and therefore Chapter 3 focuses on several high-impact and often used characterization tools to assess the quality of MBE grown structures. The main features touched upon include the Hall Effect, used for determining carrier concentrations, differential interference contrast microscopy (DIC), used to analyze the surface morphology of an epitaxial structure, and x-ray diffraction (XRD). XRD is critical in the analysis of SL structures as it provides a direct mechanism to probe many facets of the grown structures including, but not limited to, the material quality, the growth thicknesses of bulk and SL layers, alloy compositions, and epilayer strain. The analysis techniques discussed in this chapter are later applied to the study of the crystal quality of a variety of IC related structures including SL and alloy calibration samples and

several ICTPV and ICL devices.

Interband cascade devices, especially the ICL, are highly complicated structures to grow, which often require many calibration runs to achieve accurate results. Prior to the efforts put forth in this dissertation, the successful growth of a GaSb-based ICL had not yet been demonstrated on the GENxplor in our group. Much of the early work in this dissertation focused on efforts to achieve successful growth of such structures, which included many calibrations of alloy and SL epilayers that form the larger ICL structure. These techniques and growth calibration results are reported in Chapter 4, and include calibration and optimization studies of InAsSb alloys lattice-matched to GaSb, InAs/AlSb SLs, and the GaSb buffer layer. The techniques developed for these ICL structures are later applied to ICTPV devices, which are further discussed in the second half of Chapter 4, as well as ICL structures reported in Chapter 7.

Chapter 5 presents a brief overview of device fabrication as well as many details of ICL characterization used to analyze the performance of the devices reported here. This includes both the cw and pulsed spectra and the current-voltage-power (IVL) testing and the associated figures of merit which may be extracted. Included is a discussion of how to accurately calibrate the pulsed output power results in order to calculate properties such as the external quantum efficiency (EQE).

Chapter 6 reports recent efforts by our group to extend the emission wavelength of InAs-based ICLs beyond 10 μm, while maintaining high performance, and is approached from two directions based on the design of the optical waveguide and the design of the W-QW active region. Details of the expected optical parameters based on waveguide simulations are presented as well as how modifications to the W-QW active layer sequence, using a new barrier material, can enhance the long wavelength emission of InAs-based ICLs. The performance characteristics for a set of initial InAs-based ICLs, which compare these two alterations are

presented. Afterwards, a follow up study with several additional InAs-based ICLs with refinements to the design based on the initial testing are reported. New world records were achieved in terms of lasing wavelength using the conventional W-QW structure as well as the total output power of devices with the conventional W-QW structure. Also, new records were set for the longest emission wavelength in cw mode for an ICL as well as the longest emission wavelength achieved among all III-V interband lasers.

The improvements to the waveguide for long-wavelength InAs-based ICLs were applied to GaSb-based ICLs operating at shorter wavelengths in the MIR, the results of which are reported in Chapter 7. These results demonstrate the first ever successful growth of GaSb-based ICLs on the GENxplor based on the growth studies conducted in Chapter 4. The figures of merit, extracted from the device testing, are comparable to state-of-the-art GaSb-based ICLs with the conventional design, with some devices showing improved thermal characteristics. This indicates the considerable potential of the modified waveguide structure for GaSb-based ICLs operating at shorter wavelengths and could be realized with future growth and design refinements.

Lastly, a brief summary of the important techniques and concepts covered in this dissertation are presented in Chapter 8, as well as several lines of inquiry which may be explored in the future to achieve higher quality ICL growth as well as potential improvements in the performance of both InAs-based and GaSb-based ICLs.

Chapter 2

Molecular Beam Epitaxial Growth

Many different types of crystal growth techniques exist today, but in order to effectively grow superlattice (SL) heterostructures, an epitaxial growth technique is required. Epitaxial growth involves extending the underlying crystal structure of the seed/substrate material through the grown SL structures. Of the various epitaxial techniques, including molecular beam epitaxy (MBE), chemical vapor deposition (CVD), metal organic chemical vapor deposition (MOCVD), liquid phase epitaxy (LPE), and physical vapor deposition (PVD), perhaps none stand out quite as much as MBE. This technique is ideal for controlled, layer-by-layer growth of SL heterostructures as it offers atomic layer precision of single crystalline materials, which is required for interband cascade devices. Section 2.1 will detail the physical mechanisms underpinning MBE growth. Section 2.2 will discuss strain in MBE grown structures, while Section 2.3 will present different perspectives for achieving strain balance in MBE growth. Lastly, Section 2.4 will showcase the equipment used to grow some of the interband cascade structures reported in this dissertation.

2.1 Principles of MBE Growth

MBE growth is achieved through the use of sophisticated equipment that allows for the precise control of atomic and molecular beams of vaporized elemental material. Components of the MBE system are housed in a central chamber referred to as the growth chamber, which is kept under ultra-high vacuum (UHV) conditions, with a chamber pressure $< 10^{-9}$ Torr. This pressure is maintained through the use of a pumping system and a cryoshroud that is located in between the substrate

holder and the external panels and is cooled with liquid nitrogen (LN). The material used for growth originates in a component called an effusion cell, as depicted in Fig. 2.1.[1] Heat is applied until the material begins to evaporate, where the cryoshroud helps to thermally isolate each cell to minimize thermal interference between adjacent cells during growth. The elemental material used to grow is of high purity, often referred to as five 9's or six 9's (i.e., 99.999% or 99.9999% purity levels). Mechanical shutters control the flow (or flux) of the evaporated material from the effusion cells. Because of the UHV conditions inside the growth chamber, the mean free path of the vaporized material is very long (upwards of more than 1 km). This means that when the shutters open and material is allowed to flow out, it does so in a directional, beam-like manner where the divergence is small, forming the so-called molecular beam. These shutters are controlled with an actuator that is connected to a computer that can be programmed to control how long a shutter may be opened. This allows for the sequential growth of different materials with varying compositions. The effusion cell configuration is such that the outflow of the material is aimed directly at the substrate used for growth.

Material growth at the substrate surface is a kinetic process where group III (cations) and group V (anions) atoms/molecules meet and combine. In order to promote a clean, layer-by-layer growth process, the substrate temperature is carefully controlled as there exists a careful interplay of material quality and substrate temperature. The purpose is to encourage material that is arriving at the surface to stick in the out-of-plane direction, but to have a high degree of surface mobility. If the substrate temperature is too low, the arriving material will stick more closely to the arrival point. Conversely, if the substrate temperature is too high, the arriving material may desorb back into the growth chamber atmosphere. In both cases, this will reduce the uniformity of the layer-by-layer growth process

and lead to poor material quality of MBE grown structures. Therefore, most materials will have an optimum window of substrate temperature during growth. This allows the arriving cations and anions to rapidly spread across the surface in order to find clean bonding sites in the growth plane for highly uniform 2D layers. Additionally, the substrate is rotated during growth in order to improve the uniformity of the deposition process.

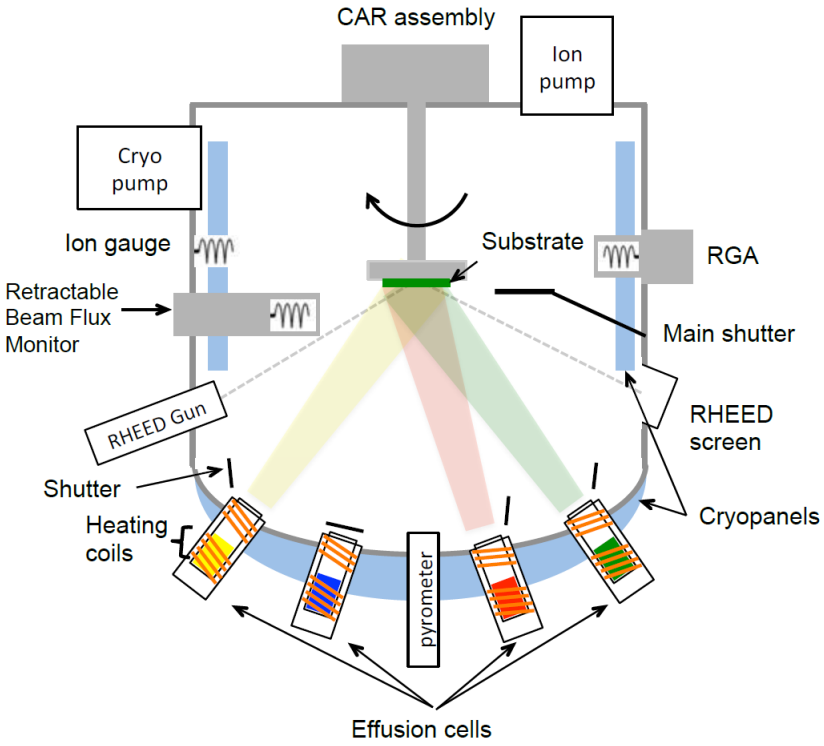

Figure 2.1: Qualitative schematic of an MBE chamber showing various components used for growth.[1]

In order to monitor the amount of material in a given beam flux, an ion gauge is used inside of the growth chamber and is often referred to as the beam flux monitor (BFM). The BFM is setup such that it consistently measures the flux at approximately the same position inside of the chamber every time a measurement is made. It is set up to measure the flux at the location of the substrate holder. Though the growth is a kinetically driven process, the molecular fluxes used for growth of III-V materials are generally never in a perfect 1:1 stoichiometric ratio.

The reason for this is that the group V materials used (Sb and As) have much higher vapor pressures than the group III materials. This means that it is much easier to have these group V materials desorb from the surface during growth. Meanwhile, group V atoms only incorporate in group V sites, and this feature allows for a much larger flux of group V to be used in order to create a background pressure (or overpressure) so that group V desorption does not take place during growth. Oftentimes this overpressure of group V can be more than one order of magnitude larger than that of the group III pressure. For the case of Sb-based materials, often the V:III ratio falls into the range of $1.5 < \text{V:III} < 3.5$. As has an even higher vapor pressure than Sb, and often its ratio falls in the range of $5 < \text{V:III} < 15$. Because of the overpressure of group V material required, the growth rate of a given material is said to be group III limited, and therefore the group III flux can be used as the direct control for the growth rate of a given layer. The primary tool used to both monitor the growth in real time, as well as calibrate the growth rates of the various group III cells, is the reflection high-energy electron diffraction system (RHEED).

2.1.1 Reflection High Energy Electron Diffraction

The RHEED system is an *in-situ* growth characterization tool that can provide real time information about the quality and type of growth taking place inside the MBE chamber. This system employees an electron gun, where a current of several amps passes through a Tungsten filament, chosen due to its low work function, which causes thermionic emission of electrons. A large accelerating voltage is applied, creating high energy electrons with energies ranging between 10-15 KeV, while magnetic optics are used to focus the electrons into a narrow beam. The electron beam impinges on the growth surface at a shallow glancing angle ($\approx$ 1-3

deg) so that only interactions between the electrons and the first few atomic layers of the lattice take place. The beam is reflected and diffracted onto a phosphorus (RHEED) screen that is protected with a shutter when not in use. Because the wavelength of the electron beam is similar to that of the atoms forming the crystal lattice, the diffraction pattern is sensitive to the atomic arrangement. A depiction of this feature is shown in Fig. 2.2. On the outside of the chamber, a sensitive camera shrouded in a black cloth can capture a live view of the diffraction pattern on the RHEED screen and transmit the information to computer software for analysis.

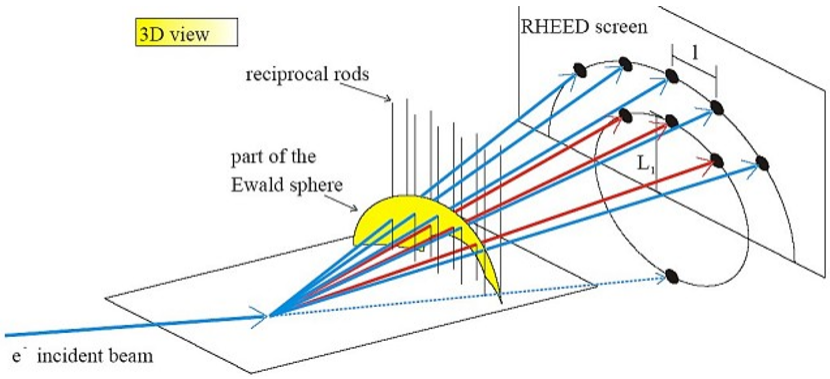

Figure 2.2: Qualitative diagram of the RHEED image formation process showing the beam interaction with the crystal surface and the subsequent diffraction pattern on the phosphorus (RHEED) screen.

Fig. 2.3 shows a typical RHEED pattern for several different growth regimes. The left most figure depicts a diffuse and spotty (rough) pattern, indicating a 3D growth mode. As the surface begins to get filled in during growth, the dots in the RHEED pattern begin to stretch out, indicating a quasi-3D-like surface. The arrival of a streak-like pattern indicates quasi-2D layer formation, while a streaky and clear pattern with bright peaks heralds 2D, layer-by-layer growth with an atomically smooth surface.

These types of observations provide qualitative information about the real time

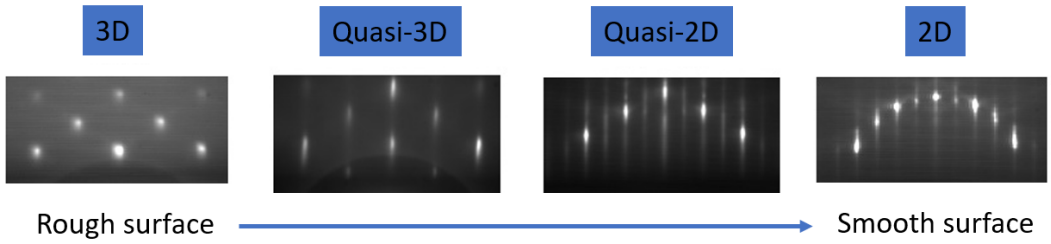

Figure 2.3: The evolution of a rough to smooth surface (left to right) as determined from the RHEED pattern during growth.

surface reconstruction process and are essential during growth of heterostructures as a smooth surface is mandatory for good material quality. Surface reconstruction refers to the process by which the crystal structure of a semiconductor surface is modified due to the presence of atoms or molecules on the surface. During the growth process, the surface can undergo a structural transformation due to the interactions with the substrate and the deposition conditions. In some cases, the surface atoms may rearrange themselves into a different crystal structure. In other cases, additional atoms may be incorporated into the surface layer, leading to a new surface stoichiometry or composition. The result of this will present as a variation in the diffraction image taken by the RHEED system. This type of RHEED is referred to as *Static* RHEED. The RHEED technique can also be used to determine one of the most critical aspects of MBE growth, the growth rate of the various group III materials.

2.1.2 Determining Growth Rates using RHEED

When RHEED is used to determine group III-limited growth rates it is referred to as *Dynamic* RHEED.[66] This technique is based on the principle that the intensity of the specular reflection (zeroth order diffraction peak) is sensitive to the factional variation of a single layer (monolayer, ML) of material. We can imagine an atomically smooth surface as our reference point. This surface can

be called a 0 ML surface, as growth has not yet started to take place as shown in Fig. 2.4. Because every atomic site is occupied, the RHEED pattern will have a very intense/bright central diffraction peak. As growth begins, atomic sites on the surface begin to get filled in and a competition between constructive and destructive interference begins, which decreases the brightness of the center diffraction peak, reaching a minimum brightness after 0.5 ML of material has been deposited. As more of the surface fills in, the intensity of the center peak begins to increase and once again reaches a maximum when $\approx$ 1 ML has been grown. These intensity variations over time are referred to as RHEED oscillations, where the period between successive maxima or minima yield the time it takes to grow a single monolayer of a given material and is used to calibrate the growth rates (GR) of the various group III sources. With a known GR the open/close time of a given shutter can be programmed to control the precise layer thickness of heterostructure layers.

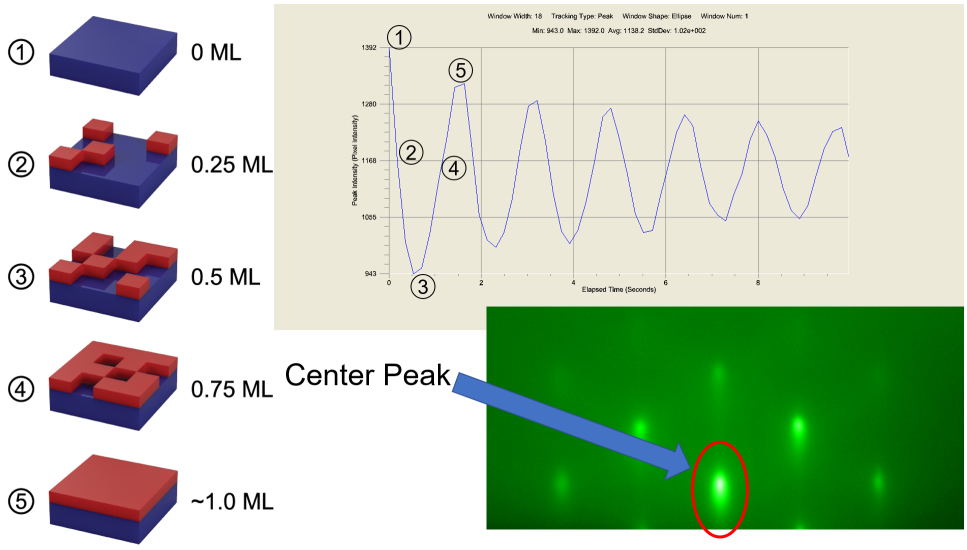

Figure 2.4: Depiction of the evolution of the growth surface of a single monolayer of material and the corresponding intensity variation (taken from In GR calibrations in 2018) of the central diffraction peak measure by RHEED.

2.1.3 Growth Rate Calibration on the GENxplor

The procedure for conducting a growth rate calibration study on the GENxplor first involves the choice of substrate. Both the Ga and the Al GRs may be calibrated by growing GaAs and AlAs on a GaAs substrate. Though AlAs is a distinctly different binary material, its lattice constant ($a_{AlAs} = 5.660$ Å) is approximately equal to that of GaAs ($a_{GaAs} = 5.653$ Å), amounting to a difference of only 0.124%. First, an oxide desorption (OD) process takes place (similar to growing a full IC structure), which involves heating the substrate high enough to remove the passive oxide layer formed on the surface from exposure to the atmosphere. OD temperatures are known quantities for the typically used substrates and may be confirmed by a visual inspection of the RHEED pattern at the surface, indicated by a bright, spotty pattern.

For GaAs, the OD temperature was measured by both the thermocouple and the pyrometer, though the pyrometer is out of range at these elevated temperatures. The OD was carried out at $T_{thermocouple} = 760°C$ ($T_{pyrometer} = 724°C$) for 10 minutes. Afterwards the substrate temperature was lowered to $T_{sub} = 740°C$, and a buffer layer of GaAs was grown for 45 minutes. A buffer layer ensures transformation of a 3D surface from the OD process into a smooth 2D surface. Next, the RHEED filament current is turned down until just the main diffraction peak is visible under an As overpressure. Then the Ga shutter is opened for approximately 10-15 seconds to grow GaAs and the oscillations in the diffraction intensity are recorded, from which the GR is inferred. This is repeated three times at a given temperature and the GR is then averaged. For AlAs, after each series of RHEED oscillations is recorded, GaAs is grown for about 1 min, to ensure good crystal quality for subsequent AlAs growth. Afterwards, the Ga and Al cell temperatures are reduced slightly, and a fresh GaAs layer is grown before

repeating the RHEED oscillation measurement. This is then continued 5 or 6 times to generate a data set over a wide range of GRs.

The calibration proceeds in much the same way for InAs, except that the an InAs buffer layer on GaAs is grown for substantially longer due to the larger lattice mismatch of InAs compared with GaAs (a_{InAs} = 6.058 Å compared to a_{GaAs} = 5.653 Å). After OD, the substrate temperature is lowered to T_{sub} = 490°C for InAs growth, where the buffer layer is grown for 2 hours. Generally, there will still exist a slightly spotty/slightly streaky pattern, indicating a quasi-2D surface. This is to be expected since the InAs lattice constant has such a large mismatch to that of GaAs. In principle, using an InAs or even a GaSb substrate for this calibration would be better, however, those substrates are not as cost effective as GaAs. On the GENxplor, there are two In source cells named In1 and In2, and therefore a separate calibration for each source should be completed.

Table 2.1 reports the various parameters from a GR study in the spring of 2020. In the table, the term flux is used (sometimes referred to as the beam equivalent pressure) to quantify the amount of group III material present at the substrate. This value represents the difference between the measured background pressure inside of the growth chamber when all source cells have their shutters closed and the pressure inside of the growth chamber after the various group III cells have been opened for 30 seconds. The growth rate of a group III material follows an Arrhenius relationship of the form GR $\approx$ B $\times$ flux $\approx$ Aexp(-E_a/k_bT), where A and B are fitting parameters, E_a is the activation energy of a material, k_b is the Boltzmann constant, and T is the cell temperature. Thus, a plot of the log(GR) and log(flux) as a function of 1/T will yield a linear relationship, as demonstrated in Figures 2.5 to 2.7.

Since the growth is group III limited, as discussed in Section 2.1, the ratio of the GR of a material and the square of its lattice constant is equal to that of

Table 2.1: The various parameters of the GR calibration conducted in the Spring of 2020. The source material cell temperatures are reported as measured from the thermocouple.

Parameters and Results for the growth rate Calibration Study in Spring 2020					
Material	Tip (°C)	Base (°C)	T_{sub} (°C)	flux (Torr)	GR (ML/s)
GaAs	1095	895	740	8.11×10^{-7}	0.782
GaAs	1085	885	740	6.78×10^{-7}	0.648
GaAs	1075	875	740	5.49×10^{-7}	0.526
GaAs	1065	865	740	4.61×10^{-7}	0.427
GaAs	1055	855	740	3.78×10^{-7}	0.348
AlAs	990	1090	740	1.85×10^{-7}	0.605
AlAs	980	1080	740	1.51×10^{-7}	0.503
AlAs	970	1070	740	1.26×10^{-7}	0.411
AlAs	960	1060	740	1.03×10^{-7}	0.336
AlAs	950	1050	740	6.10×10^{-8}	0.269
InAs 1	960	780	490	1.45×10^{-6}	0.951
InAs 1	950	771	490	1.26×10^{-6}	0.825
InAs 1	940	771	490	1.09×10^{-6}	0.688
InAs 1	930	764	490	9.40×10^{-7}	0.581
InAs 1	920	756	490	7.83×10^{-7}	0.487
InAs 1	910	750	490	6.67×10^{-7}	0.408
InAs 1	895	738	490	5.15×10^{-7}	0.313
InAs 1	880	726	490	4.03×10^{-7}	0.234
InAs 1	865	715	490	3.03×10^{-7}	0.174
InAs 2	960	780	490	9.48×10^{-7}	0.773
InAs 2	950	770	490	7.61×10^{-7}	0.611
InAs 2	940	760	490	6.08×10^{-7}	0.477
InAs 2	930	750	490	4.86×10^{-7}	0.373
InAs 2	920	740	490	3.85×10^{-7}	0.293
InAs 2	910	730	490	3.06×10^{-7}	0.230
InAs 2	900	720	490	2.41×10^{-7}	0.179

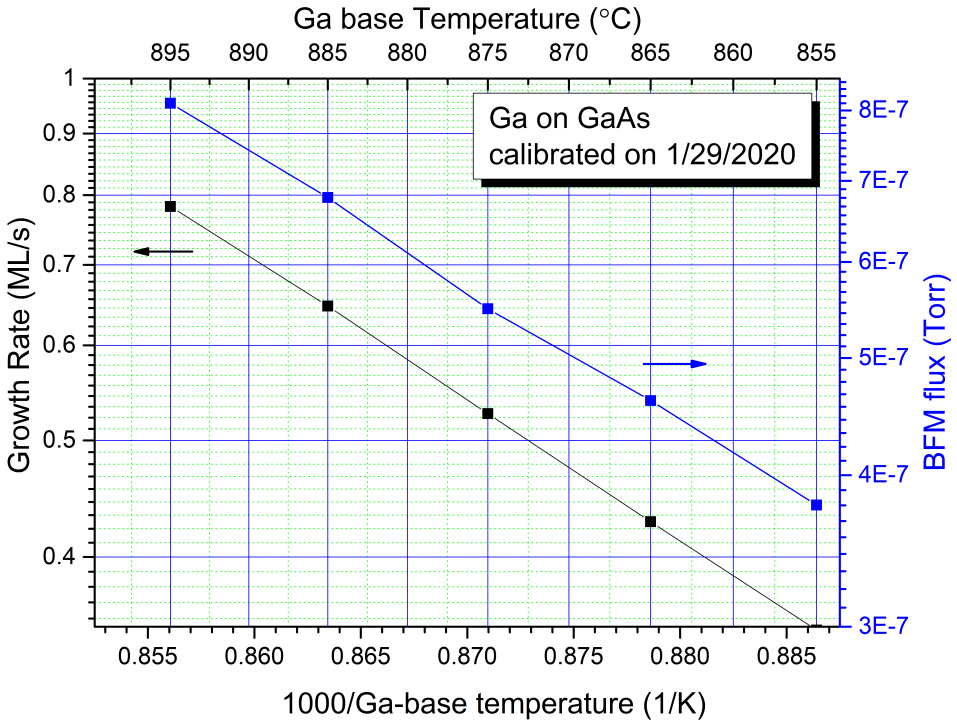

Figure 2.5: Plot of the GR in monolayers (ML) per second and the beam flux as a function of the temperature of the Ga effusion cell for the GaAs GR study in spring of 2020.

a different binary with the same group III material and the square of its lattice constant. This provides a method to extend the results for the Ga/Al/In GRs determined by growing GaAs/AlAs/InAs to that of GaSb/AlSb/InSb. As an example for InAs to InSb, this takes the mathematical form

$$\frac{GR_{InSb}}{a^2_{InSb}} = \frac{GR_{InAs}}{a^2_{InAs}} \rightarrow GR_{InSb} = \frac{GR_{InAs}a^2_{InSb}}{a^2_{InAs}} \tag{2.1}$$

2.2 Strain in MBE Grown Structures

There are two types of epitaxial growth, homoepitaxy and heteroepitaxy. The former refers to growth of a chosen material on a substrate of the same material. For example, the growth of GaSb on a GaSb substrate. Heteroepitaxy, on the

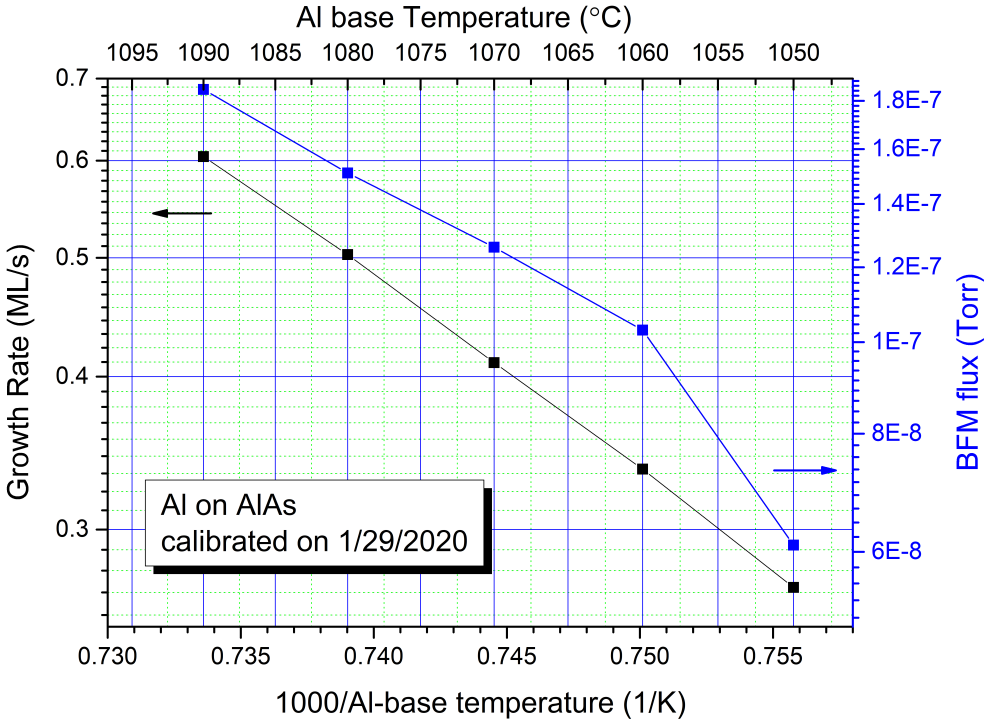

Figure 2.6: Plot of the GR and the beam flux as a function of function of the temperature of the Al effusion cell for the AlAs GR study in spring of 2020.

other hand, refers to growth of a material layer (epilayer) that is different from that of the chosen substrate material. An example is the growth of InAs on a GaSb substrate. From a growth perspective, the primary concern is the difference of the lattice constant of the epilayer compared to that of the substrate because, as previously stated, the purpose of epitaxial growth is to extend the underlying crystal structure of the substrate up through the grown material. This presents a challenge then for heteroepitaxial growth as a given epilayer will be forced to take on the lattice constant of the substrate. This will strain the epilayer, causing a buildup of strain energy. Often when strain is discussed it will refer to the strain in the growth plane (x-y direction) and may be called biaxial strain.

There are two types of strain that may occur during growth, depending on the lattice constant difference between the epilayer (a_{epi}) and the substrate (a_{sub}).

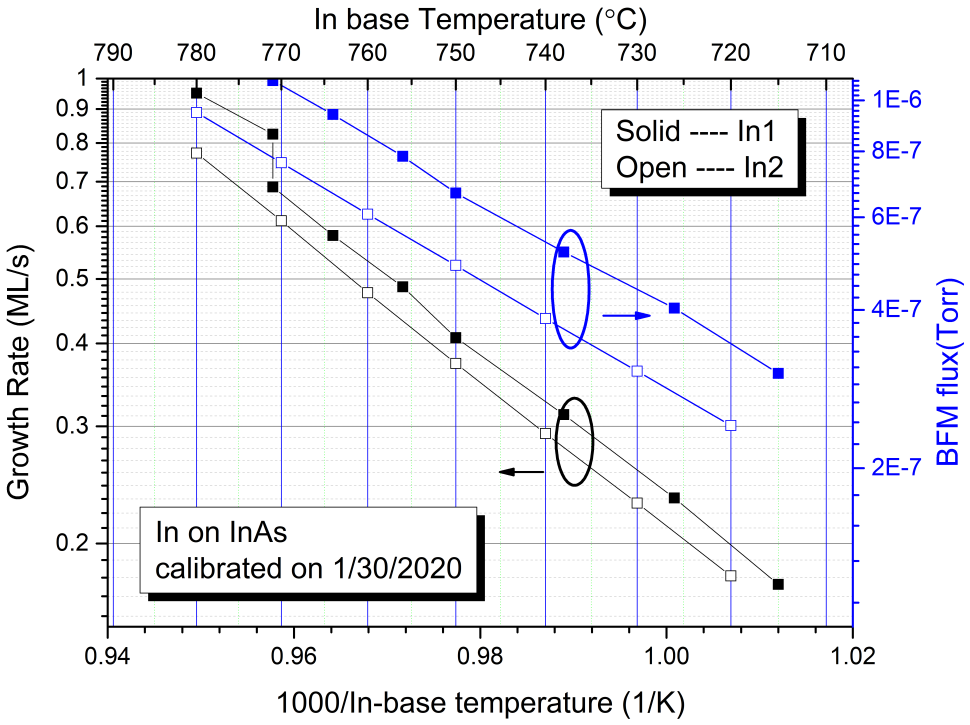

Figure 2.7: Plot of the GR and the beam flux as a function of the temperature of the In effusion cell for the InAs GR study in spring of 2020.

If $a_{epi} < a_{sub}$, then the atoms will experience a tensile biaxial strain as shown in Fig. 2.8. Because of this pulling of the atoms in the plane of growth, the lattice constant in the perpendicular direction (a_z) will be shortened somewhat, undergoing compressive strain. Conversely, if $a_{epi} > a_{sub}$, then compressive biaxial strain will occur in the growth plane and the epilayer a_z will experience tensile strain as shown in Fig. 2.9.

In order for successful growth of heterostructures, balancing the type of strain that occurs in periodic structures is critical. For example, consider a two layer SL structure composed of InAs and AlSb grown on GaSb. Here $a_{InAs} < a_{GaSb} < a_{AlSb}$, thus an InAs ML will experience tensile biaxial strain while a ML of AlSb will experience compressive biaxial strain. Because of these alternating strain types, the overall SL structure is said to be in strain balance, or strained to the GaSb

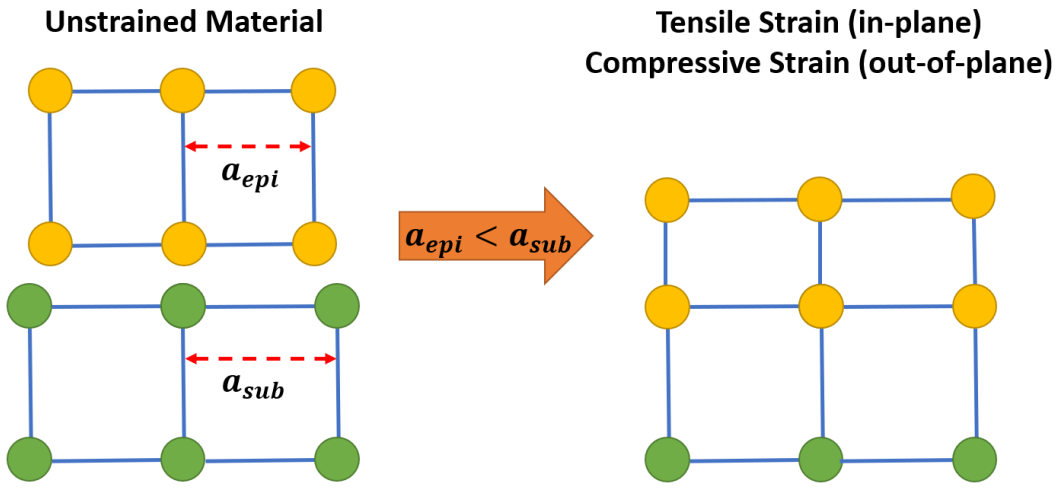

Figure 2.8: Depiction of biaxial tensile strain occurring in an epilayer with a lattice constant that is smaller than the substrate lattice constant.

substrate because the net strain imposed on the SL structure as a whole is kept to a minimum. Thus, a strain balanced system is formed which takes on dependencies related to distinct material properties, and which is the subject of Section 2.3. The following section presents a brief mathematical treatment of strain.

2.2.1 Mathematical Definition of Strain

From the classical theory of elasticity, a solid material grown by MBE is treated as a continuous medium[2, 67], which is a valid approximation since the strains that the individual layers are subject to are small. For a crystal undergoing elastic deformation,

$$\vec{R} = \vec{r} + \Delta\vec{r} \tag{2.2}$$

where a small displacement $\Delta\vec{r}$ modifies the spatial position of point $\vec{r}$ within the material to point $\vec{R}$. An example of various deformations is shown in Fig. 2.10. These deformations of the crystal give rise to strains within the material given by,

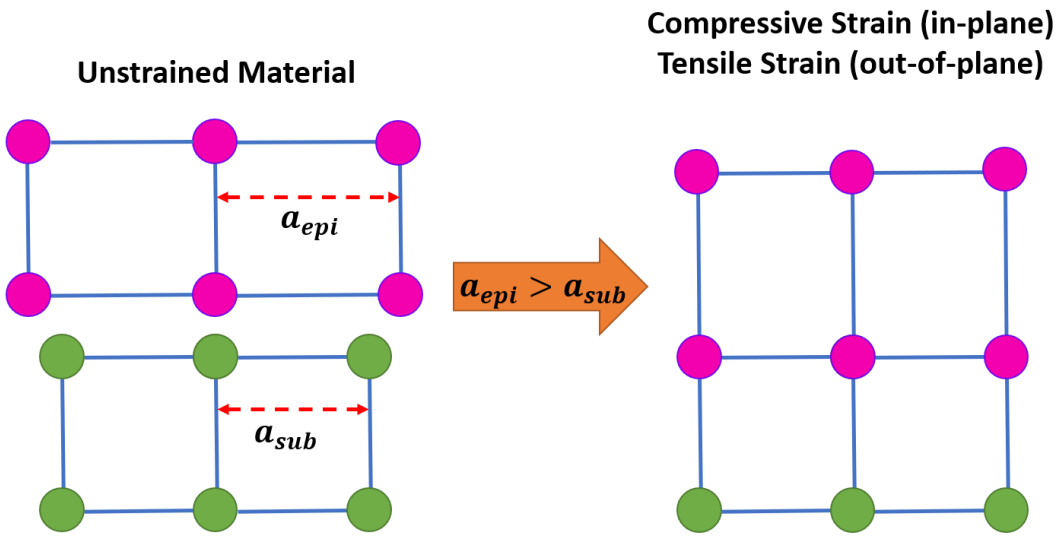

Figure 2.9: Depiction of biaxial compressive strain occurring in an epilayer with a lattice constant that is larger than the substrate lattice constant.

$$\epsilon_{ij} = \frac{1}{2}\left(\frac{\partial \Delta \vec{r_i}}{\partial x_j} + \frac{\partial \Delta \vec{r_j}}{\partial x_i}\right) \tag{2.3}$$

where ϵ_{ij} is a strain tensor of the form,

$$\epsilon_{ij} \equiv \epsilon = \begin{pmatrix} \epsilon_{11} & \epsilon_{12} & \epsilon_{13} \\ \epsilon_{21} & \epsilon_{22} & \epsilon_{23} \\ \epsilon_{31} & \epsilon_{32} & \epsilon_{33} \end{pmatrix} \tag{2.4}$$

for 1,2,3 = x,y,z. A similar matrix form can be given to the stress tensor, σ_{ij} and the two physical quantities are related to each other by,

$$\sigma_{ij} = \sum_{k=1}^{3}\sum_{l=1}^{3} C_{ijkl}\epsilon_{kl} \tag{2.5}$$

where C_{ijkl} is the elastic stiffness tensor which will be defined later in Section 2.3.

Strain, and its management, is of critical importance for MBE grown structures. This is especially true for strained layer supperlattices (SLS) since the goal of such endeavors is to build large periodic structures composed of very thin layers

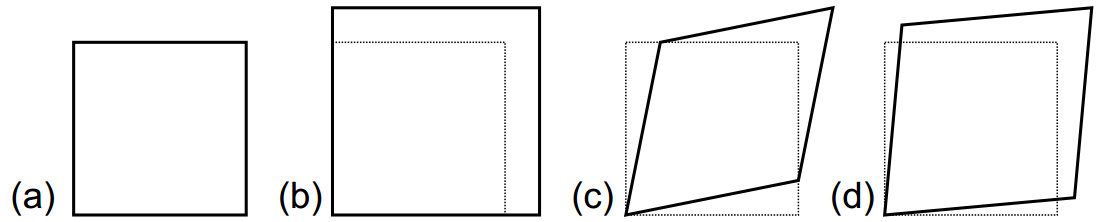

Figure 2.10: Deformation of a square (**a**). (**b**) Pure hydrostatic deformation ($\epsilon_{xx} = \epsilon_{yy} = 0.2, \epsilon_{xy} = 0$), (**c**) pure shear deformation ($\epsilon_{xx} = \epsilon_{yy} = 0, \epsilon_{xy} = 0.2$), and (**d**) mixed deformation ($\epsilon_{xx} = \epsilon_{yy} = 0.1, \epsilon_{xy} = 0.1$)[2]

of alternating materials where strain induced defects have the potential to wreak havoc within the device. If too much strain energy is built up from improper balancing, relaxation will occur through the formation of various types of defects within a material. Because of this, a number of theories have been developed in order to predict the structural characteristics of the SLS system of interest and are generally referred to as strain balance methods.

2.3 Strain Balance Methods

As discussed previously, the aim for SLS growth is to utilize complementary materials to achieve strain balance by alternating layers of compressive and tensile strain. The question then arises; what additional constraints should one consider in order to achieve a strain balanced system? The most basic proposal was put forth by Matthews and Blakeslee in their 1976 paper which considered a two layer SLS.[68] Here one can define the thickness and relaxed lattice constants of the constituent materials of the SLS as t_1, t_2 and a_1,a_2, along with the lattice constant of the substrate that the SLS is to be grown upon as a_o. Their concept was to consider the overall lattice constant of the SLS based on the relative composition of each layer which formed the SLS. Their strain matching condition is that the substrate lattice constant should equal the average lattice expression of the form:

$$a_o = a_1\left(\frac{t_1}{t_1+t_2}\right) + a_2\left(\frac{t_2}{t_1+t_2}\right) \quad = \frac{a_1t_1 + a_2t_2}{t_1+t_2} \tag{2.6}$$

Note that the absence of consideration for the elastic constants of the various materials of interest infers the assumption of identical elastic properties. However, the above assumption is flawed and because of that, a number of other approaches were used to attempt to account for the strain inherent in the system, generally referred to as thickness weighted methods. These ideas suggest that a strain balanced structure may emerge from equivalent strain thickness products between the tensile and compressive layers.

Though the previous methods mentioned above give approximately good results and are physically intuitive, they carry no physical constraints. In 2002 Ekins-Daukes et al., proposed a new model which they called the Zero-Stress Method.[69] Their model imposed a physical constraint, namely the requirement that there should be zero average in-plane stress of the SLS, in isolation, as this corresponds to the lowest energy state for the structure as a whole. The layer thicknesses of the SLS should be chosen such that the in-plane lattice constants of the resulting SLS structure should be equal to that of the substrate (i.e., $a_{x/y,SLS} = a_o$). In this way, no additional stress is accumulated when combining the SLS with the substrate.

2.3.1 Derivation and Extension of the Zero Stress Method

First, we may begin by considering a semiconductor layer with unstrained lattice constant a_1 that is to be pseudomorphically strained onto a substrate with in-plane lattice constant a_o, which is the standard biaxial stress condition for heteroepitaxial growth. This is to say that the lateral lattice mismatch will be forced to zero, where the deposited material sits in the adsorption sites of the substrate. In this case, the strain components of the epitaxial layer are given by:

$$\begin{aligned} \epsilon_{xx} &= \epsilon_{yy} = \frac{a_o - a_1}{a_1} = \epsilon \\ \epsilon_{zz} &= -\nu\epsilon_{xx} \\ \epsilon_{xy} &= \epsilon_{yz} = \epsilon_{zx} = 0 \end{aligned} \tag{2.7}$$

where $\nu = 2\frac{C_{12}}{C_{11}}$ is the biaxial relaxation constant for cubic crystals, which describes the strain between perpendicular and parallel layers within the SLS. The shear strains are generally assumed to be zero for growth along the (001) direction.[4, 69] The terms C_{11} and C_{12} are elastic stiffness constants (with units of force per area) and come from the elastic stiffness tensor. This was described in 2.5, which relates the stress to the strain in a structure based on Hooke's law for isotropic materials, and has the matrix form:

$$\begin{pmatrix} \sigma_1 \\ \sigma_2 \\ \sigma_3 \\ \sigma_4 \\ \sigma_5 \\ \sigma_6 \end{pmatrix} = \begin{pmatrix} C_{11} & C_{12} & C_{13} & C_{14} & C_{15} & C_{16} \\ C_{21} & C_{22} & C_{23} & C_{24} & C_{25} & C_{26} \\ C_{31} & C_{32} & C_{33} & C_{34} & C_{35} & C_{36} \\ C_{41} & C_{42} & C_{43} & C_{44} & C_{45} & C_{46} \\ C_{51} & C_{52} & C_{53} & C_{54} & C_{55} & C_{56} \\ C_{61} & C_{62} & C_{63} & C_{64} & C_{65} & C_{66} \end{pmatrix} \begin{pmatrix} \epsilon_1 \\ \epsilon_2 \\ \epsilon_3 \\ \epsilon_4 \\ \epsilon_5 \\ \epsilon_6 \end{pmatrix} \tag{2.8}$$

In the notation above, 1-3 refer to x, y, and z (or xx, yy, zz for the stress and strain), while 4-6 refer to the cross terms for the shear strain (i.e., yz, zx, and xy). The elastic stiffness tensor above is written in a generalized form but can be recast into a simpler form depending on the material system of interest. Since the topic of this dissertation is III-V materials, which have a zinc blende cubic crystal structure, symmetry arguments for this type of crystal structure greatly simplify Eq. 2.8 so that the stress-strain relationship may be rewritten as:

$$\begin{pmatrix} \sigma_1 \\ \sigma_2 \\ \sigma_3 \\ \sigma_4 \\ \sigma_5 \\ \sigma_6 \end{pmatrix} = \begin{pmatrix} C_{11} & C_{12} & C_{12} & 0 & 0 & 0 \\ C_{12} & C_{11} & C_{12} & 0 & 0 & 0 \\ C_{12} & C_{12} & C_{11} & 0 & 0 & 0 \\ 0 & 0 & 0 & C_{44} & 0 & 0 \\ 0 & 0 & 0 & 0 & C_{44} & 0 \\ 0 & 0 & 0 & 0 & 0 & C_{44} \end{pmatrix} \begin{pmatrix} \epsilon_1 \\ \epsilon_2 \\ \epsilon_3 \\ \epsilon_4 \\ \epsilon_5 \\ \epsilon_6 \end{pmatrix} \tag{2.9}$$

Since the two layers in the SLS are composed of alternating layers of compressive and tensile strain, they form by definition a strained system. Thus, a strain energy density will build up within the structure as it is grown. The strain energy density within a layer is given by,

$$U = \frac{1}{2}\left(\sum_{i=1}^{6} \sum_{j=1}^{6} C_{ij}\epsilon_i\epsilon_j \right) \tag{2.10}$$

which, when expanded for a cubic system using Eq. 2.9 becomes,

$$U = \frac{1}{2}C_{11}\left(\epsilon_1^2 + \epsilon_2^2 + \epsilon_3^2\right) + \frac{1}{2}C_{44}\left(\epsilon_4^2 + \epsilon_5^2 + \epsilon_6^2\right) + C_{12}\left(\epsilon_1\epsilon_2 + \epsilon_2\epsilon_3 + \epsilon_3\epsilon_1\right) \tag{2.11}$$

By substituting terms from 2.7, the average strain energy density in the layer may be written as,

$$\begin{aligned} U &= \left(C_{11} + C_{12} - \frac{2C_{12}^2}{C_{11}}\right)\epsilon^2 \\ &= A\epsilon^2, \text{for } A = \left(C_{11} + C_{12} - \frac{2C_{12}^2}{C_{11}}\right) \end{aligned} \tag{2.12}$$

where the coefficient A is defined in terms of a specific layer's elastic constants.

Extending this result to a two layer SLS, one may write the average strain energy density of the two layer system in a form similar to 2.6 as,

$$U_{avg} = \frac{A_1\epsilon_1^2 t_1 + A_2\epsilon_2^2 t_2}{t_1 + t_2} \tag{2.13}$$

which is a statement that each material contributes some portion of the total amount of strain energy within the two layer SLS based on the relative thickness of each of the materials present. The pseudomorphic requirement of the zero stress method, which constrains the lateral stress to zero, also connects the strain between both layers, under the condition of alternating strain types, by

$$\epsilon_2 = \frac{a_1}{a_2}\epsilon_1 + \frac{a_1 - a_2}{a_2} \tag{2.14}$$

The pseudomorphic constraint may be determined from the average strain energy density by,

$$\sigma_{av} = \frac{\partial U_{av}}{\partial \epsilon_1} = \frac{2}{t_1 + t_2}\left(A_1 t_1 \epsilon_1 + A_2 t_2 \epsilon_2 \frac{a_1}{a_2}\right) = 0 \tag{2.15}$$

By substituting the definition of ϵ found in 2.7 one may arrive at the exact result of Ekins-Daukes for the zero stress method for a two layer SLS,

$$a_o = \frac{A_1 t_1 a_1 a_2^2 + A_2 t_2 a_2 a_1^2}{A_1 t_1 a_2^2 + A_2 t_2 a_1^2} \tag{2.16}$$

The physical description of 2.16 is that a zero stress condition is achieved when a SLS is formed in such a way as to match the overall in-plane lattice constants of the resulting SLS structure to that of the desired substrate. Note that no particular emphasis or requirements are placed on the out-of-plane lattice constant of the SLS, compared with the substrate. However, often times more complicated SLS structures are required to achieve specified device performance. For example, the standard active core for a W-structure ICL is composed of a five layer sequence of AlSb/InAs/Ga_xIn_{1-x}Sb/InAs/AlSb. In fact, the complete

cascade period of a modern ICL (active + injection regions) may be composed of as many as 20+ layers. Therefore, when designing such SL structures with a high number of distinct material layers, minimizing the potential for the structure to relax is of key importance.

Though not explicitly discussed in their paper, the result of 2.16 may be extended to an n-layer SLS structure. By rewriting the result of Eq. 2.16, the generalized form becomes more straightforward,

$$a_o = \frac{\left(\frac{A_1 t_1}{a_1} + \frac{A_2 t_2}{a_2}\right)}{\left(\frac{A_1 t_1}{a_1^2} + \frac{A_2 t_2}{a_2^2}\right)} \tag{2.17}$$

so that, for an n-layer SLS the result becomes,

$$a_o = \sum_{i=1}^{n} \frac{A_i t_i}{a_i} \left(\sum_{i=1}^{n} \frac{A_i t_i}{a_i^2}\right)^{-1} \tag{2.18}$$

2.3.2 Relating Zero-Stress to Measured Results

The result of 2.18 yields a powerful tool in designing a strain-balanced system when a periodic structure has many individual layers. As will be discussed in detail in 3.3, x-ray scans of a grown structure most often yield information on the out-of-plane lattice constant of the SLS. Since the Zero-Stress method only provides design input about the expected in-plane lattice constant of the SLS, one must be able to determine the expected a_z of the epilayer, which results from the use of the Zero-Stress method, in order to compare with measured results. To do this, first consider the definition of the out-of-plane strain found in 2.7. This strain component may also be written in terms of the out-of-plane lattice constant as,

$$\epsilon_{zz} = \nu\epsilon_{xx} = \frac{-2C_{12}}{C_{11}}\left(\frac{a_o - a_1}{a_1}\right) = \frac{a_z - a_o}{a_o} \tag{2.19}$$

where a_z is the strained out-of-plane lattice constant for a single layer structure. Solving for the out-of-plane lattice constant, one finds

$$a_z = \nu a_o\left(\frac{a_1 - a_o}{a_1}\right) + a_o \tag{2.20}$$

If one considers a two layer SLS, one may write the net out-of-plane lattice constant in a form similar to 2.6 as,

$$\begin{aligned} a_{z,net} &= \frac{a_{z,1}t_1 + a_{z,2}t_2}{t_1 + t_2} = \frac{N_1 a_{z,1}^2 + N_2 a_{z,2}^2}{N_1 a_{z,1} + N_2 a_{z,2}} \\ N_i &= \frac{t_i}{\frac{a_{i,relaxed}}{2}} \end{aligned} \tag{2.21}$$

where $a_{z,1/2}$ and $t_{1/2}$ represent the strained out-of-plane lattice constant and strained layer thickness of layer 1 and layer 2, respectively. Unlike 2.6, one may write the net out-of-plane lattice constant in this way precisely because it is defined in terms of the strained values of the material, and the only requirement imposed by the zero stress method is that of the pseudomorphic constraint of Eq. 2.15. Furthermore, the strained layer thicknesses may be rewritten in terms of the number of monolayers of the material in said layer and the relaxed out-of-plane lattice constant of that material as shown above. This is because the number of monolayers in a given growth is carefully calibrated, as discussed in 2.1.2. Because the growth rate along with the shutter opening times are known, the total amount of deposited material may be inferred. As before, it is straightforward to generalize the result of 2.21 for an n-layer structure, while also utilizing the result of 2.20, as

$$a_{z,net} = \sum_{i=1}^{n} N_i \left[\nu_i a_o \left(\frac{a_i - a_o}{a_i} \right) + a_o \right]^2 \left(\sum_{i=1}^{n} N_i \left[\nu_i a_o \left(\frac{a_i - a_o}{a_i} \right) + a_o \right] \right)^{-1} \quad (2.22)$$

Here the values for the a_i's come directly from the result of 2.18. Thus, based on the result of the Zero-Stress method, an expected out-of-plane lattice constant may be determined and compared with experimental results.

While the Zero-Stress method is the more physically intuitive way in which to design MBE grown heterostructures, it should be noted that if the individual lattice constants of the materials involved are relatively close together to begin with, such as those of the 6.1 Å family, then the deviation between the results of the traditional Matthews-Blakeslee relation and Zero-Stress are actually somewhat small. On the other hand, when the lattice constants of the materials involved deviate more significantly from each other and the chosen substrate, a more properly strain balanced heterostructure should emerge from the use of the Zero-Stress method.

For example, consider the absorber region of a typical ICTPV which is formed from a combination of GaSb/InSb/InAs/InSb with thicknesses of 25.1/1.2/20.5/1.2 Å, respectively, grown on a GaSb substrate. Using the traditional Matthews-Blakeslee relation of Eq. 2.6, the computed lattice constant of the absorber would be $a_{epi} = 6.09906$ Å. Compared with the substrate ($a_{GaSb} = 6.09590$ Å) results in a difference of about 0.0518%. Using the generalized Zero-Stress method of Eq. 2.18, the computed in-plane lattice constant is $a_{epi} = 6.09341$ Å, which results in a difference of about -0.0409% compared to the GaSb substrate. By using Eq. 2.22, a predicted $a_{z,epi} = 6.09819$ Å is found. This result is just slightly smaller than that of the Matthews-Blakeslee relation, but is consistent with the perspective of generating a minimally strained system. Though the results are similar, since the Matthews-Blakeslee relation does not consider any physical constraints in the

system, it cannot give a complete physical picture of the resulting heterostructure and the Zero-Stress method should be used.

2.4 Experimental MBE Setup

2.4.1 MBE Cell Configuration

Apart from the long wavelength InAs-based ICLs that will be the topic of Chapter 6, all other structures discussed in this dissertation were grown using the Veeco GENxplor at OU. This system first began operation in 2015 and is a vertical reactor with 10 ports housing the material cells for growth as shown in Fig. 2.11. The vertical setup, as opposed to a horizontal setup, permits the effusion cells to hold more source material allowing for extended growth campaigns before needing to vent the system to refill the sources. The group III cells are sources for Ga, Al, In, where two In cells are utilized. Having the option of two In sources facilitates the use of two different In GRs. This minimizes the downtime during growth compared to having a single In source because to use two different GRs with a single source requires a long pause during growth to change the cell temperature. This feature is especially beneficial to ICL growth as the structure is already quite complicated and requires many hours to grow a single wafer. A slow GR is mandatory in the QW active region but not as necessary during the long periods of thick InAs or InAsSb grown for the optical cladding.

Valved cracker effusion cells are used for the group V materials (As and Sb). The cracking feature allows for the thermal dissociation of larger, polyatomic molecular species into smaller, more reactive species like Sb_2 and As_2. These cells also incorporate a needle valve that is located in the hot zone of the cracking region, to provide better mechanical control of the group V flux than just using a shutter. This provides more flexibility in controlling group V growth parameters,

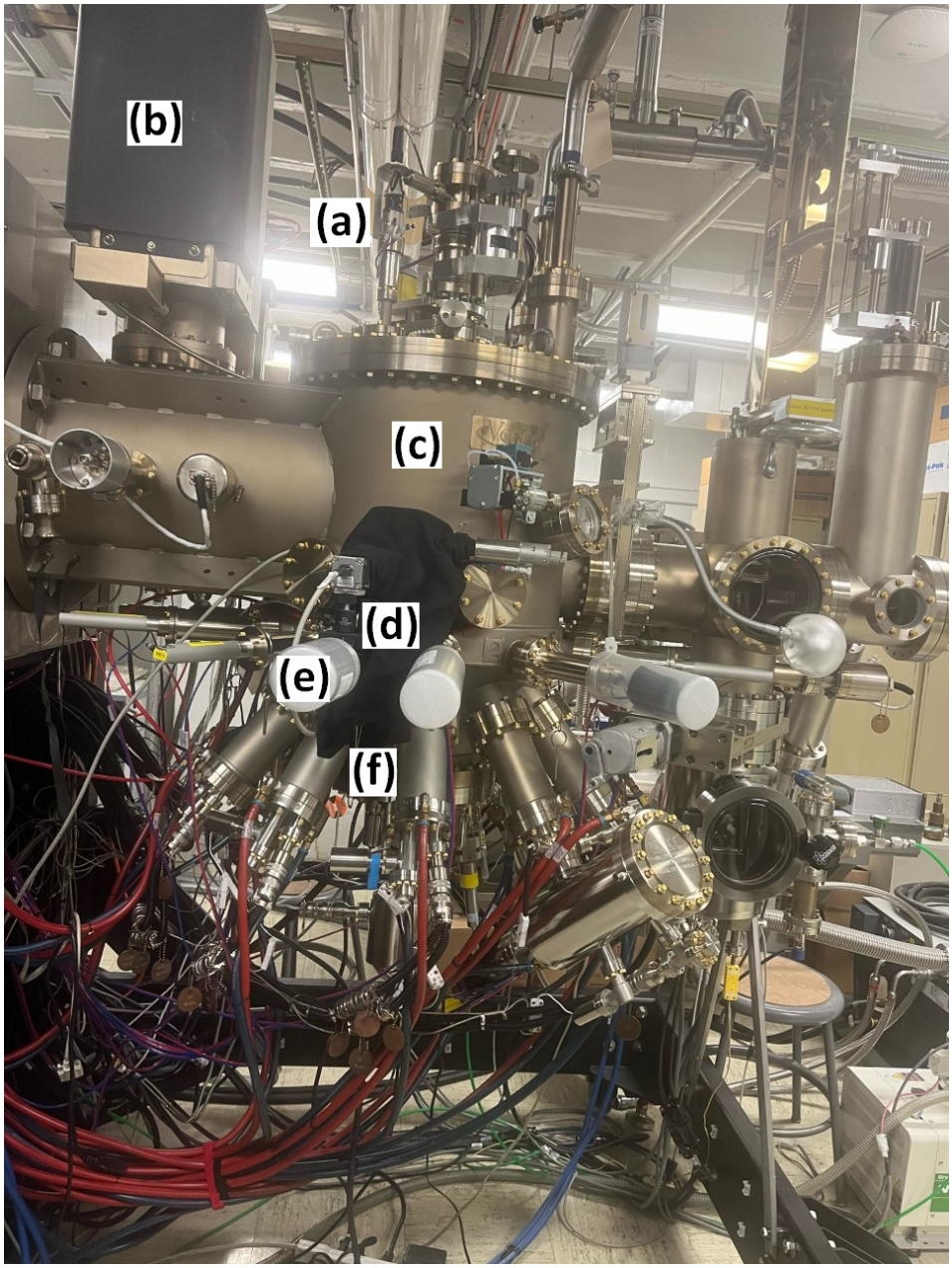

Figure 2.11: The Veeco GENxplor system used for the growth of many of the structures reported in this dissertation. Several components are labeled: (a) The substrate rotation motor, (b) the cryopump, (c) the growth chamber, (d) the RHEED camera and screen enclosed by a black cloth, (e) the shutters for each cell placed circularly around the system, (f) the various effusion cells placed circularly around the system as well as their cooling water supply (blue) and return (red) lines. Not pictured is the RHEED gun, which is on the other side of the MBE system.

especially for mixed group V alloys, as the beam flux can be changed quite easily during growth by simply adjusting the valve opening, instead of needing to change the cell temperature.

In addition to group III and V sources, three doping sources are also utilized. Si and Be are used for n-type and p-type doping, respectively. In addition, Te doping is provided with a GaTe source which allows for the n-type doping of GaSb and AlSb. Although Be acts as an acceptor in both As-based and Sb-based compounds, Si cannot be used for n-type doping of both materials because Si is an atmospheric dopant that acts as a donor in As-based materials, while it is an acceptor in Sb-based materials.[70] These features have opened up the opportunity for us to grow some of the Sb-based structures reported in this dissertation, perhaps most notably GaSb-based ICTPVs and ICLs.

2.4.2 Achieving UHV Conditions

Maintaining the system pressure at UHV conditions is critical for consistent MBE growth over long periods of time and across multiple growth runs. To facilitate this, the growth chamber is protected against atmospheric influence associated with loading substrates and unloading grown wafers by two different chambers as shown in Fig. 2.12. The first chamber is called the load/lock (or entry/exit) chamber (Fig. 2.12b) and is the only one of the three compartments that is exposed to atmosphere while the MBE system is under UHV conditions. When a substrate needs to be loaded into the MBE, this chamber is vented, and a substrate may be placed inside. The load/lock chamber is then closed and pumped down to about 10^{-2} Torr. This chamber will then be baked to ≈ 200°C using a heat lamp for at least 2 hours, though often times upwards of 8 hours of baking is done. This helps liberate any potential atmospheric contaminants from the chamber walls and allows the pump to further reduce the atmosphere to about

10^{-2} to the high 10^{-2} Torr range. Next the substrate may be moved to the buffer chamber shown in Fig. 2.12c. This chamber is typically kept at a pressure of 10^{-9} Torr and acts as a buffer between the growth and loading chambers. A transfer arm (Fig. 2.12e) is then used to transfer the substrate into the MBE growth chamber (as well as out of it upon completion of a growth).

The UHV conditions are achieved using a three-stage pumping process. The first stage employees a NeoDry15E dry vacuum pump with an ultimate pressure of about 7×10^{-3} Torr and is directly connected to the load/lock chamber. Next a Gamma Vacuum TiTan ion pump that is connected to the buffer chamber is used to further reduce the chamber pressure. The ion pump works on the trapping principle that a cloud of electrons produced by an electric discharge are stored in the anode region. These electrons then ionize incoming gases and molecules. The resulting ions are then accelerated to a chemically active cathode, in this case a cold Ti cathode, where they become trapped and thus removed from the atmosphere. The ion pump has a manufacturer ultimate pressure of about 7.5 $\times$ 10^{-11} Torr, though generally pressures in the vicinity of 10^{-9} are observed. Lastly, a Helix Cryo-Torr cryopump is connected to the growth chamber which helps maintain a consistent UHV condition of 10^{-10} Torr. The cryo pump consists of a cold head and a vacuum vessel. It uses an 80 K condensing array, a 15 K array, cold head heaters, and an 80 K radiation shield to remove gases from the growth chamber, which helps generate the vacuum condition as the gasses are condensed and absorbed onto the cooling arrays. Low temperatures are maintained through the use of high pressure helium refrigerant from a He compressor. The 80 K condensing array condenses water and hydrocarbon vapors. The 15 K array condenses nitrogen, oxygen, and argon and uses specially processed charcoal to help trap helium, hydrogen, and neon.

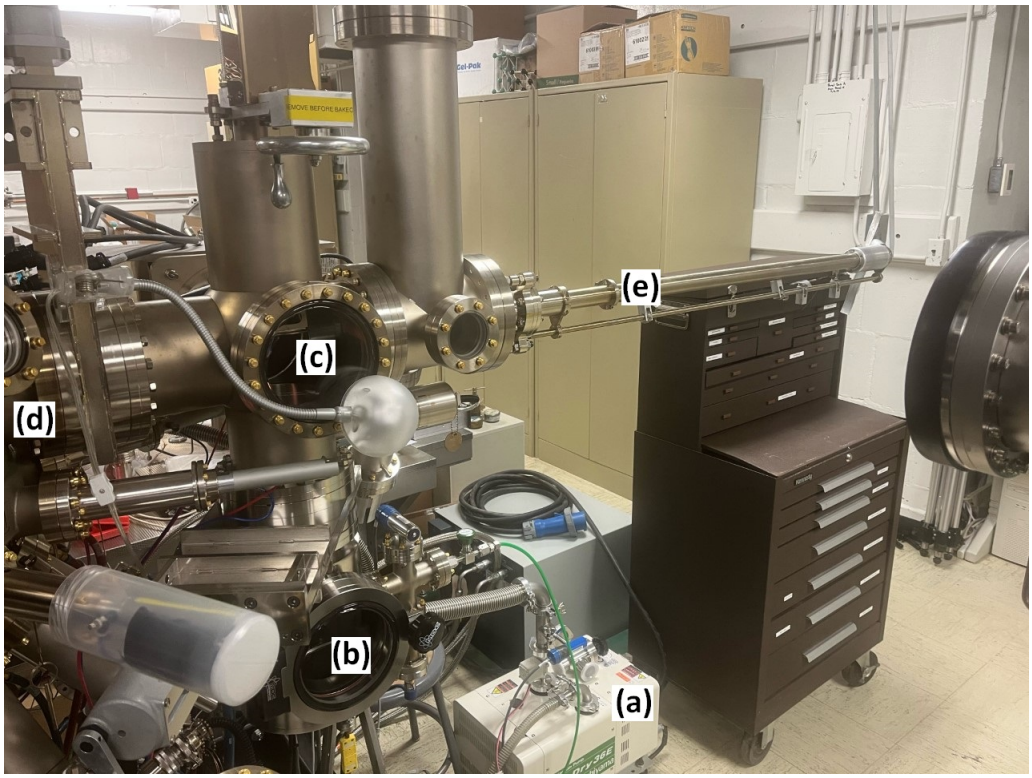

Figure 2.12: (a) The dry vacuum pump used to pump down the system to about 10^{-3} Torr as well as to pump down the load/lock (entry/exit) chamber (b). The buffer chamber (c) is placed between (b) and the growth chamber (d). A transfer arm (e) can be used to move the sample in between (c) and (d) before and after growth.

2.4.3 Temperature Monitoring During Active Growth

As previously mentioned, tight control over the substrate temperature is critical for achieving high quality growth. The GENxplor offers two options for monitoring the substrate temperature in real time during growth. The most basic approach uses a thermocouple that is installed on the backside of the substrate heater to monitor the temperature. This method is okay as it reliably and quickly measures the temperature of the heater, however, the temperature of the backside of the substrate heater and the front side where the substrate is located differ slightly. Also, the configuration of the thermocouple will vary between different MBE systems, and so a reliable comparison is hard to achieve. Furthermore, the heat will need to travel through the thick substrate and all of the various epilayers grown, each with distinct and finite thermal conductivities. This means that the temperature of the growth surface will decrease over time, as the overall thickness of the heterostructure increases. Thus, the difference in the thermocouple reading and the true growth surface temperature changes continuously during MBE growth.

A more consistent method to measure the substrate temperature involves the use of Pyrometry (sometimes referred to as Optical Thermometry). A pyrometer is a device that measures light and is calibrated to indicate temperature. The principle of this measurement tool as it applies to MBE growth surfaces is that the hot surface will radiate thermal energy which can be measured by the pyrometer. The pyrometer measures the intensity from the hot object across a narrow spectral range where its emissivity remains constant over an operating temperature interval. In that case, the Planck blackbody distribution law can be used to determine the temperature for a given emissivity.[71] The pyrometer's emissivity calibration can be made in conjunction with RHEED techniques. Common MBE structures have known temperatures when certain growth transitions or surface reconstructions

occur. For example, GaAs has a well-known oxide desorption temperature of 580°C, and so visual confirmation of this surface process occurring with RHEED may be used to calibrate the pyrometer temperature reading. However, it is important for the wavelength range of the detector to be small and centered at a photon energy higher than the substrate's bandgap. One would nominally prefer to avoid seeing the emission from the substrate heater, thus a wavelength limitation for the detector is mandatory. One must be careful in choosing a pyrometer to use based on the preferred substrate of the project. For the IC devices reported here, growth was conducted mainly on GaSb substrates, which have a bandgap of 0.726 eV (1.71 μm) at 300 K. The pyrometer used in the GENxplor is the BASF EX11984, which has a measurement wavelength of 1.6 μm over a temperature range of 25°C to 700°C, which is the typical growth temperature range for III-V materials. Thus, this particular pyrometer is ideal for growth on GaSb substrates (and also incidentally for InAs substrates) but cannot be used for GaAs growth since it has a larger bandgap of 1.42 eV (0.87 μm) at 300 K. For III-V MBE growth such as InAs, InSb, and GaSb, calibration of the pyrometer is set by the surface reconstruction that occurs after a thin layer is grown and is determined from RHEED.[72] A more detailed description of this calibration procedure can be found in Ref. [1].

2.5 Summary of MBE Growth

To summarize, MBE is an epitaxial technique offering precise layer-by-layer growth that is ideal for heterostructures needed for devices such as ICTPVs and ICLs. The system as a whole involves many complex parts and there exist many growth parameters that can be adjusted to modify the growth outcome such as the growth temperature, III-V fluxes, and growth rates. While RHEED is an *in-situ* technique that can provide qualitative feedback about the quality of the growth,

additional techniques to quantify the quality of the growth are needed, which will be the subject of Chapter 3.

Chapter 3

Material Characterization

While RHEED may be used to qualitatively assess the condition of an MBE grown structure *in-situ*, quantitative information about a structure's surface morphology, crystalline quality, and doping concentration after a structure has been fully grown and removed from the MBE chamber are of the highest importance for providing feedback to the grower. This chapter will focus on some of the commonly utilized material characterization tools available after removing a grown structure from the MBE system.

3.1 Measuring the Doping Concentration

As discussed in Section 2.4.1, both n-type (Si and Te) and p-type (Be) doping is provided by the GENxplor. The doping concentration in a structure is directly related to the temperature of the dopant cell during growth as well as the GR of a material. Therefore, a calibration must be done to relate the dopant cell temperature to a known doping concentration for a given material thickness. The Hall Effect is a useful tool that can be used to measure the carrier concentration in doped structures.

3.1.1 The Hall Effect

Consider a charged particle moving through a conducting material in the presence of a uniform magnetic field. If an electron of chare -e travels in a direction perpendicular to the direction of the field, then it will be subjected to the Lorentz force

$$\vec{F} = e(\vec{E} + \vec{v} \times \vec{B}) \tag{3.1}$$

This force will act in a direction that is perpendicular to both the direction of the magnetic field and the velocity of the charged particle, which will cause a separation of charge types within a conducting material. This leads to a buildup of positive charge on one side of the material (ionized donors, for example) and negative charge (conduction electrons, for example) on the other. The resulting asymmetry in the charge distribution generates an electric field that opposes the continued buildup of additional charge, thus establishing an electric potential between the two sides of the material called the Hall voltage (V_{Hall} or V_H) as shown in Fig. 3.1.

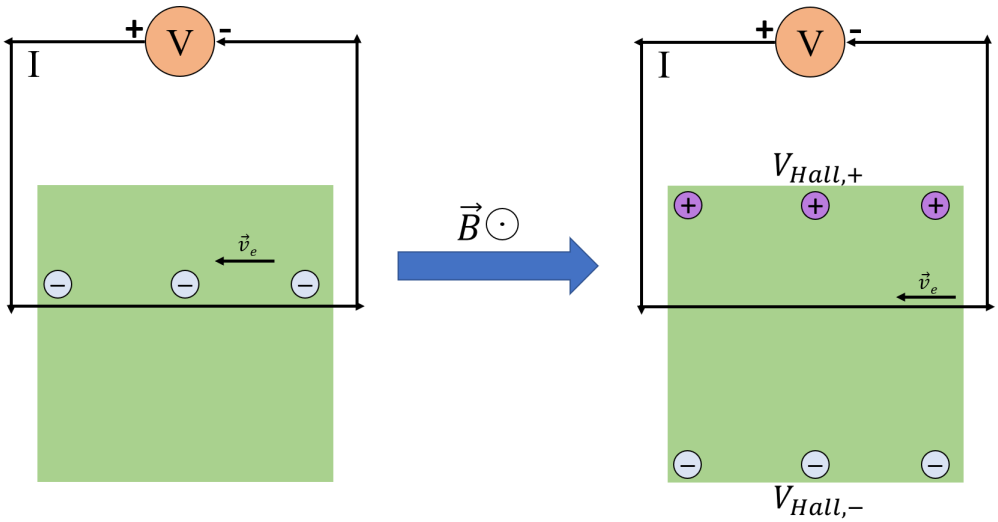

Figure 3.1: Qualitative depiction of the Hall Effect with a magnetic field oriented out of the surface.

For a simple metal, involving only a single charge carrier type and of thickness t, the V_H takes on the common form[73]

$$V_H = \frac{BI}{ent} \tag{3.2}$$

where n is the carrier concentration. Oftentimes the V_H is rewritten in terms of the Hall coefficient (R_H) as

$$V_H = \frac{R_H B}{t} I, \text{for } R_H = \frac{1}{en} \tag{3.3}$$

Therefore, if one measures the V_H for a constant drive current as a function of the applied magnetic field, the magnitude of the slope of the data will yield the carrier concentration and the sign will indicate whether the carriers are electrons or holes. Furthermore, if the thickness of the epilayer is known from careful GR calibration, both the 2D and 3D carrier concentrations may be inferred!

3.1.2 The van der Pauw Technique

In 1958, L. J. van der Pauw presented a theory of a way to measure the sheet resistance and Hall effect of a flat sample with arbitrary shape, and this idea forms the basis for a practical method to perform Hall effect measurements. The method requires several conditions, including that the contacts are placed at the edges of the sample, the contacts are sufficiently small relative to the sample itself, the sample is homogeneous, and the sample is simply connected.[74] Based on the reference image in Fig. 3.2, he was able to show that Eq. 3.4 is true for any arbitrary geometry, where d is the material thickness and R_s is the sheet resistance.

$$e^{\left(\frac{-\pi d R_{AB,CD}}{R_s}\right)} + e^{\left(\frac{-\pi d R_{BC,DA}}{R_s}\right)} = 1 \tag{3.4}$$

In Eq. 3.4, the term $R_{AB,CD}$ represents the resistance based on the potential difference between terminals D and C (i.e., $\Delta V_{DC} = V_D - V_C$) per unit current through contacts A and B, and similarly for $R_{BC,DA}$. The sheet resistance (R_s) for a sample of thickness d is given as

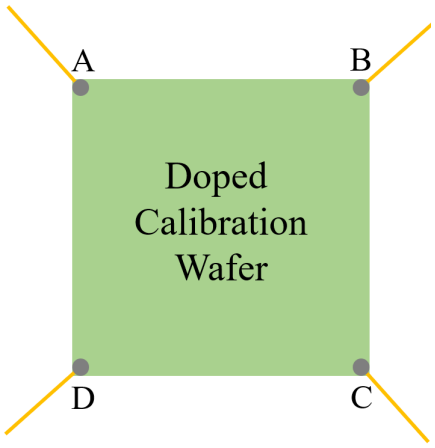

Figure 3.2: Depiction of the geometry of the Hall samples measured in this dissertation. The typical size of the samples ranged from 5×5 mm to 10×10 mm. Indium metal is used for the contact and high purity gold is used for the leads.

$$R_s = \frac{\pi d}{ln(2)} \left[\frac{R_{AB,CD} + R_{BC,DA}}{2} \right] f\left(\frac{R_{AB,CD}}{R_{BC,DA}} \right) \tag{3.5}$$

where f is the van der Pauw correction factor. For a symmetric sample with equally spaced contacts, the resistance terms $R_{AB,CD} = R_{BC,DA}$, and so f = 1.[75] The R_s can be used to determine the carrier mobility, as will be discussed in Section 3.1.3.

3.1.3 Conducting Hall Measurements

There are several different sample geometries that can be used for Hall measurement, with a clover shape being the most ideal. However, this requires fabrication of the sample to be measured. A sample with a square geometry with contacts either at the midpoints of each of the four sides or in each of the four corners provides a suitable geometry that facilitates ease of testing with minimal fabrication. A wafer to be measured is cleaved into a 5×5 mm to 10×10 mm square where it is mounted onto the cold finger of a cryostat with cryo grease. Only RT Hall measurements were conducted in this dissertation, as the goal is to have devices that operate at RT. Indium (In) is used to solder high purity gold wires to each of

the four corners of the sample as shown in Fig. 3.2, which are then connected to pins for electrical testing.

Hall effect measurements are conducted in a three step process. First, a simple 2-point IV measurement is made in order to ensure that the contacts have an Ohmic behavior, as indicated by a linear I-V relationship. Next, a series of 4-point measurements are made consisting of the following permutations: I_+,I_- = A,B/B,C/C,D/D,A where the corresponding potential difference is measured at V_+,V_- = D,C/A,D/B,A/C,B. This measurement will result in the measurement of $R_{AB,CD}$ and $R_{BC,DA}$ from Eq. 3.5, and thus the sheet resistance and the resistivity ($\rho = R_s/d$) of the sample. The third and final step involves sweeping the current through the sample while sweeping an externally applied magnetic field from 0 to 0.133 T. From a plot of the V_H as a function of applied magnetic field, the Hall resistance can be determined and thus the carrier concentration (2D) and mobility according to

$$n = \frac{B}{eR_H} = \frac{0.133[\mathrm{T}]}{e \times \text{measured Hall resistance}[\Omega]} \tag{3.6}$$

$$\mu = \frac{1}{en\rho} \tag{3.7}$$

Note that n and μ are the 2D carrier concentration (n_{2D}) and mobility, respectively. In order to determine the 3D carrier concentration (n_{3D}) and mobility, one should divide by the epilayer thickness.

3.1.4 Doping Calibration Studies on the GENxplor

Each time the MBE system is opened to atmosphere for maintenance, the various source cells are refilled. When this is done, a new calibration for GR and doping for each source must be completed after the MBE system is back under

UHV conditions. Because the depletion of the dopant material (Si, GaTe, Be) is generally a very slow process, a doping calibration study only infrequently needs to be completed. A doping calibration study involves growing 500 nm to 2 μm of material on a chosen substrate with the dopant cell of choice active at a fixed temperature. This is then repeated at least 2-3 more times with slightly different dopant cell temperatures so that one has 3-5 calibration samples to measure. The GR of the material is known thanks to careful calibration with RHEED oscillations, and so the total thickness of the material is known. The results are configured in an Arrhenius plot as a function of the inverse of the dopant cell temperature. Figures 3.3 to 3.5 show the GENxplor doping calibration for Si-doped InAs, Te-doped GaSb, and Be-doped GaSb, respectively, from February 2020 compared to previous studies.

It is important to point out that the carrier concentration in a doped MBE grown structure (wafer) is not just a function of the dopant cell temperature, but also of the GR of the material grown. In fact, the carrier concentration is inversely proportional to the GR, meaning that a slower growth rate at a fixed dopant cell temperature will result in a higher incorporation of that dopant material into each layer grown, effectively increasing the carrier concentration. Conversely, if a higher GR is used then the incorporation will be reduced, leading to a lower carrier concentration. Therefore, consideration of the GR of a given epilayer in a complicated structure like an ICL is of critical importance if that layer is to be doped. Oftentimes the most critical layers (generally the cascade region) are grown with slow GRs in order to ensure uniform, and good material quality, while faster growth rates may be used if a thick layer is to be grown, in order to reduce the overall growth time. Also note that since III-V MBE growth is group III limited, the doping calibration for one type of binary will apply to other binaries or ternary

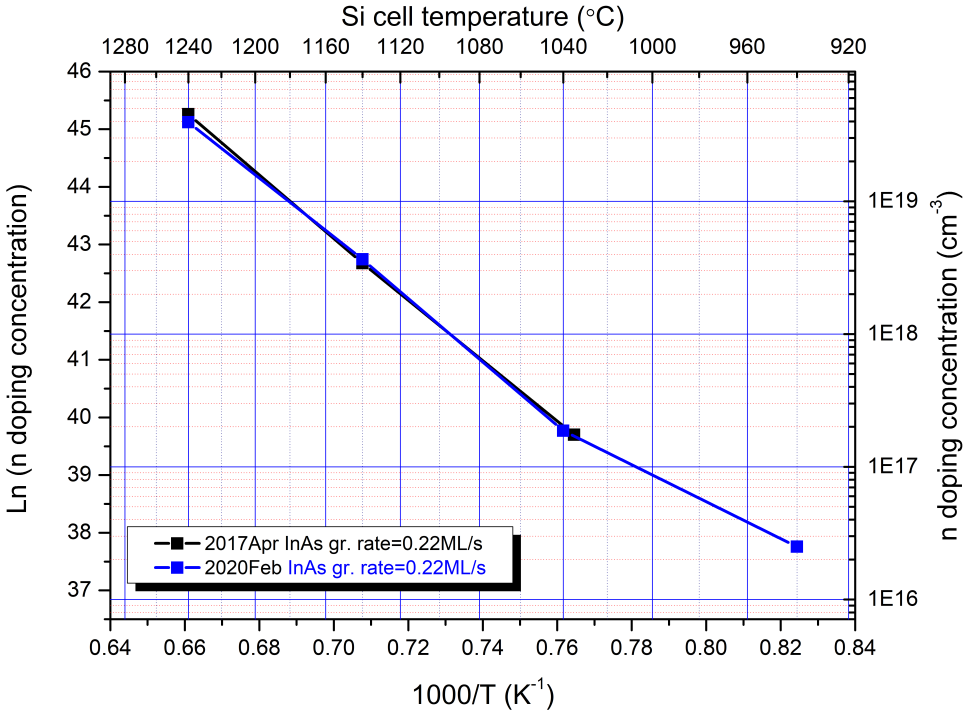

Figure 3.3: Plot of the natural log of the n-doped (Si) carrier concentration in InAs as a function of the inverse of the Si cell temperature. A recent calibration in Feb. 2020 (blue) is plotted against a previous calibration from April 2017 (black) showing the high degree of consistency over time.

alloys as long as the same, single group III material is used. For example, since a Si-doped InAs calibration is completed, this profile can, in principle, be used if one chooses to Si-dope InSb or $InAs_xSb_{1-x}$, as long as the same GRs are used.

The thickness of the epilayer grown during a doping calibration study is an important consideration, depending on the system in question. For example, Si doping of InAs requires a thicker layer of InAs because this material suffers from an electron accumulation layer stemming from native surface defects. InAs tends to adjust its energy bands such that the Fermi level becomes located above the conduction band minimum.[76] Thus this accumulation layer can potentially contaminate the Hall measurement if a low doping concentration is being measured. It has been verified in the literature that the accumulated charge is in the range of

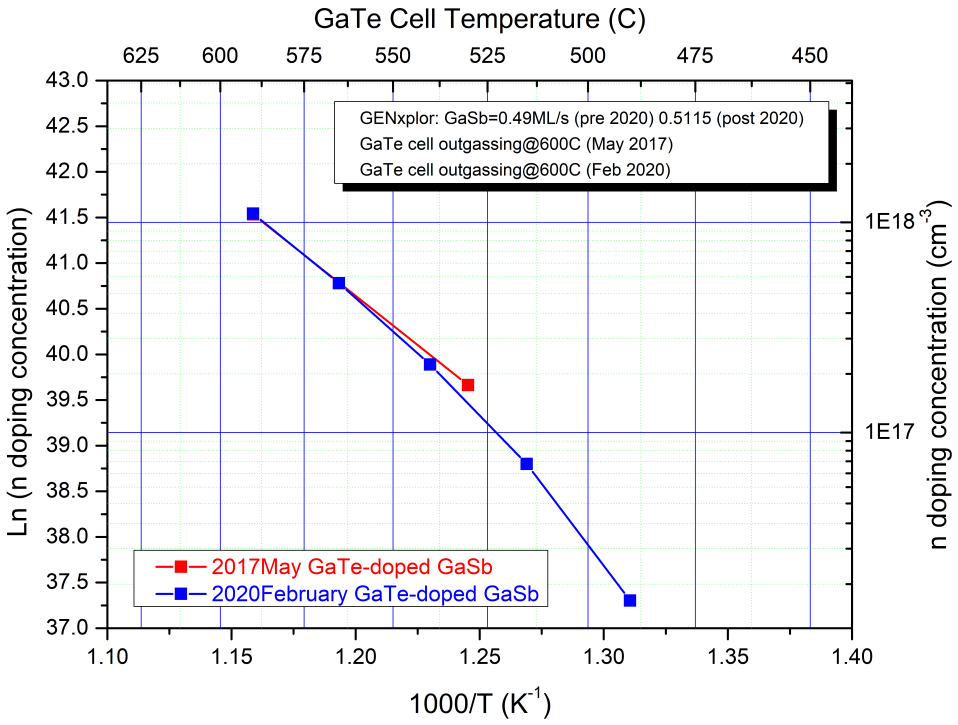

Figure 3.4: Plot of the natural log of the n-doped (Te) carrier concentration in GaSb as a function of the inverse of the GaTe cell temperature. A recent calibration in Feb. 2020 (blue) is plotted against a previous calibration from May 2017 (red) showing a slight difference at higher cell temperature due to the slightly different GRs used during calibration.

around 10^{12} cm^{-2}.[76, 77] This can be problematic as it would introduce another carrier and the one carrier Hall model as discussed above would no longer be valid. Therefore, one must grow a thick enough epilayer such that the n_{2D} is sufficiently larger than the accumulated charge in InAs when the Si doping concentration is low. Table 3.1 lists relevant parameters and Hall measurements for the calibration samples shown in Figures 3.3 to 3.5.

3.2 Differential-Interference-Contrast Microscopy

The first technique used to examine and characterize a grown wafer is that of differential-interference-contract (DIC) microscopy (sometimes referred to as

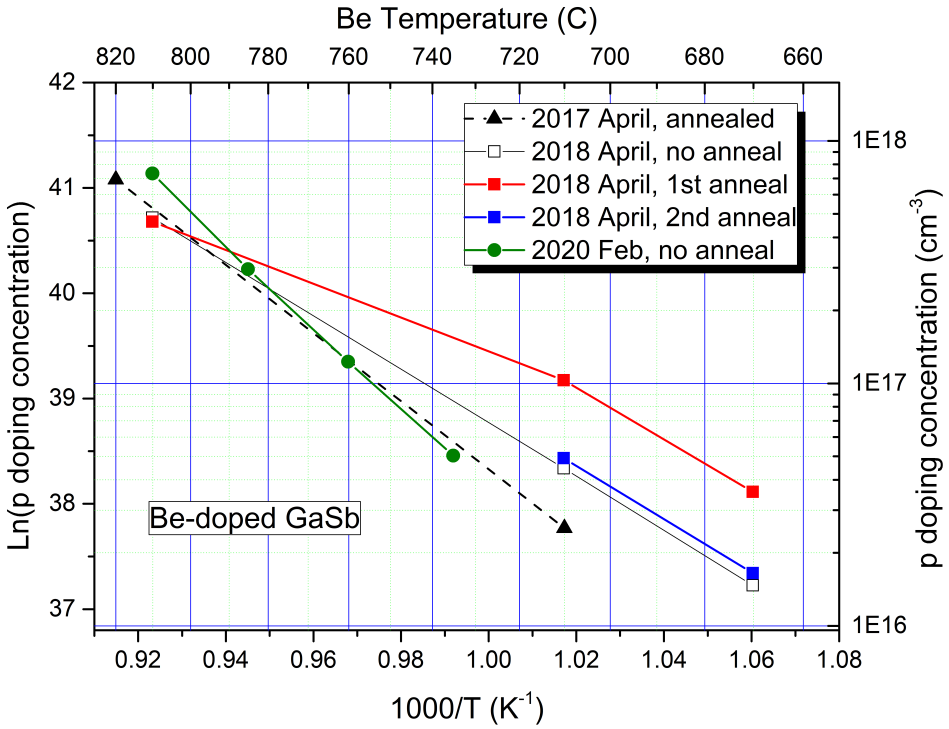

Figure 3.5: Plot of the natural log of the p-doped (Be) carrier concentration in GaSb as a function of the inverse of the Be cell temperature. Several calibration studies are shown between 2017 and 2020 related to contact annealing.

Nomarski interference microscopy). DIC is an optical microscopy technique that is used to evaluate the surface morphology, which is to say the surface quality, of a grown wafer. First, light incident onto the sample surface, which is generated by a lamp and passes through a polarizer, is divided into two beams which are polarized orthogonal to each other. The two coherent beams travel to the surface and are recombined later. Due to various topographic features on the wafer surface, some of which may have different refractive indices, there will exist an optical path difference when the beams are brought to recombine causes destructive interference. A second polarizer is used to modulate the position at zero optical path difference, in order to bring the two beams back into the same plane. This adds contrast to the image, which visually shows as an intensity variation in the color across

Table 3.1: The various parameters of the doping calibration conducted in the Spring of 2020. Dopant cell temperatures are reported as measured from the thermocouple.

Parameters and Results for the Doping Calibration Study in Spring 2020					
Sample	Dopant	GR (ML/s)	Cell T (°C)	n_{2D} (μm^{-2})	n_{3D} (μm^{-3})
n-InAs1	Si (n)	0.22	940	6.3×10^{12}	2.50×10^{16}
n-InAs2	Si (n)	0.22	1040	3.3×10^{13}	1.87×10^{17}
n-InAs3	Si (n)	0.22	1140	3.6×10^{14}	3.65×10^{18}
n-InAs4	Si (n)	0.22	1240	3.0×10^{15}	3.94×10^{19}
n-GaSb1	GaTe (n)	0.5115	490	3.2×10^{12}	1.59×10^{16}
n-GaSb2	GaTe (n)	0.5115	515	1.4×10^{13}	7.08×10^{16}
n-GaSb3	GaTe (n)	0.5115	540	1.05×10^{13}	2.11×10^{17}
n-GaSb4	GaTe (n)	0.5115	565	2.6×10^{13}	5.13×10^{17}
n-GaSb5	GaTe (n)	0.5115	590	5.46×10^{13}	1.1×10^{18}
p-GaSb1	Be (p)	0.5115	735	8.17×10^{12}	5.03×10^{16}
p-GaSb2	Be (p)	0.5115	760	1.54×10^{13}	1.23×10^{17}
p-GaSb3	Be (p)	0.5115	785	2.59×10^{13}	2.96×10^{17}
p-GaSb4	Be (p)	0.5115	810	3.57×10^{13}	7.13×10^{17}

the image. Thus, a pseudo-3D like surface effect is rendered, where one may adjust the position of the 2nd polarizer to scroll through contrast features on the image surface, allowing for the determination of surface defects as either pits or clusters. Effectively, this allows for a sort of color mapping of the wafer surface that provides high contrast and allows one to examine the various types of surface defects present.

In III-V MBE growth, the dominant defect type is the oval hillock as shown in Fig. 3.6. These types of defects have been studied extensively in the MBE growth of GaAs[78–80] and were thought to be due to oxidation of the Ga source material or spitting of Ga from the source crucible. However, these defects should have higher Ga compositions, which is not observed. Furthermore, metal organic chemical vapor deposition (MOCVD) was also used to rule out this effect as MOCVD is a chemical deposition process that does not involve any spitting of source materials like in MBE[80, 81]. The accepted growth model in GaAs (and

by extension, GaSb) is that the formation of oval hillock defects takes place due to propagating stacking faults that form a polyhedral pit. These stacking faults arise from surface defects/contaminants from the substrate surface. Therefore, it is unlikely that growth can be achieved with a surface defect density that is less than that of the bare substrate used for growth (generally about 10^3 cm^{-2}).

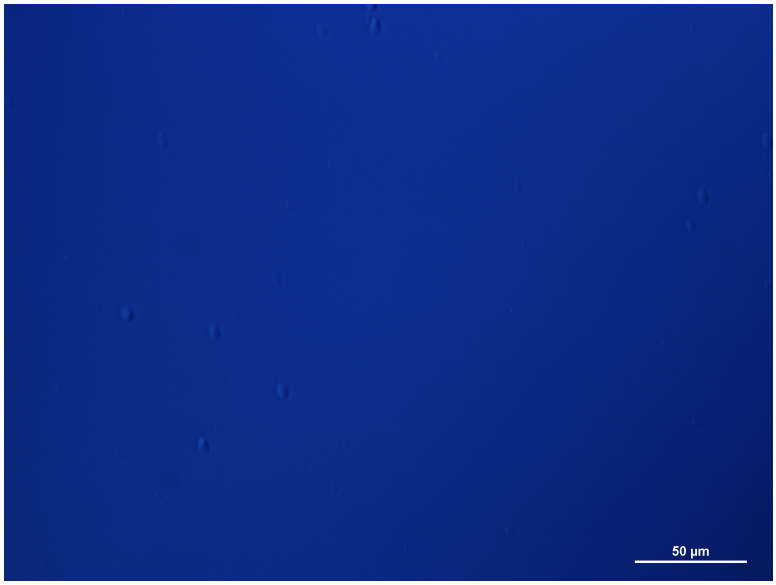

Figure 3.6: Example of typical oval hillock defects under 40X magnification in Y065V, an ICTPV structure taken in Nov. 2018.

Besides visual inspection of the nature of a surface defect on a grown wafer, DIC also provides a means by which to quantify the average surface defect density. The NIS-Elements D software allows one to define an area of the wafer where one may visually count the number of defects in order to determine the surface defect density. For example, consider Fig. 3.7 which shows the surface of an ICTPV sample (Y072V). An automatic calibration in the software between pixels and the physical dimension (such as μm) is activated based on the magnification selected. In the example, an area of approximately 123,000 μm^2 is traced out, within which roughly 45 defects may be observed. This amounts to a surface defect density of 3.67×10^4 cm^{-2}. This measurement should be done at several different

locations on the wafer surface to arrive at an average surface defect density. For IC structures, degradation of device performance was previously observed for structures with defect densities greater than 10^6 cm^{-2}, while the background defect density from the substrates used for growth is approximately 10^3 cm^{-2}, according to the manufacturer. Therefore, for III-V IC growth, structures with an average surface defect density of between 10^3–10^5 cm^{-2} are suitable for fabrication and device characterization.

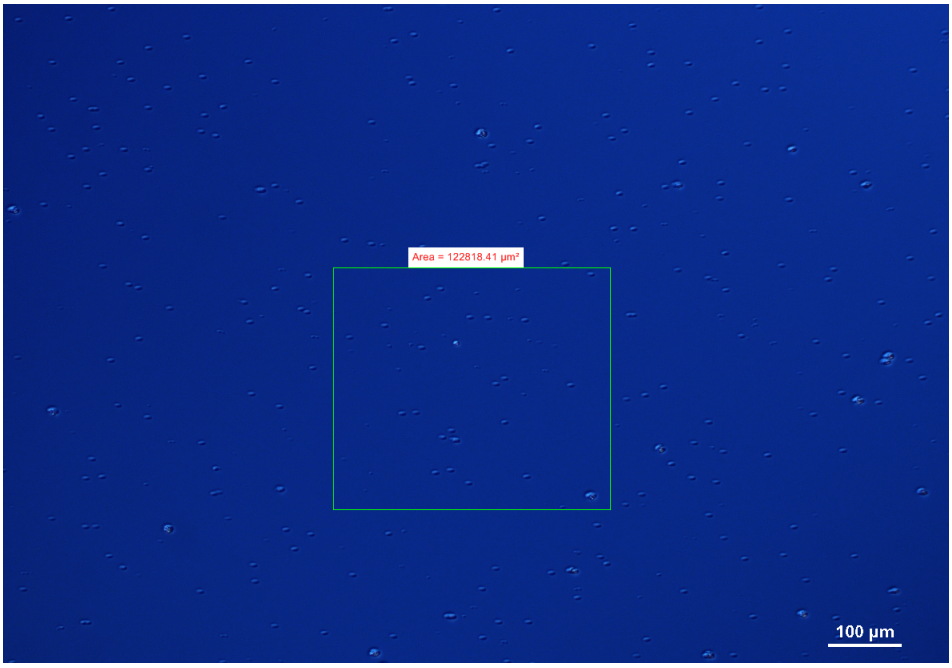

Figure 3.7: Example of a surface defect count showing about 45 defects in the traced out area on the surface of an ICTPV structure (Y072V) taken at 10X magnification in April 2019.

3.3 X-ray Diffraction

Perhaps no better material characterization tool exists for probing the crystalline quality of an MBE grown wafer than x-ray diffraction (XRD). This versatile technique can provide information regarding strain, layer thicknesses, alloy composition, interface quality, SL period, and structural defects, all of which may

be compared with the intended structure design.[4] Furthermore, the type of XRD employed to study materials in this dissertation is non-destructive and only requires a small piece of the grown wafer (i.e., no device fabrication is required). Because the energy of the x-ray photons is large, so too is the penetration depth, allowing deep probing of grown materials. First a treatment of diffraction within a crystalline solid will be presented, followed by a discussion of how to extract relevant information from the XRD pattern as well as the XRD setup used in this dissertation.

3.3.1 The Reciprocal Lattice and Crystal Diffraction

XRD involves the interaction of waves with solid matter, where scattering and absorption take place. It is generally considered that the best treatment for this interaction is in reciprocal space, which is the Fourier transform of the spatial function of the original lattice in real space (direct lattice). The reciprocal lattice is defined as follows: For a given direct lattice of points $\mathbf{R}$, a point $\mathbf{G}$ is a point in the reciprocal lattice if and only if

$$e^{i\mathbf{G}\cdot\mathbf{R}} = 1 \tag{3.8}$$

for all points $\mathbf{R}$ of the direct lattice.[3] The reciprocal lattice may be constructed based on the direct lattice, which has the form

$$\mathbf{R} = n_1\mathbf{a}_1 + n_2\mathbf{a}_2 + n_3\mathbf{a}_3 \tag{3.9}$$

where n_i are integers and $\mathbf{a}_i$ are unit lattice vectors. The unit lattice vectors of the reciprocal lattice ($\mathbf{b}_j$) have the property that

$$\mathbf{a}_i \cdot \mathbf{b}_j = 2\pi\delta_{ij} \tag{3.10}$$

Under this condition, the unit lattice vectors of the reciprocal lattice have the form

$$\mathbf{b}_1 = \frac{2\pi\mathbf{a}_2 \times \mathbf{a}_3}{\mathbf{a}_1 \cdot (\mathbf{a}_2 \times \mathbf{a}_3)}, \mathbf{b}_2 = \frac{2\pi\mathbf{a}_3 \times \mathbf{a}_1}{\mathbf{a}_1 \cdot (\mathbf{a}_2 \times \mathbf{a}_3)}, \mathbf{b}_3 = \frac{2\pi\mathbf{a}_1 \times \mathbf{a}_2}{\mathbf{a}_1 \cdot (\mathbf{a}_2 \times \mathbf{a}_3)} \tag{3.11}$$

and the reciprocal lattice vectors take on the form

$$\mathbf{G} = m_1\mathbf{b}_1 + m_2\mathbf{b}_2 + m_3\mathbf{b}_3 \tag{3.12}$$

where, as before, the m_i's are integers.

Reciprocal lattice points can be thought of as representing families of lattice planes as shown in Fig. 3.8 with the distance between planes defined as

$$d = \frac{2\pi}{\mathbf{G}} \tag{3.13}$$

To understand crystal scattering, one could consider treating the incoming wave as a particle that is subject to some potential and treat the approach using Fermi's golden rule. If doing so, and using a periodic potential, one would find that the matrix element is zero unless the difference between the incoming wavevector ($\mathbf{k}$) and the scattered wavevector ($\mathbf{k}'$) is an integer number of reciprocal lattice vectors.[3] This condition, $\mathbf{k}$ - $\mathbf{k}'$ = n$\mathbf{G}$ is known as the Laue condition and is a statement about the conservation of the crystal momentum, with the condition that when the wave leaves the crystal $|\mathbf{k}| = |\mathbf{k}'| = 2\pi/\lambda$ representing conservation of energy.

Consider Fig. 3.9, which depicts an incident and scattered wave from a periodic structure. Based on this geometry,

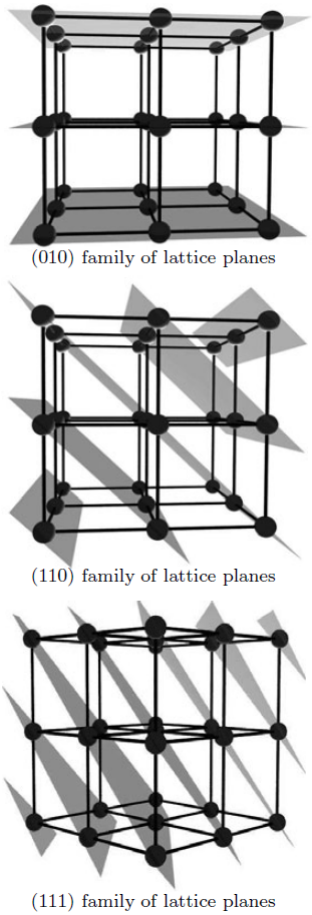

Figure 3.8: Depiction of several lattice planes in a cubic lattice.[3]

$$\hat{\mathbf{k}} \cdot \hat{\mathbf{G}} = -\hat{\mathbf{k}}' \cdot \hat{\mathbf{G}} = \sin(\theta) \tag{3.14}$$

The Laue condition may be rewritten as

$$\mathbf{k} - \mathbf{k}' = n\mathbf{G} \rightarrow \frac{2\pi}{\lambda}(\hat{\mathbf{k}} - \hat{\mathbf{k}}') = n\mathbf{G} \tag{3.15}$$

and dotting the Laue condition with the reciprocal lattice unit vector gives

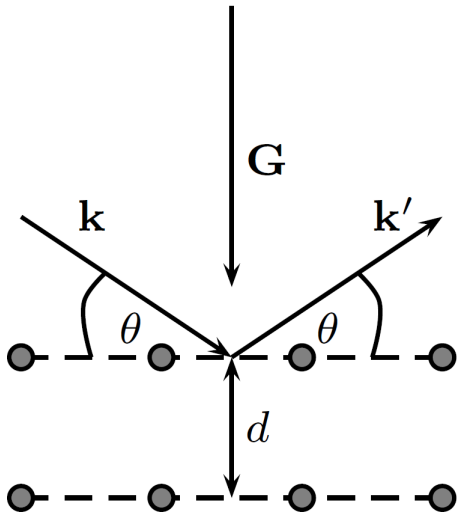

Figure 3.9: Depiction of the geometry of scattering in a crystal.[3]

$$\begin{aligned} \hat{\mathbf{G}} \cdot \frac{2\pi}{\lambda}(\hat{\mathbf{k}} - \hat{\mathbf{k}'}) &= \hat{\mathbf{G}} \cdot n\mathbf{G} \\ \frac{2\pi}{\lambda}(\sin(\theta) - \sin(\theta')) &= n|\mathbf{G}| \rightarrow \\ \frac{2\pi}{|\mathbf{G}|}(2\sin(\theta)) &= n\lambda \rightarrow \\ 2d\sin(\theta) &= n\lambda \end{aligned} \tag{3.16}$$

Here we see a familiar result, that of Bragg diffraction. The Bragg law describes that scattering from coherent waves in a crystal lattice may give rise to constructive interference. As depicted in Fig. 3.10, the component of the incident wave that reflects off of the deeper layer travels an extra distance of 2dsin(θ) and in order to have constructive interference, this extra distance must be equal to an integer number n of wavelengths. Understanding how the real space points connect to the reciprocal space points allows one to utilize the Bragg law to gather relevant growth information from the XRD diffractograms.

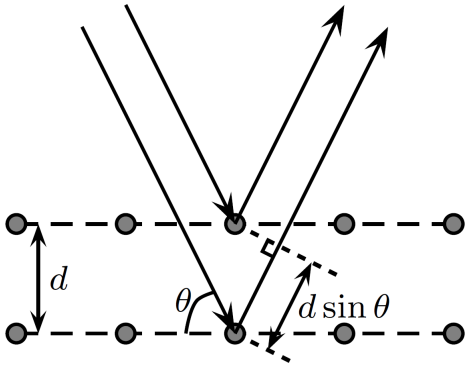

Figure 3.10: Depiction of Bragg diffraction from two planes of atoms in a crystal. The extra distance traveled by the wave striking the lower plane is 2dsin(θ).[3]

3.3.2 Analyzing XRD Spectra

In a mathematical sense, the reciprocal lattice points are true points which would result in delta like spikes in the XRD spectrum. However, in a real XRD measurement, the reciprocal lattice points are volumes instead that become broadened due to several factors including the finite layer thickness of the epilayers, variations in the lattice parameters, and other experimental deviations from perfect periodicity of the direct lattice. Thus, the full width at half maximum (FWHM) provides a quantitative value which can be a good indicator of the material quality of a grown wafer. The general rule of thumb is the smaller the FWHM, the better the material quality is.

The Bragg law may be directly used to determine a number of important structural features of a grown wafer. First, consider d from Eq. 3.16 and Fig. 3.10. For a material with cubic symmetry (i.e., III-V materials) and with lattice constant a_{epi},

$$d \rightarrow d(hkl) = \frac{a_{epi}}{\sqrt{h^2 + k^2 + l^2}} \tag{3.17}$$

In this way, the Bragg law may be rewritten as

$$2d\sin(\theta) = n\lambda \rightarrow 2a_{epi}\sin(\theta) = \lambda\sqrt{h^2+k^2+l^2} \tag{3.18}$$

where λ is the wavelength of the x-ray source ($\lambda = 1.54$ Å). The variables h, k, and l are Miller indices and we set n = 1 for convenience. Here h, k, and l are set by the type of XRD scan one performs. In a symmetric scan (hkl) = (004), where the XRD directly probes the out-of-plane lattice constants of the various layers in the wafer, while in an asymmetric scan (hkl) = (110) provides information about the in-plane lattice constants. It is most common (and easier) to conduct symmetric scans as the analysis of this data is more straightforward, with the measurement quicker to complete. In this dissertation, all XRD results discussed will be from symmetric scan data.

For symmetric scans, Eq. 3.18 simplifies to

$$2a_{epi}\sin(\theta) = 4\lambda \rightarrow a_{epi} = \frac{2\lambda}{\sin(\theta_{epi})} \tag{3.19}$$

Actually, this form is general and does not need to necessarily be applied only to an epitaxial layer. In fact, Eq. 3.19 may be applied to bulk layers (whether binary, ternary, or more complex alloys), SL structures, and even the substrate itself! In general, a chosen substrate material will have a known Bragg angle (θ in Eq. 3.19) and based on the above result, the strain type may be directly identified. Fig. 3.11 shows an example of a measured (blue) XRD spectrum for an ICL (Y082L to be discussed later in Chapter 7) compared with a simulation (red) of the intended design. In the plot, the x-axis is the Bragg angle, where if $\theta_{epi} < \theta_{sub}$ then $a_{epi} > a_{sub}$ and there is tensile strain in the z-component of the epilayer lattice constant, meaning biaxial compressive strain. Conversely, if $\theta_{epi} > \theta_{sub}$ then $a_{epi} < a_{sub}$ indicating a measured compressive out-of-plane strain, inferring biaxial tensile strain.

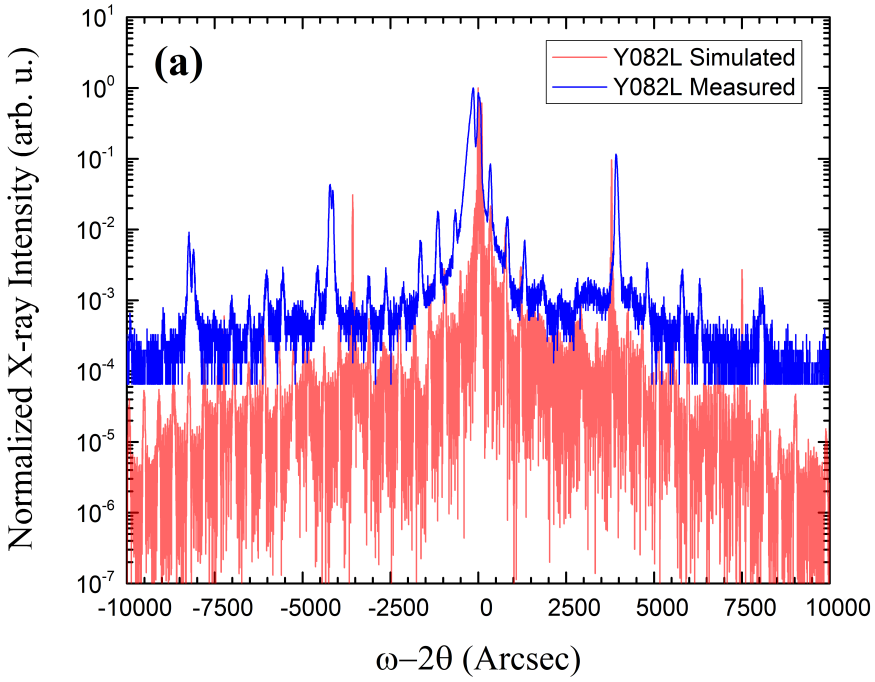

Figure 3.11: Example of a measured (004) XRD spectrum for an ICL (Y082L-blue) compared to the simulated XRD spectra (red) based on the ideal device design. The x-axis is ω relative to the peak for the GaSb substrate, which $\theta = 30.36°$. Generally, these plots are then centered to the known substrate position.

The lattice mismatch is defined as the difference between the epilayer lattice constant and the substrate lattice constant, relative to the substrate. Therefore, based on Eq. 3.19, the lattice mismatch between a given epilayer and the substrate, as determined from an XRD measurement, is

$$m = \frac{a_{epi} - a_o}{a_o} \rightarrow m = \frac{2\lambda}{a_o \sin(\theta_{epi})} - 1 \tag{3.20}$$

Because a SL is a periodic structure, it will exhibit harmonic peaks in the XRD spectrum. The SL period (average SL thickness) may be determined from the XRD spectrum by considering any two integer multiples of these harmonic peaks. Starting from the Bragg law

$$2d\sin(\theta) = n\lambda \rightarrow 2T\Delta\sin(\theta) = \Delta N\lambda \tag{3.21}$$

where T is the SL period, $\Delta \sin(\theta)$ is the difference in the Bragg angle positions of any two harmonic SL peaks, and ΔN is the difference between an arbitrary numerical count for the ith and jth peak positions. Therefore, this equation may be redefined as

$$T = \frac{|i-j|\lambda}{2\Big(\sin(\theta_i) - \sin(\theta_j)\Big)} \tag{3.22}$$

As an example, consider an InAs/AlSb SL designed to have a period of 50 Å. An XRD spectrum showed that for the -1 (ith) and +1 (jth) peaks with $\theta_{-1} = 29.416°$and $\theta_{+1} = 31.474°$, the resulting SL period measured to be T = 49.73 Å, a difference of about -0.6% thinner when compared with the intended design value.

3.3.3 Identification of Peaks in XRD Results

In order to extract relevant information from an XRD spectrum, the correct identification of a peak to an associated material or SL is critical. The most powerful technique to use for identifying peaks is to simply create XRD simulations using the Philips X'pert Epitaxy software and try to visually identify where such peaks line up. For example, the thicker layers in an ICL will typically consist of a buffer layer (InAs or GaSb), a separate confinement layer (SCL) of the same material as the buffer layer, an intermediate SL cladding layer of InAs/AlSb, a plasmon cladding layer (InAs or $InAs_xSb_{(1-x)}$), and the cascade region. Thus, a unique simulation for each of these substructures can be generated and compared with the measured XRD spectrum.

When identifying peaks, there are a couple of good rules to follow. First, the XRD intensity is sensitive to the epilayer thickness, meaning a thicker epilayer results in a stronger signal and thus a higher XRD peak intensity. In general, the substrate is the thickest layer in the entire grown wafer, so in principle it should

have the most intense XRD peak. For thick IC structures, however, only a small portion of the x-rays interact with the substrate. If the epilayer is of comparable thickness to the portion of the substrate undergoing x-ray interactions, then it is possible for a SL peak to have comparable intensity to the substrate peak. In that case, one must be careful to not assign peak designations on peak intensity alone. Comparing with simulations when considering peaks of comparable intensity is a recommended strategy, especially when dealing with non-SL structures.

When characterizing SL structures or substructures, there is a second rule that is good to follow. It is always the case that the greater the thickness of an individual period in a SL structure, the narrower the spacing (in $\sin(\theta)$) between harmonic peaks in the XRD spectrum. Conversely, the thinner an individual period of a SL is, spacing between peaks of the spectrum will be wider. Therefore, there is a reciprocal relationship between period thickness and peak spacing in XRD that is related to the fact that the XRD is probing the structure in reciprocal space. This can help quickly identify one set of harmonic peaks from another.

One of the central considerations of material characterization is to know the lattice mismatch and the type of strain a material is under. For a bulk structure, this is straightforward from the XRD data. However, for a SL structure this can be problematic because the SL structure may be quite thick which can result in comparable XRD peak intensities to those of other structures and/or the substrate. In practice, the main diffraction peak, the so-called 0th order peak will usually be the peak of maximum intensity with other harmonic peaks ($\pm$ 1, $\pm$ 2, etc...) reducing in intensity the further out in θ one gets. If the 0th order peak has comparable intensity to that of other peaks, like the substrate, one may consider the peak spacing between any two adjacent harmonic SL peaks should be equal in $\sin(\theta)$. Therefore, the difference between the -1 to 0 and the 0 to +1 peaks, for example, should be symmetric (or at least show a very low degree of asymmetry)

for the true 0th order peak, while that of the substrate peak should show a larger degree of asymmetry. Thus, this technique may be used to correctly assign XRD peaks to known SL materials. More discussion on this will be presented in Chapter 4.

3.3.4 Experimental Procedure for XRD Scans

The XRD system used to study the crystalline quality of MBE grown structures in this dissertation is the Philips HR-2 High Resolution Diffractometer with a four reflection Ge (220) incident beam monochromator. The Ge (220) monochromator is made of a single crystal of germanium that is cut in such a way that the planes of the crystal lattice are oriented to reflect X-rays with a particular wavelength. This crystal orientation allows the monochromator to select a specific wavelength of X-rays from a broader range of wavelengths produced by the X-ray source. A four-reflection geometry means that the incident beam passes through the monochromator crystal four times, resulting in increased resolution and intensity of the monochromatic beam. This design is particularly useful in high-resolution x-ray diffraction experiments, where the ability to discriminate between closely spaced diffraction peaks is crucial. The x-rays selected from the source have a wavelength of λ =1.54059 Å, corresponding to the CuKα1 transition.[82] Ideally, with a new x-ray source, the system presents an incident beam power of 1200 W, which corresponds to an unobstructed x-ray count rate of roughly 600,000 counts/s, and a minimum FWHM resolution of 14 arcsec. However, often count rates somewhat less were observed due to the reduced lifetime of the x-ray source. Nevertheless, a full x-ray count in excess of 290,000 counts/s or more was generally observed, which is enough to conduct high resolution XRD. The sample stage was controlled using the Philips PC-MRD software, with minimum step sizes of

0.00025°and 0.001°for Omega (ω) and 2Theta (2θ), respectively.

In order to acquire the most accurate data, a careful calibration of the various parameters available to the scan program is essential. To understand this, consider the top-down view of the XRD setup shown in Fig. 3.12. In a resting (home) state, the detector is in direct line of sight to the x-ray source. When conducting an XRD measurement, the wafer is placed on the sample holder, directly in the middle of the source-to-detector line of sight. The sample holder is moved back, and the full x-ray count is measured. Then the sample holder is moved forward to impinge on the beam until the measured count rate has fallen by approximately one half. This ensures that many of the x-rays are available to interact with the wafer. Next, a symmetric (004) scan is set within the software in order to collect data on the out-of-plane lattice constant(s) of the structure to be measured. Within the software, the substrate material is chosen, which initiates stage movement of the sample and the detector to preprogrammed positions based on the known Bragg angle of the substrate (bottom figure). This involves rotation of the sample with respect to the incident beam through angle ω, and rotation of the detector forming an angle 2θ between the incident and diffracted beam. Additionally, the sample stage may be rotated about a horizontal axis with respect to the beam of angle ψ to ensure that the [001] direction is in the diffraction plane defined by the incident beam and the diffracted beam.

To perform a symmetric scan of an IC structure there are three main steps, consisting of initial angular movements to lock on to the maximum signal intensity of the diffracted beam, followed by refined motions to further optimize the signal intensity, and lastly a full high resolution scan to collect the intensity data. To do this, first an ω scan is performed, typically with the following settings: 3° range, 0.005° step, 0.1 s/step. This means that 1.5° on the left and right side of

the substrate peak position will be explored by rotating the sample with a fixed detector position. This is a fast scan, lasting only 1 minute and afterwards, the stage is moved to the peak intensity position determined from the scan. The reason that the peak intensity may not line up with the preprogrammed Bragg angle of the substrate is due mostly to the sample mounting, which may not be exactly flat on the sample holder (i.e., not fully parallel with the incident beam). Additionally, there may be some small tilt between the substrate and the epilayer, lattice deviations from the assumed or relaxed values, and small errors in the motor controls of the stage.

Next, a more refined ω scan is done to further maximize the peak intensity signal, with scan settings of 0.2° range, 0.002° steps, and 0.2 s/step dwell times. After that, a ψ-optimization program is executed which consists of a series of small ω scans at different ψ angles. This is a critical scan as it ensures that the XRD scan is made through the center of the reciprocal lattice point by optimizing the intensity collected across a minimum width. This is followed by a repeat of the second step as a final check of alignment to the peak intensity position.

The final step involves a full $\omega-2\theta$ scan. Here the 2θ drive is moved at double the angular speed of the ω drive. The typical settings for a high resolution XRD scan of a full ICTPV or ICL structure are: 7° range, 0.001° step, 1 s/step, which takes considerably longer than the calibration scans, amounting to about 2 hours. This ensures a wide enough scan field to collect multiple harmonic peaks from the various SL structures in this IC device, as well as high enough resolution to distinguish closely spaced fringe peaks. The collected data may be analyzed with the previously discussed perspectives. Detailed analysis of XRD data from several IC structures will be presented in Chapters 4, 6, and 7.

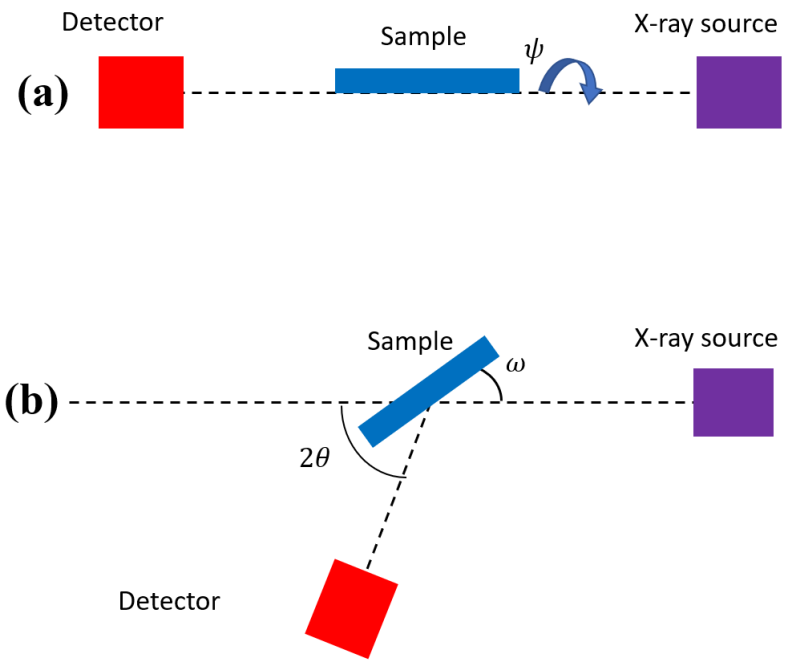

Figure 3.12: A top-down view of the XRD setup. The top image (a) shows the home state of the stage, where a sample is placed directly between the x-ray source and the detector. The bottom (b) shows the position of the stage after moving to the Bragg angle of the substrate to perform signal calibration. The angle ω is formed between the sample and the x-ray beam, while θ is formed between the incident beam and the diffracted beam. The last angle, ψ is a tilt of the sample holder which rotates the sample with respect to the beam horizontal as depicted in (a).

3.4 Other Material Characterization Tools

While Hall measurements, DIC, and XRD were the primary instruments with which to analyze the quality of a grown structures, they do not constitute the only tools. Other widely utilized techniques include scanning electron microscopy (SEM) and atomic force microscopy (AFM). SEM provides topographic information and real time imaging of the surface of the wafer. Of particular note is its use in studying surface defects, ridge fabrication quality, and facet quality in an ICL. An SEM equipped with an energy dispersive spectrometer (EDS) can be used to check the elemental composition of various defects and layers, since an SEM is sensitive

to the atomic number contrast (z-contrast) of a material. AFM can be used to probe the overall surface roughness of a wafer, giving indications as to good or bad material quality. Chapter 4 will present several growth studies of various IC structures used in both ICLs and ICTPVs with extensive discussion on material characterization based on the techniques presented in this chapter.

Chapter 4

Growth Studies of IC Structures

Devices based on the interband cascade design are made of layer structures that are complicated to grow. They consist of several different superlattices, bulk layers, ternary layers, and various connecting regions. In the case of an ICL, there are three SL structures, two of which consist of a bottom InAs/AlSb SL as well as a top InAs/AlSb SL, which is used for part of the waveguide to confine the optical wave. The third SL is the cascade region which consists of the W-QW active region as well as the injection region, which is composed of both the election and hole injectors. Additionally, as will be one of the central topics of Chapter 6, thick layers of heavily n-doped (n^+) InAs or $InAs_xSb_{1-x}$ are also grown above and below the cascade region and act as the outer most optical cladding, depending on the type of substrate used for growth. In the case of an IC thermophotovoltaic device (ICTPV), there are also three SL structures; two unipolar barriers consisting of an electron barrier and a hole barrier, and the doped absorber composed of an InAs/GaSb SL.[83]

The GENxplor was brought online during 2015, with much work dedicated to various GR and doping calibrations. In 2016, the transition from the Gen2 to the GENxplor for IC structures was carried out. Much of the growth study efforts reported in this dissertation took place between late 2016 and early 2020. As discussed previously, the GENxplor has several enhanced features that are ideal for growing GaSb-based ICLs, that is to say an ICL grown on a GaSb substrate. At the time, there was recent work on an advanced waveguide structure for long wavelength InAs-based ICLs which used the plasmon-enhanced waveguide for better optical confinement and heat extraction.[9, 84–89] This work was also

applied to InAs-based ICLs operating at 4.6 μm[7], which yielded quite successful results, with an InAs-based ICL operating at RT with the lowest threshold current density measured at that time. This technique is explored for GaSb-based ICLs in Chapter 7, which outlines recent success in that implementation. The beginnings of this project lie in optimizing the growth of these critical structures on the GENxplor. Sections 4.1, 4.2, and 4.3 detail several growth studies related to optimizing various components of the GaSb-based ICL growth. These techniques, originally developed for GaSb-based ICLs, are later applied to GaSb-based ICTPV structures in Sections 4.4.2, 4.4.3, and 4.5.

4.1 $InAs_xSb_{1-x}$ Alloy Calibration

Applying the plasmon enhanced waveguide to a GaSb-based ICL, originally composed of n^+-doped InAs on InAs-based ICLs, meant growing n^+-doped $InAs_xSb_{1-x}$ lattice matched to GaSb. This alloy, with its heavy Si-doping, had not yet been grown on the GENxplor and because of the differences between the former MBE system and the new one a series of growth studies were required to accurately grow this material.

4.1.1 Critical Thickness Criteria

The first consideration when growing a ternary alloy like $InAs_xSb_{1-x}$ is to ask what proportion of As and Sb will yield ideal lattice matching to the GaSb substrate for the ICL. The second component is to know how tight the control of the group V composition need to be in order to grow thick (> 1 μm) alloy layers without introducing enough defects to lead to a relaxed/partially relaxed overall structure. The answer to these questions can be addressed by considering the Matthews-Blakeslee critical thickness model.[90, 91] The premise for this discussion

is that a preexisting threading dislocation in the substrate can replicate in the growing epilayer, bending over to create a length of misfit dislocations (a chain of dangling bonds) at the substrate/epilayer interface once a critical thickness of the grown epilayer is reached. This, in turn, causes partial or full relaxation of the epilayer. The following discussion follows the mathematical treatment as described in [4]. Consider Fig. 4.1, which depicts the bending of a threading dislocation originating at the substrate surface and running through the growing epilayer to form a line of misfit dislocations. Here there is a glide force (F_G) acting on the dislocation of the form

$$F_G = \frac{2Gb\epsilon h(1+\nu)\cos(\lambda)}{(1-\nu)} \tag{4.1}$$

where G is the shear modulus, b is the length of the Burgers vector (a vector representing the distortion of the lattice due to a dislocation), ϵ is the strain as previously described, h is the thickness of the epilayer, ν is the Poisson ratio, and λ is the angle between the Burgers vector and the line in the interface that is perpendicular to the intersection of the glide plane with the interface.

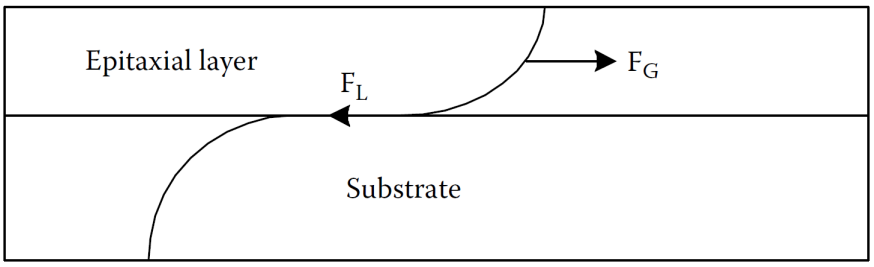

Figure 4.1: The bending of a grown-in threading dislocation to create a length of misfit dislocation at the interface between an epilayer and the substrate.[4]

There also exists a line tension (F_L) acting opposite to the glide force of the form

$$F_L = \frac{b(1-\nu\cos^2(\alpha)[ln(h_c/b)+1]}{8\pi|\epsilon|(1+\nu)\cos(\lambda)} \tag{4.2}$$

where α is the angle between the Burgers vector and the line vector for the dislocations. Here we assume that G is equal between the substrate and the epilayer, where the critical thickness condition occurs when $\mathrm{F}_G = \mathrm{F}_L$. Thus, the epilayer mismatch as a function of the critical layer thickness is

$$m = \frac{b(1-\cos^2(\alpha))}{8\pi h_c(1+\nu)\cos(\lambda)}\left[ln\left(\frac{h_c}{b}\right)+1\right] \tag{4.3}$$

When $\mathrm{h} < \mathrm{h}_c$, the F_G is unable to overcome the F_L and the dislocation is said to be stable. Conversely, if $\mathrm{h} > \mathrm{h}_c$, threading dislocations are able to move about to create misfit dislocations at the interface, which causes relaxation in the mismatch strain. For zinc blende materials, it is assumed that $\cos(\alpha) = \cos(\lambda) = 1/2$ and $\mathrm{b} = a/\sqrt{2}$. The typical Poisson ratio of $\nu = 1/3$ for III-V materials is also assumed. Ideally, the alloy composition results in a lattice constant that matches that of the substrate. Under this condition, a thick epitaxial layer may be grown. As shown in Fig. 4.2, the tolerable lattice mismatch quickly decreases with increasing epilayer thickness. For the plasmon cladding to be grown for GaSb-based ICLs, the thickness may range between 1-1.5 μm, thus very tight control over the lattice mismatch must be maintained, which means that the alloy compositions cannot deviate too far from their ideal values without introducing some degree of relaxation.

The lattice mismatch for a ternary alloy such as $\mathrm{InAs}_x\mathrm{Sb}_{(1-x)}$ (with a general form of $\mathrm{XY}_y\mathrm{Z}_z$) may be determined as

$$y = \frac{a_{epi} - a_{XY}}{a_{XZ} - a_{XY}}; z = \frac{a_{epi} - a_{XZ}}{a_{XY} - a_{XZ}} \tag{4.4}$$

Using Eq. 4.4 for the GaSb lattice constant (i.e., setting $a_{epi} = a_{sub}$) results in an As and Sb composition of $\mathrm{InAs}_{0.91}\mathrm{Sb}_{0.089}$ to achieve a proper latticed matched

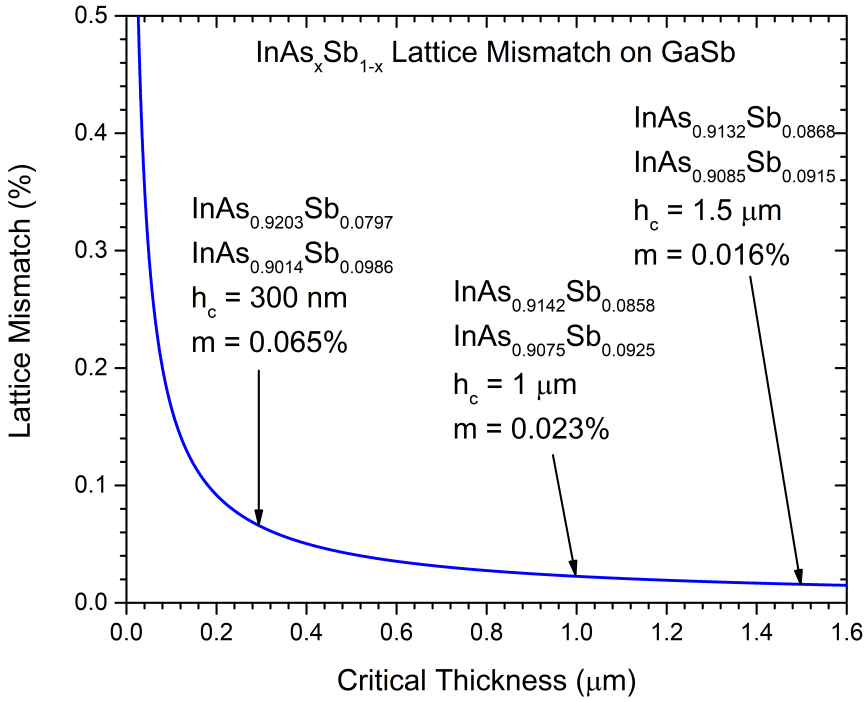

Figure 4.2: Plot of the mismatch percent as a function of the critical thickness of an epilayer based on Eq. 4.3. Several different $InAs_{0.91}Sb_{0.089}$ layer thicknesses and their associated mismatch values are referenced.

condition for GaSb for sufficiently thick alloy layers.

4.1.2 Initial Alloy Calibration Efforts

Because the plasmon cladding is a highly Si-doped ternary alloy, both a doping calibration as well as an alloy composition calibration need to be conducted. A reasonable choice is to use semi-insulating (SI) GaAs as the substrate material, since it will not contribute any background carriers to the doping calibration. Though the lattice mismatch between the intended $InAs_{0.91}Sb_{0.089}$ and the GaAs substrate is quite large, relaxed layers of the alloy may be grown. This allows for an initial estimate of the proper As and Sb MBE growth parameters while simultaneously completing the doping calibration. This could not be done on a GaSb substrate because the GaSb/InAsSb interface is known to be semimetallic,

Table 4.1: MBE Growth Parameters for the initial InAsSb composition + doping calibration in the Fall of 2016. In the table, the valve values are in units of Mil (1 mil = 25.4 μm) and the Flux values have the units of (Torr).

MBE Growth Parameters for the initial InAsSb Calibration					
Wafers	Si T (°C)	As Valve	As Flux	Sb Valve	Sb Flux
M052	1330	70	2.22×10^{-6}	30	4.23×10^{-8}
M053	1290	69	2.20×10^{-6}	25	3.71×10^{-8}
M054	1240	70	2.23×10^{-6}	25	4.05×10^{-8}
M055	NA	69	2.21×10^{-6}	23	3.38×10^{-8}
M056	1330	130	6.99×10^{-6}	43	8.47×10^{-8}

which leads to massive flooding of the InAsSb layer by electrons from the valence band of GaSb.[92] Several wafers were initially grown with varying MBE growth parameters, primarily changes to the Si doping cell temperature as well as the As and Sb valve openings and associated fluxes, as shown in Table 4.1. In this study, the substrate temperature was kept fixed at T_{sub} = 490°C and the In GR used was 0.25 ML/s.

Fig. 4.3 shows the measured XRD patterns for these calibration wafers, while Fig. 4.4 depicts the doping calibration as well as the associated alloy composition as determined from the XRD measurements. In Fig. 4.3, the substrate peaks of both GaAs and GaSb are centered at 0 arcsec in order to show the relative differences between the relaxed InAsSb alloy peaks on GaAs and the strained InAsSb peak on GaSb. In the latter the thickness of the alloy layer is measured to be about 1.2% too thin, with the Sb composition about 1.6% less than the ideal value of 8.91%. A high carrier concentration level approaching 10^{19} cm^{-3} is required for the plasmon cladding, which was successfully achieved as demonstrated from the doping study in Fig. 4.4. Additionally, growth with the second In source (In1), using a much faster GR = 0.6 ML/s (M056) also achieved the necessary doping level needed. Since the plasmon cladding layers are so thick in the full ICL structure, having the ability to use two different In cells with different GRs can greatly reduce the

growth time. Also, an undoped alloy calibration wafer (M055) was grown on a GaSb substrate ($T_{sub/pyro}$ = 490/419 °C) and demonstrated only a slight deviation from the intended layer thickness of 300 nm and alloy composition required, as shown in Fig. 4.5. The thickness of the layer may be measured from the XRD pattern due to the Pendellosung fringes (sometimes referred to as Pendellosung oscillations). This is a thin film interference effect that can occur because the x-rays may scatter from different planes of the crystal lattice. The scattered x-rays have a variation in their path lengths which results in constructive and destructive interference giving rise to oscillations in the diffraction pattern. Generally, only crystals with a high crystal purity and smooth surface can exhibit this feature, which typically corresponds to thin epilayers. For thicker epilayers, the fringes become extinguished due to layer nonuniformities, surface roughening, and defect formation.

4.1.3 Revised InAsSb Alloy Calibration

The initial alloy calibration successfully demonstrated the approximate growth conditions required for growing InAsSb lattice matched to GaSb. However, this study was done for a 300 nm thick layer. Because of the tight requirement of the As and Sb compositions in the alloy for thick layers, it was decided that further calibration studies should also use GaSb buffer layers, grown before the growth of InAsSb, with a thickness of about t = 500 nm. This is to ensure a 2D growth surface for the alloy, as the OD process can render a 3D growth surface, which facilitates defect propagation from the substrate through the epitaxial layer. The layer thickness was initially held fixed at t = 300 nm during this study, and then increased incrementally later for thicker alloy layer growth. The As and Sb valves and their associated fluxes were only slightly adjusted. The main parameter that

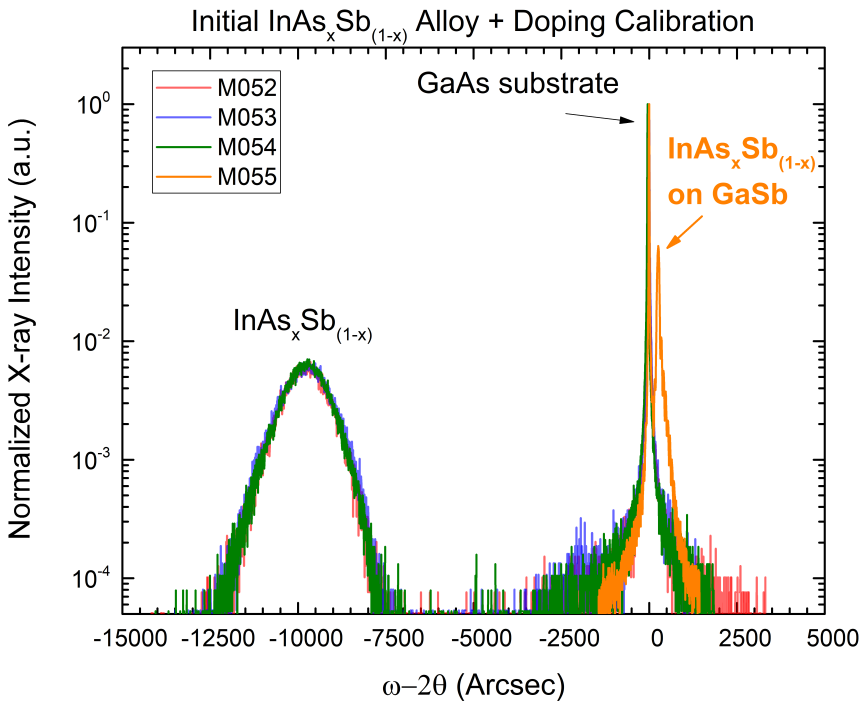

Figure 4.3: Normalized XRD pattern for several calibration structures grown on GaAs (M052/53/54) as well as one (M055) grown on a GaSb substrate. The position of both the GaAs and GaSb substrate peaks are set to 0 arcsec in order to demonstrate the relative separation of the InAsSb alloy peaks grown on the two difference substrates. The relaxed InAsSb peak can be seen clearly, centered at roughly -10000 arcsec for the test structures grown on GaAs, while that grown on the GaSb substrate is much closer, indicating a strained system.

was varied was the substrate temperature as determined from the thermocouple reading. The temperature was varied from 390°C to 560°C, extending lower and higher than temperature ranges previously adopted in the literature[93], since the thermocouple arrangement can vary between different MBE systems. It was observed from DIC and XRD that an ideal temperature seemed to fall within the 400-430°C range, as depicted from the XRD patterns in Fig. 4.6

With an understanding of the appropriate temperature range for good crystalline quality growth of InAsSb, several additional structures were grown with increased thicknesses and adjusted As and Sb fluxes. This culminated in wafer

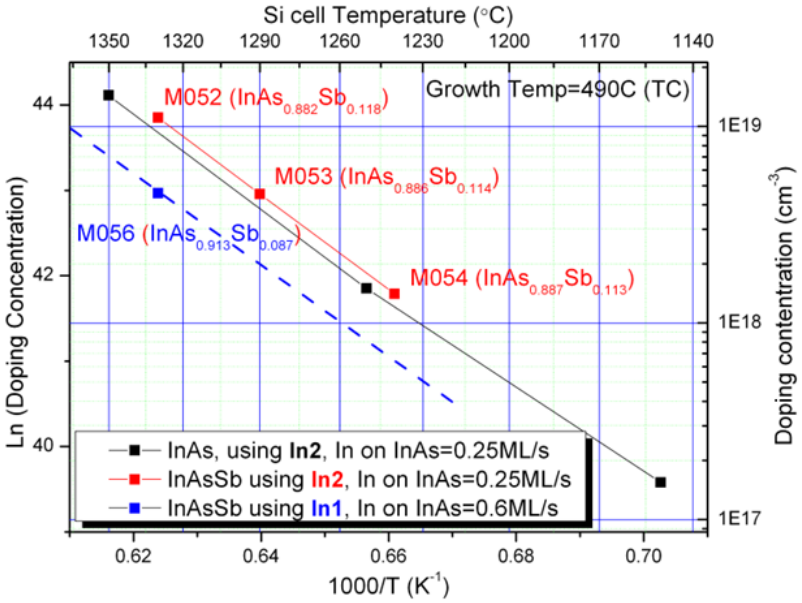

Figure 4.4: Arrhenius plot of the doping concentration as a function of 1/T according to Hall measurements. The wafer names also show the extracted alloy composition values from the XRD patterns.

M189, which was grown to be 1.2 μm thick, at a T_{sub} = 405°C with an As valve opening of 132 mils, corresponding to an As flux of 4.67×10^{-6}. The Sb valve opening was 49 mils, corresponding to an Sb flux of 1.2×10^{-7}. The V_{As}/III ratio was 8.01, while the V_{Sb}/III ratio was 0.21, similar to that found in previous InAsSb growth.[94] Fig. 4.7 shows the measured XRD pattern for M189 (blue) along with the simulated XRD pattern (red) for a 1.2 μm thick $InAs_{0.911}Sb_{0.089}$ layer on GaSb. The extracted alloy composition from the measured XRD pattern was $InAs_{0.9115}Sb_{0.0885}$ which very closely matches the intended design. Fig. 4.8 shows the surface morphology as taken from DIC imaging, which demonstrates a smooth surface with few defects. Table 4.2 lists some of the XRD results from a series of InAsSb calibration wafers grown across two growth studies.

Table 4.2: MBE Growth Parameters for the later InAsSb composition calibration in the Spring of 2017. In the table, the Sb fraction is calculated assuming the alloy is strained to the substrate. The MBE system was down for a period of several weeks between M141 and M164, and thus the growth calibration changed and needed to be redone. The values of h_c are calculated based on Eq. 4.3 using the Sb fractions determined from the measured XRD data.

MBE Growth Parameters for the later InAsSb Calibration					
Wafer	T_{sub} (°C)	Sb frac (%)	t nominal	t measured	h_c (μm)
M124	430	6.915%	300 nm	354.3 nm	0.11 μm
M125	400	7.829%	300 nm	350.8 nm	0.22 μm
M138	420	8.974%	300 nm	363.3 nm	13.2 μm
M140	425	8.175%	300 nm	333.1 nm	0.34 μm
M141	420	8.940%	600 nm	-	100 μm
M164	415	5.677%	300 nm	-	0.06 μm
M168	405	5.660%	300 nm	334.9 nm	0.06 μm
M171	405	8.312%	300 nm	347.9 nm	0.43 μm
M172	405	8.505%	300 nm	332.7 nm	0.65 μm
M173	405	9.823%	300 nm	332.9 nm	0.30 μm
M174	405	8.766%	600 nm	662.8 nm	1.8 μm
M175	405	8.305%	1.5 μm	-	0.42 μm
M189	405	8.855%	1.2 μm	-	3.8 μm

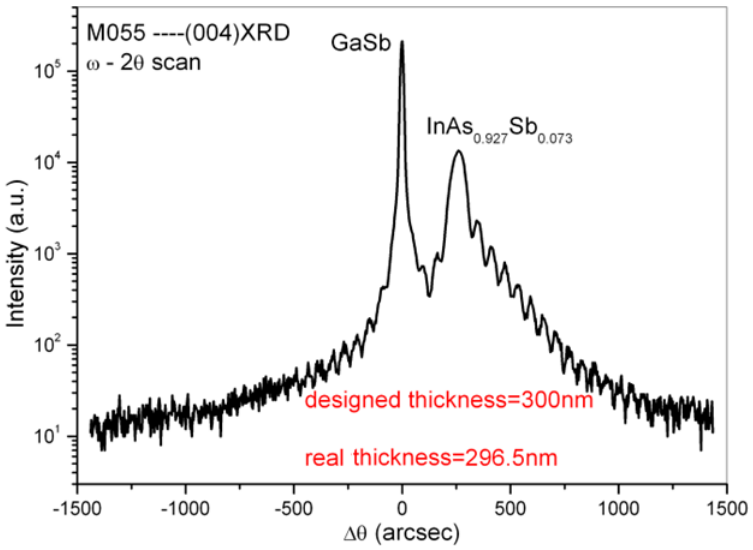

Figure 4.5: XRD pattern for M055, an InAsSb alloy calibration wafer grown on GaSb. For this thin epilayer, the Pendellosung fringes may be observed to the left and right of the substrate/alloy peaks.

4.1.4 First Attempt at GaSb-based ICL Growth

The result of the first growth attempt of a GaSb-based ICL (Y039L) is shown in Fig. 4.9. It is clear from both the XRD and the DIC inspection that the material quality is quite poor. The surface is laden with defects and the SL peaks in the XRD are not aligned well to the simulated pattern, with quite broad FWHM values, again another indication of inferior material quality. The full structure was then broken into three distinct components and grown individually to try to access where the problem was coming from.

An LED structure was made to have the same cascade region as Y039L, and two were grown with slightly different GRs. The GR of the first test structure was GR = 0.45 ML/s (Y040LED), while that of the second was GR = 0.2 ML/s (Y041LED). Both structures exhibited smooth surfaces with few defects determined from DIC imaging as shown in Fig. 4.10. Furthermore, both structures had quite good XRD patterns that closely matched the intended design when compared

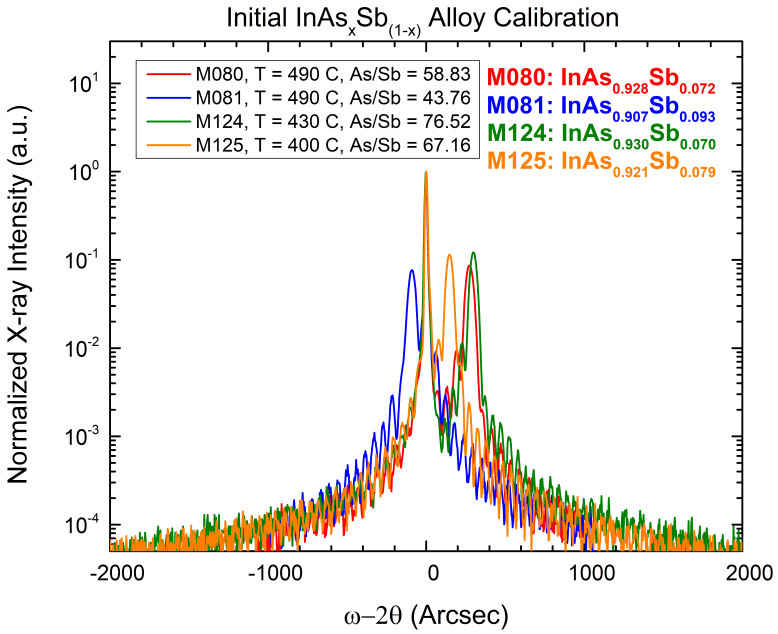

Figure 4.6: XRD pattern for several InAsSb alloy calibration wafers grown on GaSb. The key describes several MBE growth parameter adjustments such as the substrate temperature, the As/Sb ratio, and the extracted alloy composition from the measured XRD.

against the simulated pattern as shown in Fig. 4.11. The FWHM in the measured XRD patterns for both devices were quite narrow, indicating good material quality. Additionally, the peak positions of the SL peaks closely matched that of the simulated pattern, indicating a proper strain-balanced condition was achieved. The extracted lattice mismatch showed tensile strain in the out-of-plane lattice constant of the SL cladding with mismatch values of 0.143% and 0.1031% for Y040LED and Y041LED, respectively. The thickness of the cascade period deviated from the intended design by +5.47% and -0.84% for Y040LED and Y041LED, respectively. Y040LED showed a cutoff wavelength during device testing of 6.3 μm, while the cutoff for Y041LED was 3.3 μm. Both were designed to have a cutoff wavelength of 4.6 μm, and this striking deviation shows that the device operation is robust with respect to growth deviations, a theme later explored in Chapter 7. These results confirm that the cascade region was not directly responsible for the

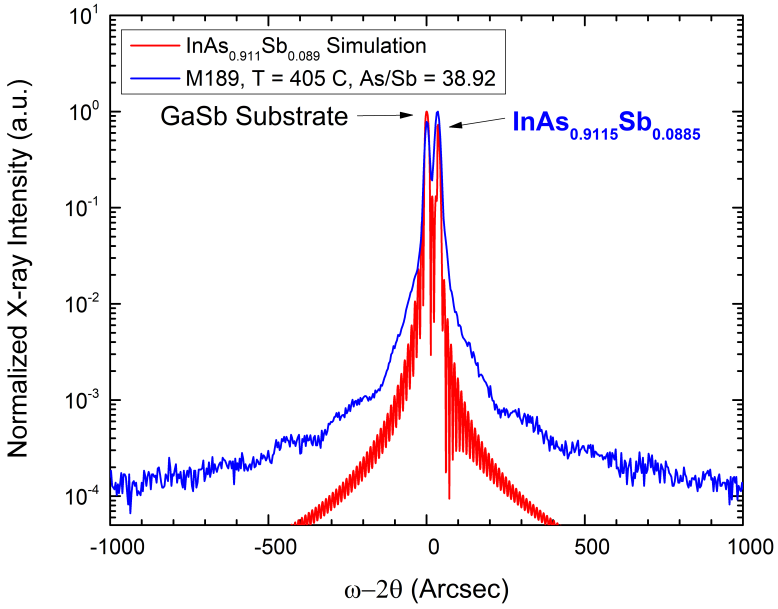

Figure 4.7: XRD pattern of wafer M189 (blue), a 1.2 μm thick InAsSb layer grown on a 500 nm GaSb buffer. Also shown is the simulated XRD pattern (red) of $InAs_{0.911}Sb_{0.089}$ on GaSb.

poor material quality of Y039L.

Next, both the InAsSb plasmon cladding and the InAs/AlSb SL were individually grown. The repeated alloy layer growth closely matched the final calibration wafer (M189). However, the grown InAs/AlSb SL showed significant deviations from the intended design. In the full ICL structure of Y039L, a total of 180 periods of InAs/AlSb with individual layer thickness of 26.5 Å and 23.5 Å were grown below and above the cascade region (i.e., a total of 360 periods). In the InAs/AlSb test structure, only 180 periods total were grown. The XRD results are shown in Fig. 4.12, where it can be seen that the FWHM of the SL peaks are quite broad, indicating poor material quality. This was likely due to the choice of MBE growth conditions, since those had not yet been optimized on the GENxplor. Furthermore, atomic force microscopy (AFM) was performed on the InAsSb test wafer (M190)

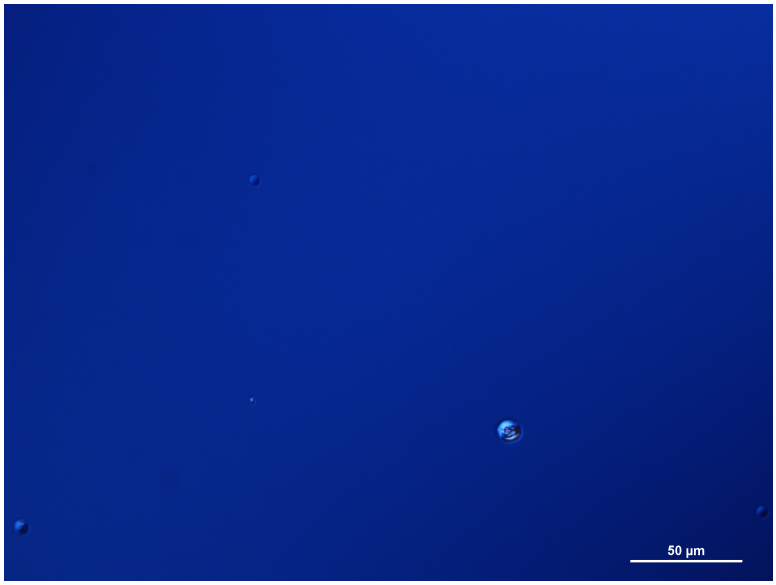

Figure 4.8: DIC surface image of M189 taken under 40X magnification, which exhibits few defects and a very smooth background.

as well as the InAs/AlSb SL test structure (M191). The results of which may be found in Fig. 4.13, which show the AFM imaging of a 5×5 μm square area of the surface of both wafers. Even though M191 has an overall thinner total epilayer thickness than that of M190, the RMS surface roughness was 5× larger. Considering that M191 was only 1/2 of the total thickness of the SL in the full ICL structure, this rough surface would only compound in the full ICL growth. This further supported the idea that the main material quality issue in Y039L came from the InAs/AlSb SL. Therefore, a new growth study would need to be completed, this time targeting the optimization of the InAs/AlSb SL.

4.2 Optimizing the InAs/AlSb SL

Initial work for an InAs/AlSb SL optimization study consisted of varying the As and Sb fluxes while keeping the T_{sub} fixed. However, DIC and XRD measurements confirmed that the flux variations led to inferior material quality, meaning that the fluxes that were already in use were closer to the ideal setting for this structure,

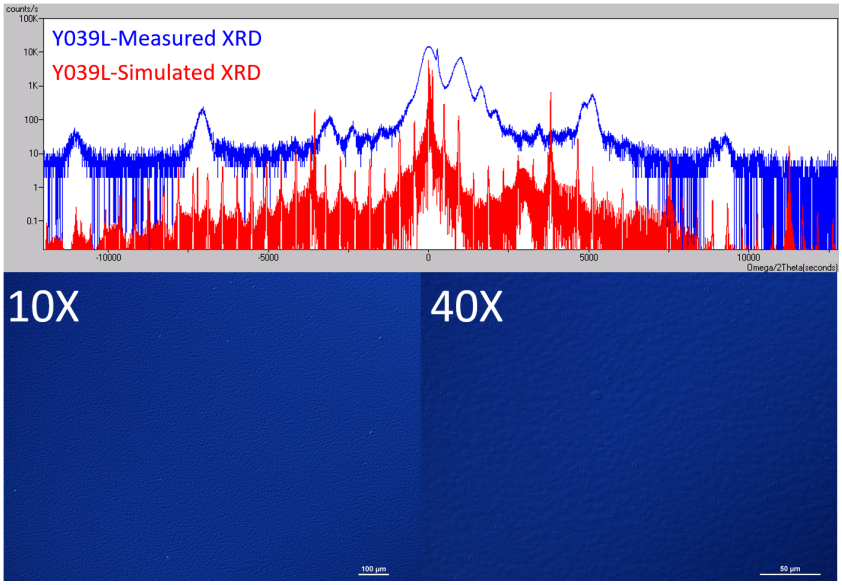

Figure 4.9: Measured (blue) and simulated (red) XRD patterns for Y039L, which shows significant deviations due to reduced crystalline quality. This is confirmed with DIC imaging, which shows a very rough and heavy defect surface.

given the other assortment of MBE parameters in use. Aside from group V flux variations, another consideration may be based on the ideal growth parameters for the individual binary materials and attempting to strike a balance between those for the InAs/AlSb SL, since the structure has a near equal distribution of the constituent binaries. For AlSb, it is known to show better surface morphology at elevated growth temperatures, approaching the limit of 560°C.[95] On the other hand, InAs growth was shown to be optimized at much lower temperatures, in the vicinity of 430-450°C.[96] It turns out, these two extremes can make it challenging to find a balance when growing the SL cladding. Previously, a substrate temperature of T_{sub} = 490°C was used to grow the SL cladding. A new growth study was conducted which tested several additional temperatures higher than those previously used. Included among these were T_{sub} = 520°C, 540°C, and 560°C.

Of these growths, the wafers grown at T_{sub} = 520°C (M221) and 540°C (M220)



Figure 4.10: DIC imaging under 40 × magnification for Y040LED (left) and Y041LED (right). Both structures have quite smooth surfaces, with few defects.

were the only ones with a reasonable FWHM. However, in both test structures, the XRD position of the 0th order SL peaks and the associated harmonics were all shifted to larger angular positions when compared with the simulated XRD pattern. This feature was more pronounced in the structure grown at 520°C. Fig. 4.14 shows the XRD pattern for M220, grown at T_{sub} = 540°C (blue) compared with a simulated XRD pattern of an ideal structure (red). This shifting of the SL peaks in the grown wafers indicates that there is a strain-balance issue, with the $a_{SL} < a_{sub}$ resulting in tensile biaxial strain (compressive out-of-plane strain). One explanation for this issue could be that the thickness of the deposited material is off (i.e., a GR calibration issue) and thus proper strain-balancing was not established. However, analysis of the ± 1 and ± 2 harmonic SL peaks finds that the average period thickness of the SL was 51.2 Å, deviating by only +2.43% larger than the intended design value of 50 Å.

Another explanation is that the interface between InAs and AlSb is not atomically smooth, but instead composed of one or more layers of an intermixing of the group III and/or V materials in such a way as to be thick enough to affect the overall strain-balancing in the system, as expressed in the XRD scans. This effect has been explored extensively in the literature for the InAs/GaSb SL[97–104],

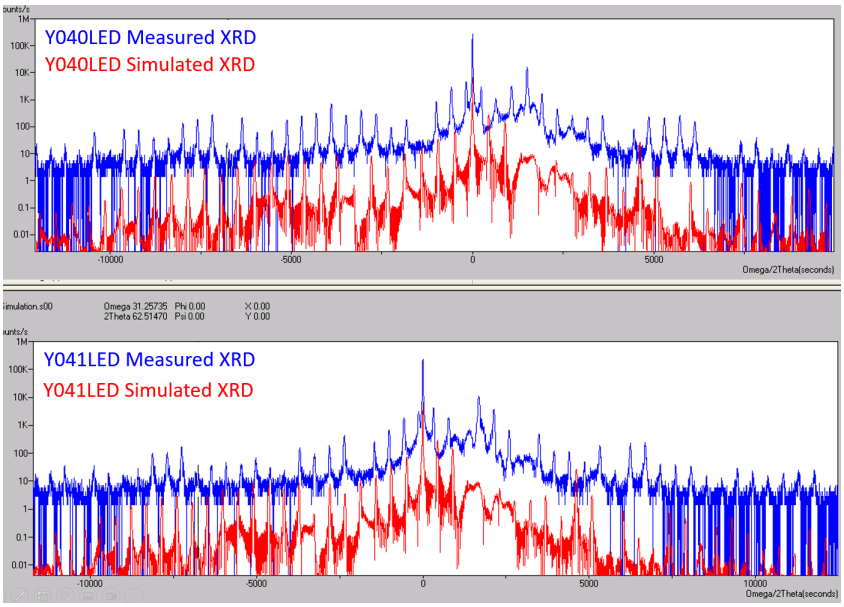

Figure 4.11: Measured (blue) and simulated (red) XRD patterns for both Y040/41LED. It may be observed that the FWHM of the SL peaks arising from the cascade region of the LED are very narrow, indicating good material quality. Furthermore, most of the SL peaks also align with the intended design, indicating good strain-balancing.

and less so for the InAs/AlSb SL.[105–107] Some of the major findings of these studies suggest that the interfaces are generally spread over a few MLs, often with graded compositions due to the interface intermixing. The interface bond type has little impact on the relative intensity of the SL peaks in the XRD measurement. The growth order of the SL materials can play a role in the carrier dynamics of the overall SL structure, due to potential electron and hole confinement. In the case of InAs on GaSb, the interface tends to be rougher than for GaSb on InAs, with an overall thicker interface in the latter. In the InAs/GaSb SL, most of the intermixing occurs prior to the growth of the GaSb layer due to the lower vaporization enthalpies of In and As (227 kJ/mole and 32 kJ/mole, respectively) compared with Ga and Sb (255 kJ/mole and 68 kJ/mole, respectively). This makes it easier for an As anion to become displaced from the lattice compared with Sb, and In compared with Ga, with the more favorable displacement typically

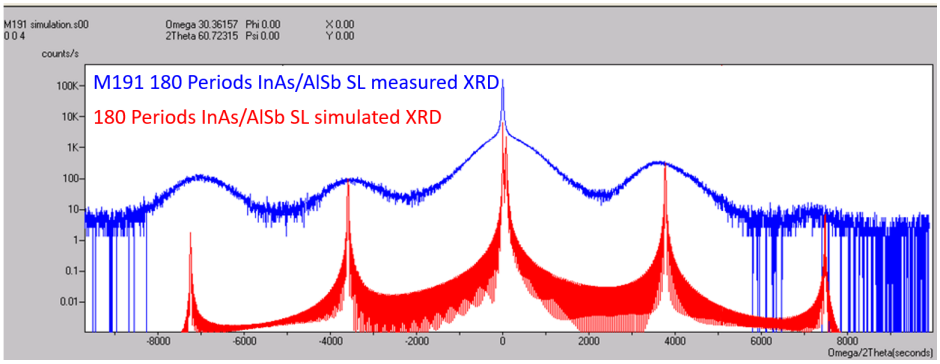

Figure 4.12: Measured (blue) and simulated (red) XRD patterns for a 180 period InAs/AlSb SL test structure (M191). The SL peak FWHM is very broad, indicating poor material quality which likely stems from non-ideal MBE growth conditions.

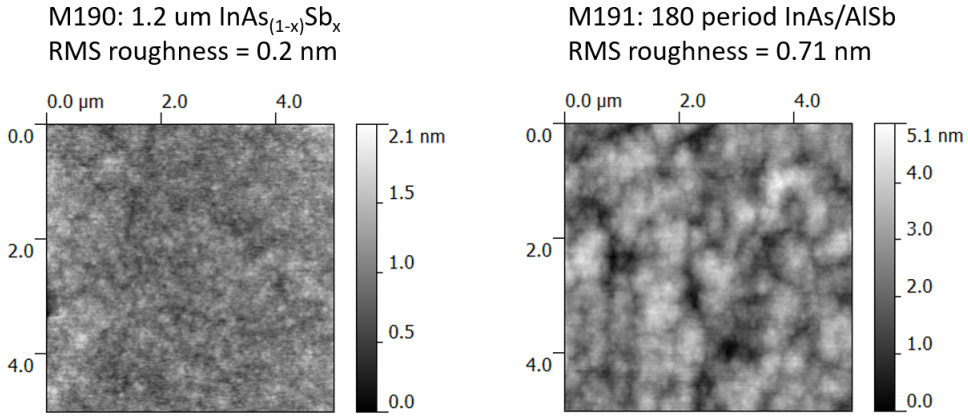

Figure 4.13: The measured AFM imaging of a 5×5 μm square of the surface of M190 and M191. This measurement shows that the RMS surface roughness of the InAs/AlSb structure is nearly 5× larger than for the thicker InAsSb layer.

occurring among the group V anions. This same principle should apply in the InAs/AlSb SL explored here.

To probe this topic, a simulation of an ideal InAs/AlSb SL with thicknesses of 26.5 Å and 23.5 Å, respectively, was generated. Several additional simulations of various SL combinations with slightly different forced interfaces were also generated, some of which are shown in Fig. 4.15. First, a 2 Å AlAs interface was inserted at the start of the AlSb layer growth shown in black. This represents the largest degree of forced biaxial tensile strain, providing an upper bound for interfacial alloy considerations (i.e., As = 100% and Sb = 0%). Two other simulations are also

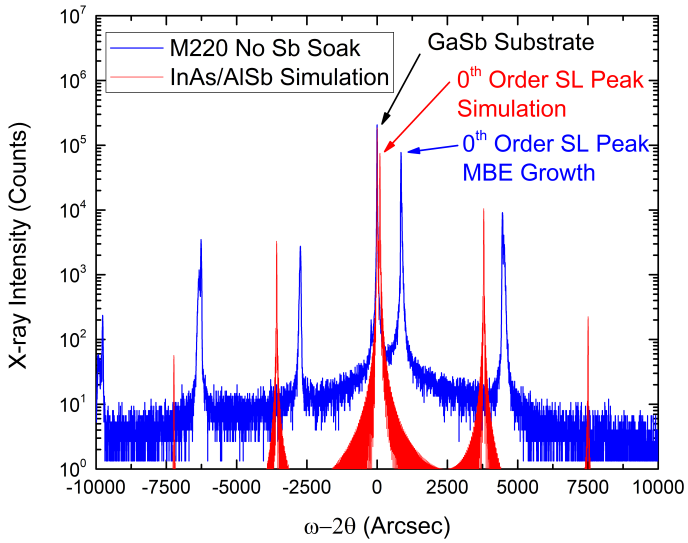

Figure 4.14: Measured XRD pattern (blue) for M220, a 180 period InAs/AlSb (26.5/23.5 Å) SL compared to the simulated XRD pattern (red). The FWHM of the various XRD peaks for M220 are quite narrow, indicating good material quality, however all peaks are shifted to higher angular position with respect to that observed in the simulation.

shown in the figure, which include interfacial alloy compositions of $AlAs_{0.9}Sb_{0.1}$ and $AlAs_{0.95}Sb_{0.05}$, in which the 0th order peak from M220 falls. Therefore, it is reasonable to assume that there exists some average graded interfacial composition that varies between these values.

Controlling the nature of interfaces in SL structures has been a topic of interest in the growth community, with migration enhanced epitaxy (MEE) considered to be the best way to control the abruptness of an interface. This technique involves forcing an interface based on the shutter sequencing used during the growth. For example, in an InAs/GaSb SL an InSb-like interface may be formed after the GaSb layer is grown by closing the Ga shutter and flooding the growth chamber with Sb for several seconds. This creates an Sb-rich condition in the growth chamber where one may open the In shutter for 1-2 seconds to grow a very thin layer of InSb, before proceeding to close the Sb shutter and open the As shutter for InAs growth. In this way, the type of interface may be selected to arrive at a better

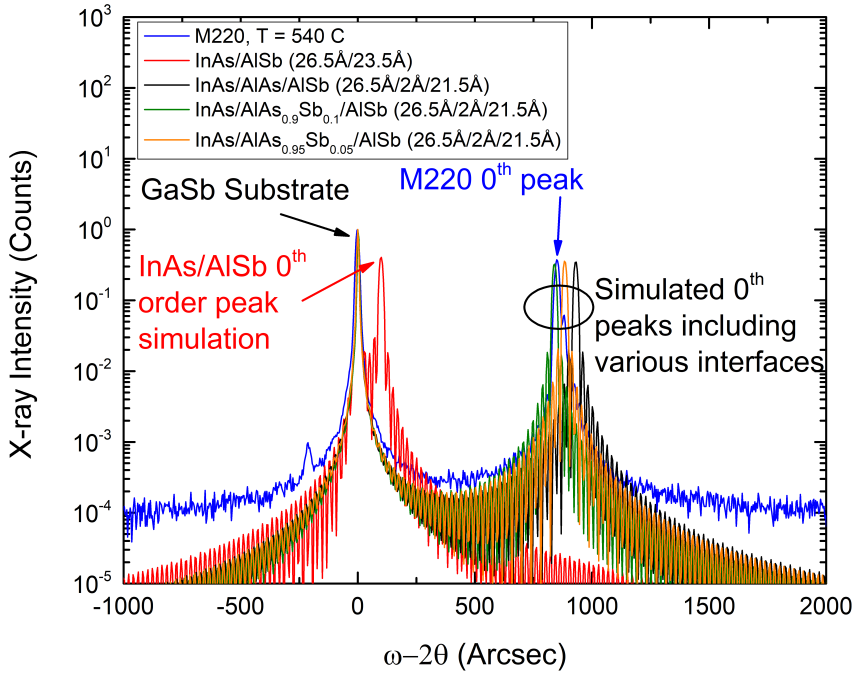

Figure 4.15: Measured XRD pattern (blue) for M220, a 180 period InAs/AlSb (26.5/23.5 Å) SL compared to a plot of the simulated XRD pattern (red) as well as several other simulations using a variety of different interface combinations.

overall strain-balanced SL system with higher crystal quality.

To study this in the GENxplor, a series of MBE growths were developed for the InAs/AlSb SL which intentionally forced AlSb-like interfaces between the InAs and AlSb layers by reducing the possibility for AlAs/AlAsSb-like interface formation. The shutter sequence is as follows: after InAs growth, the In and As shutters are closed. Next the Sb shutter is opened for a variable amount of time, which is called the Sb soak. This allows several seconds to pump out residual As from the growth chamber while simultaneously flooding the chamber with Sb. Afterwards, the Al shutter is open and the AlSb layer is grown. Lastly, both the Al and the Sb shutters are closed and the In and As shutters are opened for the next InAs layer growth. In this way, there is very little As available to form AlAs/AlAsSb interfaces when the AlSb layer is grown, thus minimizing the average thickness of the interfacial layer. In this growth study, three additional SL structures were

grown, with the already grown M220 acting as a control (with an Sb soak time of 0 seconds). The grown structures were M227, M233, and M234 with Sb soak times of 2, 4, and 8 seconds, respectively. The results of this study are shown in Fig. 4.16 and indicate that the degree of biaxial tensile strain becomes significantly reduced with an increasing Sb soak time, almost identically matching the 0th order peak position between experiment and simulation upon reaching a soak time of 8 seconds. DIC also confirms that there is little impact to the surface quality when utilizing these long Sb soaks. This does add a non-negligible increased amount of time to the overall ICL growth, however, and carries with it the possibility of issues of increased impact due to flux instability over a long growth time. For example, just implementing an Sb soak of 8 seconds after each InAs layer in the SL cladding, across all 360 periods, would amount to an additional 48 minutes of growth time added. In fact, these Sb soaks were found to be so critical for high quality GaSb-based ICL growth, that they were added to virtually every possible layer where there exists an As to Sb transition, and thus potential for interfacial intermixing, in the full ICL structure growth. The importance of this result cannot be overstated. This Sb soak technique has allowed for the first successful growth of full GaSb-based ICL structures on the GENxplor. The material characterization and device performance of those ICLs are the topic of Chapter 7.

4.3 Optimizing the GaSb Buffer Layer

As briefly discussed in Section 3.2, the typical defect observed in III-V ICL or ICTPV growth is the oval hillock, which tends to originate from the substrate surface. Such defects can potentially propagate through the device active region and act as recombination centers for the carriers.[108] On the other hand, if such defects form closer to the surface (i.e., shallow defects) they tend not to have

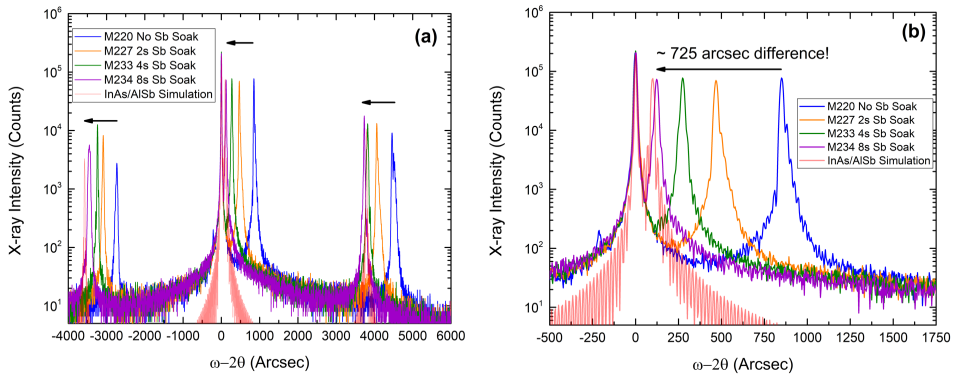

Figure 4.16: Measured XRD patterns (blue, orange, green, purple) for several InAs/AlSb SL structures with variable Sb soak times in order to reduce the strain-balance issues associated with a rough interface. These are compared with a simulation (red) which has an atomically abrupt interface.

any influence on the electrical properties of the device. One study on quantum cascade structures showed that surface defect densities in the range of $10^2 - 10^5$ cm^{-2} tended to have a low impact on the overall device performance, because the defects occupy only a small fraction of the overall volume of the device (i.e., $<$ 5%).[109] Oval defects may also form from droplet spitting, which may occur, for example in the Ga source cell, leading to small deposited droplets of Ga or GaO_2 on the surface of the wafer. This effect, though minimized in modern MBE growth by using differentially heated cells with a high tip temperature[110, 111], is still an ever present source of potential defect formation. Nonetheless, quality growth of IC related structures should endeavor to minimize the quantity of defects with careful consideration of MBE growth parameters. Since oval hillock defects tend to originate from the substrate surface, a careful optimization of the GaSb buffer layer can help to stymie their propagation through the epilayers.

4.3.1 Experimental Setup and Substrate Preparation

The first consideration is the quality of the GaSb substrate surface, prior to GaSb buffer layer growth. Typically, GaSb wafers are purchased as epi-ready,

meaning that the passive surface oxide layer is relatively thin. This in turn makes it easier for the OD process to remove the oxide layer, prior to growth. However, it is possible that the oxide layer becomes thicker over time, after being shipped from the manufacturer. This may especially be the case once the wafer is exposed to atmosphere after a piece of the overall wafer is cleaved off for growth. The remaining wafer that is put into storage may sit for several days or weeks before seeing use. In that way, the oxide layer may become thicker over time and thus harder to remove during OD. One test in this GaSb buffer layer studied followed the method described by Refs [112, 113], in which chemical treatment of the substrate prior to loading it into the MBE system is used. This treatment involves degreasing the wafer with a standard alcohol rinse beginning with Acetone, followed by Methanol, and finally Isopropyl (IPA) alcohols. Next the wafer is etched for 5 minutes in undiluted (approximately 36.5-38%) HCl to chemically thin the oxide layer. Lastly the wafer (M372) is then rinsed in (IPA) and left in the alcohol until it is ready to be installed on the substrate holder and loaded into the MBE chamber, in order to protect the newly etched surface from additional atmospheric contamination.

In addition to this, two other techniques were also explored. It has been shown that the temperature of the buffer layer growth can dramatically impact the propagation of defects from the substrate into an InAs/GaSb SL grown after the buffer layer.[104] Therefore, part of this study investigates the quality of GaSb buffer layers grown at various substrate temperatures. Also, Sb stabilization fluxes during heat up and cool down periods of the substrate were investigated.[112] The idea of group V stabilization fluxes is that group V material at a certain flux level may condense on the wafer surface at sufficiently low temperatures, causing the formation of defects. This may be a concern when using a large group V flux during a high temperature oxide desorption (OD) process and then subsequently

Table 4.3: MBE Growth Parameters for the GaSb buffer layer growth study. All structures were grown with a V_{Sb}/III_{Ga} of about 2.5. All flux values reported have the unit of Torr. The Sb flux during heating/cooling (h/c) times varied by about 50% overall.

MBE Growth Parameters for the GaSb buffer layer growth study					
Wafer	HCl Etch	OD T (°C)	Grow T (°C)	Sb h/c	Sb Growth
M371	no	515	424	1.1×10^{-6}	1.1×10^{-6}
M372	yes	505	452	1.1×10^{-6}	1.1×10^{-6}
M373	no	525	498	7.4×10^{-7}	1.06×10^{-6}
M374	no	525	480	9.4×10^{-7}	1.06×10^{-6}

decreasing the substrate temperature for epilayer growth. A large enough Sb flux is needed during the GaSb OD process to prevent Sb desorption from the surface, but afterwards during substrate cooling to the growth temperature for GaSb (and similarly after GaSb growth), a reduced Sb flux level should be used to prevent any condensation. Therefore, three additional wafers were grown to test these features (M371, M373, and M374). Table 4.3 lists the various MBE growth parameters for the four GaSb buffer layers in this growth study.

All four structures were grown on 1 cm × 1 cm GaSb wafer pieces and underwent a 10 min OD process, followed by subsequent cooling to the necessary growth temperature. A 1 μm thick layer of GaSb was grown with a Ga GR = 0.52 ML/s and a V_{Sb}/III_{Ga} of about 2.5. All temperatures reported in Table 4.3 are pyrometer readings. M371 had the lowest T_{sub} while M373 had the highest. The OD temperature of M371 was 10°C higher than M372 and equally lower compared with M373 and M374. M372 underwent a 3 minute degrease in each of the alcohols mentioned above, a 5 min HCl etch, and then a 5 min IPA rinse. As shown in Table 4.3, the required OD temperature for the HCl etched wafer was slightly lower than for the non-etched wafers, indicating a thinner oxide layer. M373 and M374 had reduced Sb flux levels during periods of substrate temperature change. The Sb flux level was reduced by about 50% for M373 during these periods, while

the Sb flux level in M374 was reduced by about 20%.

4.3.2 Material Characterization of GaSb Buffer Layers

The material quality of the GaSb buffer layers was investigated with DIC, SEM, and AFM. Overall, it was found that M373 had the best crystal quality with an average surface defect density of 2.58×10^4 cm^{-2} and an RMS surface roughness of only 2.4 nm. M374 was quite similar to M373, with an average surface defect density of 2.82×10^4 cm^{-2} and an RMS surface roughness of only 1.5 nm. M371 had nearly 2× more surface defects and a 7× rougher surface. The typical height of a defect on M373 and M374 ranged from 7 to 17.5 nm, while those on M371 were observed to be as large as 116 nm. M372 was by far the worst quality wafer. Though it had an average surface defect density similar to that of M371, and an average defect height of only 26.8 nm, the background surface was considerably inferior as shown in DIC imaging in Fig. 4.17. Therefore, growths beginning after this study (starting from Y068V and onward) adopted the MBE growth parameters of M373/374 for growing GaSb buffer layers.

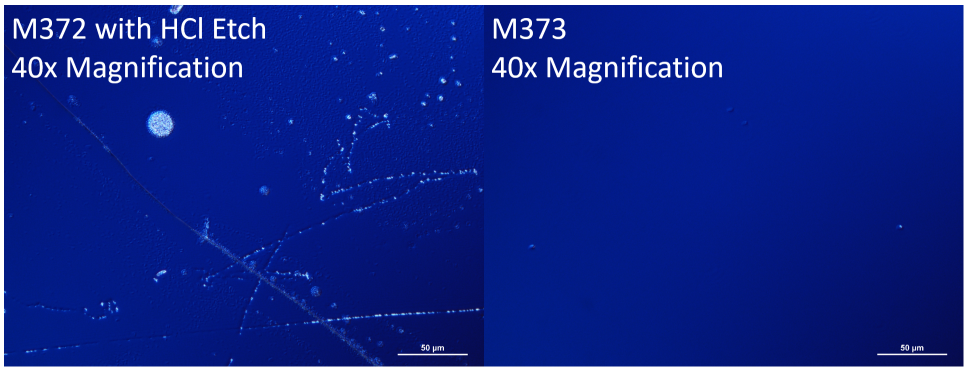

Figure 4.17: DIC imaging of the worst (M372, left) and best (M373, right) wafers from the GaSb buffer layer growth study under 40× magnification.

4.4 Growth Studies for ICTPVs

Reported in this dissertation are three growth studies related to proposed structural enhancements for ICTPV devices. First, Section 4.4.1 presents some basic details for the ICTPV device operation. Next, Section 4.4.2 will present the results of implementing the Sb soak technique for ICTPV devices. Section 4.4.3 will describe how to accomplish growing graded doping profiles within the absorber region of ICTPV devices. Lastly, Section 4.5 will present some details of the resonant cavity enhanced (RCE) ICTPV device and the necessary growth studies needed to accurately grow those required structures.

4.4.1 A Brief Review of ICTPV Operating Principles

Interband cascade thermophotovoltaics (ICTPVs) are a class of photovoltaic structure which absorbs infrared radiation from a blackbody (1000-2000 K) using an absorber material with an optimum bandgap range of 0.2-0.4 eV.[83, 114] Using a thick InAs/GaSb type-II SL as the absorber can satisfy this energy range, where the absorbers are sandwiched in between unipolar barriers to form tandem cells that are connected in series as shown in Fig 4.18. Actually, the first photovoltaic operation of an IC structure was demonstrated from devices that were fabricated from ICL wafers.[115] Clearly there are similarities between these two types of devices, where instead of hole and electron injectors used to quickly extract carriers from one cascade stage to the next, electron and hole barriers are used to provide an ideal transport pathway for these carriers, resulting in smooth carrier transport. In the ICTPV the individual absorber thickness in a single cascade stage is typically designed to be thinner than the diffusion length in order to ensure efficient collection of the photo-generated carriers. However, the total absorber thickness is designed to be longer than the overall diffusion length in order to maximize the utilization

of incident photons. In the case of an ICL, each injected electron can generate a new photon with each cascade stage it passes through. Reversing this design for the ICTPV results in needing multiple photons to generate a single electron, and consequently the maximum attainable quantum efficiency for ICTPV devices is reduced by $1/N_c$, where N_c is the number of cascade stages. This would seem to indicate that a single stage ICTPV would be the preferred design, however, this topic is not so simple and is extensively explored in Refs [116–121]. Overall, it was shown that the device performance of a single-stage ICTPV is limited by a small collection efficiency that is associated with the relatively short diffusion length. Meanwhile, multi-stage ICTPVs with thin individual absorbers can circumvent this issue, resulting in an enhanced collection efficiency.

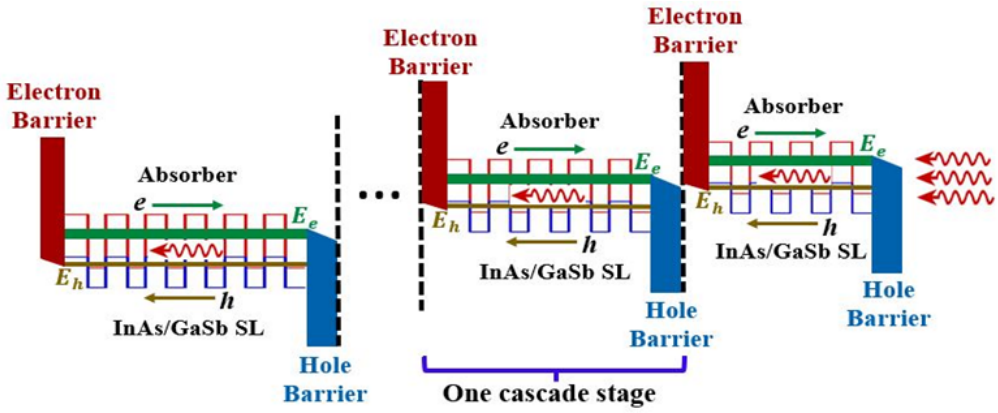

Figure 4.18: Schematic illustration of a multistage ICTPV cell under forward bias. The green arrows indicate the ideal transport path for electrons, while the gold arrows indicate the ideal transport path for holes.

4.4.2 Interface control via Sb-soaking in ICTPVs

Early work on ICTPVs by our group culminated in the first successful growth demonstration of GaSb-based ICTPV devices with 1, 3, and 5 cascade stages (Y033V, Y034V, and Y035V, respectively). The cascade structure consisted of an InAs/GaSb SL p-doped (Be) absorber repeated a variable number of times,

Table 4.4: Extracted material characterization details from XRD measurements of some of the early ICTPV devices. The DA 0th order peak to substrate spacing is presented in units of arcseconds. Also shown is the perpendicular mismatch and the out-of-plane strain type.

Material Characterization Details from XRD of early ICTPVs				
Wafer	Period Error	DA/sub spacing	mismatch	strain type
Y054V3	+1.45%	281.1	-0.23%	compressive
Y055V	- 1.61%	281.2	-0.23%	compressive
Y056V	+1.32%	491.9	-0.41%	compressive
Y057V	- 0.84%	500.7	-0.41%	compressive
Y058V	- 3.18%	393.6	-0.32%	compressive
Y059V	- 1.96%	310.2	-0.26%	compressive

sandwiched between an AlSb/GaSb electron barrier and an InAs/AlSb hole barrier. Thin layers of InSb were added into many parts of all three SL structures for strain balancing/interface purposes. For Y033V, the doped absorber (DA) was repeated 481 times. In Y034V, the DA was repeated 195× in the first stage, 156× in the second stage, and 130× in the third stage, for a total period of also 481. In Y035V, the total DA period was increased to 525, broken down as: 145/120/100/85/75 among the five stages. Later, ICTPV structures with additional stages and DA periods were grown, including Y054V (6-stage), Y055V (7-stage), Y056/57V (8-stage), Y058V (6-stage), and Y059V (8-stage). Y054V and Y055V both had the typical 4-layer DA consisting of GaSb/InSb/InAs/InSb with thicknesses of 25.1/1.2/20.5/1.2 Å in the growth direction, for an overall period thickness of 48 Å. ICTPVs afterward had modified DA structures consisting of GaSb/AlSb/$Al_{0.7}In_{0.3}Sb$/AlSb/GaSb/InAs with layer thicknesses of 15/0.5/7/0.5/15/27 Å in the growth direction, for an overall period thickness of 65 Å. Table 4.4 presents the material characterization details for these ICTPV devices. Of importance to note are the rather large lattice mismatches measured for the 0th order peak for the DA. Here we can see that all of the structures had a rather large degree of tensile biaxial strain (compressing out-of-plane strain).

The structures toward the end of the list in Table 4.4 were grown not long after the InAs/AlSb SL cladding growth study had been completed, where the Sb-soaking technique was developed to enhance the overall quality of the SL. There was a thought that this technique may also result in higher quality DAs in the ICTPV structures, considering the SL structures are somewhat similar between the ICTPV and the ICL SL cladding. Furthermore, because the DA is much thicker (overall) than the SL cladding, having in many cases 500+ periods compared to the roughly 300-360 periods for the InAs/AlSb SL, the effect of incorporating the Sb-soaking could be dramatic. On the other hand, the InAs/AlSb SL is somewhat different from the DA for the ICTPV in that the former truly alternates strain with each layer grown (i.e., $a_{InAs} < a_{GaSb} < a_{AlSb}$), whereas the basic InAs/GaSb DA requires thin layers of InSb to be incorporated in order to achieve strain balance to the GaSb substrate.

To explore this possibility, during a later growth campaign a repeat growth of Y059V was conducted (Y064V) in order to verify that the optimal MBE growth parameters had not deviated too much over time. Then a second ICTPV was grown (Y067V), which was identical to Y064V with the exception that Sb-soaks similar to those discussed previously were inserted after every InAs layer growth in the DA. The surface quality as assessed with DIC showed that both Y064V and Y067V were of similar quality, with an average surface defect density ranging in the high 10^3 cm^{-2} to low 10^4 cm^{-2} range. However, some areas of the surface of Y064V showed drastic increases in the defect density, peaking at 1.2×10^6 cm^{-2}. This effect was not observed for Y067V. The XRD patterns for both wafers were measured, which are shown in Fig. 4.19 (blue and green) along with the simulated XRD pattern of the intended device structure (red). The effect of the Sb-soak is clear, resulting in a significant reduction in the lattice mismatch, bringing the 0th order DA peak in line with the predicted position in the simulation. The lattice

mismatch for Y064V, extracted from the XRD data, was 0.29% with a separation from the substrate peak of 356.5 arcsec, corresponding to tensile biaxial strain (compressive out-of-plane strain). For Y067V, the position of the 0th order DA peak was shifted approximately 396 arcsec to the left, with a peak/substrate separation of only 41 arcsec, resulting in a significant reduction in the lattice mismatch (by nearly an order of magnitude) to only 0.034% as well as a flip in the type of strain, now showing a slight degree of compressive biaxial strain (tensile out-of-plane strain). Furthermore, the RMS surface roughness measured with AFM was found to be 18 nm in Y064V and was reduced by a factor of about 3, to 5.8 nm in Y067V.

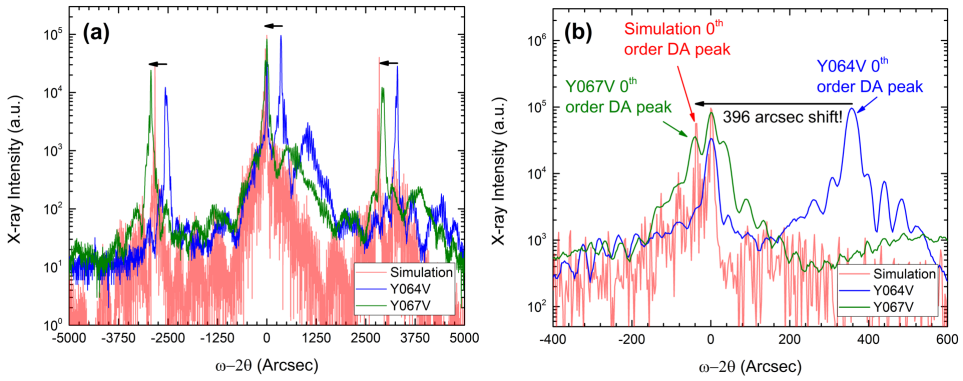

Figure 4.19: Measured XRD patterns (blue, orange, green, purple) for several InAs/AlSb SL structures with variable Sb soak times in order to reduce the strain-balance issues associated with a rough interface. These are compared with a simulation (red) which has an atomically abrupt interface.

Because of these improvements in the material quality, all other ICTPV structures grown by our group after this point continued to utilize Sb-soaks in the DA region. It is unclear, however, if this change has had any practical effect on the device's performance. Optical characterization of these two devices showed that the latter device had a higher/more uniform activation energy, indicating superior material quality, corroborating what was observed with XRD, DIC, and AFM measurement. Y067V also had larger wavelength, temperature, and bias dependent quantum efficiency compared with Y064V. Furthermore, the conversion efficiency

in Y067V was 6.8%, compared to 5.9% for Y064V. However, some of these small improvements in performance could potentially be due to non-uniformities across the wafer during MBE growth or small variations during device processing. Additional, systematic studies should be performed to further investigate the effect of Sb-soaks during DA growth for ICTPV performance. Nonetheless, this technique does dramatically improve the crystalline quality of the wafer, opening up the possibility for thicker or more complex growth structures in the future.

4.4.3 Graded Doping Profiles in the Absorber of an ICTPV

One thought for improving the performance of ICTPV devices is to try to enhance the extraction and collection of photo-generated carriers from the DA in multistage ICTPV structures. This could potentially be accomplished by introducing a gradient to the doping profile in the DA of each cascade stage in such a way as to generate a built in electric field originating at the hole barrier and pointing in a direction toward the electron barrier, which would act to enhance the extraction of the photo-generated carriers. Initially, this was first attempted in Y065V and Y066V by adjusting the Be doping from a fixed starting value to a fixed final value in each DA for every cascade stage (in this case both devices had 8 stages). Practically for the MBE growth, this amounts to choosing the Be cell temperatures (T_{start} and T_{end}) such that the doping levels at the start and end of a given DA match the necessary doping values for the intended design. For Y065V, the doping level started at p = 6×10^{16} cm^{-3} and was to be uniformly reduced to 1×10^{16} cm^{-3} across the DA in each stage. These corresponded to Be cell temperatures of 702°C and 629 °C, respectively. Similarly, for Y066V the starting value was p = 3.2×10^{16} cm^{-3} and was reduced to the same final value, where the starting Be cell temperature was 675 °C. Therefore, in the sequence of

growth steps, after completion of the electron barrier, a step was added to the growth program to change the Be cell temperature to its lower temperature value, and after completion of the DA growth in any given cascade stage, another step was added to increase the Be cell temperature back to its starting value. This was possible because there was Be doping in the electron barrier, but not the hole barrier. Therefore, during growth of the hole barrier in each cascade stage, there was time to reset the Be cell temperature. The final piece of the puzzle is to tell the dopant cell how to change the cell temperature, i.e., the ramping rate (in units of °C/min). To determine this, consider Fig. 4.20 which depicts a single cascade stage with N layers of Be-doped absorber layers. The overall DA sequence begins with a known starting p-doping level, corresponding to a known starting Be cell temperature. At the completion of the Nth layer, a known ending p-doping level should be achieved, corresponding to a known Be cell temperature. This will occur over a time interval Δt that is known based on the GR of the materials. Also, Sb-soaks that are used must also be taken into account for the overall ramp rate. Therefore, the rate (in °C/min) that the Be cell needs to be ramped will correspond to $r = (T_{start}\text{-}T_{end})/\Delta t$.

The details of the Be cell ramp rates needed are shown in Fig. 4.21, which lists the various growth times for each DA period in the various cascade stages, the ΔT of the Be cell needed in each DA period, and the associated Be cell ramp rate to achieve the graded doping profile. This ended up not being the correct method to achieve a smooth doping profile across the entirety of the cascade stages. The reason is because each DA has a different number of total periods, and thus by choosing a starting and ending doping level in each DA period, the overall ramp rate of the Be cell is different in each cascade stage by a fairly large margin. This then means that the doping gradient in each stage is different, with a decreasing slope as the stage number progresses from 8 to 1 (i.e., in the growth direction),

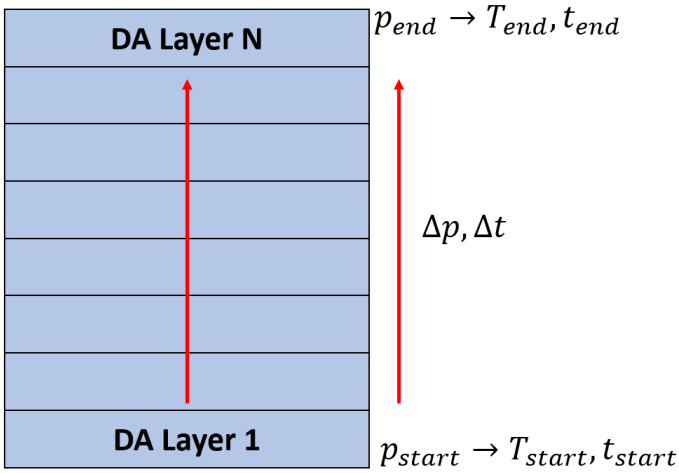

Figure 4.20: Depiction of a single cascade stage with N layers of doped absorbers (DAs). The overall DA sequence begins with a known starting p-doping level, corresponding to a known starting Be cell temperature. At the completion of the Nth layer, a known ending p-doping level should be achieved, corresponding to a known Be cell temperature. This will occur over a timer interval Δt that is known based on the GR of the materials.

creating a sort of disjointed doping profile between the cascade stages, as shown in Fig. 4.21.

A better method is to choose the starting doping level and the necessary gradient. In this way, one may ensure a smooth doping profile across any number of cascade stages. For MBE growth, this means then that the ending dopant level in any given DA, and the corresponding Be cell temperature, are the unknowns. Fortunately, the logic developed when discussing Fig. 4.20 is still relevant, where the needed cell temperature may be determined as $T_{end} = T_{start}$-rΔt. This new approach was applied to several additional ICTPV structures. First a 16-stage device (Y073V) was grown with p = 4.2×10^{16} cm^{-3} linearly reduced to 4.2×10^{16} cm^{-3} in the final cascade stage with a doping profile of dp/dx = 7.17×10^{20} cm^{-4}. Two additional devices were grown, Y074V and Y075V, both starting with p = 3.8×10^{16} cm^{-3}, linearly reduced to 2.0×10^{16} cm^{-3} and 1.2×10^{16} cm^{-3}, respectively, with rates of dp/dx = 7.2×10^{20} cm^{-4} and 7.14×10^{20} cm^{-4}, respectively. The MBE

Stage	DA Period	Total Growth Time (s)	Total Growth Time (min)	deltaT End DA to EB	ramp rate (deg C/min) across DA	ramp rate (deg C/min) across HB
1	97	6136.585	102.276	73	0.71375	7.67117
2	84	5314.156	88.569	73	0.82421	7.67117
3	75	4744.782	79.080	73	0.92312	7.67117
4	67	4238.672	70.645	73	1.03334	7.67117
5	61	3859.089	64.318	73	1.13498	7.67117
6	56	3542.770	59.046	73	1.23632	7.67117
7	52	3289.715	54.829	73	1.33142	7.67117
8	48	3036.660	50.611	73	1.44237	7.67117

Stage	DA Period	Total Growth Time (s)	Total Growth Time (min)	deltaT End DA to EB	ramp rate (deg C/min) across DA	ramp rate (deg C/min) across HB
1	97	6136.585	102.276	46	0.44976	4.83389
2	84	5314.156	88.569	46	0.51937	4.83389
3	75	4744.782	79.080	46	0.58169	4.83389
4	67	4238.672	70.645	46	0.65115	4.83389
5	61	3859.089	64.318	46	0.71519	4.83389
6	56	3542.770	59.046	46	0.77905	4.83389
7	52	3289.715	54.829	46	0.83898	4.83389
8	48	3036.660	50.611	46	0.90889	4.83389

Figure 4.21: MBE growth parameters for Y065V (top) and Y066V (bottom) including the total growth time for the DA in each cascade stage, the ΔT of the Be cell needed in each DA period, and the associated Be cell ramp rate to achieve the graded doping profile.

parameters for Y074V are shown as an example of this new approach in Fig. 4.22. Of note is the quite consistent Be temperature ramp rate in each cascade stage, which ensures a more linear doping profile.

p2 end Calculated (cm^-3)	Single Stage Time (s)	Total Stage Time (s)	T1 (deg C)	T2 (deg C)	Cell Ramp rate (deg C/min)	Stage
2.00E+16	67.492	2632.1951	686.264	661.473	0.5651	15
2.09E+16		2497.2107	686.264	663.137	0.5557	14
2.18E+16		2362.2263	686.264	664.871	0.5434	13
2.28E+16		2227.2420	686.264	666.547	0.5312	12
2.37E+16		2092.2576	686.264	667.809	0.5292	11
2.42E+16		2024.7654	686.264	668.651	0.5219	10
2.51E+16		1889.7811	686.264	669.918	0.5190	9
2.55E+16		1822.2889	686.264	670.765	0.5103	8
2.60E+16		1754.7967	686.264	671.612	0.5010	7
2.65E+16		1687.3045	686.264	672.037	0.5059	6
2.69E+16		1619.8123	686.264	672.462	0.5112	5
2.74E+16		1552.3202	686.264	673.313	0.5006	4
2.78E+16		1484.8280	686.264	673.74	0.5061	3
2.83E+16		1417.3358	686.264	674.592	0.4941	2
2.88E+16		1349.8436	686.264	675.447	0.4808	1

Figure 4.22: MBE growth parameters for Y074V, as an example, which includes the total growth time for the DA in each cascade stage, the ΔT of the Be cell needed in each DA period, and the associated Be cell ramp rate to achieve the graded doping profile.

Unfortunately, this exercise in attempting to improve the collection of photo-generated carriers by introducing a doping profile to generate an internal electric field did not result in the performance improvement that was desired. Part of the issue could be due to the Be doping calibration being conducted by growing Be-doped GaSb. However, the DA also includes other materials like InAs, for

which the dopant incorporation rate can be considerably different. GaSb is grown at approximately 2× the GR of InAs or InSb, and therefore the doping levels in the InAs and InSb layers are proportionately increased by this same factor compared with GaSb, as their slower GR yields a larger overall dopant incorporation. Thus, the actual doping profile, even in the later grown ICTPV structures, will exhibit a saw-tooth like shape through every period of the DA. Nevertheless, the MBE techniques developed here will be applicable to future growth campaigns. Though these were some of the final ICTPV structures grown by our group, future efforts in this work could consider reducing the GaSb GR to be equal to that of the InAs/InSb GR in the DA regions. In this way, a more linear doping profile may be established, however this does come at the cost of more MBE complexity and an increased overall growth time, which will demand increased stability of the various material cells used for this growth.

4.5 The Resonant Cavity Enhanced ICTPV

As previously mentioned, multi-stage ICTPVs circumvent some of the issues seen in single-absorber devices related to the short diffusion length and small absorption coefficient. However, multi-stage ICTPVs still suffer from effects related to a large dark saturation current density[122], associated with the narrow bandgap of the DA, and a short carrier lifetime.[123] A promising way to mitigate these issues is to substantially increase the photocurrent by placing the active structure inside a resonant microcavity. The enhanced optical field inside the cavity permits the recycling of unabsorbed photons, thus allowing the quantum efficiency (QE) to be appreciably improved at the resonant wavelength. Also, the wavelength selectivity provided by the cavity is consistent with the spectral control in a TPV system. The following sections present recent investigations and progress

in realizing resonant cavity enhanced (RCE) ICTPV devices. This includes the study and growth of the distributed Bragg reflector (DBR) and the corresponding ICTPV devices.

4.5.1 Details of the Distributed Bragg Reflector

To form an optical cavity on a semiconductor substrate, a bottom DBR mirror with a high reflectance (R > 90%) is typically required. The quarter-wavelength stack DBR operates on the principle that an incident light beam on a multilayer-stack of alternating high and low index materials will experience partial reflection at every interface of the stack, thus the intensity of the incident beam diminishes as it travels through the stack, while the intensity of the reflected beam increases. The thickness of the two materials used in the stack follows

$$t_{high/low} = \frac{\lambda}{4n_{high/low}} \tag{4.5}$$

where $t_{high/low}$ is the thickness of a single layer of the high and low index materials forming the stack, λ is the target wavelength for peak reflectance, and $n_{high/low}$ are the indices of refraction of the two materials in the stack. As the RCE ICTPV device is intended to be grown on a GaSb substrate, the bottom DBR mirror is composed of an m-period GaSb/AlAsSb quarter-wavelength stack that is lattice-matched to GaSb. The refractive index at the target wavelength of the ICTPV operation (4 μm) for GaSb and AlAsSb is close to 3.78 and 3.18, respectively. Based on Eq. 4.5, the individual layer thicknesses of GaSb and AlAsSb necessary for the design are 264.6 nm and 314.2 nm, respectively. To determine the number of periods (m) that are required to achieve the desired reflectance, in this case > 90%, consider that the reflectance for a quarterwave-stack may be determined from

$$R = \left(\frac{\left(\frac{n_{low}}{n_{high}}\right)^m - \frac{n_{sub}}{n_o}\left(\frac{n_{high}}{n_{low}}\right)^m}{\left(\frac{n_{low}}{n_{high}}\right)^m + \frac{n_{sub}}{n_o}\left(\frac{n_{high}}{n_{low}}\right)^m} \right)^2 \tag{4.6}$$

where n_o is the index of refraction of the material that the incident light travels through just as it enters the DBR. While a thin film may be used to enhance the reflection of the optical cavity formed with the DBR, for the purposes of this initial investigation the semiconductor/air interface (R $\approx$ 30%) was used to act as the top mirror in the initial designs, thus reducing the overall complexity of the MBE growth. Therefore, in this case $n_o = 1$ and Eq. 4.6 may be plotted as a function of the number of periods in the DBR as shown in Fig. 4.23.

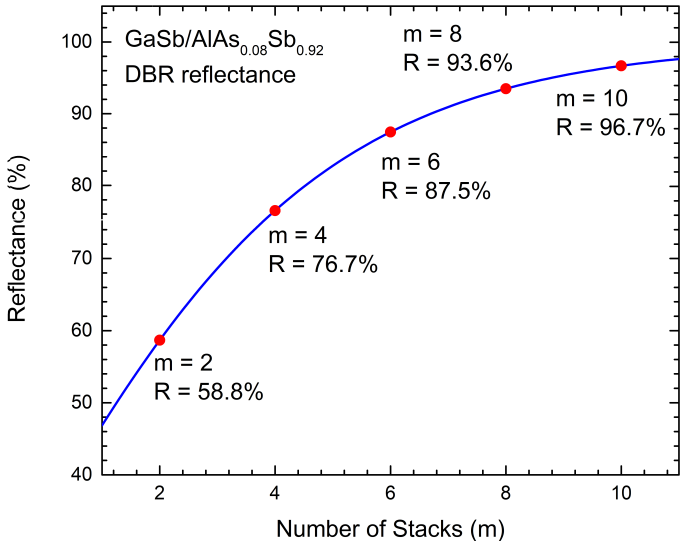

Figure 4.23: Plot of the reflectance of a GaSb/$AlAs_{0.08}Sb_{0.92}$ DBR as a function of the number of periods (m) based on Eq. 4.6 with index values for GaSb and AlAsSb at a target wavelength of 4 μm. A target reflectance greater than 95% can be achieved with 10 periods.

From this it may be determined that 10 periods satisfy the requirement of a DBR with $>$ 95% reflectance. This low stack count adds only a slight additional complexity to the overall MBE growth of the ICTPV structure. In order to successfully grow the DBR structure, an alloy calibration for $AlAs_xSb_{1-x}$ must be

completed.

4.5.2 $AlAs_xSb_{1-x}$ Alloy Calibration

Based on perspectives presented in Section 4.1, the lattice matched condition for AlAsSb to GaSb occurs with an As and Sb composition of 8% and 92%, respectively. An initial 1 μm thick AlAsSb alloy (M375) was grown on GaSb using a V_{As}/III = 9.48 and a V_{Sb}/III = 3.68, corresponding to an As valve opening of 31 mils and an Sb valve opening of 210 mils. The Sb flux was reduced by about 59%, from 1.03×10^{-6} Torr, by reducing the valve opening to 145 mils during heating/cooling phases of the substrate based on the perspective of Sb stabilized flux that was previously discussed. Oxide desorption was performed for 10 minutes at a temperature ranging between 520-522°C, according to the pyrometer. After, the substrate temperature was lowered to 477°C for growth of the GaSb buffer layer and AlAsSb epilayer. The grown alloy was characterized with XRD (Fig. 4.24) where the FWHM of the peak was observed to be rather broad, indicating some degree of relaxation. The extracted alloy composition from the XRD data was $AlAs_{0.195}Sb_{0.805}$ (if fully relaxed) and $AlAs_{0.14}Sb_{0.86}$ (if fully strained), therefore the actual alloy composition was likely somewhere between these two values.

Clearly there was too much As incorporation into the alloy, resulting in a tensile biaxial strain (compressive out-of-plane strain), which impacted the material quality. Several additional alloy calibration wafers were grown with slight variations to the As valve opening and the corresponding flux quantity, while largely keeping the same Sb flux and growth temperature. These parameters are listed in Table 4.5, while the resulting XRD patterns of the grown alloys are shown in Fig. 4.25. A total of only 1.2 mils (29.4 μm) of the As valve opening was explored, which resulted in a range of As compositions in the grown wafers of between 5.3%-10.6%. This actually rides the limitation of the GENxplor, which from experience is known

Table 4.5: MBE growth parameters for a series of early AlAsSb alloy growth studies. The Sb and As valve open values are given in mils (1 mil = 25.4 μm) and the fluxes are listed in units of Torr. The alloy compositions are extracted from the measured XRD patterns and are assumed to be the strained compositions.

MBE Growth Parameters and XRD Extracted Alloy Compositions					
Wafer	Sb Valve	Sb Flux	As Valve	As Flux	Composition
M376	230	1.18×10^{-6}	21	8.97×10^{-8}	$AlAs_{0.053}Sb_{0.947}$
M377	230	1.18×10^{-6}	21.3	1.04×10^{-7}	$AlAs_{0.074}Sb_{0.926}$
M378	232	1.18×10^{-6}	22.2	1.17×10^{-7}	$AlAs_{0.106}Sb_{0.894}$
M379	232	1.18×10^{-6}	21.7	1.10×10^{-7}	$AlAs_{0.093}Sb_{0.907}$
M380	233	1.18×10^{-6}	21.5	9.59×10^{-8}	$AlAs_{0.082}Sb_{0.918}$

to show no change in the BFM background pressure reading until the As valve is opened beyond 20 mils. Thus, at the As cell temperature settings of 1000/850/529 (°C) for the cracker/tip/base, which are generally left unchanged between growth runs in a given growth campaign, there appeared to be very little room to adjust and optimize the growth parameters of this alloy.

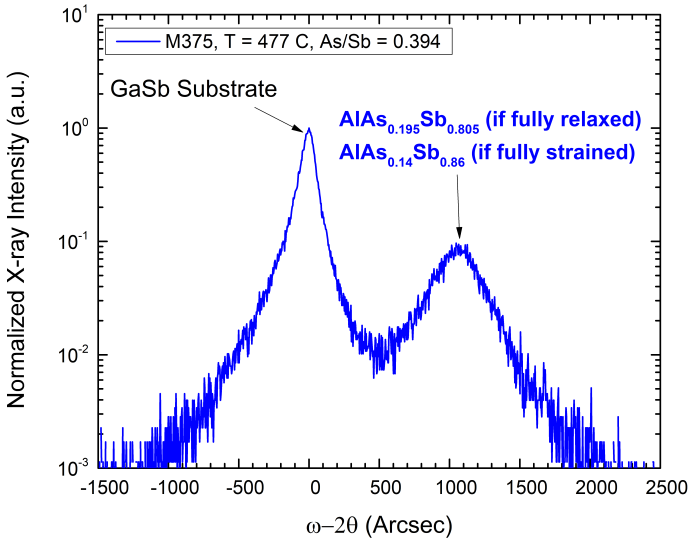

Figure 4.24: Measured XRD pattern for M375, the first growth of the AlAsSb alloy for the DBR mirror. The FWHM of the peaks are rather broad due to the reduced material quality associated with the incorrect alloy composition.

Since M380 exhibited an alloy composition rather close to the desired result, the first DBR structure was grown (M388, to be discussed in Section 4.5.3). The results

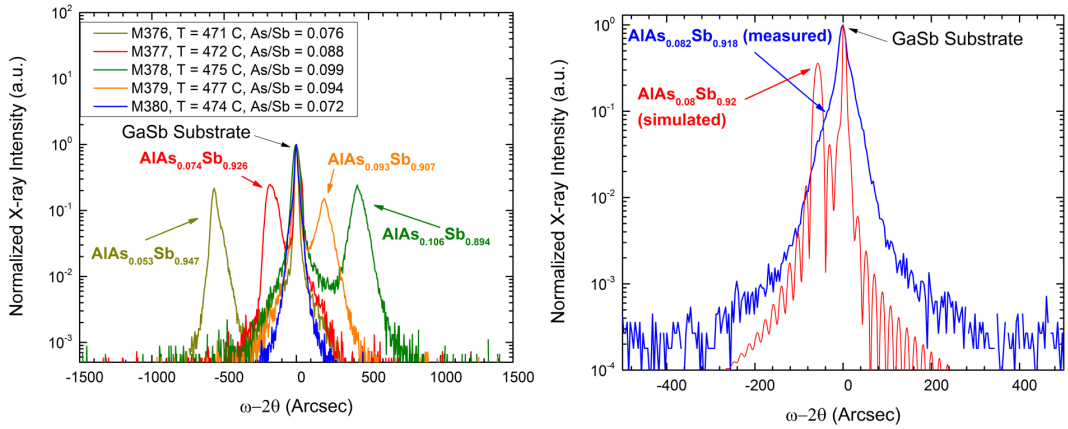

Figure 4.25: Measured XRD patterns for a series of AlAsSb alloys grown on GaSb. The overall As valve opening was adjusted only slightly, ranging between 21-22.2 mils, corresponding to a total valve exploration range of only 1.2 mils (29.4 μm).

of the first DBR testing showed some layer thickness deviations, and therefore additional growths were needed. However, during this time, the Ga source began to run out of material and the MBE system needed to be opened up for maintenance and refilling of the source materials. Therefore, all of the growth parameters changed and needed to be re-calibrated once the system became operational.

During the first round of AlAsSb calibration, it was noted that the As composition did not share a linear relationship with the As valve opening, and the corresponding As flux. For example, a 16% increase in the As flux from M376 to M377 only resulted in a 2.1% shift in the As composition of the alloy. This feature was explored in the second round of alloy calibration where only the first three wafers grown had As fluxes that were manually adjusted by small changes to the As valve with a sort of "guess and check" method that was based on XRD pattern measurement. These three wafers were M393, M395, and M396. First M393 was grown with similar growth parameters to M376, resulting in an As composition of 5.90%. Next the As valve was opened to a larger value of 23 mils to establish upper and lower bounds for the experiment. This resulted in an As composition of 9.97% for M395. A third wafer was grown, M396, with an As valve opening of 22 mils,

exactly between that of M393 and M395. If a linear relationship existed between the valve opening, and subsequent flux, then the composition would be expected to show as 7.94%. However, XRD testing of M396 resulted in an extracted alloy composition of 8.87%. The valve openings for these three wafers were plotted as a function of the measured As composition of the alloy. The data was fit with several different curves, where a power fit of the form $y = y_o + A(|x - x_c|^p)$ seemed to result in the best fit as demonstrated in Fig. 4.26. This makes sense because the valve opening is circular, so the resulting flux (and its incorporation into the growing alloy) should be proportional to the surface area of the valve opening. Here x_c allows for centering the fit and x represents the As composition at a given valve opening, while y_o represents the fact that the growth chamber does not have a measurable amount of As present until the valve is sufficiently opened. Based on this fit, a value of x = 8% was used to try to dial in the exact As valve opening required to achieve a perfect alloy composition. Two additional growths were done and added to the fitting as shown in Fig. 4.26. The fit results in a y-intercept of $y_o = 20.951$, which is quite close to the observation that there is no measurable background pressure change until the As valve has been opened beyond 20 mils. This effort presented a more systematic and repeatable method to achieving consistent As compositions and high quality alloy growth, allowing for the growth of DBR structures with reflectance values that could meet the RCE ICTPV needs.

4.5.3 Growth and Testing of the DBR

The MBE growth of the DBR is somewhat challenging because it requires stable fluxes and precise control of the growth rates to achieve accurate layer thicknesses and the lattice-matched alloy composition. A small deviation in the thickness can result in a noticeable shift of the reflectance peak from the designed location. The

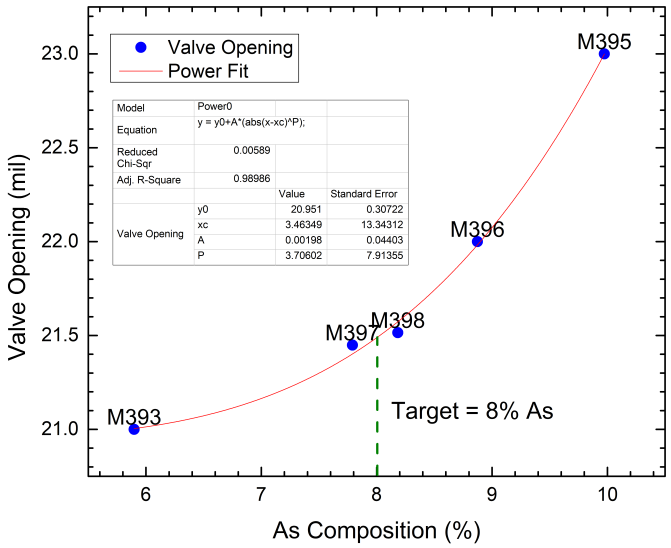

Figure 4.26: Plot of the As valve settings as a function of the measured As composition for several grown wafers. A power fit was used to predict the ideal valve setting to achieve an 8% As composition.

DBR for the RCE ICTPV consists of a 10 period GaSb/$AlAs_{0.08}Sb_{0.92}$ quarter-wave stack with a target reflectance of greater than 95% near 4 μm. This is achieved using the design shown in Fig. 4.27, where the refractive index of GaSb and $AlAs_{0.08}Sb_{0.92}$ used in the design are 3.78 and 3.186, respectively. After initial alloy calibration was completed, the first DBR test structure was grown (M388). The material quality was examined with DIC and XRD, where the surface defect density was measured to be 9.77×10^3 cm^{-2} as shown in Fig. 4.28, with only a slight amount of background surface roughness, indicating relatively good strain balancing and crystal quality. This is confirmed with XRD measurements which yielded narrow FWHM values of around 50 arcseconds. From the XRD data, it was observed that the SL period thickness was approximately 5.7% too thin, compared with the intended design. The intended overall thickness for a single period was 578.7 nm and the measured result from XRD was 545.6 nm. Consequently, one may expect a rather large shift in the position of the peak reflectance of this DBR as for a quarter-wave stack designed with a 4 μm target wavelength, the thickness

deviation would result in a potential peak reflectance at 545.6/578.72× 4μm = 3.77 μm.

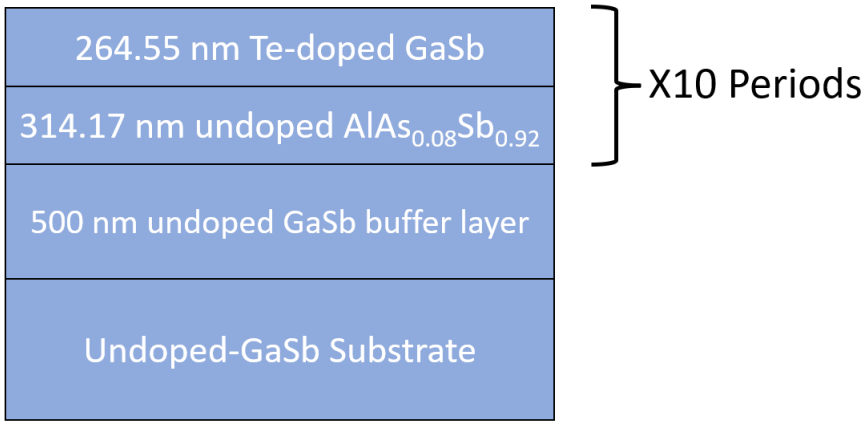

Figure 4.27: Schematic diagram of the intended DBR structure for the RCE ICTPV.

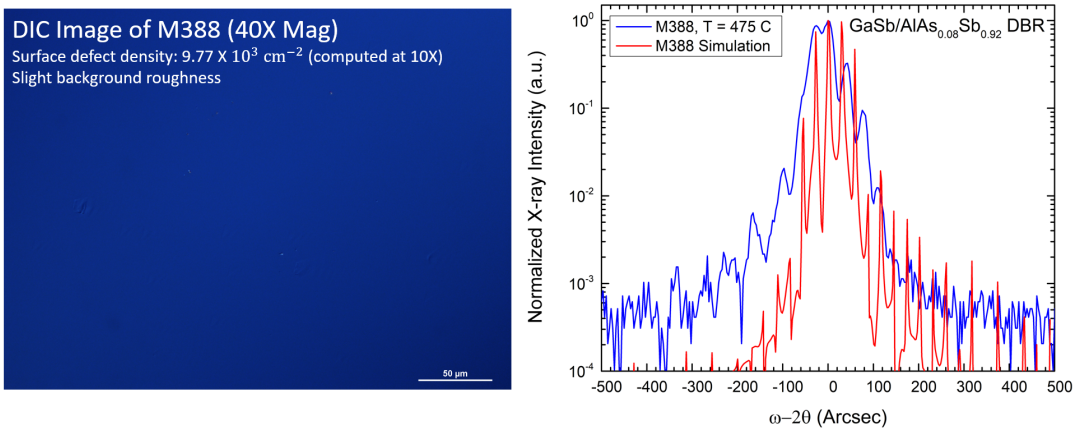

Figure 4.28: DIC image of the surface of M381 (left) which shows only a slight amount of background surface roughness. Measured XRD pattern (blue) compared with a simulation (red) for M381. Qualitatively it is seen that there is a SL period variation based on the placements of the harmonic peaks relative to the simulation.

Indeed, when the reflectance of M388 was measured, it was found to peak close to 97% at 3.74 μm, shifted nearly as much as initially anticipated as shown in Fig. 4.29. A simulated DBR reflectance spectra may be generated based on Eq. 4.6 assuming a layer thickness deviation observed in XRD, which is also shown in the figure. The approximate matching of the simulated reflectance compared

with the measured result indirectly validates the values of n used for GaSb and $AlAs_{0.08}Sb_{0.92}$ at 4 μm.

As discussed in Section 4.5.2, shortly after this time the MBE chamber was opened, and all material calibrations needed to be redone. After completing the AlAsSb alloy calibration with M398, new DBR structures were grown, with growth parameters adjusted after several iterations in order to match the previous material quality. Next, the shutter open/close times for growth were adjusted based on the measured position of the peak reflectance until a center wavelength of about 4 μm was established with wafers M411 and M412, shown in Fig. 4.29.

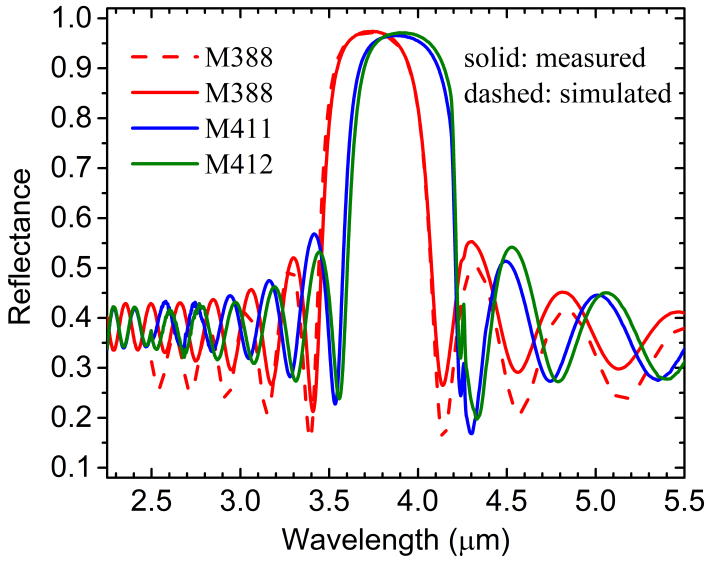

Figure 4.29: Measured (solid) and simulated (dashed) reflectance spectra for three GaSb/$AlAs_{0.08}Sb_{0.92}$ DBR mirrors with ten periods.

Additionally, the spectral width of the high reflection zone may be estimated from

$$\Delta\lambda = \frac{4}{\pi}\lambda_{design} \arcsin\left(\frac{n_{high} - n_{low}}{n_{high} + n_{low}}\right) \tag{4.7}$$

which when calculated based on the intended design yields $\Delta\lambda = 0.44$ μm. The spectral width for M411, averaged over several positions was 0.58 μm, deviating

from the intended design by about 31% (similarly for M412). This can be mainly attributed to some slight broadening related to small variations in material compositions and quality. Nevertheless, peak reflectance results of 96.6% at 3.88 μm and 97.1% at 3.93 μm for M411 and M412, respectively, were achieved. Furthermore, at the targeted operation at 4 μm both M411 and M412 showed acceptable reflectance values of 95.5% and 96.5%, respectively. Integration of this DBR structure into the ICTPV in order to recycle unabsorbed photons would result in a predicted enhancement to the quantum efficiency of 44% with a corresponding increase in the conversion efficiency from around 5% to 23%, based on perspectives from Refs.[123, 124]. Unfortunately, only initial attempts at integration of the DBR into the ICTPV were conducted as the Covid pandemic interfered with this project. Nonetheless, the MBE techniques developed here will be applicable to future growth campaigns and the promise of the resonant optical cavity to enhance the conversion efficiency of ICTPV devices should be further explored.

Chapter 5

Device Fabrication and Characterization

5.1 Fabrication and Characterization Introduction

Chapters 2 and 3 discussed many of the details on MBE growth and material characterization, while Chapter 4 presented a series of growth studies targeting interband cascade related structures. The growth of a structure design, like an ICL, represents the first step in the overall research process. The second primary step for a grown structure to become a laser device is the fabrication step, while the third and final step is device characterization, which creates a feedback loop in the overall research. This chapter will mainly focus on discussion of the device fabrication and the typical methods used to characterize ICL devices.

5.2 Device Fabrication

Regarding device fabrication, the grown semiconductor wafer is processed into a device using contact photolithography and wet, or dry, chemical etching, depending on the type of fabrication being conducted. There are two main types of device processing which may be done to create an ICL: broad-area fabrication (BA), which uses wet chemical etching, and narrow-ridge fabrication (NR), which may use a combination of both wet and dry chemical etching. In the latter, the dry chemical etching is performed with a reactive ion etching (RIE) system. In BA fabrication, laser ridge widths between 100-150 μm wide are defined, while in NR fabrication the laser ridge widths are substantially narrower, 10-30 μm wide and there are advantages as well as disadvantages for each type of fabrication. One the one hand, BA fabrication is less complex and time consuming, resulting

in a more uniform result with greater yield than NR fabrication, which requires much more careful alignment during the photolithography steps as well as several additional steps including the deposition of an insulating layer on the laser ridge sidewall. However, BA fabrication suffers more from thermal gradients between the active region of the ICL and the heat sink, which can hinder performance at higher temperatures as will be discussed in more detail in 5.4. Determining which fabrication method to use depends on a number of factors, but generally speaking for quick turnaround or initial testing of new ICL structures, BA fabrication is preferred, while NR fabrication may be the better choice if the ICL structure is more mature or if thermal issues are a consideration.

In general, the typical fabrication process involves several steps which include, cleaning the wafer surface using solvents (Acetone/Methanol/Isopropyl Alcohol (IPA)), dehydration baking of the wafer in an oven/hot plate, spin coating the wafer in the desired photoresist, photolithography, wet chemical etching to define the laser ridge, deposition of an insulating layer such as SiO_2/Si_3N_4 (for NR fabrication only), opening up windows on the top of the laser ridges in order to create Ohmic contacts, deposition of a desired contact metal using either thermal evaporation or magnetron sputtering to provide top contacts, and finally liftoff to define the metal contacts. More in-depth details for the various processing steps may be found in reference [125], with a general depiction (not to scale) of a fabricated ICL shown in Fig. 5.1.

After the wafer has been followed these processing steps, it may also undergo lapping which involves slowly grinding away the substrate to thin the wafer and improve its thermal characteristics as well as making it easier to cleave. After lapping, the typical thickness of the wafer is approximately 150-200 μm. Regardless of if the wafer has been thinned or not, the final processing step involves deposition of the contact metal on the back side of the wafer (substrate side) in order to

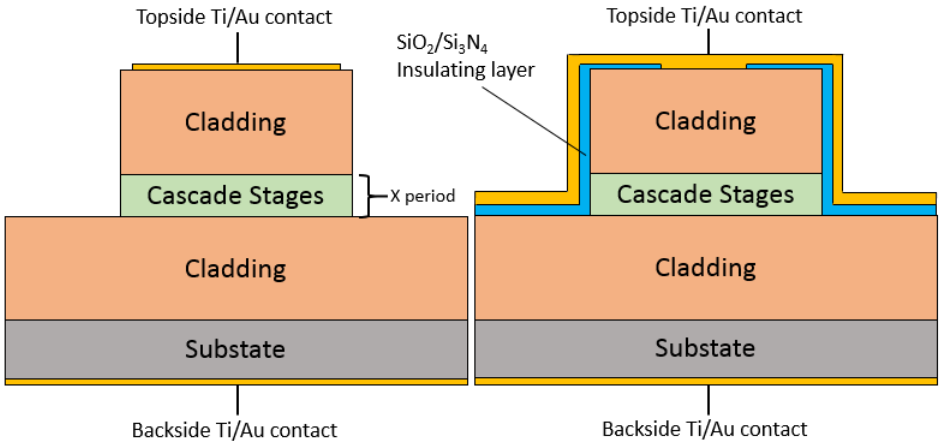

Figure 5.1: Schematic diagram of the BA (left) and NR (right) fabrication process.

provide a back contact for the ICL. Afterwards, the wafer may be cleaved into laser bars with widths of $\sim$ 0.5-3 mm, which are the cavity lengths for the ICL. These cleaved facets may act as the end mirrors to form the laser cavity due to the sharp refractive index contrast between the facet and the atmosphere. The length of each laser bar is such that 8-10 individual ICLs are housed. The cleaved facets act as the mirrors for the cavity and are generally left uncoated, which means that approximately 50% of the light generated will exit the rear of the ICL and will, therefore, not be captured in the measurement. The cleaved laser bar is then mounted on a copper heat sink with In solder used to provide thermal contact. A (type of bonder here) is used to wire bond up to 8 ICLs to a ceramic package also connected to the copper heat sink using Au wire. The wire connecting the ICL to the package can be thought of as a small fuse, so at least two wires are connected to each ICL in order to prevent a wire from burning out with larger currents as depicted in Fig. 5.2, where the inset also shows the configuration of the copper heat sink, laser bar, and ceramic package. Once all components have been mounted onto the copper heat sink, it is then ready to be attached to the cold finger of the cryostat for measurement.

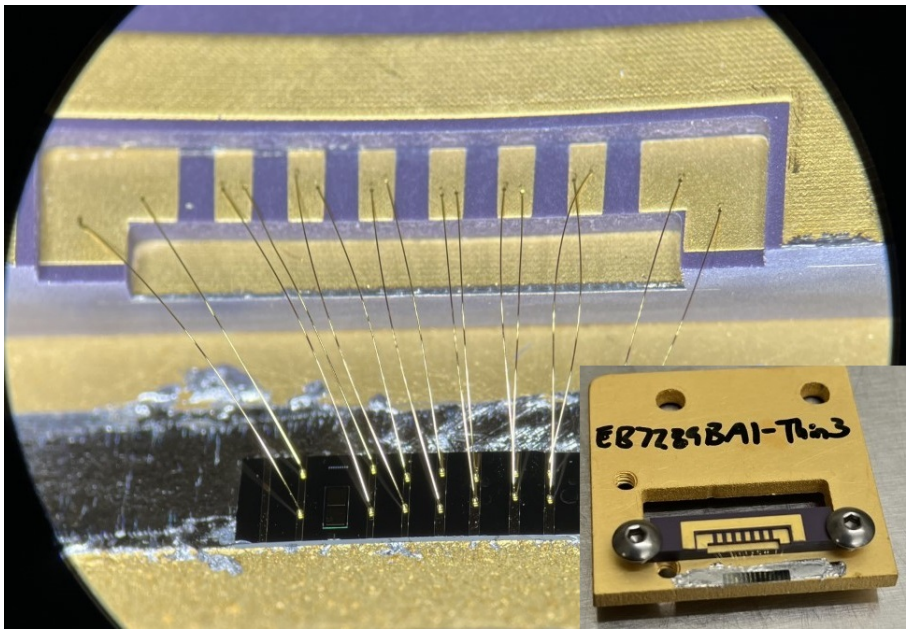

Figure 5.2: Each ICL is connected by at least two Au wires to the contact pads of the ceramic package so that burnout from large injection currents may be prevented. The inset shows the final configuration of the ICLs ready for measurement.

5.3 ICL Performance Characterization

The primary measurement technique utilized for ICL testing is known as electroluminescence, meaning light production by way of electricity. Here the ICL is injected with a current, where the internal voltage shift initiates the cascade process as each injected electron transitions through the array of QWs. There are a number of performance characteristics which may be measured directly from the light emitted from the ICL. The following sections detail the primary characteristics ascertained from both the emission spectrum and the current-voltage-light (IVL) measurements.

5.3.1 ICL Emission Spectrum

The ICL may be tested after pumping down the cryostat to at least 10^{-2} Torr and cooled with liquid nitrogen. Typically, an ILX Lightwave LDP-3811 laser

diode driver is used as the current source for the ICL for both cw and pulsed spectra collection. The ILX is capable of operating in either cw or pulsed mode with current limit settings of 200 mA and 500 mA, respectively. If an ICL needs to be tested at higher injection currents, as may commonly be the case for pulsed measurement of long-wavelength ICLs, a secondary current source is used: the Avtech AV-107C-B. Similar to other semiconductor lasers, the ICL is an index guided laser with a rectangular shaped cross section, which means that the beam profile of the device is vertical elliptical as shown in Fig. 5.3[126].

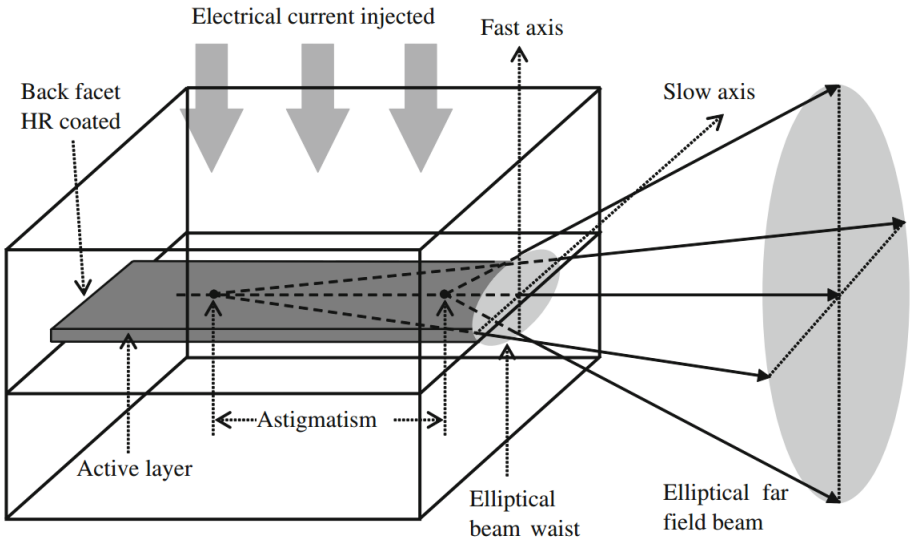

Figure 5.3: A semiconductor laser with a thin active layer. The emitted beam forms an elliptical pattern, where the divergence in the ”fast axis” direction is more pronounced than in the ”slow axis” direction.[2]

This occurs because as the laser is operated, a small portion of the laser field leaks out of the active layer, causing the elliptical shape and leading to the characteristic beam divergence. The beam elliptical ratio is not even between the vertical and horizontal dimensions, however. Generally speaking for the ICL, one could say that the dimension in which the active layer is most spatially confined is the dimension in which the beam divergence is the greatest. Oftentimes, the axis with the greatest beam divergence may be referred to as the “fast axis”,

and consequently, the other axis as the "slow axis". Practically speaking for measurements, this means that one or more optical lenses are required in order to guide the highly divergent beam to the detector of interest for the measurement being conducted.

In the case of measuring the emission spectrum of the ICL, a single half convex lens is used in order to generate parallel light rays from the divergent beam. These parallel light rays are then sent into a Nicolet 8700 Fourier transform infrared spectrometer (FTIR). The FTIR is made up of a Michelson interferometer which has a single fixed reference mirror and a second moving mirror, which passes through the zero-delay position of the balanced interferometer configuration. In addition, there are two ports for internal detectors consisting of a fixed back detector, which houses a deuterated triglycine sulfate (DTGS) detector, and a front detector, which houses a mercury-cadmium-telluride (MCT) detector that can be removed. The DTGS detector has a wide spectral responsivity, with a low sensitivity. For most measurements conducted, the MCT detector is used due to its higher sensitivity within the spectral bands of interest as shown in Fig. 5.4. There are also a series of internal mirrors to guide the laser radiation entering into the FTIR as well as a couple of infrared sources, which may be used for calibration of the detectors. The interferogram collected by the detector undergoes a Fourier transform processing which converts the raw interferogram into a spectrum that can be analyzed by the software.

An example spectrum, which has been normalized, is shown in Fig. 5.5, which depicts a laser device exhibiting stimulated emission. The clear indicator is in the linewidth of the spectrum as spontaneous emission is broader, being composed of many wavelengths of light, while the onset of stimulated emission shows the characteristic narrow linewidth of approximately 10-30 nm[127]. From the emission spectrum, a direct measurement of the emission wavelength can be conducted.

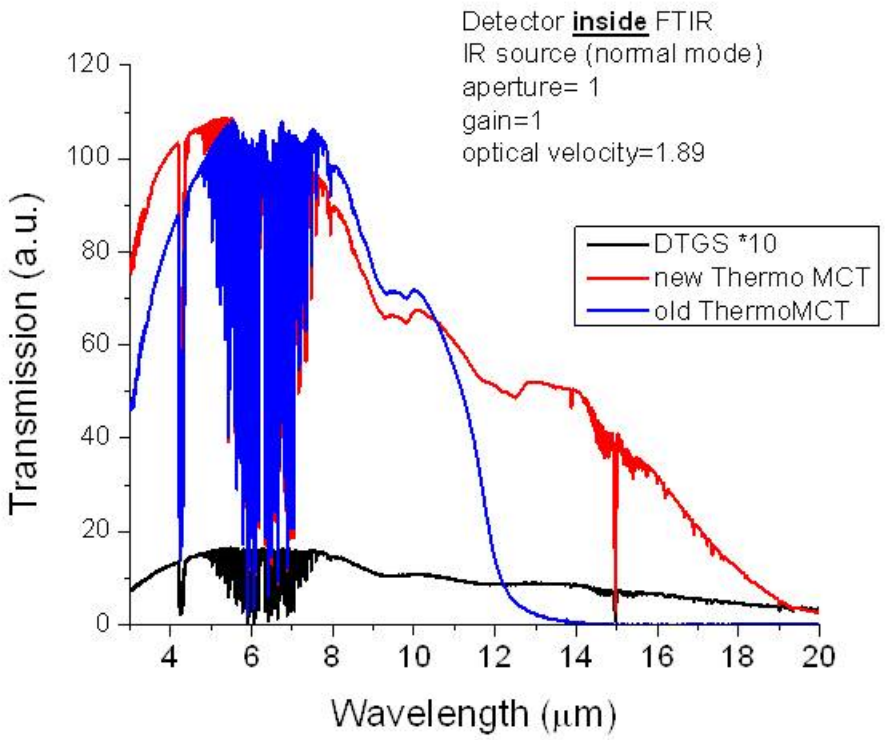

Figure 5.4: A comparison of the spectral response and sensitivity of the various internal detectors for the FTIR using the internal infrared source.

Also, the threshold current (I_{th}) may be determined and based on the cavity length and ridge width, the threshold current density (J_{th} in units of A/cm^2) can be deduced. Additionally, the emission spectrum can give perspective to the quality of the laser emission as a tight linewidth can indicate good efficiency in the stimulated emission process, while a slightly broader linewidth may indicate a reduced stimulated emission efficiency with more competition from spontaneous emission processes, among other considerations[128].

Of particular interest is the temperature dependence of the ICL's emission spectrum as any practical application involving an ICL must require the device to operate at temperatures that are at least accessible by a thermoelectric cooler, approximately 45°C between the device and its ambient temperature[62, 129]. Measurements begin at LN temperatures and incrementally rise toward room

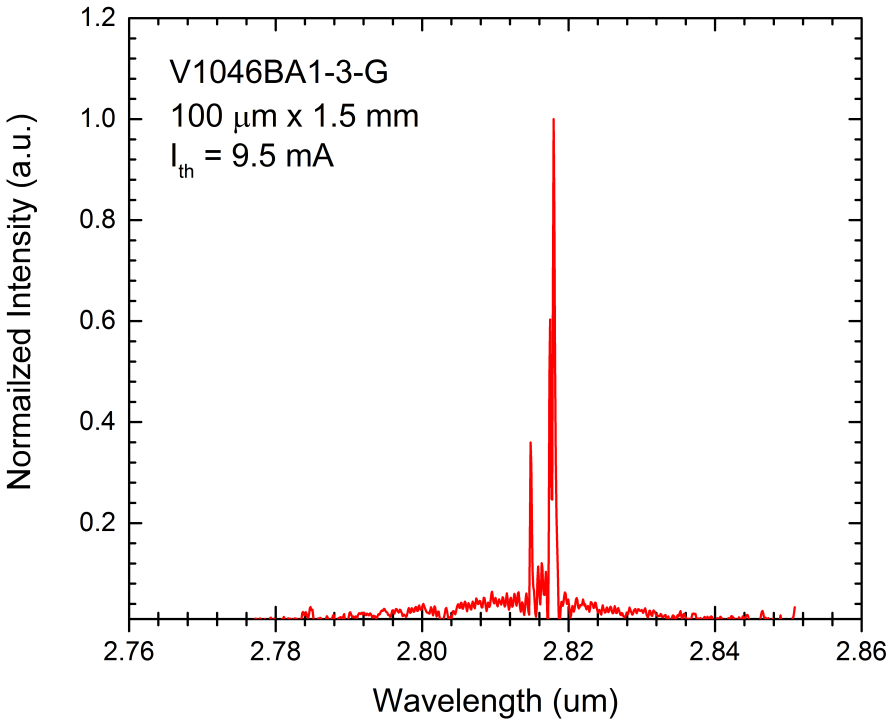

Figure 5.5: The spectral response of a type-I GaSb-based ICL operating at 80 K, with a threshold current of 9.5 mA and a wavelength of 2.82 μm. The laser ridge width is 100 μm, while the cavity length is 1.5 mm.

temperature in order to find the maximum operating temperature of the ICL, both in cw and pulsed modes, respectively. During the measurement process, a typical redshift is observed in the emission wavelength of the device due to the bandgap narrowing with increasing temperature. This feature arises because of the expansion of the crystal lattice, changing the electron-phonon interaction, which is often described by the empirical Varshni formula[130]. This allows for a temperature tuning of the emission wavelength of the ICL as shown in Fig. 5.6, which can be quite useful for applications involving spectroscopy. In the example shown, a type-I ICL operates at 80 K with an emission wavelength of 2.82 μm in cw mode, which redshifts to 3.19 μm at room temperature in pulsed

mode (approximately narrowing the bandgap by 11.6 %), resulting in a wavelength tunability of 1.69 nm/K. In addition to shifting the wavelength with temperature, the J_{th} also varies as,

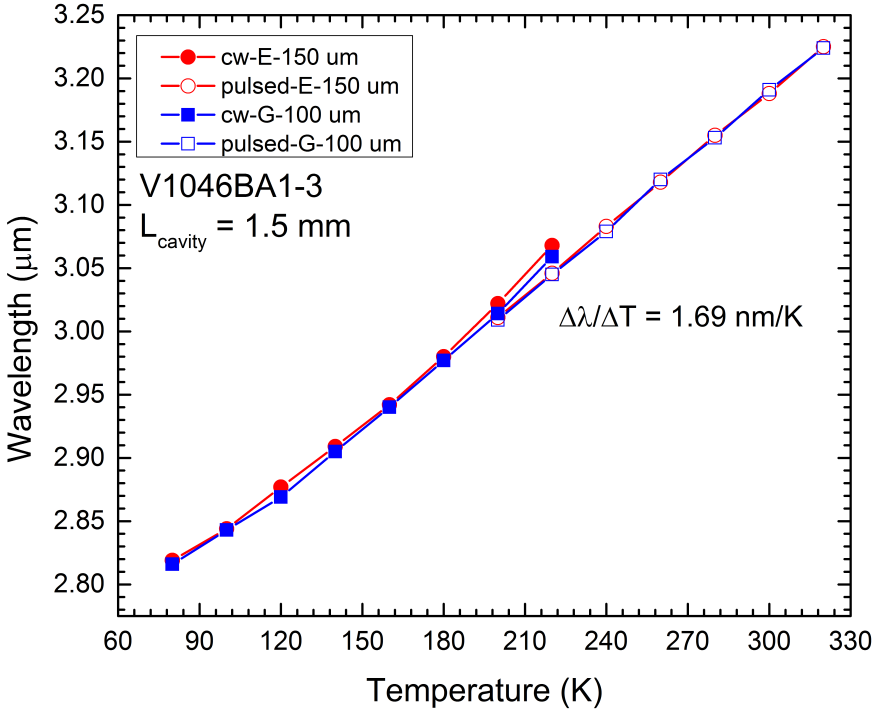

Figure 5.6: Example showing the wavelength tunability with temperature for a type-I ICL operating with an 80 K emission wavelength of 2.82 μm in cw mode, which redshifts to 3.19 μm at room temperature in pulsed mode, resulting in a tuning of 1.69 nm/K.

$$J_{th}(T) = J_{th}(T_1)e^{\frac{T-T_1}{T_o}} \Rightarrow J_o e^{\frac{T}{T_o}} \tag{5.1}$$

where T_o is the so-called characteristic temperature of the device, which serves to summarize the temperature-dependent loss and the carrier redistribution in **k**-space due to the change of the Fermi distribution with temperature. As the temperature of the ICL increases, the populated states below the quasi-Fermi level

begin to become unpopulated, while nonlasing states become populated. Thus, the overall gain decreases in the system and to combat this, the quasi-Fermi level must be compensated by supplying a larger current[2] in order to inject more carriers into the system. From Eq. 5.1, the characteristic temperature is often determined for experimental purposes across the entire temperature range of the working ICL as,

$$T_o = \frac{T_{upper} - T_{lower}}{ln\left(\frac{J_{th,upper}}{J_{th,lower}}\right)} \tag{5.2}$$

where $T_{upper/lower}$ refer to the highest and lowest temperature measurements made (in either cw or pulsed modes), and $J_{th,upper/lower}$ refer to the threshold current densities corresponding to the upper and lower temperature measurements, respectively.

Inevitably, as the temperature continues to rise the ICL will eventually no longer function in cw mode due to heating effects and will need to be further investigated by pulsed operation as discussed in more detail in Sec. 5.4. Generally speaking, there will exist a small difference in comparing the cw and pulsed data near the region of maximum temperature for cw operation as can be seen in Fig. 5.6. To better understand this difference, it may be characterized by a thermal resistance (R_T)[131] related to the difference between the active region temperature of the ICL and its substrate, which is in direct contact with the cold finger of the cryostat (acting as the heat sink), and may be described by,

$$T_a = T_{sub} + R_T V_{th} J_{th} \Rightarrow R_T = \frac{T_a - T_{sub}}{V_{th} J_{th}} \tag{5.3}$$

Experimentally, one can determine the R_T value by comparing the temperature data in the vicinity of the maximum cw operating temperature where the pulsed

result begins to deviate from the cw result. In that way, Eq. 5.3 becomes,

$$R_T = \frac{T_{cw} - T_{pulsed}}{V_{th,cw} J_{th,cw}} \tag{5.4}$$

Because of the existence of the thermal resistance, there should exist a maximum operating temperature, and consequently a maximum J_{th}, for the cw emission of the device which may be defined by substituting the result of Eq. 5.3 into Eq. 5.1 in the following way,

$$\begin{aligned} J_{th} = J_o e^{\frac{T}{T_o}} \Rightarrow J_o e^{\frac{T_{sub} + R_T V_{th} J_{th}}{T_o}} \\ T_{sub} = T_o ln\left(\frac{J_{th}}{J_o}\right) - R_T V_{th} J_{th} \end{aligned} \tag{5.5}$$

To predict the maximum cw J_{th} of the device, and determine the temperature at which that may occur, one may simply differentiate Eq. 5.5 in the standard way,

$$\begin{aligned} \frac{dT_{sub}}{dJ_{th}} = \frac{T_o}{J_{th}} - R_T V_{th} = 0 \\ \Rightarrow J_{th,max} = \frac{T_o}{R_T V_{th}} \\ T_{sub,max} = T_o \left[ln\left(\frac{T_o}{R_T V_{th} J_o}\right) - 1 \right] \end{aligned} \tag{5.6}$$

Eq. 5.6 implies a linear relationship between the J_{th} and the characteristic temperature of an ICL, and therefore a larger characteristic temperature is preferred for better device performance under cw operation at higher temperatures.

Lastly, the voltage efficiency of the ICL may be determined from the cw emission spectrum. This unitless parameter characterizes how efficient the ICL is based on the photon energy of the lasing emission, the threshold voltage of the device at a given temperature, and the number of cascade stages in the ICL and is written as,

$$V_e(T) = \frac{N_c\left(\frac{hc}{\lambda(T)}\right)}{eV_{th}(T)} \tag{5.7}$$

where N_c is the number of cascade stages, λ(T) is the temperature dependent lasing wavelength determined from the emission spectrum, and e is the electron charge which may be written as 1 if the units of the photon energy are given in [eV]. Ideally for a fixed number of cascade stages and a set emission wavelength, the ICL will have a low threshold voltage leading to a large voltage efficiency, indicating good performance. Conversely, an ICL operating with a relatively large V_{th} would manifest a small or reduced voltage efficiency. While the cw and pulsed emission spectrum measurements can provide a wealth of information about the performance of the ICL, the complete picture cannot be told without access to the IVL characteristics of the device.

5.3.2 ICL IVL Characteristics

Complementary to the ICL emission spectrum measurements are the current-voltage-output power (or light) (IVL) characteristics of the ICL. Typically for cw IVL testing, a Keithley 2100 6 1/2 digital multimeter is used to measure the voltage of the device, while either an ILX Lightwave LDP-3811 or an ILX Lightwave LDC-3744B are used to supply current to the ICL during cw operation. The LDC-3744B has a larger current range than the LDP-3811, however the compliance voltage is only 10 V, compared with the LDP-3811 with a compliance voltage of 25 V, meaning the V_{th} of the ICL may dictate which current source is used. To collect the output power from the ICL under cw operation, a PM3 Coherent PowerMax thermopile power meter connected to a LabMax Top display, which can be adjusted to the emission wavelength of the ICL to better capture the output of the device, is used. The power meter sensor is placed directly in front

of the cryostat window in order to capture as much of the incident radiation as possible, though some loss is present due to beam divergence, as well as backside loss since the facets are generally left uncoated.

An example of a typical IVL result is shown in Fig. 5.7, with the IV results and IL results marked to their appropriate axes. First a semiconductor laser may begin to emit a small amount of light through spontaneous emission processes, but as population inversion into metastable states rapidly begins to dominate, a dramatic shift in the slope of the IL curve can be observed, indicating the onset of lasing with stimulated emission. From the IL data, the I_{th} may be determined at the location of this dramatic slope shift, and consequently the J_{th} as before. Actually, the J_{th} determined by IVL measurements is generally a bit more accurate (by way of being slightly smaller) than that determined by way of the FTIR spectrum results. As the laser is driven with increasing current, the output power will continue to rise until thermal processes begin to hinder the laser performance, at which point the laser reaches thermal rollover and the output power begins to decrease. Thermal rollover is an effect that is generally caused by a combination of two factors. The first comes from the resistive heating of the laser cavity which can affect the refractive index of the materials. In this case, the increasing cavity temperature can cause a drop in the refractive index leading to a decrease in the optical output power. The second effect occurs through optical gain saturation. This affects how the laser is able to efficiently convert input electrical power to output optical power, whereby continuing to increase the current causes the optical gain to become so low that the laser output power begins to rapidly drop off. Where the slope of the IL curve begins to flatten, the maximum output power of the ICL may be determined, typically listed in units of mW/facet as the back facet of the ICL is left uncoated, where approximately 50% of generated light escapes.

In addition to determining the maximum cw output power of the ICL, the

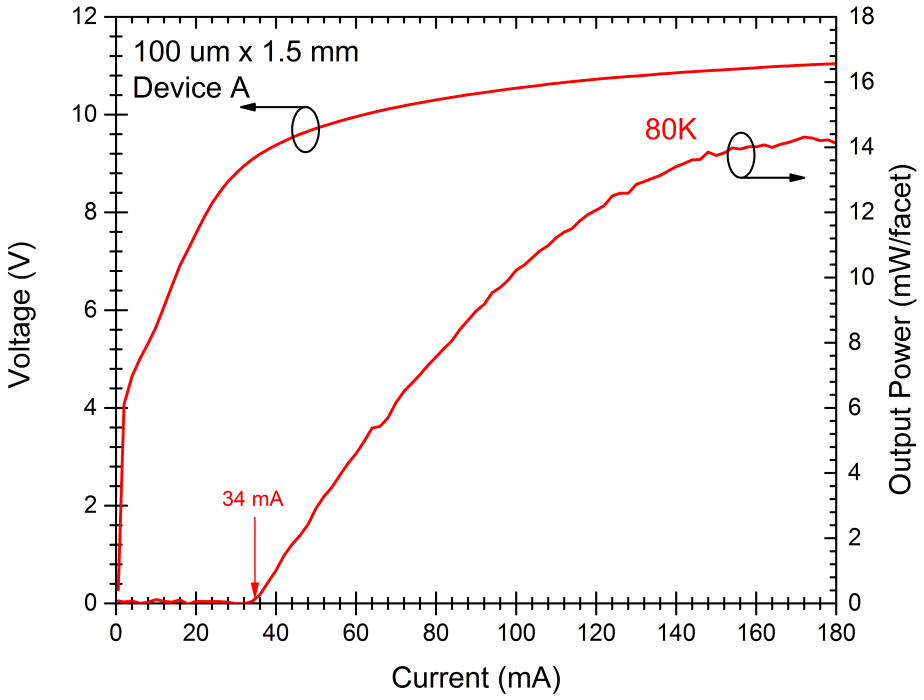

Figure 5.7: An example IVL result showing the typical IV characteristics for an ICL, albeit with a large V_{th}, on the left. On the right is the IL result, which lists the I_{th}, maximum output power, and thermal rollover of the ICL.

IL results may be differentiated to show the differential power of the ICL. Often, the differential power is referred to as the slope efficiency, and is related to the external quantum efficiency of the ICL in the following way,

$$\frac{dP}{dI} = \eta_s = \frac{hc\eta_e}{\lambda q} \tag{5.8}$$

where η_s is the slope efficiency, $\frac{hc}{\lambda}$ is the photon energy, q is the electron charge, and η_e is the external quantum efficiency (sometimes referred to as the differential quantum efficiency), which characterizes the efficiency of the laser in converting electron-hole-pairs (EHP) into emitted photons from the device, after internal optical losses occur. The external quantum efficiency of the ICL is related to the

internal quantum efficiency as,

$$\eta_e = \frac{1}{2}\eta_i \frac{\alpha_m}{\alpha_m + \alpha_i} \tag{5.9}$$

where η_i is the internal quantum efficiency, similar to the external quantum efficiency, except that it describes the efficiency of the laser in converting EHPs into photons within the laser cavity. Additionally, α_m and α_i refer to the mirror loss and the internal optical loss, respectively. Because the experimental IL data results in a series of values for the η_s, only the largest value is used in computing the η_e and this value then represents the accepted value for the ICL. However, one must be careful in choosing this value, because it is possible that a localized spike in the IL date due to noise in the measurement could occur. If this happens, then it would present as a significantly larger dP/dI value and could give the wrong indication about the η_e. Therefore, the general trend around the largest EQE value should also be observed to verify that it is in line with other nearby data points. It should be noted that if the intended application of the ICL is to maximize the output of the device, then it is generally preferred to increase the N_c in order to increase the η_s[132]. However, this comes with the drawback of increased potential for heating within the ICL and possible hindered performance at higher operating temperatures. Heating when testing an ICL is a major contributor for diminished performance, and so one must endeavor to reduce this facet of the experiment in whatever way they can. The following section discusses several options for addressing this concern.

5.4 Pulsed IVL Measurements

In cw operation, the ICL can generate more heat than it is able to dissipate, leading to an active region temperature that is much higher than the heat sink

temperature, and consequently causing a significant heating issue which limits the performance of the ICL. There are several fabrication techniques one could adopt in order to work around such a problem. One method involves decreasing the required I_{th}, which consequently also reduces the heat generated within the device and can be achieved in two different ways. For the first, instead of conducting BA fabrication with ridge sizes between 100-150 μm wide, one could go with narrow ridge (NR) fabrication, creating much smaller ridge widths, typically 10-30 μm wide. The second way is to simply use a facet coating on one side of the laser to capture more of the light generated within the device as approximately 50% of the generated light escapes from each end of the lasing cavity. On the other hand, instead of focusing on reducing the I_{th} by way of fabrication techniques, one could instead opt for epi-side-down mounting in order to bring the laser ridges directly into contact with the heat sink to improve the heat dissipation, since the generated heat within the laser active region may flow directly into the heat sink without the need to travel through the bottom optical cladding as well as the thick substrate. The primary drawback to these considerations is that they increase the complexity of the fabrication/mounting process, with potentially more room for errors. In contrast to cw operation, pulsed operation utilizing a low duty cycle is a solution which can eliminate the potential for heat buildup within the device by significantly reducing the average time the ICL is being powered.

5.4.1 Pulsed IVL Experimental Setup

Under cw operation, the power output from an ICL can be directly measured from the use of the thermopile power meter. However, under pulsed operation the duty cycle of the ICL is typically set to around 0.5% by using a pulse with of 1 μs with a repetition rate of 5 kHz. With such a low duty cycle, the average light intensity on the thermopile power meter is simply too low to register a reading. In

such a situation, an external LN cooled MCT detector sensitive in the spectral region of the laser emission can be used to collect the emission. The detector's response can then be directed into a lock-in amplifier to isolate the signal from any noise present. The lock-in amplifier relies on the orthogonality of sine waves to isolate a small signal from a noisy background. In order to extract a signal with a low signal-to-noise ratio, typically a strong reference signal is required, and since the ICL is modulated at 5 kHz, the reference signal of the power supply is used. The lock-in then multiplies the measured signal by the reference signal which serves to suppress any noise present and selects out the first order components of the Fourier wave, converting the AC signal into a DC signal. The details of the experimental setup are depicted in Fig. 5.8 and Fig. 5.9.

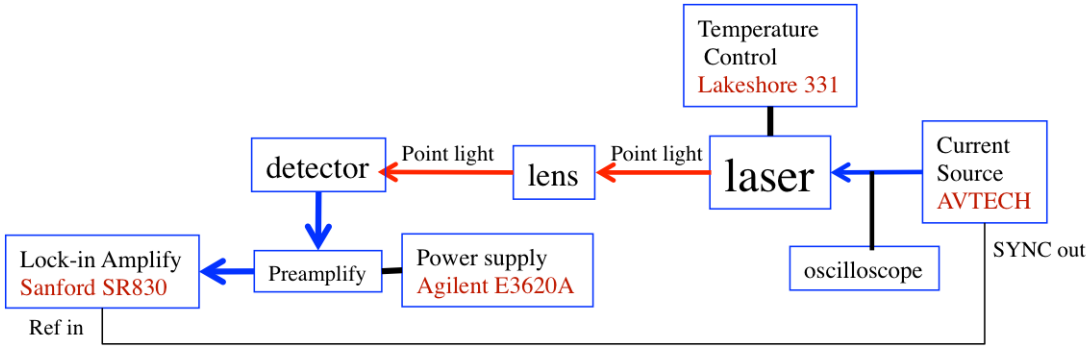

Figure 5.8: Experimental setup diagram for IVL measurements in pulsed mode.

As opposed to the spectra collection, in this setup two lenses are needed in order to guide the light into the external MCT detector. Similar to the spectra collection, the first lens collects the highly divergent beam from the ICL, converting it into parallel rays. The second lens then converges these parallel rays at its focal length which can be aligned to the small semiconductor chip inside of the MCT detector housing. The external MCT is biased at +/- 15 V and its signal is sent through a preamplifier before arriving at the lock-in amplifier. The external MCT has a much higher sensitivity than the thermopile power meter, and can easily

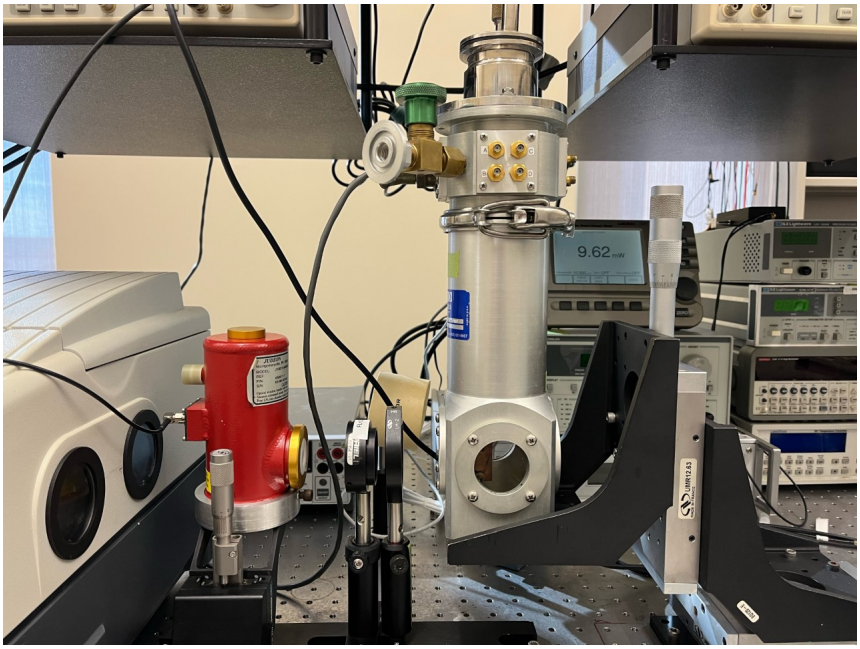

Figure 5.9: Experimental setup for IVL measurements in pulsed mode showing the alignment of the two lenses needed to guide the beam into the MCT detector.

saturate the lock-in amplifier. Experimentally, this begins to occur as the signal from the lock-in approaches 1 mV as shown in Fig. 5.10. In order to avoid such a situation, a neutral density filter (NDF) should be placed after the second lens in order to attenuate some of the light intensity before it reaches the detector. Typical filters used here include 10X, 100X, and 1000X attenuation factors.

This method provides pulsed IVL data that one can qualitatively draw conclusions from, however, one of the primary functions of the pulsed IVL result is to extract the slope efficiency, η_s, in order to determine the external quantum efficiency (EQE), η_e, at a given temperature. Since the results measured by the lock-in amplifier are in units of mV, direct extraction of the EQE from the as-is data cannot be done (recall the definition of slope efficiency from Eq. 5.8). Therefore, a calibration must be done so that the data from the lock-in can be given in units of power (mW, W, etc...).

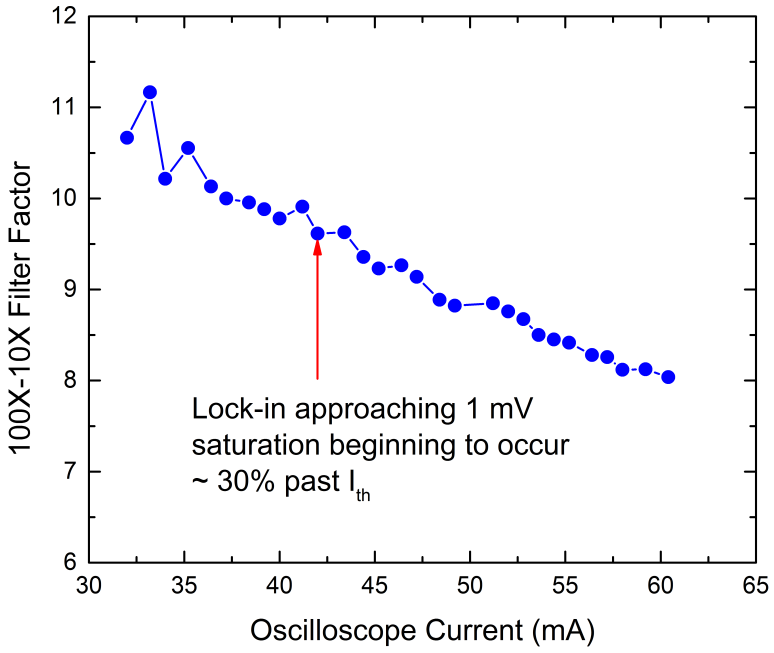

Figure 5.10: Filter attenuation factor between the 100x and 10x filters showing the 10x filter data beginning to saturate, which dramatically decreases the attenuation factor.

5.4.2 Pulsed IVL Calibration

A form to relate the signal measured by the lock-in amplifier to the peak power, P, of the laser can be determined as follows. Consider that the intended pulse shape of the signal driving the ICL, and the resulting signal being sent to the lock-in should be a square wave, though in practice the experimental pulse shape deviates from this mathematical model as will be discussed later, as depicted in Fig. 5.11[5, 133], where T is the pulse period, T_1 is the pulse width, and P is the peak signal received, in this case corresponding to the peak power of the laser. Such a periodic function can be modeled by a Fourier series as,

$$f(t) = a_o + \sum_{i=1}^{\infty} \left[a_n cos\left(\frac{2n\pi t}{T}\right) + b_n sin\left(\frac{2n\pi t}{T}\right) \right] \tag{5.10}$$

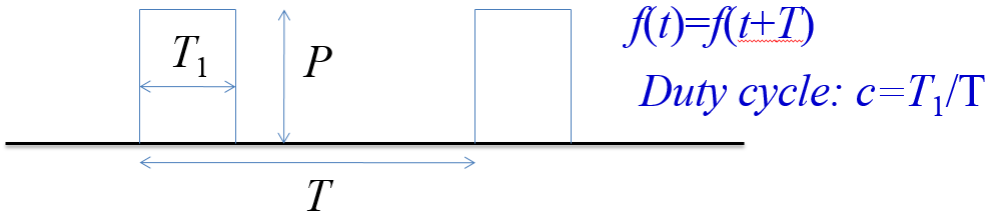

Figure 5.11: Theoretical depiction of a square pulse shape for the signal being measured by the lock-in amplifier.[5]

As previously discussed, the lock-in only extracts the first order harmonic terms of the Fourier wave. These two terms are given by,

$$\begin{aligned} a_1 &= \frac{2}{T}\int_0^{T_1} P cos\left(\frac{2\pi t}{T}\right) \mathrm{d}t = \frac{P}{\pi} sin(2\pi c) = \frac{2P}{\pi} sin(\pi c) cos(\pi c) \\ b_1 &= \frac{2}{T}\int_0^{T_1} P sin\left(\frac{2\pi t}{T}\right) \mathrm{d}t = \frac{P}{\pi}\Big(1 - cos(2\pi c)\Big) = \frac{2P}{\pi} sin^2(\pi c) \end{aligned} \tag{5.11}$$

where after integration over the period of pulsed wave, the duty cycle, c, has been used as described in Fig. 5.11. From these first harmonic components, the displayed value on the lock-in amplifier is given by,

$$R = \sqrt{a_1^2 + b_1^2} = \frac{2P}{\pi} sin(\pi c) \tag{5.12}$$

Experimentally, Eq. (5.12) may be used to determine the peak power of the laser based on the pulsed IVL measurement by collecting two different sets of data using two different duty cycles. The reason one must use another duty cycle, in addition to the typical 0.5% used to collect the IVL data, is so that the thermopile power meter can be used to calibrate the peak power result. In this case, a duty cycle of 50% is sufficient to allow enough incident light intensity on the thermopile power meter so that it can generate an accurate reading. These two sets of measurements will yield two sets of equations based on Eq. (5.12),

Table 5.1: Experimentally determined neutral density filter attenuation factors over time.

Neutral Density Filter Experimental Attenuation Factors			
Date	10x Factor	100x Factor	1000x Factor
11/24/21	10.409	106.44	641.42
3/16/22	9.885	98.66	731.88

$$\begin{aligned} R_1 &= \frac{2P_1}{\pi} sin(\pi c_1) \\ R_2 &= \frac{2P_2}{\pi} sin(\pi c_2) \end{aligned} \tag{5.13}$$

for $c_1 = 50\%$ and $c_2 = 0.5\%$ duty cycles, respectively. By taking the ratio of the results of these two measurements, and simplifying for a 50% duty cycle, the peak power value of the pulsed IVL result of interest can be obtained,

$$P_2 = \frac{P_1 R_2}{R_1 sin(\pi c_2)} \tag{5.14}$$

Typically, a NDF filter will be used after the second lens in order to attenuate the signal to avoid saturating the lock-in amplifier as described previously. In that case, Eq. (5.14) should be modified to account for this by multiplying the lock-in measured values (R_i's) by the calibrated filter attenuation factor. A simple ratio of the unfiltered with the 10x filtered data will provide the 10x attenuation factor. Similarly, with the 100x/10x and the 1000x/100x results to determine the other attenuation factors, recent calibration results are shown in Table 5.1. Also, the thermopile power meter is placed in front of the cryostat window to collect the incident light from the ICL. Therefore, the light has also been attenuated by the cryostat window used in the measurement. Depending on the intended emission wavelength of the ICL, two different windows are used: CaF_2 for shorter wavelengths and ZnSe for longer wavelengths. Their spectral transmission windows are shown in Fig. 5.12.

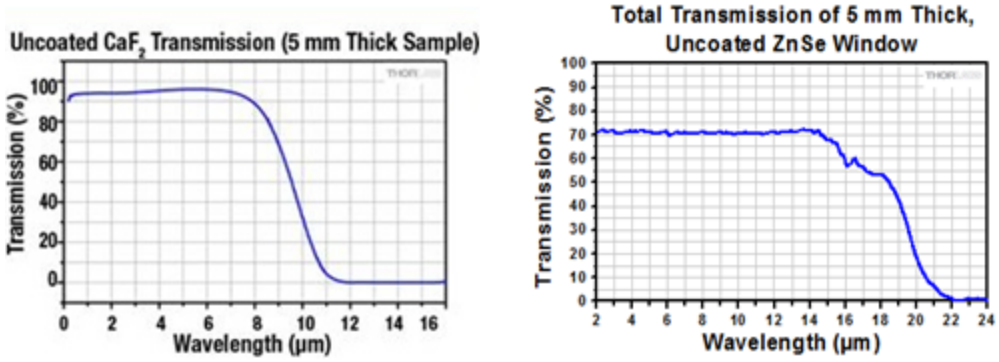

Figure 5.12: Spectral transmission for a CaF2 cryostat window (left) and a ZnSe cryostat window (right)[Data courtesy of ThorLabs].

Therefore, by taking into account these experimental details, Eq. 5.14 becomes,

$$P_2 = \frac{\frac{2P_{PM}}{\gamma} R_2 f_{2x}}{R_1 f_{1x} sin(\pi c_2)} \tag{5.15}$$

where P_{PM} is the average power as detected by the thermopile power meter and is modified by a factor of 2 in order to account for the 50% duty cycle used in the calibration, γ is the cryostat window attenuation factor, and $f_{1/2x}$ refer to the filter attenuation factors of the NDFs used in the measurement with duty cycles 1/2, respectively. Thus, after conducting NDF attenuation calibrations, as well as a small series of pulsed measurements with a 50% duty cycle to calibrate the thermopile power meter, one may finally determine the conversion factor in order to relate their lock-in reading at 0.5% duty cycle (R_2) to the peak power coming from the laser. It should be noted, however, that this result slightly underestimates the true peak power of the laser because there are losses due to beam divergence in both the thermopile power meter calibration, as well as in the collected light intensity from the external MCT during the pulsed IVL measurement.

5.4.3 Pulsed Duty Cycle Deviation

During the pulsed IVL testing of EB7289BA1-1A (see Chapter 6 for full results), it was observed that the η_s, and thus the corresponding η_e, differed at the same operating temperature (110 K) when two different sources were used. At the time, the ILX LDP-3811 source had an internal transformer malfunction and did not operate correctly under the 500 mA range limit, thus only the 200 mA range limit could be used. In order to accurately determine the EQE though, enough data past the threshold point must be collected. There was concern that the ILX source would hit the 200 mA current limit at elevated temperatures, thus a second source (the Avtech) was to be used at higher temperatures. It was observed that there was a significant decrease in the EQE at the next temperature step when using the Avtech source. To investigate this feature, the temperature was decreased back down to 110 K and the pulsed IL curve was remeasured. It was observed that there was a significant difference in the measured result when compared to the ILX source, repeatable on two different days, as shown in Fig. 5.13.

The output power of an ICL at a given temperature and its corresponding η_s and η_e values should be inherent properties of the device and should not depend on the source one uses. Therefore, this feature must be related to the source itself. Indeed, it was observed on the oscilloscope during pulsed operation of EB7289BA1-1A that the Avtech source began to turn on at around 100 mA, while the ILX abruptly turns on. For this reason, the Avtech is typically not used under 100 mA. Furthermore, it was also observed that at higher injection currents, the ILX still turned on abruptly; however, the Avtech had a slow "turn-on" as shown in Fig. 5.14. Typically, the current reading is measured at the end of the pulse, as this is the most stable portion of the pulse due to the initial overshoot. Here we see that the first time the injection current from the Avtech crosses the measurement

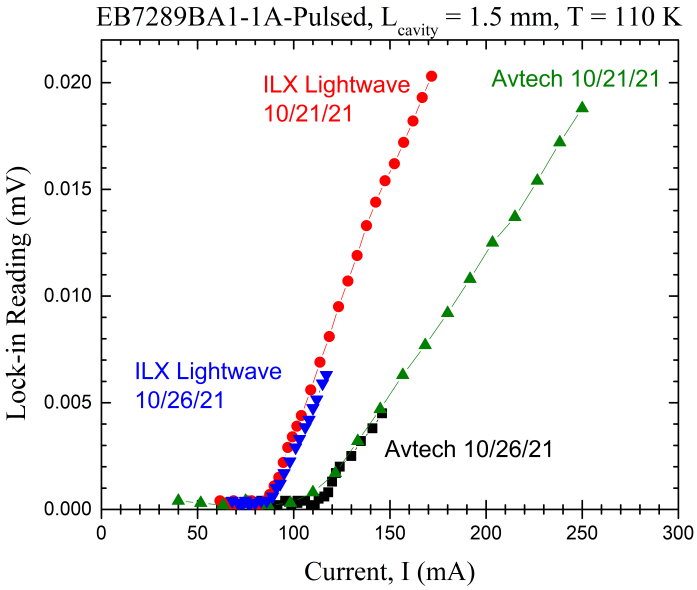

Figure 5.13: Pulsed IVL curve for EB7289BA1-1A taken with two different current sources and on two different dates.

point occurs approximately 240 ns into the 1 μs pulse, while for the ILX the pulse crosses this threshold in less than 10 ns. Because of this, the "on" time of the Avtech is about 20% lower compared to that of the ILX, effectively decreasing the duty cycle from 0.5% to 0.4%. When this factor is taken into account for the lock-in conversion, it is observed that the output power curves in Fig. 5.13 directly line up on each other, verifying the principle.

5.4.4 Direct Calculation of the Pulse Delay

During the testing of EB7523BA3-2F (full details in Chapter 6), the topic presented in Section 5.4.3 was revisited. A "true" or "effective" pulse width when using the Avtech at a given temperature, for a given device, may be inferred. Instead of trying to estimate the pulse time delay from the oscilloscope and using that to modify the conversion factor, the value of c_2 from Eq. 5.15 can be manipulated for the Avtech source to cause it to match the EQE result obtained

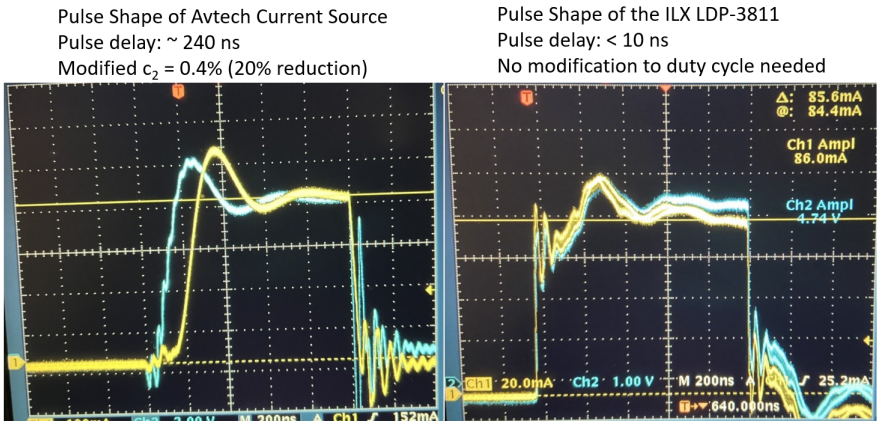

Figure 5.14: Oscilloscope comparison under the same injection current for EB7289BA1-1A using the Avtech source (left) and the ILX LDP-3811 (right), which shows a significant pulse delay or "turn-on" time for the Avtech.

under the same conditions with the ILX (which was recently repaired and calibrated from the manufacturer) using a 0.5% duty cycle(in this case, a value of 0.325% was used). In this way, we have a way to estimate the actual pulse delay as

$$\begin{aligned} Duty\ cycle(\%) &= (pulse\ width \times repetition\ rate) \times 100 \\ c_{2,ILX} &= (1\ \mu s \times 5\ kHz) \times 100 = 0.5\% \\ c_{2,Avtech} &= ([1\ \mu s - \Delta t]) \times 5\ kHz) \times 100 = 0.325\% \end{aligned} \tag{5.16}$$

From Eq. 5.16, it can be found that Δt = 350 ns, which is relatively close to the estimated delay from the oscilloscope during the testing of EB7289BA1-1A. Implementing this for the IL curve of EB7523BA3-2F is shown in Fig. 5.15, which also considers using the displayed current value from instead of the measured current value at lower current injection levels.

5.5 Summary of Device Characterization

In summary, there are multiple considerations one must make when conducting characterization of ICL devices that must be made in order to both extract and

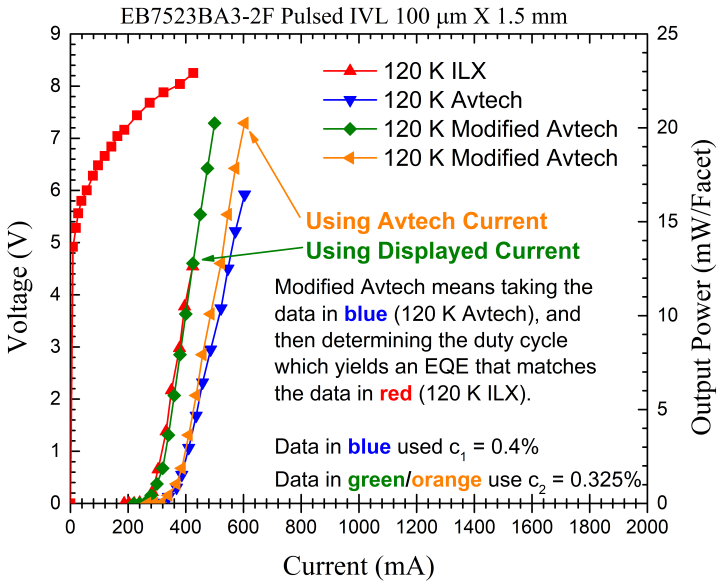

Figure 5.15: Measured IL curve under pulsed operation for EB7523BA3-2F using the Avtech and ILX current sources and different scaling methods.

comprehend the data one acquires. Analysis of the data is not limited to the above considerations, as well be discussed later. Chapter 6 will present several features of the InAs-based ICL for long-wavelength operation (> 10 μm) as well as the device characterization of multiple InAs-based ICLs. Chapter 7 will then focus on some recent advancements made in mid-wavelength GaSb-based ICLs designed to operate between 3.3-3.4 μm.

Chapter 6

InAs-based Interband Cascade Lasers

As briefly discussed in Section 1.6, the ICL is formed of two general structures, the active region, which is responsible for generating photons, and the waveguide, which is responsible for confining and guiding the laser light. The active region of the modern ICL is generally composed of a W-structure, consisting of two InAs electron quantum wells (QW), with a GaInSb hole well sandwiched in-between. Generally, AlSb barriers encapsulate the InAs layers. The InAs/GaInSb/InAs structure forms a type-II band alignment where photon generation occurs from the spatially indirect transitions of electrons from the InAs QW to the GaInSb hole well. The active region itself is then sandwiched in-between an electron injector (which also acts as a hole barrier), formed of a SL of InAs and AlSb and a hole injector (which also acts as an electron barrier), formed of a SL of AlSb and GaSb. These three structures, the W-QW active region, the electron, and the hole injectors form one cascade stage of the ICL as shown in Fig. 6.1. The ICL is operated under forward bias, where an electron is injected into the W-QW active region to generate a photon, and afterward is then quickly extracted into the next cascade stage. The interface between the electron and the hole injector forms a semimetallic interface as the conduction band edge of InAs sits just below the valence band of GaSb, which can be thought of as acting as a generation source for electrons and holes. To be clear, the carriers are injected with the injection current used operate the device, however, based on the band edge perspective this is just one method to visualize the carrier dynamics of the ICL. After an electron has recombined in the GaInSb hole well, it will cross the AlSb barrier and enter into the hole injector. The electron may then tunnel and scatter into

the conduction band of the next electron injector stage where it is recycled and injected into the next cascade stage. In this way, a single electron may create as many as N_c photons, where N_c is the number of cascade stages in the ICL, as it travels through the device, allowing for quantum efficiencies greater than 100%, circumventing the conventional limit of unity. The photon wavelength is determined by the electron and hole energy levels in the W-QW active region, which may be tailored by choosing the layer thicknesses of the InAs and GaInSb layers grown.

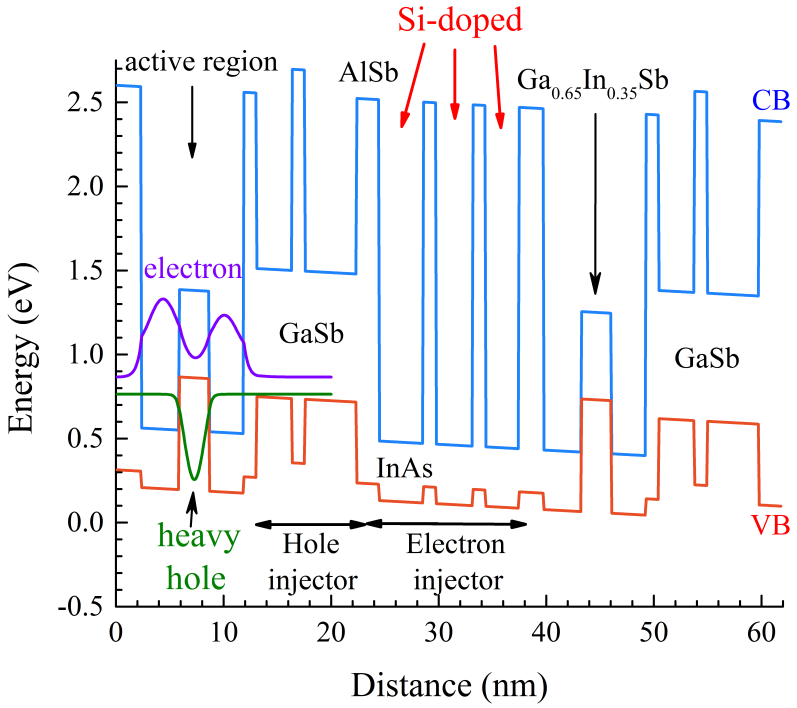

Figure 6.1: Qualitative band diagram of the modern ICL with typical features including the W-QW active region, the GaInSb hole injector, and the heavily Si-doped and also thinned electron injector.

The second major configuration of the ICL is the waveguide, which helps confine the light to the resonant cavity. There are generally two types of losses for the ICL; carrier losses related to electrons being lost in the system before they are able to traverse the cascade stages to generate photons, and optical losses where the

generated photons may scatter or be absorbed due to factors such as free-carrier absorption and inter-valence-subband transitions in the system. Optical losses occur mainly in the waveguide structure used for the ICL, and as will later be shown, this provides a design knob to turn which may be used to minimize such losses. For the GaSb-based and InAs-based ICLs, the waveguide used differs substantially, however structurally, both have a similar component sequence as shown in Fig. 6.2. In the modern GaSb-based ICL, the typical waveguide consists of a cascade region, two separate confinement layers (SCLs), formed of lightly doped (low 10^{17} cm^{-3}) GaSb, and two (top and bottom) cladding layers formed of InAs/AlSb short period SLs, previously discussed in Section 4.2. The InAs-based ICL uses a distinctly different waveguide, which will be discussed in Section 6.1. The rest of this chapter is dedicated to the InAs-based ICL for long wavelength operation. Topics to be investigated include discussion on why InAs-based ICLs may perform better than GaSb-based ICLs at longer wavelengths, the design changes that were implemented to achieve superior performance, and a series of measured results. Discussion on recent results for GaSb-based ICLs, which take advantage of the advancements made for InAs-based ICLs will be the topic of Chapter 7.

6.1 InAs-based ICLs for Long Wavelength Operation

GaSb-based ICLs have demonstrated efficient RT operation in the 3-6 μm range[17], however extending their operation to longer wavelengths (i.e., $> 10\mu$m) is challenging.[17, 134–136] This is mainly related to the growth of thick SL cladding layers and the thermal properties of GaSb-based ICL structures. The thermal management of the ICL is critical to achieving efficient RT operation. The active region of the ICL generates most of the heat in the device, and the

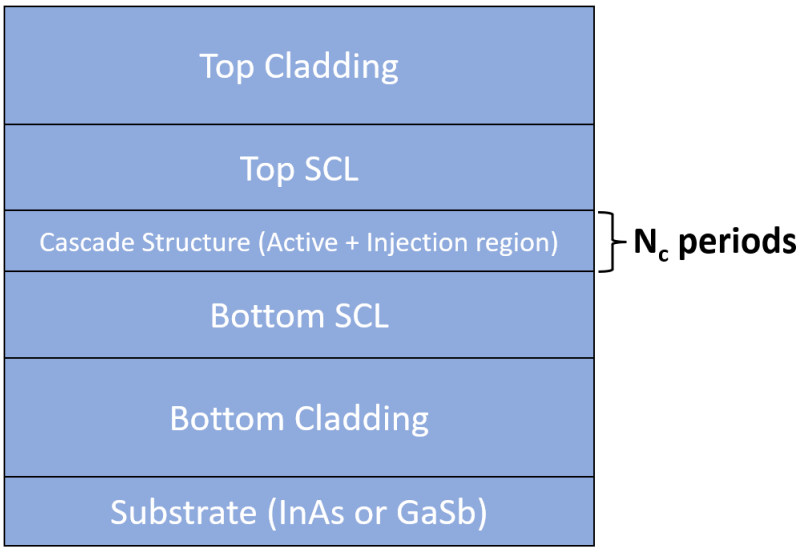

Figure 6.2: Qualitative depiction of the general layer structure for the ICL, where a different waveguide is typically used, depending on the type of ICL grown (GaSb-based or InAs-based).

heat extracted from the active region must pass through the waveguide and the substrate of the ICL to reach the heat sink. The thermal conductivity of the bulk InAs or GaSb substrate is 0.27 W/cmK and 0.32 W/cmK, respectively, while that of the InAs/AlSb SL used in GaSb-based ICLs is quite low ($\approx$ 0.03 W/cmK).[137] Thus the InAs/AlSb SL reduces the efficiency of the heat extraction. Also, as the operating wavelength of an ICL is extended to longer parts of the MIR, the optical confinement of the wave with the active region diminishes as the wave extends farther into the cladding, which affects the required threshold gain. Therefore, the optical cladding must be made thicker in order to accommodate the longer optical wave decay length in order to maintain as much overlap with the active region as possible. This would amount to increasing the thickness of the InAs/AlSb SL cladding, which also increases the complexity of the MBE growth as more shutter sequences would be required. Furthermore, because of the low thermal conductivity of the InAs/AlSb SL cladding, the overall thermal resistance of the ICL would also increase, reducing the efficiency of the heat extraction from the

device even further.

One solution to alleviate this concerns is to, instead, grow ICL structures on InAs substrates and replace the InAs/AlSb SL cladding with n^+-doped InAs plasmon-enhanced cladding in combination with undoped InAs separate confinement layers (SCLs).[84–87] This InAs-based approach[136] enabled pulsed lasing up to 55°C near 7.1l μm[89] and extended the ICL operation to 11.1 μm[88], the longest wavelength at the time among III–V interband lasers. However, the threshold current density (J_{th}) of the latter, long wavelength device, was relatively high (e.g., 95 A/cm^2 at 80 K in the continuous wave (cw) mode near 10.8 μm) and operated only up to 97 K and 130 K in cw and pulsed modes, respectively. This relatively modest device performance can be improved significantly by using an advanced waveguide configuration, which was later developed for InAs-based ICLs operating near 4.6 μm.[7] By reintroducing a thin InAs/AlSb SL as an intermediate SL cladding layer between the SCL and the plasmon cladding layer, the advanced waveguide configuration can enhance the optical confinement and simultaneously reduce the optical loss, resulting in a low J_{th}. It should be noted that the plasmon-enhanced waveguide ICLs can also be achieved on GaSb substrates with heavily doped n^+-InAsSb layers and GaSb SCLs[6, 138, 139] at the cost of more complicated carrier transport and MBE growth as will be the topic of Chapter 7.

The question of pushing ICLs to longer emission wavelengths is really a push to find out, fundamentally, if the ICL technology can support longer emission wavelengths with low threshold current densities and if so, just how far out into the MIR can the ICL design be propelled. This question is approached from two different directions. First, an advanced waveguide (Section 6.1.1) is implemented, similar to shorter wavelength InAs-based ICLs[7], for InAs-based ICLs designed to emit beyond 10 μm in order to more efficiently extract heat from the device while

also minimizing the threshold gain (g_{th}) and subsequent threshold current (I_{th}) required for lasing. The second approach (Section 6.1.2) attempts to understand how the active region may be redesigned to allow for enhanced emission at longer wavelengths in conjunction with the advanced waveguide approach.

6.1.1 Advanced Waveguide Design

The waveguide structure for an InAs-based ICL has traditionally been composed of two InAs SCLs and two n^+-doped InAs plasmon cladding layers which encompass the cascade region, the latter of which takes advantage of the plasmon-enhanced effect that was originally developed for long wavelength QCLs.[140–142] Here the high doping level in InAs reduces its refractive index significantly, reaching as low as 3, which provides a large refractive index contrast against the active region to prevent leakage of the laser light. For example, a typical GaSb-based ICL with $n_{cascade} = 3.45$ would use a waveguide composed of GaSb SCL (n = 3.73) and the InAs/AlSb SL (n = 3.35), which provides a refractive index contrast of $(n_{cascade}\text{-}n_{InAs/AlSb})/n_{cascade} \approx 2.9\%$. By replacing the SL with the n^+-doped InAs plasmon cladding (n = 3) for an InAs-based ICL with a similar cascade region design amounts to a refractive index contrast of about 13%. Also, the highly doped InAs plasmon cladding has an increased thermal conductivity compared to the InAs/AlSb SL and is far less complex to grow, which is especially useful at longer wavelengths where a thicker cladding layer is required. However, this comes at the cost of adding increased free carrier absorption loss within this section of the waveguide.

Adding back in a thin InAs/AlSb SL as an intermediate SL cladding between the n^+-InAs plasmon cladding and the undoped InAs SCL provides enhanced confinement of the optical wave within the QW active region while simultaneously

suppressing the extension of the optical wave into the n^+-InAs plasmon cladding, thus also reducing the free carrier absorption loss. To illustrate this, consider Fig. 6.3, which shows simulated plots for two short wavelength InAs-based ICLs with unoptimized waveguides. The first waveguide is composed of an undoped InAs SCL and an n^+-InAs plasmon cladding (blue), while the second (red) also utilizes the InAs/AlSb SL intermediate cladding between the SCL and plasmon cladding layers. Both waveguides have equal thicknesses for the n^+-InAs plasmon cladding of 0.7 μm in the top cladding and and 1.0 μm in the bottom cladding. In the first waveguide, the InAs SCL is thick (0.96 μm) in order to reduce the extension of the optical wave into the heavily doped plasmon cladding so that the free-carrier losses may be minimized. The consequence of this is a reduced confinement in the cascade active region. In the second waveguide, a 0.75 μm thick InAs/AlSb SL is placed on either side of the cascade region to form the advanced waveguide structure and the InAs SCL thickness is reduced to 0.21 μm, for a total thickness of these two components of 0.96 μm, which matches the SCL thickness in the first waveguide.

The estimated optical parameters from the waveguide simulation are also shown in Fig. 6.3. It should be emphasized that this is not an optimized waveguide, but merely an example to illustrate the key differences between these two waveguides. The waveguide loss (α_{wg}) is calculated based on the free-carrier loss only, which is determined according to $\alpha_i = 4\pi \mathrm{k}/\lambda$ where k is the complex portion of the refractive index (i.e., an index of the form $\tilde{n} = n + ik$). The k-value that is taken in the calculation comes from the effective refractive index determined for the entire waveguide structure, which may slightly underestimate the full contribution to the free-carrier loss, but is nonetheless a good approximation. In Fig. 6.3 it may be observed that the optical wave is squeezed more tightly within the cascade

active region in the second configuration, which results in a predicted increase in the optical confinement from 17.2% to 22.1%, a decrease in the free-carrier absorption from 10.4 cm^{-1} to 9.16 cm^{-1}, and a corresponding decrease in the required threshold gain for lasing from 83.7 cm^{-1} to 60 cm^{-1}. This effort is implemented for the first time in InAs-based ICLs designed to emit beyond 10 μm. The structure design and the corresponding performance of an initial series of ICLs is presented in Section 6.3, while a revised design and follow-up testing is reported in Sections 6.4 and 6.5, respectively.

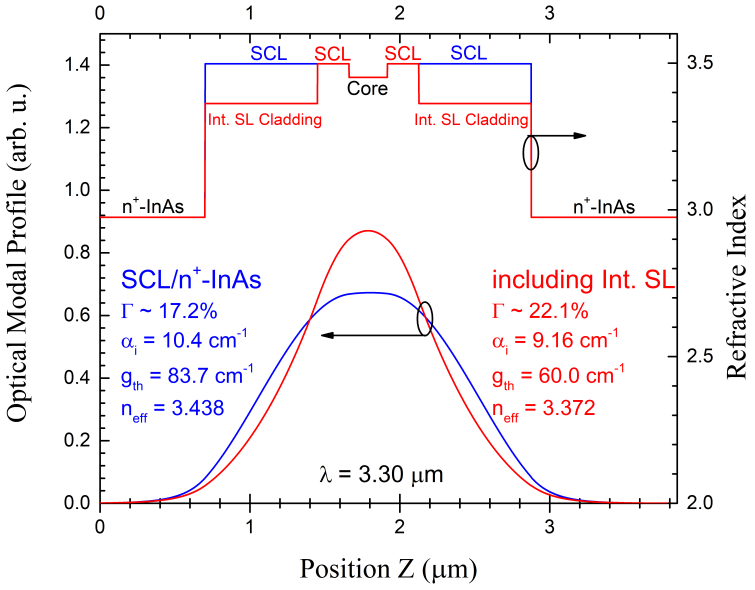

Figure 6.3: Simulated optical modal profile and refractive index for two hypothetical waveguides for InAs-based ICLs with similar layer thicknesses. The first waveguide (blue) is composed of the n^+-InAs plasmon cladding and undoped InAs SCL, while the second (red) also incorporates an intermediate SL cladding formed of a thin InAs/AlSb SL.

6.1.2 Active Region Innovation

Parallel to the work on an advanced waveguide to enhance long wavelength performance, the active region may also be redesigned based on band edge perspectives in type-II heterostructures.[8] It is well known from quantum mechanics that a

bound state in a finite potential well will move up or down depending on the height of the barrier. In the context of semiconductor heterostructures, this corresponds to the position of the conduction band edge of the barrier forming material. What is less well studied is the potential impact that the valence band edge of the barrier material may play. Within the W-QW active region, interband tunneling occurs in the type-II broken-gap region, occurring between the InAs and the GaInSb QWs. As Ref. [8] points out, in order to have resonant interband tunneling between the conduction and valence bands, there must exist a quasibound state within the broken-gap region. This is to say that there must exist a localized state with a finite lifetime that decays due to tunneling, unlike a true bound state which has an infinite lifetime. In order for this to occur, either the InAs QW or the GaInSb QW must be wider than a critical thickness, which is called the transition well width. The calculation of the transition well width presented considers a 4-layer sequence of AlSb/InAs/AlSb/GaSb, where the ΔE between the InAs/GaSb SL is approximately 0.15 eV, and AlSb acts as the barrier material. In the limit of a relatively thick barrier, the transition well width takes the form[8]

$$W_{ctd} = \frac{2W_{ct}}{\pi} tan^{-1}\left(\sqrt{\frac{(E_{c1} - E_{v4})(E_{v4} - E_{v2})}{(E_{v4} - E_{v1})(E_{v4} - E_{c2})}}\right) \tag{6.1}$$

where W_{ct} is the transition well width in the conduction band for the QW structure formed from a three layer material sequence of GaSb/InAs/GaSb, described in Ref. [143], which represents exactly the half wavelength of an electron in the QW. W_{ct} has the physical dimension of 80 Å, and $E_{i,j}$ are the conduction/valence band energies of the jth material layer.

This yields some insight into how one may choose materials to manipulate the transition well width. Here we see that layers 2 and 4 are the InAs and GaSb layers, which must remain compositionally fixed as they are responsible for the

interband tunneling and subsequent photon generation. However, layers 1 and 4 are the AlSb barrier material, which may be changed so long as the new material is still capable of acting as a barrier to form the QW. In that context, we see that the term E_{v1} falls in the denominator, which if decreased will lead to a reduction in the transition well width. Effectively what this means is that if a barrier material is chosen which has a lower valence band edge compared to another barrier material (i.e., the standard AlSb barrier), then the electronic energy level in the InAs QW will be reduced.

Now, it is well known that the InAs QW width in an ICL must be made wider in order to support long wavelength emission. However, this comes at the cost of a reduced electron-hole wavefunction overlap with the GaInSb QW, which means the recombination rate is reduced which can limit the performance. In principle then, if two structures each have the same InAs QW width, but one also has a barrier material with a lower valence band edge, that QW structure will have a reduced electronic energy level, thus generating longer wavelength photons. This means that at longer wavelengths, instead of increasing the InAs QW width, one could preserve the thinner InAs QW by changing the type of barrier material used. This then preserves a larger electron-hole wavefunction overlap, which would also enhance the emission at longer wavelengths. From Eq. 6.1, this could be achieved by using As or P containing compounds in the barrier (i.e., AlAsSb, GaInP, InAsP, AlGaPAs). For the design of some recent InAs-based ICLs, we have opted to insert $InAs_{0.5}P_{0.5}$ barrier layers around the W-QW active region, which are somewhat lattice matched to InAs, with a slightly tensile strain, to test this idea.

6.1.3 Band Edge Diagrams

In order to generate the band edge diagram for a cascade stage in an ICL, the various band offsets must be calculated, which also take strain effects into account

as described in Eq. 2.7. Many III-V band parameters for binary semiconductor materials and their related alloys have been reported in Ref. [144], and those parameters are used here. In Ref. [144], it is important to note that GaSb is taken as the reference level, and since this work focuses on the InAs-based ICL system, the valence band energy level must be set to the reference level of InAs by adjusting the valence band offset (VBO) values of all materials involved. The parameters required to model the band structure include the conduction band edge (E_c), the light hole (E_{lh}) and heavy hole (E_{lh}) band edges, and the heavy hole effective mass (m_{hh,z^*}). The conduction band edge is equal to $E_c = E_v + E_g + dE_c$, where the latter term is the conduction band edge offset, which accounts for strain induced shifts and has the form

$$dE_c = a_c(\epsilon_{xx} + \epsilon_{yy} + \epsilon_{zz}) \tag{6.2}$$

where a_c is the conduction band deformation potential corresponding to shifts of the conduction band edge with applied strain[144], the values of which for III-V materials are widely reported in the literature. The light and heavy hold band edges have the form $E_{lh/hh} = E_v + dE_{lh/hh}$, where the latter term is, again, the light and heavy hold band offsets due to strain. For cubic materials, these terms have the form

$$\begin{aligned} dE_{lh} &= a_v(\epsilon_{xx} + \epsilon_{yy} + \epsilon_{zz}) + ... \\ &\quad + \frac{1}{2}\left(\sqrt{\Delta_{so}^2 + 2\Delta_{so}(\epsilon_{zz} - \epsilon_{xx}) + 9b^2(\epsilon_{xx} - \epsilon_{zz})^2} - b(\epsilon_{xx} - \epsilon_{zz}) + \Delta_{so}\right) \\ dE_{hh} &= a_v(\epsilon_{xx} + \epsilon_{yy} + \epsilon_{zz}) + b(\epsilon_{xx} - \epsilon_{zz}) \end{aligned} \tag{6.3}$$

In Eq. 6.3, a_v is the valence band deformation potential corresponding to shifts of

the valence band edge with applied strain, Δ_{so} is the spin-orbit splitting energy which separates the light and heavy hole bands, and b is the shear deformation potential. With these parameters calculated for a given material, the band diagram may be modeled using the k · p method.[145] The band diagrams presented in the following chapters are meant to convey a qualitative depiction of the structure of the cascade stage for the InAs-based and GaSb-based ICLs, and no rigorous analysis will be used, outside of contextualizing wavefunction overlaps between the two different ICL styles, based on the QW barrier material. Additionally, the 2-band approximation is used for the simulations, when Δ_{so} is assumed to be very large, which decouples the bands into a single heavy hole band and a band for the conduction and light holes, where the light hole offset becomes $dE_{lh} = \epsilon_{xx}(a_\nu + b) + \epsilon_{yy}a_\nu + \epsilon_{zz}(a_\nu - b)$, a form that exactly matches that of the heavy hole band. For the purposes here, this greatly reduces the computational speed without jeopardizing the quality of the figure.

6.2 InAs-based ICL Design and Material Characterization

The first implementation of the concepts discussed thus far resulted in the growth (at Sandia National Laboratories), fabrication, and testing of two InAs-based ICL wafers: EB7289, which incorporated just the advanced waveguide, and EB7342, which incorporated both the advanced waveguide and the change to the QW active region barrier material. Both ICLs were designed with 20 cascades stages, many more than the state of the art GaSb-based ICLs operating at shorter wavelengths, which typically have 5-7 stages. This is done to accommodate the wider spread of the optical wave and help compensate for the reduced wavefunction overlap at longer wavelengths. Both also shared the same advanced waveguide with layer thicknesses of the intermediate SL cladding and InAs SCL layers of 1.65 and

0.83 μm, respectively, as it was unknown to what extent, if any, the influence on the emission wavelength from the modified barrier architecture. The top n^+-InAs plasmon cladding layer thickness was 1.1 μm, while the bottom was 2 μm, thicker in order to help suppress the leakage of the optical wave into the substrate. The doping level of the plasmon cladding was 3.2×10^{18} cm^{-2}, which was lowered by approximately 54% compared with Ref. [88] to reduce optical losses due to free carrier absorption. The predicted optical loss due to free carrier absorption from Ref. [88] was 14.8 cm^{-1}[133], while that predicted here for EB7289 is 9 cm^{-1}. A simulation of the optical modal profile and refractive index is shown in Fig. 6.4, in which a lasing wavelength of 10.5 μm was used in the simulation. Shown in the figure is the predicted optical confinement factor with the active region which has the form

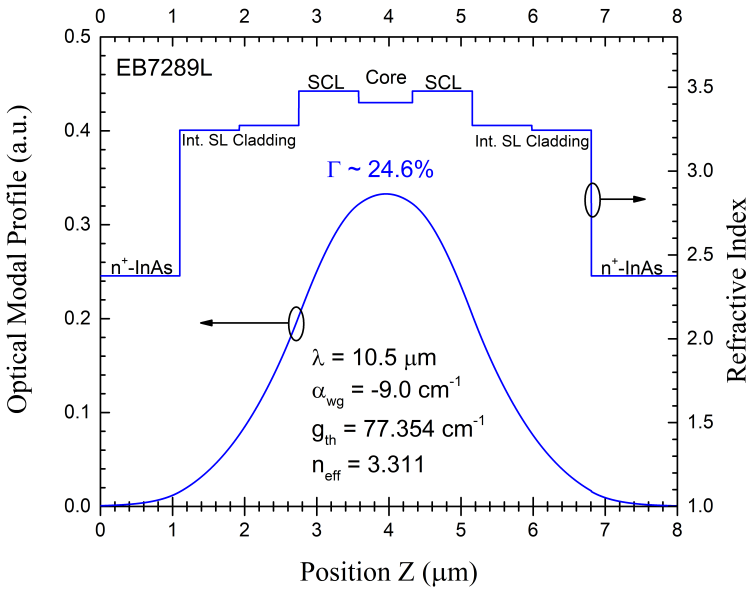

Figure 6.4: Calculated optical modal profile and refractive index of the waveguide for EB7289 at 80 K with an emission wavelength λ measured from the pulsed spectra of 10.5 μm.

$$\Gamma = \frac{\alpha_i + \alpha_m}{g_{th}} \tag{6.4}$$

Also listed are the predicted waveguide loss due to free carrier absorption (α_{wg}), the threshold gain (g_{th}), and the effective refractive index of the waveguide (n_{eff}). In each of the SL intermediate cladding layers, to reduce the free carrier absorption loss even further, there are two segments with different doping levels. The segment that is closer to the cascade region has lower doping resulting in a slightly higher real part of its refractive index.

In addition to adapting the advanced waveguide for both ICLs, the second ICL had a modified active region compared with the first in order to enhance its long wavelength operation. In the EB7289, a typical W-shape QW active region formed from $AlAs_{0.11}Sb_{0.89}$/InAs/$Ga_{0.65}In_{0.35}Sb$/InAs/$AlAs_{0.11}Sb_{0.89}$ was employed with layer thicknesses of 23/34.5/28/31.5/12 Å in the growth direction. When extending operation to longer wavelengths, a thicker InAs layer is needed, which leads to a reduced electron-hole wavefunction overlap in this type-II QW as the electrons and holes are mainly localized at different layers. This could cause the optical gain (generated from the spatially indirect interband transition in the type-II QW) to be insufficient to overcome the increased loss at a long wavelength and, thus, render the lasing unreachable as previously discussed. In order to test the idea that a QW with a lower valence band edge for the barrier material could indeed lead to a lower interband transition energy for photon emission at longer wavelengths, the second ICL wafer (EB7342) used a modified active region consisting of a $AlAs_{0.11}Sb_{0.89}$/$InAs_{0.5}P_{0.5}$/InAs/$Ga_{0.65}In_{0.35}Sb$/InAs/$InAs_{0.5}P_{0.5}$ QW grown with layer thicknesses of 19/16/26.5/28/21.5/16 Å, respectively. Here it may be seen that the InAs layer thicknesses were substantially reduced (e.g., 26.5 vs 34.5) compared to that in the first ICL wafer. The band edge diagram of one cascade

stage along with the layer sequence for the second ICL wafer is given in Fig. 6.5, which is a qualitative illustration rather than an exact description considering that there exist some uncertainties and variations in material parameters due to several factors such as interfacial compositions and strains.

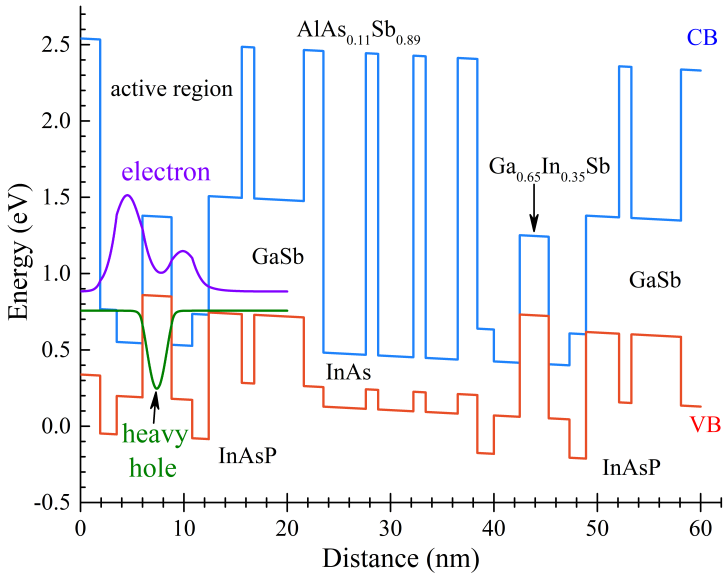

Figure 6.5: Illustrated band edge diagram of one cascade stage and the layer sequence for EB7342, which includes $InAs_{0.5}P_{0.5}$ barriers in the QW active region.

Notice in Fig. 6.5 that $AlAs_{0.11}Sb_{0.89}$ is used in the band simulation instead of the typical AlSb barrier. This is because the MBE system that the wafers were grown in presented a large background As pressure during periods of time where the As shutter was closed, resulting in a small As incorporation into some of the Sb-containing layers, which was accounted for in the design. The grown wafers were characterized with DIC and XRD to assess their material quality. The average surface defect density from the DIC imaging was 1.47×10^4 and 8.15×10^3 cm^{-2} for EB7289 and EB7342, respectively. Their XRD patterns are shown in Fig. 6.6, where good agreement is observed between the measured (blue) and simulated (red) results. The average thickness of the cascade period deviated by about +0.92% and -0.95% for EB7289 and EB7342, respectively. Both ICL wafers

showed a slight biaxial compressive strain in the intermediate SL cladding, with perpendicular mismatches of about +1.5% and +1.4%, respectively.

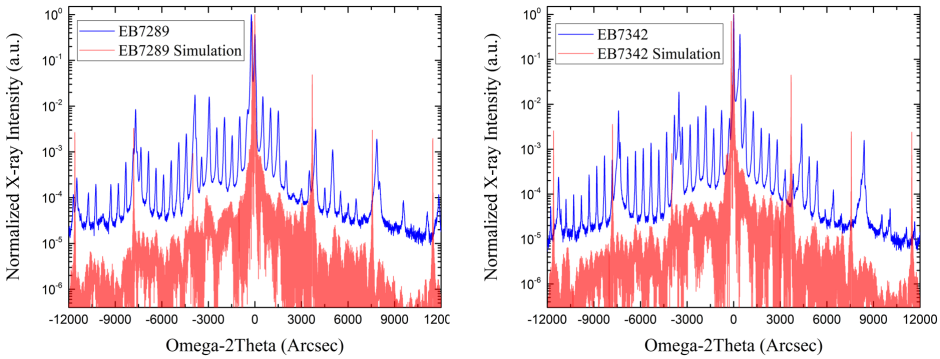

Figure 6.6: Measured (blue) and simulated (red) XRD patterns for EB7289 (left) and EB7342 (right), which demonstrates good crystalline quality.

The grown wafers were fabricated into 100-μm-wide (EB7289BA1-1A and EB7342BA1-3G) and 150-μm-wide (EB7289BA1-1E and EB7342BA1-3F and 3E) broad area (BA) mesas using wet chemical etching as shown in Fig. 6.7. The etch depth proceeded about 10% into the bottom cladding, in order to ensure isolation of the cascade stages and to account for any non-uniformity in the etch depth across the wafer. The wafers were left un-thinned and cleaved into 1.5-mm-long laser bars without facet coating, which were mounted epi-side up on copper heat sinks for testing.

The fabrication quality of the laser ridge as well as the facet were investigated with SEM prior to mounting the laser bars for testing. It was generally observed that the ridge walls had some non-uniformities in the shape of the etch, but that the overall etch depths were sufficient (also measured with a profilometer during fabrication). Several SEM images are shown in Fig. 6.8. The first image (a) was taken at 100,000× magnification and shows the deposited Ti/Au contact metal, with nominal thicknesses of 30/300 nm, respectively. The second (b) was taken at 10,000× magnification and shows the overall facet quality of a laser bar from

EB7342. Visible in the image are many of the growth structures, which have clear enough contrast so as to have their thicknesses measured with the SEM software. Also listed are the intended design thicknesses, which by comparison confirm that there was generally good agreement between design and growth. The last image (c) was taken at 50,000× magnification and shows the cascade region of EB7289, where there exists a high enough resolution that the number of individual stages may be counted.

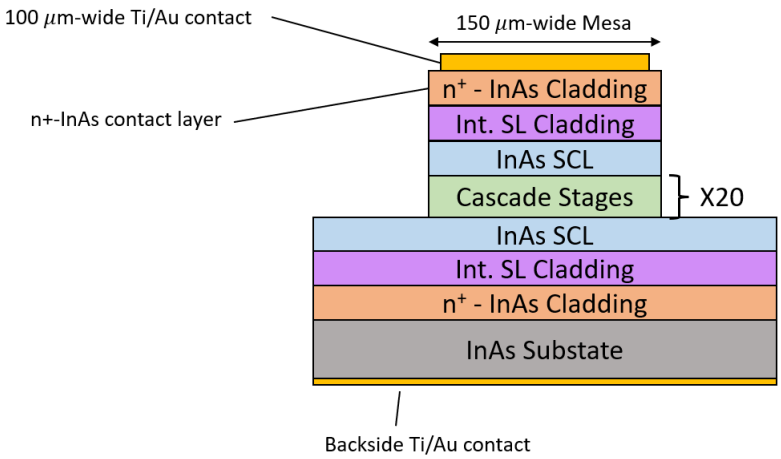

Figure 6.7: Illustration of the BA fabricated wafers for EB7289 and EB7342.

6.3 Initial InAs-based ICL Results

Multiple BA devices from both ICL wafers were able to operate in pulsed mode, however only EB7289 was also able to operate in cw mode. A discussion as to why will be presented later. Temperature dependent spectra and power measurements were performed for devices from both wafers, in accordance with characterization techniques discussed in Section 5.3. Section 6.3.1 presents measurement and performance analysis for devices from EB7289, while Section 6.3.2 presents those for devices from EB7342.

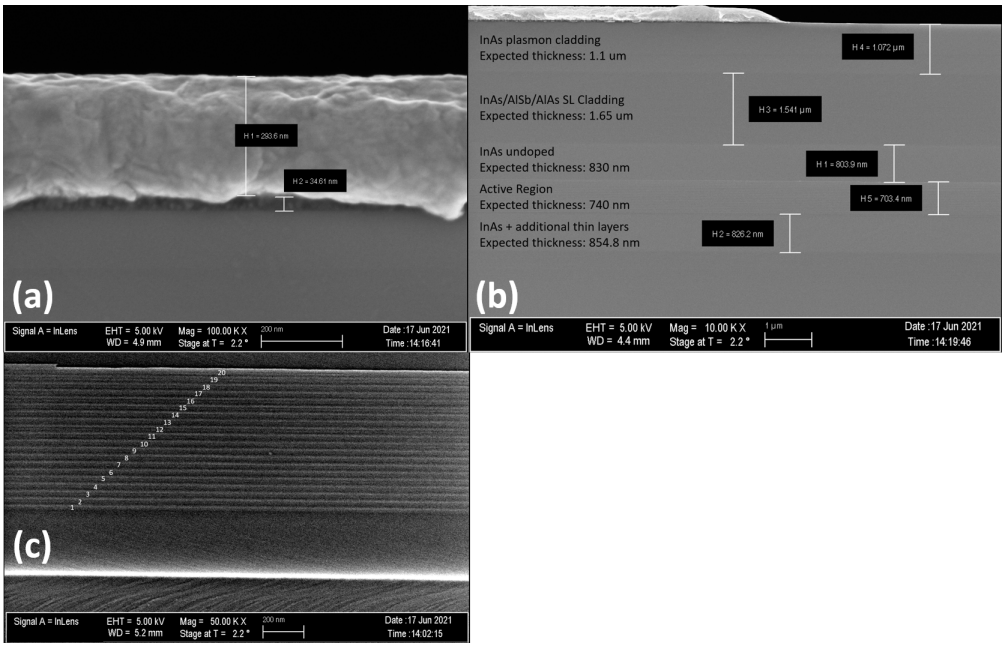

Figure 6.8: SEM images taken at (a) 100,000×, (b) 10,000×, and (c) 50,000× magnifications for several laser bars after fabrication showing various measurements performed on the IC structures with the SEM software.

6.3.1 EB7289 Results

Several BA devices from EB7289 were able to operate in cw mode above 100 K and in pulsed-mode above 130 K with lasing wavelengths near 11 μm, as shown in Fig. 6.9. In the cw mode, a representative device from the first ICL wafer, EB7289BA1-1A, lased at 10.2 μm at 80 K and operated up to 107 K at an emission wavelength of 10.65 μm as shown in the inset in Fig. 6.10. At 80 K, the J_{th} was ≈23 A/cm^2, which was a reduction of about four times compared with the previously reported 20-stage ICL with similar wavelength described in Ref. [88], but 2.3 times that of a 15-stage ICL emitting at 9 μm at 80 K.[9] The threshold voltage (V_{th}) of this device was 9.2 V at 80 K, which is significantly higher than the typical value [3.9 V (Ref. [88])] of previous 20-stage ICLs. The abnormally high V_{th} could be caused by a possible problem in the carrier transport, which is not understood at this moment. The high V_{th} and the corresponding possible issue

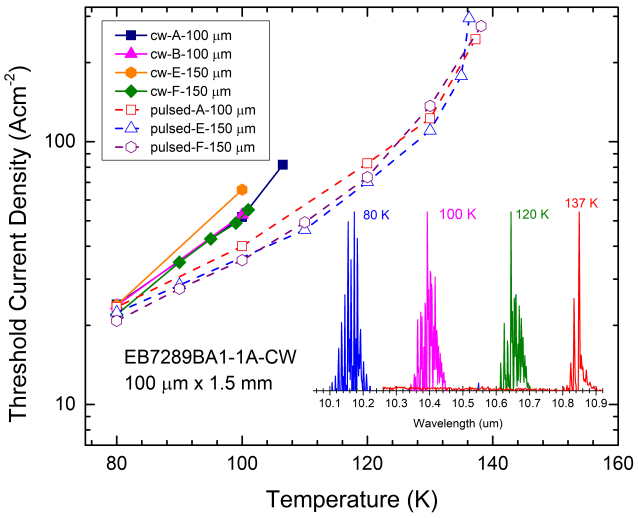

Figure 6.9: Threshold current density (J_{th}) as a function of temperature (T) for several devices made from the first ICL wafer. The inset depicts the pulsed lasing spectrum for device EB7289BA1-1A at various temperatures.

in carrier transport limited the maximum cw and pulsed operating temperatures, which is reflected by the maximum allowable threshold current density (82 A/cm^2 in a cw mode and <300 A/cm^2 in a pulsed mode) as shown in Fig. 6.9. This suggested that there was significant room for improvement for ICLs at this long wavelength.

On the other hand, the maximum cw output power for this device was 14.3 mW/facet with an injection current of 172 mA at 80 K, which is an increase of approximately four times compared with that for the ICL in Ref. [88] and comparable to that (15 mW for the 9 μm ICL at 200mA) discussed in Ref. [9]. Appreciable output power was obtained at temperatures up to 103 K as shown in Fig. 6.10. The actual output power should be somewhat higher because the measurement does not account for beam divergence loss. Several devices from wafer EB7289 exhibited similar output powers. The increase in the output power from these devices clearly indicates that the optical internal loss is reduced in the advanced waveguide configuration compared to previous ICLs with only

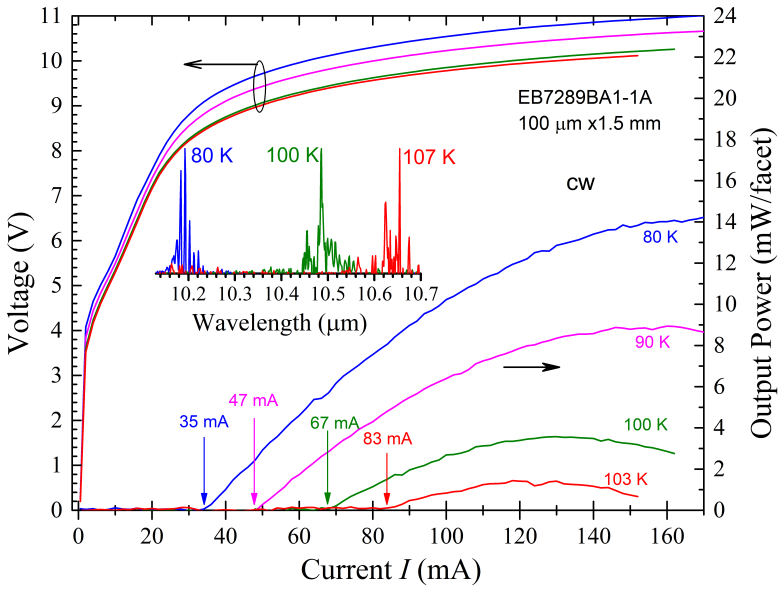

Figure 6.10: Current–voltage- and output power characteristics for EB7289BA1-1A in cw mode, where arrows indicate threshold at various temperatures. The inset shows the cw emission spectra between 80 and 107 K.

plasmon-enhanced cladding layers and InAs SCLs and serves to help confirm that the advanced waveguide structure helps to enhance the performance for long wavelength InAs-based ICLs.

Under pulsed operation, EB7289BA1-1A was able to operate up to 137 K at a wavelength of 10.85 μm, as shown in the inset in Fig. 6.9, a slightly higher temperature than that in Ref. [88], with a J_{th} of 245 A/cm^2. As shown in Fig. 6.11, the slope efficiency was nearly insensitive to temperature from 80 to 110 K. These data may be differentiated to determine the differential power and used to find the extracted external quantum efficiency (EQE), which reached ≈290% at 80 K, indicating the cascaded emission of photons in the ICL and dropped to ≈60% at 130 K. According to the optical properties and threshold current densities, this laser should be capable of operating well above 130 K. The fact that the lasing was only up to 137 K suggests possible issues beyond the optical properties, which need to be investigated in the future.

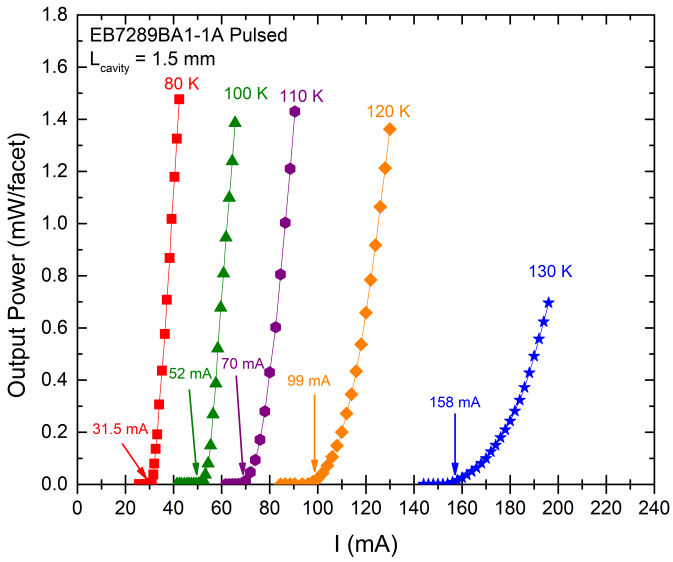

Figure 6.11: Pulsed output power as a function of the injection current at several temperatures for EB7289BA1-1A.

6.3.2 EB7342 Results

The devices from EB7342 were only able to operate in pulsed mode, with a 1 μs pulse width and 5 kHz repetition rate for a total duty cycle of 0.5%. Several devices operated at temperatures up to 120 K at wavelengths beyond 13 μm as shown in Fig. 6.12 (and the inset in Fig. 6.13), which is the longest ever reported among III-V interband lasers. This verified the theoretical prediction[8] that P-containing barrier layers could lower the electronic energy level in a QW with reduced InAs layer thicknesses.

A representative device from the second ICL wafer, EB7342BA1-3G, lased at a wavelength of 12.7 μm in pulsed mode at 80 K, albeit with a large J_{th} of 179 A/cm^2. The maximum operating temperature for this device was 115 K at a lasing wavelength of 13.23 μm, which represents a new record for long wavelength operation among III-V interband lasers. Also, three more devices from this wafer

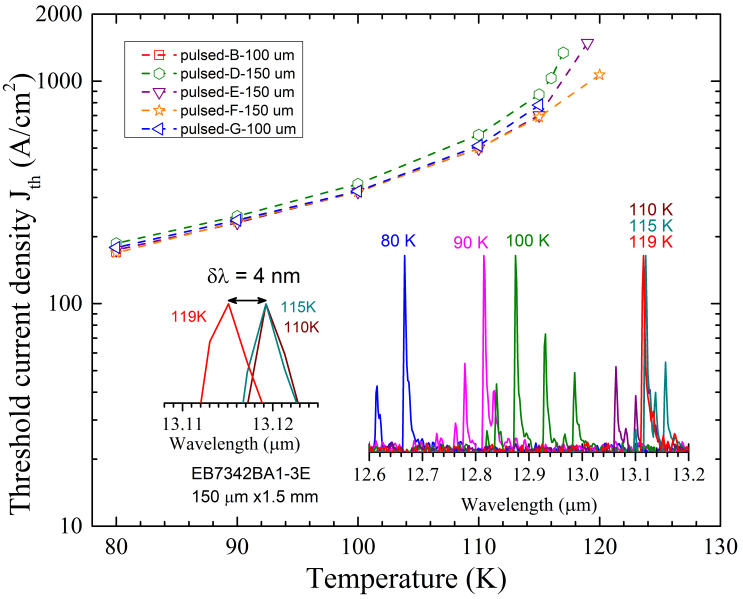

Figure 6.12: J_{th} as a function of T for several devices from the EB7342. The right inset shows the pulsed lasing spectrum for EB7342BA1-3E, while the left inset shows a zoomed in view depicting the blue shift of 4 nm with increasing T near the maximum operating temperature.

(EB7342BA1-3E, 3D, and 3F) were able to lase at slightly higher temperatures of 119, 117, and 120 K, respectively. However, the lasing wavelength for device 3E at 119 K was shorter at 13.11 μm (similarly for device 3D). This is due to the band filling effect, as shown in the insets in Fig. 6.12 (for device 3E), which can occur in mid-IR lasers and placed an upper wavelength limit of 9.5 μm for optically pumped Sb-based type-II QW lasers.[146] The effect occurs because as lasing emission is pushed toward longer wavelengths with increasing temperature, the waveguide loss rapidly increases and there also tends to be a reduced modal overlap with the gain medium. Taken together, these effects cause an increase in the threshold current density and thus the number of carriers at higher energy states, which shifts the peak optical gain to a higher energy, resulting in the blue shift of the lasing wavelength rather than a red shift with narrowing bandgap when temperature is increased. This blue shift effect is also a limiting factor for

longer wavelength operation, because one cannot simply increase the optical gain to reach the threshold with high current injection. The observed blue shift for device EB7342BA1-3E from 115 to 119 K is approximately 4 nm, as indicated in the inset of Fig. 6.12.

Compared with devices from EB7289, those from EB7342 consistently lased with significantly higher threshold current densities and only in pulsed-mode operation, though they have the same waveguide structure with an identical doping profile. The threshold voltage for devices made from EB7342 was ≈7.5 V at 80 K and increased at higher temperatures due to the rapid increase in the threshold current as shown in Fig. 6.13, which is also higher than what is typically expected and implies similar issues as in devices from wafer EB7289. Nevertheless, devices from EB7342 sustain lasing at higher threshold current densities (>1000 A/cm^2) as shown in Fig. 6.12. This suggests that possible issues related to carrier transport might be less severe in EB7342, which is also reflected by a lower voltage (≈6 V) at 75 mA as shown in Fig. 6.13 compared to that (>9 V in Fig. 6.11) in devices made from EB7289. Considering that the transparency carrier density is usually low at low temperatures[147] and devices from EB7342 lased at substantially longer wavelengths with a modified active QW region, the higher threshold current density may be mainly related to high optical internal loss due to more free-carrier absorption and other mechanisms such as intersubband transitions in QWs. To examine this, the peak output power as a function of the injection current (I) for device EB7342BA1-3F was measured and shown in Fig. 6.13. The extracted EQE was 41% at 80 K, 18% at 100 K, 12% at 110 K, 5.3% at 115 K, and 0.67% at 120 K, which are much lower than that obtained from device EB7289BA1-1A. This suggests that high internal absorption loss is a major cause for the higher threshold current density in devices made from wafer EB7342.

Nevertheless, the innovative QW active region, with $InAs_{0.5}P_{0.5}$ barriers, pro-

duced sufficient gain at moderate threshold current density to overcome the increased absorption loss at such a long wavelength. Although this innovative QW architecture is in its infancy with some unexplored aspects, it was able to open up a promising approach to further improve the ICL device performance in the long wavelength region.[148] Section 6.4 presets updated, and recently published[149], results on a new set of InAs-based ICLs with modifications to the waveguide and QW active region based on the results in Ref. [148], presented above.

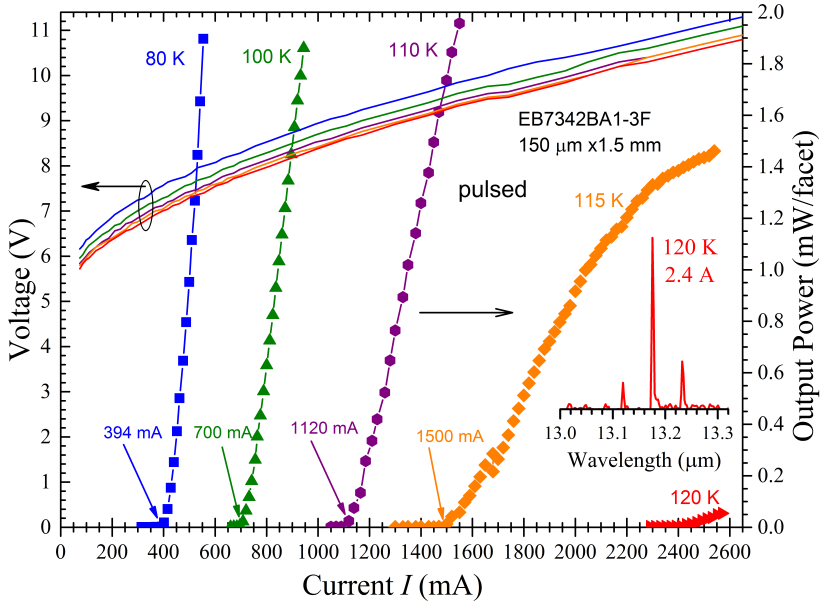

Figure 6.13: Pulsed current–voltage- and output power characteristics at several temperatures for EB7342BA1-3F. The inset is its lasing spectrum at 120 K.

6.4 Revised InAs-based ICL Design

In the previous work[148], there were some uncertainties in the expected operating wavelength for InAs-based ICLs that incorporated the advanced waveguide and those that utilized the modified QW active region, leading to unoptimized design choices which chiefly manifested in high internal absorption losses, leading to relatively large J_{th}'s, low EQEs, low output powers, and limited temperature

performance. Therefore, several adjustments to the waveguide were made to reduce the internal loss and to better confine the optical wave within the QW active region. Additionally, the parameter space of the $InAs_{0.5}P_{0.5}$ barrier thickness and how this can affect the ICL performance was further explored.

Since the expected emission for these ICLs was to be beyond 11 μm at higher operating temperatures, the waveguide layer thicknesses were slightly increased for better confinement. Compared to the previous design[148], the thicknesses of the individual components were increased by about 18%, 5%, and 7% for the InAs SCL, InAs/AlSb SL intermediate cladding, and the n^+-InAs plasmon cladding layers, respectively. To further reduce losses due to free carrier absorption in the n^+-InAs plasmon cladding, the doping concentration there was reduced by about 13%. Also, the doping in the injection region was reduced by about 31% to try to improve the carrier transport and reduce the required V_{th} for lasing. The calculated optical modal profile and refractive index based on a slab waveguide model for a representative device (EB7541) with the standard W-QW active region are shown in Fig. 6.14. As before, in each of the SL intermediate cladding layers, to reduce the free-carrier absorption loss, there are two segments with different doping levels. The segment that is closer to the cascade region has lower doping resulting in a slightly higher real part of its refractive index. Depicted in Fig. 6.14 are the waveguide loss (α_{wg}), estimated threshold gain (G_{th}), the effective refractive index of the entire waveguide (n_{eff}), and the optical confinement factor (Γ). In the simulation, the internal loss (waveguide loss) is calculated based on the overlap of the optical wave with the plasmon cladding, corresponding to just free carrier absorption, which gives a lower bound (LB) estimate to the overall internal loss within the device. The emission wavelength λ of each device was measured at 80 K in pulsed mode operation, which prevented potential redshifts that could be caused by local heating, and used in the waveguide simulations. The various

optical parameters based on the waveguide simulations of the other devices in this study are listed in Fig. 6.15.

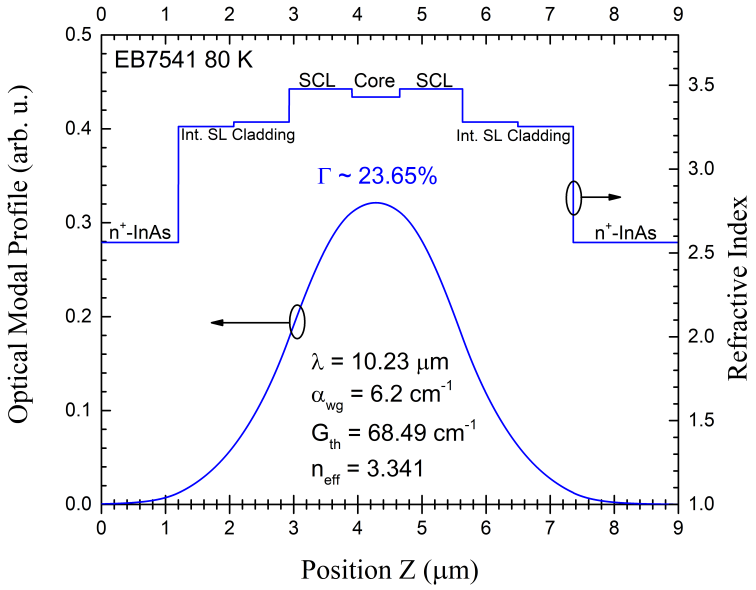

Figure 6.14: Calculated optical modal profile and refractive index of the waveguide for EB7541 at 80 K with an emission wavelength λ measured from the pulsed spectra of 10.2 μm. Also shown are estimated optical parameters of the waveguide based on the simulation results.

Device name	InAsP barriers-InAs QW thickness (Å)	80 K λ (μm)	Γ (%)	α_{wg} (cm^{-1})	G_{th} (cm^{-1})	n_{eff}
EB7541	No-35/31	10.2	23.65	6.2	68.49	3.341
EB7547	No-36.5/31.5	10.9	23.33	7.3	74.15	3.324
EB7523	Yes-25/20	11.8	22.61	8.7	82.69	3.300
EB7539	Yes-26/20	12.1	22.39	9.3	86.19	3.292

Figure 6.15: Calculated optical parameters of the four 20-stage InAs-based ICLs in this study, with the 80 K emission wavelength λ measured from the pulsed spectra.

For a comparative study, four ICL wafers (EB7541, EB7547, EB7523 and EB7539) were grown by MBE (at Sandia National Laboratories) on InAs substrates, all of which incorporated the advanced waveguide with the changes mentioned above. Two of the ICL wafers (EB7523 and EB7539) also included the

$InA_{0.5}P_{0.5}$ barriers in the QW active region. For EB7541 (EB7547), a regular W-QW structure[56, 150, 151] was used, consisting of a layer sequence of $AlAs_{0.89}Sb_{0.11}$/InAs/$Ga_{0.65}In_{0.35}Sb$/InAs/$AlAs_{0.89}Sb_{0.11}$, with thicknesses of 22/35 (36.5)/28/31 (31.5)/12 Å. For EB7523 (EB7539), the active region had a layer sequence of $AlAs_{0.89}Sb_{0.11}$/$InA_{0.5}P_{0.5}$/InAs/$Ga_{0.65}In_{0.35}Sb$/InAs/$InA_{0.5}P_{0.5}$, with thicknesses of 19/16/25 (26)/28/20/16 Å in the growth direction. Here the InAs layer thicknesses in the latter wafers were reduced by about 30% in the first InAs QW and about 35% in the second InAs QW compared to the devices which did not include $InA_{0.5}P_{0.5}$ barriers. Based on a two-band k·p model[152, 153], the estimated wavefunction overlaps for EB7541 and EB7547 were 16.7% and 15.6%, respectively. The inclusion of the $InA_{0.5}P_{0.5}$ barriers in the QW active region in EB7523 and EB7539 increased the estimated overlap to 19% and 18.2%, respectively, in accordance with the expected behavior when the InAs QW width is decreased.

6.4.1 Growth Characterization of Recent InAs-based ICLs

The ICL wafers were grown by molecular beam epitaxy at Sandia National Laboratories using solid sources except for P, which was supplied by a cracking phosphine injector. All layers were grown at 440°C. Growth rates were approximately 1.0 μmh^{-1} for InAs and InAsP and 0.49 μmh^{-1} for AlAsSb, GaInSb, and GaSb. The cladding layers were nominally InAs/AlSb SLs, but since the As source valve was left open during the cladding AlSb layer growth and the As source shutter does not fully block the As flux, layers nominally grown as AlSb contained substantial As, which was accounted for in separate lattice matching calibration growths. The As source valve was closed during critical portions of the active region growth.

The material quality was analyzed using x-ray diffraction (XRD), and the surface morphology was characterized by differential interference contrast microscopy (DIC). The XRD patterns were measured using a Panalytical X'Pert3 MRD. Symmetric scans along the (004) axis were obtained and show reasonable agreement with the simulated pattern, as detailed for a representative ICL wafer in Fig. 6.16. From the XRD patterns, the InAs/AlSb SLs of all four ICL wafers show a slight compressive strain in the growth direction (biaxial tensile strain), with a substrate/SL zero-order peak separation ranging between 14 and 50 arcsec, corresponding to a lattice mismatch of 0.12%–0.17%. The InAs/AlSb SL thickness across each of the four ICL wafers range from 0.12% thinner to 0.5% thicker, compared to the intended design. The cascade region was consistently thinner among all four wafers, ranging from 0.5% to 1.3%, compared with the design.

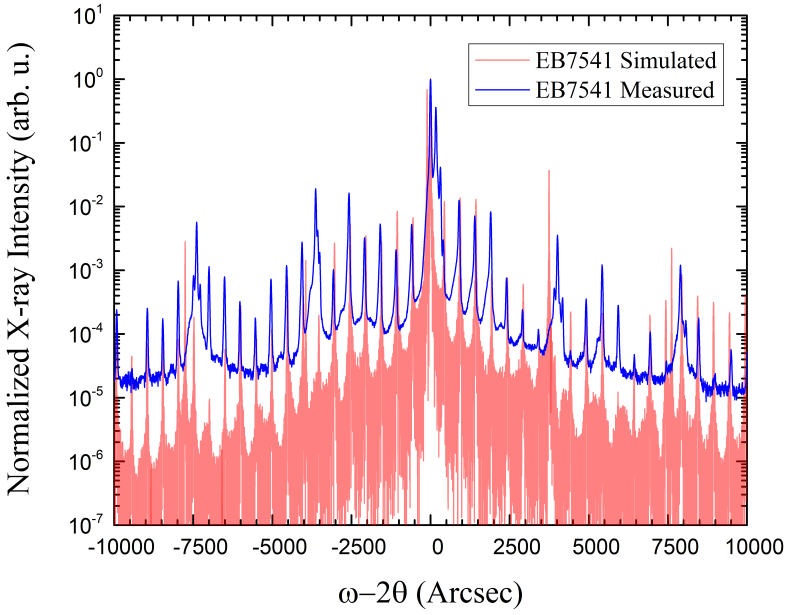

Figure 6.16: Measured XRD pattern (blue, top) compared to the simulated pattern (red, bottom) for ICL wafer EB7541.

From surface images on the four wafers, typical oval hillock defects were

observed—common to III–V ICL growth, but with little background surface roughness. The surface defect density was measured at four different locations on each of the wafers grown. The average defect density across all wafers ranged from 1.2 to 9.2 $\times$ 10^4 cm^{-2}, which are within acceptable limits for reasonable device performance.

As before, the grown wafers were fabricated into 100 μm-wide (e.g., EB7523BA3-2F, EB7539BA2-2D, EB7541BA3-3H, and EB7547BA3-2A) and 150 μm wide (e.g., EB7541BA3-1G, EB7547BA3-3C, EB7539BA2-2A) broad area (BA) mesas using standard UV contact photolithography and wet chemical etching. The wafers were left unthinned and cleaved into approximately 1.5 mm long laser bars without facet coating, which were mounted epi-side up on copper heat sinks for testing.

6.5 Recent InAs-based ICL Device Results

As before, the fabricated devices were tested using the Nicolet Fourier transform infrared spectrometer, with continuous wave (cw) power measurements carried out with a PM3 Coherent Power-Max thermopile power meter, in which the beam divergence loss was not included. Hence, the reported output power and EQE of the devices are conservative. Multiple devices from each of the four ICL wafers operated in both cw and pulsed modes, as shown in Fig. 6.17. All characteristics presented in this section are from representative devices among the many tested. Of the four ICL wafers grown, EB7541 and EB7547 are most directly related for comparison purposes as they include only the advanced waveguide. EB7523 and EB7539 include both the advanced waveguide as well as the modified QW active region. ICLs made from them have significantly longer emission wavelengths than those of EB7541 and EB7547, and consequently their threshold current densities are larger as reflected in Fig. 6.17. Detailed characteristics of their device performance

will be presented in Sections 6.5.1 and 6.5.3, respectively. A summary and outlook for long wavelength InAs-based ICLs will be discussed afterwards.

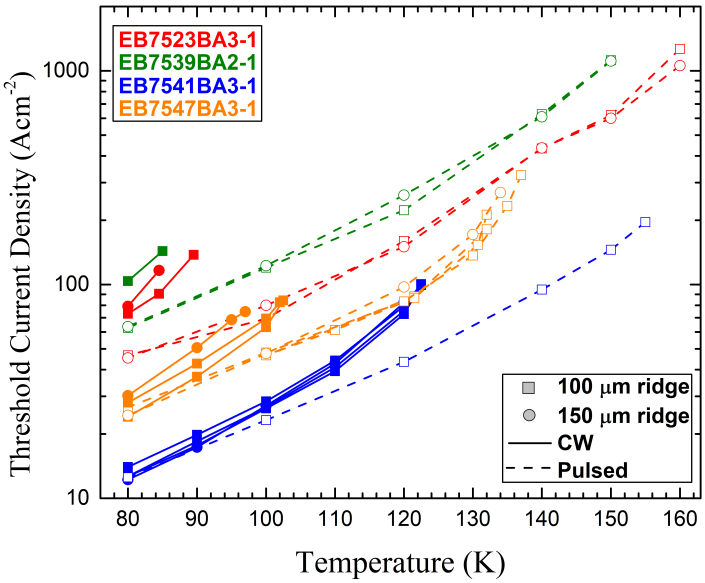

Figure 6.17: Threshold current density (Jth) as a function of temperature for several devices made from the four InAs ICL wafers.

6.5.1 EB7541 and EB7547 Results

Wafers EB7541 and EB7547 both included the advanced waveguide but did not include $InA_{0.5}P_{0.5}$ barriers in the QW active region. In cw mode, two devices from EB7541 had threshold current densities as low as 12 A cm^{-2} at 80 K, representing about a 50% reduction compared to the previous ICLs which were discussed in the previous section, and which operated at similar wavelengths.[148] These ICLs lased at 10.2 μm at 80 K and then red-shifted to longer wavelengths at high temperatures. The characteristics of a representative device, EB7541BA3-3H, are shown in Fig. 6.18. This device operated in cw mode up to 123 K, about 17 K higher than EB7289LBA1-1A, with an emission wavelength of 10.9 μm and a J_{th}

of about 101 A cm^{-2}. This device exhibited a significant increase in the measured cw output power at 80 K, just over 56 mW/facet, about four times as much as EB7289LBA1-1A[148], as shown in Fig. 6.18a. This device had a cw output power of 43 mW/facet at 200 mA, which was more than twice that (15 mW/facet) from an early ICL at the shorter lasing wavelength of 9.1 μm at 80 K and at the same current.[9] Compared to previous devices (V_{th} 9.2 V at 80 K) reported in Ref. [148], the cw threshold voltage was reduced by a factor of 2 (V_{th} 4.6 V at 80 K), resulting in a voltage efficiency (Eq. 5.7) of about 53%. However, this is still substantially less than the voltage efficiency of about 80% observed in early ICLs, which had smooth carrier transport[9, 88, 136], suggesting room for further improvement.

The extracted EQE under cw operation reached about 592% at 80 K, indicating the cascaded emission of photons in the ICL, and dropped to about 78% at 123 K as shown in Fig. 6.18a. Under pulsed operation, this device lased up to 155 K near 11.2 μm (Fig. 6.19) with a J_{th} of 196 A cm^{-2}, where the voltage efficiency dropped to 49% with a V_{th} of 4.52 V. The extracted EQE under pulsed operation reached 640% at 80 K, subsequently dropping to 137% at 150 K, as shown in Fig. 6.19. The difference in the EQE at 80 K between cw and pulsed modes is attributed to heating in the active region of the device. The heating effect increased with the higher threshold current when the heat-sink temperature was raised, which was reflected by the greater rate of decrease of the EQE in cw operation compared to that in pulsed operation, as shown in Figs. 6.18 and 6.19. This heating effect may be estimated based on the following discussion.

Since the cw operation experiences some heating compared to the pulsed operation, the EQE values that are directly measured will have been reduced by a factor compared to the pulsed case. This factor can be determined and

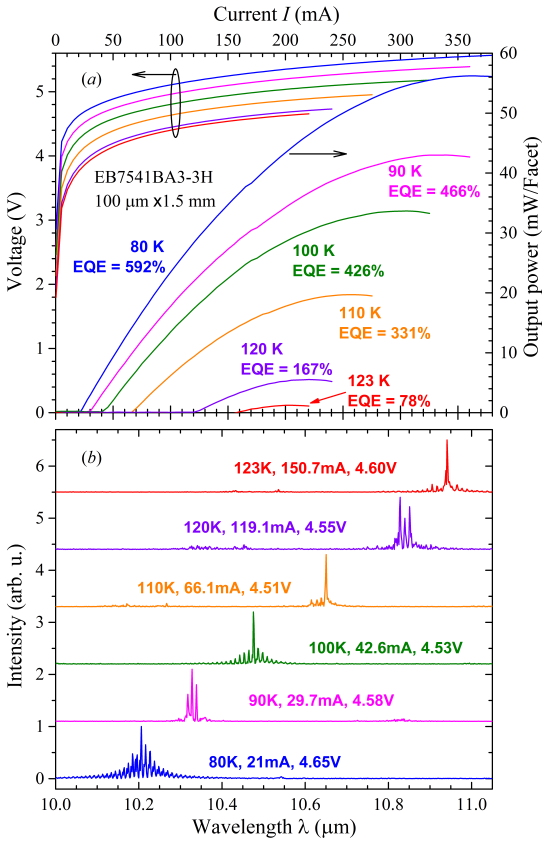

Figure 6.18: CW results for the current-voltage-power (IVL) characteristics (a) for EB7541BA3-3H along with the cw emission spectrum (b) between 80 K and 123 K.

used to modify the cw EQE result to account for reductions due to heating and then compared to the pulsed case. The maximum cw I_{th} when heating effects are considered is given by[131]

$$I_{th,max} = \frac{T_o}{R_{th}V_{th}} \tag{6.5}$$

where T_o is the characteristic temperature, R_{th} is the thermal resistance, and V_{th} is the threshold voltage at the maximum threshold current value. At the cw operating limit, the output power of the ICL should drop to 0, and at the cw minimum operating limit the output power should be at a maximum. Therefore, a factor to modify the slope efficiency (and hence the EQE) should make use of the

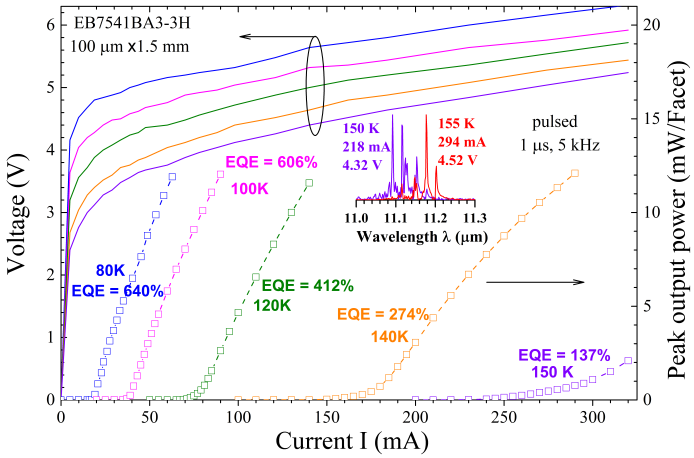

Figure 6.19: Pulsed current–voltage–power (IVL) characteristics for EB7541BA3-3H with the lasing spectrum (inset) at 150 K and 155 K.

above equation and vary between 0 and 1, which is given as

$$F = 1 - \frac{I_{th} R_{th} V_{th}}{T_o} \tag{6.6}$$

Experimentally, there are two ways to calculate these F values at different temperature increments. On the one hand, the thermal resistance is related to the temperature difference between cw and pulsed data at equivalent threshold currents. And so, the numerator could simply be replaced by the ΔT values from the J_{th} vs T plot for the various devices of interest.

However, another method could be to use the operating wavelength as the temperature comparison standard, since it does not involve the geometry of the laser ridge. However, this approximation is not as good as the former. Regardless, the procedure then is to divide the cw EQE by the calculated F factor at a given temperature and then compare it to the extracted pulsed EQE values to observe agreement. This allows one to estimate the EQE value under cw operation when a device is at elevated temperatures to check for consistency. For example, the pulsed EQE at 100 K was 606%, as shown in Fig. 6.19. Calculating the F factor

and applying it to the cw EQE at 100 K, yields a value of 609%, in good agreement with the pulsed case.

Compared to ICLs from EB7541, devices from wafer EB7547 lased at longer wavelengths as expected due to the slightly wider InAs QWs, and they had higher J_{th}, and somewhat degraded temperature performance as shown in Fig. 6.17. In cw mode, a representative device, EB7547BA3-2A, lased at 10.9 μm at 80 K, with a J_{th} of 26.7 A cm^{-2} and a V_{th} of 4.9 V. This ICL delivered an output power of 32 mW/facet as shown in Fig. 6.20, higher than any interband laser has achieved at such a long wavelength. EB7547BA3-2A lased up to 102 K in cw mode at 11.3 μm with an EQE of 189% (fig. 6.20), still exceeding the conventional limit of unity and indicating the potential for higher temperature operation. This device lased up to 137 K in pulsed mode at a J_{th} of 325 A cm^{-2} and with a lasing wavelength of 11.5 μm as shown in Fig. 6.21, which is the longest among ICLs with the regular W-QWs based on the AlSb barrier material. The extracted EQE in pulsed mode at 80 K for this device was 552%, which is comparable to that of EB7541BA3-3H.

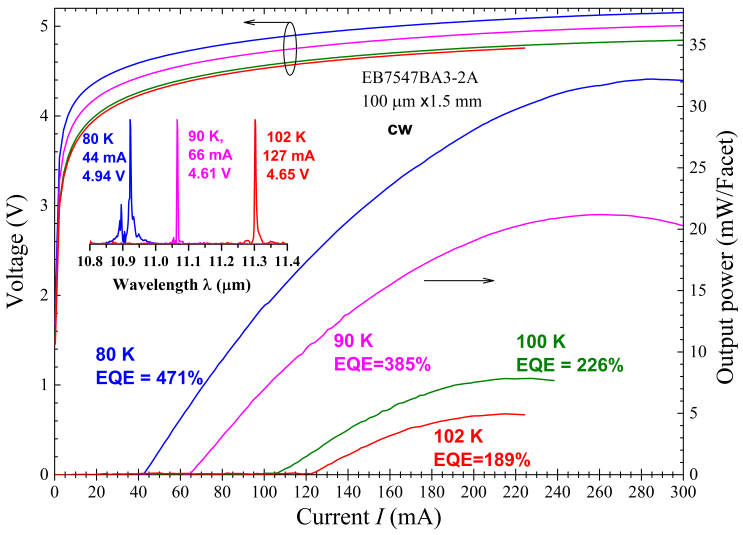

Figure 6.20: Current–voltage–power (IVL) characteristics for EB7547BA3-2A in cw mode. The inset shows the cw lasing spectrum between 80 K and 102 K.

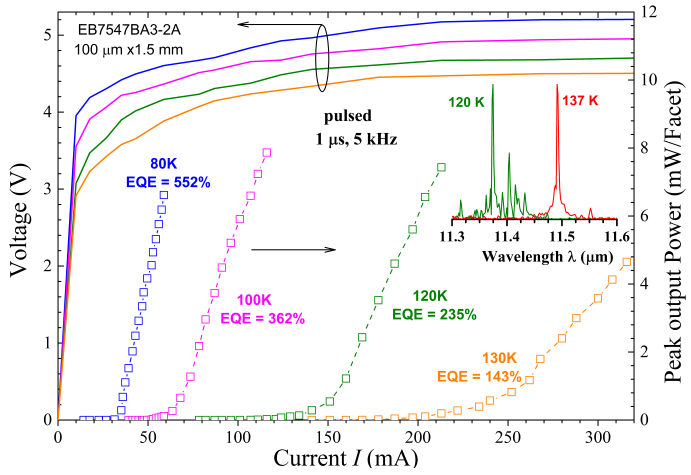

Figure 6.21: Pulsed current–voltage–power (IVL) characteristics for EB7547BA3-2A with the lasing spectrum (inset) at 120 K and 137 K.

6.5.2 EB7541 and EB7547 Summary

Considering both wafers had the same waveguide, doping concentrations, and nearly identical active region designs, the small difference in the InAs QW width only resulted in an approximately 6.9% shift of lasing wavelength at 80 K. Hence, a similar band structure, differential gain and transparency current density would be expected for both. Consequently, they should have comparable threshold current density. This is also due to the fact that the free-carrier absorption loss difference between them is less than 20% based on the simulation shown in Fig. 6.15, which is supported by the comparable EQEs observed for them at 80 K, as shown in Figs. 6.19 and 6.21.

However, the J_{th} at 80 K in devices from EB7547 are about twice that compared to devices from EB7541, very different from the above perspectives and the observed insensitivity of the J_{th} at low temperatures (e.g. 80 K) on the lasing wavelength for early ICLs.[87, 154] This suggests that extra factors beyond free carrier loss played a role in determining the J_{th} for devices from EB7547, which will be a subject of our future research. In addition to the higher J_{th}, another issue in EB7547BA3-2A

is that the EQE decreased relatively fast with the increase of temperature as shown in Fig. 6.21. Nevertheless, despite the higher J_{th}, its maximum operating temperature was only 18 K lower in pulsed mode than that of EB7541BA3-3H, since it could lase with a higher J_{th} than EB7541BA3-3H (325 A cm^{-2} vs 196 A cm^{-2}). Compared to the previous ICL in Ref. [148], though improvements have been made, the maximum allowable J_{th} in devices from both wafers is still relatively small in contrast to other ICLs. This limited their maximum operating temperature in cw and pulsed modes.

6.5.3 EB7523 and EB7539 Results

Wafers EB7523 and EB7539 both included the advanced waveguide as well as the $InA_{0.5}P_{0.5}$ barriers in the QW active region. Multiple devices from both wafers lased in both cw and pulsed modes. A representative device from the first ICL wafer, EB7523BA3-2F, lased in cw mode up to 90 K, with an emission wavelength of 12.2 μm and a J_{th} 138 A cm^{-2} as shown in Fig. 6.22. This is a significant milestone as it is the first demonstration of a BA ICL operating in cw mode, beyond 12 μm. Furthermore, the maximum obtainable output power at 80 K was 12 mW/facet (Fig. 6.22), which is comparable to and even higher than that of the previous ICLs (without $InA_{0.5}P_{0.5}$ barriers) at shorter wavelengths (10.8 and 10.2 μm).[88, 148] At 80 K the V_{th} was about 6.8 V, corresponding to a voltage efficiency of about 31%. This low voltage efficiency indicates that there are likely issues in the carrier transport for ICLs containing $InA_{0.5}P_{0.5}$ barriers. The extracted EQE at 80 K in cw mode reached 214%, as shown in Fig. 6.22 and validated the cascade process in ICLs with InAsP barriers for the first time.

In pulsed mode, this device lased at 80 K at 11.8 μm, with a J_{th} 44 A cm^{-2}, which was reduced by a factor of nearly four compared to the previous ICL in Ref. [148], while its EQE reached 451% at 80 K (Fig. 6.23), which is much higher

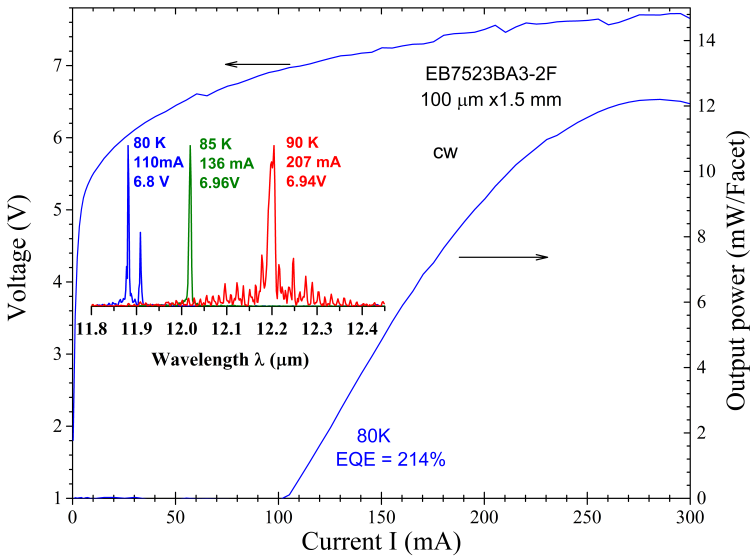

Figure 6.22: Current–voltage–power (IVL) characteristics for EB7523BA3-2F in cw mode. The inset shows the cw emission spectrum between 80 K and 90 K.

than that (41%) in the initial ICL containing $InA_{0.5}P_{0.5}$.[148] Additionally, this device operated in pulsed mode up to 160 K at 12.97 μm with a J_{th} 1267 A cm^{-2}, an increase of 40 K compared to the previous ICL.[148] Although this ICL lased at longer wavelengths near 13 μm, the operating temperature (160 K) of this device was even higher than the maximum pulsed operating temperature of ICLs at shorter wavelengths from wafers EB7541 and EB7547. These significant improvements suggest further potential of ICLs containing $InA_{0.5}P_{0.5}$ barriers.

A representative 100 μm wide device from wafer EB7539 also operated in cw mode up to 85 K with a J_{th} 143 A cm^{-2} and at a lasing wavelength of 12.4 μm (Fig. 6.24), longer than devices from EB7523 and consistent with the design. It delivered an output power of 6.4 mW/facet at 80 K with a V_{th} of about 5.7 V, which corresponds to a voltage efficiency of 35%, similar to devices from EB7523.

In pulsed operation, a 150 μm wide device (EB7539BA2-2A) lased at 80 K with a J_{th} 64 A cm^{-2}, which is reduced by about three times compared to EB7342 from Ref. [148], and 45% higher than that of EB7523BA3-2F. Furthermore, this

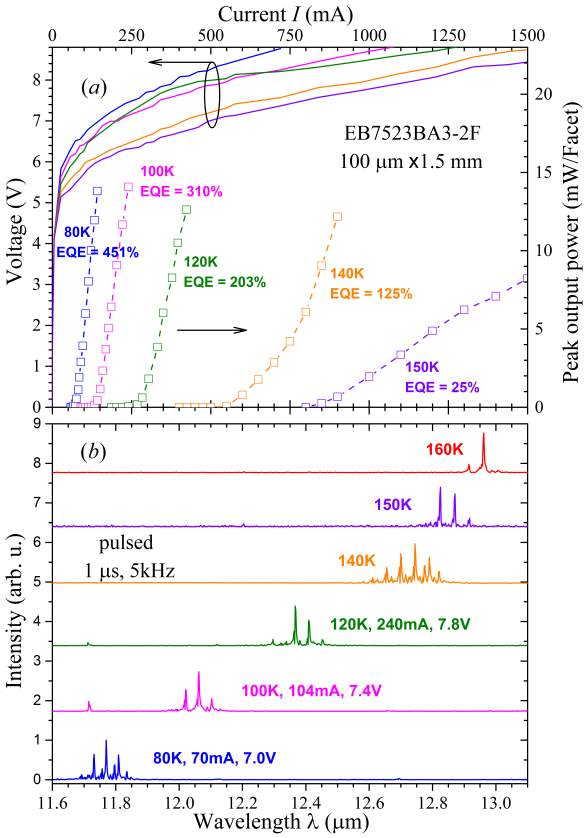

Figure 6.23: Pulsed results for the current–voltage–power (IVL) characteristics (a) for EB7523BA3-2F along with the pulsed emission spectrum (b) between 80 K and 160 K.

device lased in pulsed mode up to 150 K at 13.1 μm with a J_{th} 1111 A cm^{-2}. The extracted EQE in pulsed mode was 341% at 80 K before dropping to 9% at 150 K as shown in Fig. 6.25. Both EB7523 and EB7539 were able to hold significantly more current density at their maximum operating temperature compared with EB7541 and EB7547. Also, their differences in EQE and threshold current density are seemingly more mutually consistent in quantitative scale with their difference in the estimated free carrier absorption loss shown in Fig. 6.15, in contrast to the differences between EB7541 and EB7547.

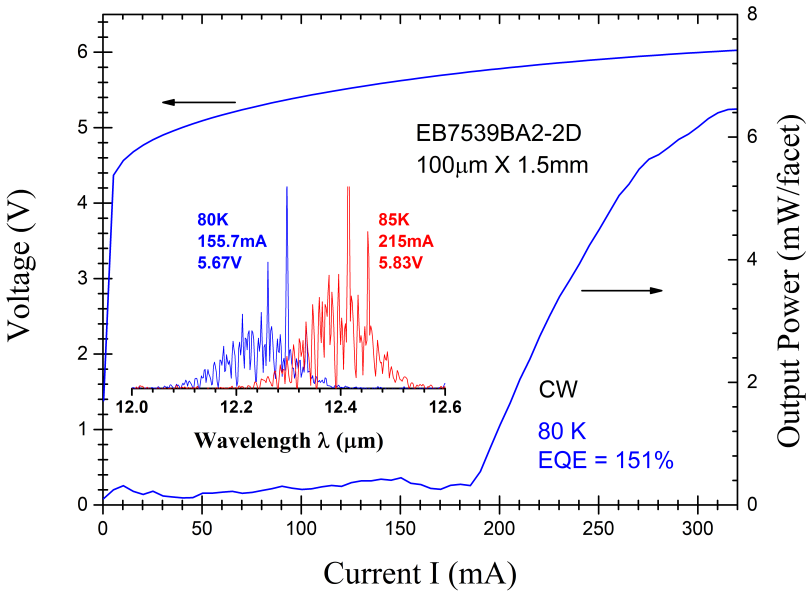

Figure 6.24: Current–voltage–power (IVL) characteristics for EB7539BA2-2D in cw mode. The inset shows the cw emission spectrum between 80 K and 85 K.

6.6 Further Discussion and Analysis

From the data presented, several additional quantities may be inferred. The effective refractive index (n_{eff}) of each device, based on the waveguide simulation, can be used to estimate the facet reflectance ($R_{1,2}$) and the subsequent mirror loss (α_m) of these devices. The laser facet basically acts as a mirror, with the light leaving normal to the plane of the facet. In this case, the Fresnel equation may be applied for TE waves

$$R = \left(\frac{n_1 \cos(\theta_i) - n_2 \cos(\theta_t)}{n_1 \cos(\theta_i) + n_2 \cos(\theta_t)} \right)^2 \tag{6.7}$$

where $n_{1,2}$ are the indices of refraction of the two materials (in this case air and the laser facet) and $\theta_{i,t}$ are the incident and transmitted angles of the laser light, where in this case $\theta_i = \theta_t = 0°$ for normal incidence. In that case, Eq. 6.7 reduces

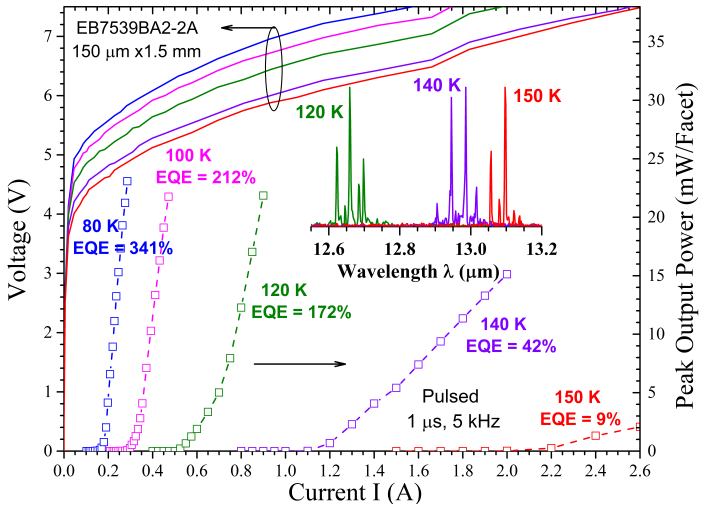

Figure 6.25: Current–voltage–power (IVL) characteristics for EB7539BA2-2A in pulsed mode. The inset shows the pulsed emission spectrum between 120 K and 150 K.

to

$$R = \left(\frac{n_{air} - n_{eff}}{n_{air} + n_{eff}}\right)^2 \tag{6.8}$$

where a value of n_{air}=1.000293[155] was used in the subsequent calculations presented here.

To calculate the mirror loss, consider that the intensity of the optical field within the cavity of length L, after 1 round trip, is given by

$$I = I_o R_1 R_2 e^{2(g-\alpha_i)L} \tag{6.9}$$

At threshold, g $\rightarrow$ $g_{th} = \alpha_i + \alpha_m$, and I $\rightarrow$ I_o=I_{th}, therefore it is the case that the round trip gain is equal to

$$R_1 R_2 e^{2(g-\alpha_i)L} = 1 \rightarrow \alpha_m = \frac{1}{2L} ln\left(\frac{1}{R_1 R_2}\right) \tag{6.10}$$

where the values of α_m may be calculated based on the measured cavity lengths

of the various laser bars tested and the estimated facet reflectances from Eq. 6.8, where $R_1 = R_2$ for all ICLs tested here. Using EB7541BA3-3H as an example, the estimated $R_{1,2}$ and α_m values are 0.291 and 8.236 cm^{-1}, respectively.

Since the waveguide simulation estimates an LB for the internal loss (α_i) by considering free carrier absorption only, an upper bound (UB) can be estimated as well. Considering pulsed mode operation at 80 K and assuming a perfect internal quantum efficiency (IQE), the UB values of the α_i can be obtained based on the extracted EQE for each device from the measured results, and using the calculated α_m from Eq. 6.10, by using Eq. 5.9. In the case of the ICLs tested here, a perfect IQE is equal to $N_c \times 100\% = 2000\%$, where $N_c = 20$ is the number of cascade stages in these devices. Based on this assumption, the UB value of the α_i for EB7541BA3-3H would be 17.5 cm^{-1}. Furthermore, an LB of the IQE can be determined based on the calculated α_m from Eq. 6.10, the measured EQE, and the LB α_i from the waveguide simulation. For EB7541BA3-3H, this results in an LB IQE of 1122%, considering a waveguide loss due only to free carrier absorption of 6.2 cm^{-1}.

By utilizing the estimated optical confinement factor (Γ) attained from the waveguide simulation, as well as the α_m from Eq. 6.10, and the UB and LB for the α_i as calculated above, an estimation of the upper and lower bounds for the threshold gain (g_{th}) can be ascertained. For EB7541BA3-3H, the resulting LB and UB for the g_{th} are 61.0 cm^{-1} and 108.8 cm^{-1}, respectively. The various estimated properties from the above discussion for the other devices presented in this work are listed in Fig. 6.26.

Based on the experimental results presented here, it can be observed that the overall performance of the ICLs follows the order: EB7541, EB7547, EB7523, and lastly EB7539. This trend is qualitatively represented in the various quantities calculated in Fig. 6.26. There it can be seen that the LB for the IQE across all four

Device	I_{th} (mA)	$R_{1,2}$	α_m (cm^{-1})	UB α_i (cm^{-1})	LB IQE	UB g_{th} (cm^{-1})	LB g_{th} (cm^{-1})
EB7541	19	0.291	8.236	17.5	1122%	108.8	61.0
EB7547	43	0.289	8.281	21.7	1039%	128.6	66.8
EB7523	66	0.286	8.345	28.7	921%	163.7	75.4
EB7539	94	0.285	8.367	49.3	612%	257.7	78.9

Figure 6.26: Several estimated device parameters based on measured results in pulsed mode at 80 K and their respective waveguide simulations.

wafers is generally much lower than the ideal value (100% per stage). If the LB IQE are valid, there could be significant current leakage and non-radiative recombination losses due to SRH and Auger processes. However, this is unlikely to be true for broad-area ICL devices at 80 K, where the required threshold carrier concentration is relatively low. Also, the defect density for the wafers is not high ($<10^5$ cm^{-2}). Hence, actual internal losses present in these devices could be substantially higher than the estimated values based only on the free-carrier absorption loss. The extra absorption loss might be caused by intersubband transitions in valence band QWs[147, 156], which was recently studied and confirmed in GaSb-based ICLs in the 4–7 μm wavelength region.[157, 158] How intersubband transitions in the valence band could affect the device performance of long wavelength InAs-based ICLs would be an interesting topic for future research.

6.7 Summary of Long Wavelength InAs-based ICLs

The implementation of the advanced waveguide configuration, using n$^+$-InAs plasmon-enhanced cladding, thin InAs/AlSb SL intermediate cladding, and undoped InAs SCLs was shown to enhance the emission of InAs-based ICLs designed to emit near 11 μm by allowing for reductions in the J_{th} required for lasing and the subsequent increase in the measured output power. Furthermore, the maximum operating temperature of these ICLs was extended. In addition to the advanced waveguide, InAs-based ICLs with the modified barrier architecture that combined

the traditional AlSb barrier material with $InAs_{0.5}P_{0.5}$ barriers was implemented here for the first time, validating the prediction in Ref. [8], and resulted in the longest operating wavelength ever achieved for an ICL, nearly 20% longer than the previous record.[88, 148] This feature also allowed for the first ever demonstration of an ICL operating in cw mode, beyond 12 μm.[149, 159]

A future iteration on this subject should consider further adjustments to the waveguide and QW layer thicknesses and doping concentrations. These adjustments should benefit the carrier transport and allow for the devices to carry larger currents and operate at higher temperatures. Furthermore, the same waveguide was used for all four of the recent ICL structures presented above. However, each ICL structure emits at a different wavelength, and so a unique waveguide tailored for the desired lasing wavelength at higher operating temperatures can further help to optimize the device performance.

Several ICLs with this P-containing barrier have now been explored with varying InAs and $InAs_{0.5}P_{0.5}$ layer thicknesses, which have helped to pave the way for better understanding of the expected lasing wavelength for this new kind of ICL. For practical applications, these long wavelength ICLs need to be capable of operating near room temperature, or at least at temperatures accessible by thermoelectric cooling. Possible issues were identified, which suggests further room for refinement. Nonetheless, the improvements presented here are encouraging and with additional adjustments such ICLs should be able to achieve better performance in the 10–13 μm range at elevated temperatures.

Chapter 7

GaSb-based Interband Cascade Lasers

We now return to the ICL that was first discussed in Chapter 4, and then elaborated upon in Chapter 6, that of the GaSb-based ICL. These ICLs have demonstrated efficient room temperature (RT) operation in the 3-6 μm range but exhibited performance below their InAs-based counterparts beyond 6 μm due partially to limited effort and the difficulties associated with the waveguide traditionally used.[17, 136] The typical waveguide used in a GaSb-based ICL consists of two Te-doped GaSb separate confinement layers (SCLs) surrounding the cascade active region, wrapped by two n-doped InAs/AlSb superlattice (SL) cladding layers, which have a low thermal conductivity and a small contrast in refractive index with the cascade region as discussed in Chapter 6.

The InAs-based ICLs have utilized a heavily n^+-doped InAs plasmon-enhanced cladding layer, instead of the InAs/AlSb SL, to improve the optical confinement and the overall thermal conductivity of the device[9, 84–89], resulting in the wavelength coverage of ICLs extending to 11.2 μm. For InAs-based ICLs operating near 4.6 μm, it was later shown that an advanced waveguide structure which combined a relatively thin InAs/AlSb SL intermediate cladding layer with the n^+-doped InAs plasmon cladding, enabled enhanced device performance by reducing the free-carrier loss and yielding improved optical confinement within the cascade active region.[7] This advanced waveguide was later shown to improve performance in long wavelength InAs-based ICLs emitting between 10-13 μm[148, 149] and was also explored in GaSb-based ICLs operating between 3.8 to 6.1 μm,[6, 138] where the plasmon enhanced cladding layer in the latter is composed of n^+-doped $InAs_{0.91}Sb_{0.09}$ for lattice matching to the GaSb substrate.

Section 7.1 discusses the first ever successful growth of GaSb-based ICLs with the advanced waveguide on the GENxplor, based on growth perspectives discussed in Chapter 4, where performance deviations are pointed out and elaborated upon. Sections 7.2 and 7.3 presents our first effort to implement the advanced waveguide in GaSb-based ICLs designed to emit between 3.3-3.4 μm. Section 7.4 follows up this first study, with a second iteration on the short wavelength GaSb-based ICL with an advanced waveguide. The results of Sections 7.2-7.4 unequivocally demonstrate the potential of the advanced waveguide for GaSb-based ICLs in this wavelength range.

7.1 Early GaSb-based ICLs with Advanced Waveguides

As discussed in Chapter 4, the development of our own Sb-soak technique to grow the InAs/AlSb SL intermediate cladding with little deviation in the 0th order peak position for GaSb-based ICLs directly led to the first ever successful growth of GaSb-based ICLs in our group on the GENxplor. These Sb-soaks were first adopted into the InAs/AlSb SL intermediate cladding as well as the InAs/AlSb SL for the electron injector and resulted in devices Y061L and Y062L, which both share an identical design, but which have slightly different growth parameters. These ICLs were designed with an advanced waveguide consisting of n^+-doped $InAs_{0.91}Sb_{0.09}$ plasmon cladding, doped to a level of 1.5×10^{19} cm^{-3}, InAs/AlSb SL intermediate cladding doped to a level of $1.5{\times}10^{17}$ cm^{-3} in the InAs layers, and lightly doped ($2.6{\times}10^{17}$ cm^{-3}) GaSb SCLs as shown in Fig. 7.1. They were designed to have 10 cascade stages and share a similar W-QW structure to the long wavelength InAs-based ICLs, composed of AlSb/InAs/$Ga_{0.6}In_{0.4}Sb$/InAs/AlSb with layer thicknesses of 23/20.5/28/18.5/12 Å in the growth direction and were designed to emit at 4.6 μm at 300 K.

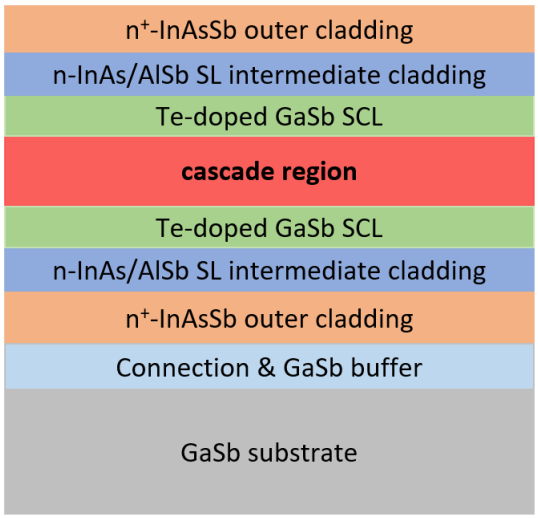

Figure 7.1: Schematic drawing of the GaSb-based ICL design.[6]

7.1.1 Growth Characteristics of Y061L and Y062L

The growth characteristics of these two ICL wafers were analyzed with DIC where the average surface defect density for these wafers was in the low to mid 10^3 cm^{-2} range as shown in Fig. 7.2. This level of surface defects is acceptable for good device performance. Both wafers presented a slightly "orange-peel"-like background surface roughness, indicative of a slight degree of partial relaxation of the crystal lattice in the epilayers. The crystalline quality was measured with XRD as shown in Fig. 7.3, which shows the XRD patterns for Y061L (blue), Y062L (green), and a simulation of the designed structure (red). According to the SL peak spacing, the InAs/AlSb SL intermediate cladding layers were about 0.2% thinner and 7.9% thicker than designed, while the cascade stages were about 6.1% and 5.8% thinner, for Y061L and Y062L, respectively. The SL intermediate cladding showed a slight tensile strain of 0.0565% in the growth direction for Y061L, while Y062L showed a slight tensile strain of 0.0352%. The peak of the InAsSb plasmon-enhanced cladding layer was deduced to be approximately within 100 arcsec of the GaSb-substrate peak, indicating a relatively lattice matched alloy

composition.

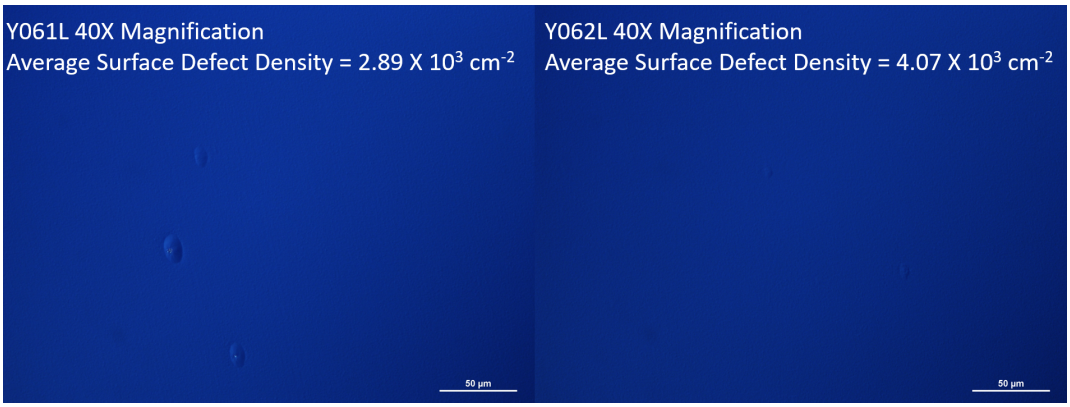

Figure 7.2: DIC images of Y061L (left) and Y062L (right) under 40× magnification. Both wafers have a similar average surface defect density as shown, where the background surface is slightly rougher for Y061L.

7.1.2 Performance Characterization of Y061L and Y062L

The grown wafers were fabricated into 100-μm-wide and 150-μm-wide broad area (BA) mesas using wet chemical etching. The etch depth proceeded about 10% into the bottom SCL, in order to ensure isolation of the cascade stages and to account for any non-uniformity in the etch depth across the wafer. The wafers were left un-thinned and cleaved into 1.5-mm-long laser bars without facet coating, which were mounted epi-side up on copper heat sinks for testing.

Devices made from Y061L operated in cw mode up to 228 K with an emission wavelength of 3.89 μm, while those from Y062L operated in cw mode up to 220 K at 3.69 μm.[6] At 80 K, the lasing wavelengths varied from 3.30-3.41 μm and 3.45-3.53 μm for several devices from Y061L and Y062L, respectively. Considering that both ICL wafers have the same design, and that laser bars from the same ICL wafer show this emission wavelength difference implies that there exist nonuniformities in the structural parameters across each wafer, and between both wafers.

Under pulsed mode operation at 300 K, devices from Y061L lased at 3.87 and

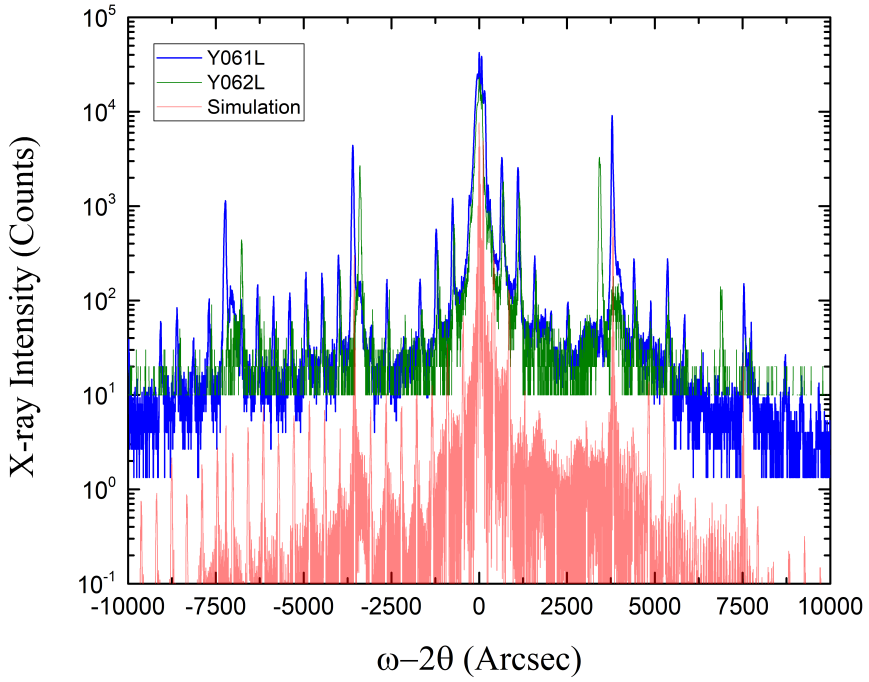

Figure 7.3: XRD patterns for Y061L (blue), Y062L (red), and the simulated pattern (red) according to the intended design.

3.98 μm, while those from Y062L emitted at 3.81 μm.[6] The emission wavelength at RT was significantly shorter than the designed value of 4.6 μm, which cannot be fully explained by the structural deviations from the XRD patterns. From the XRD, the average thickness of the cascade region was about 6% thinner, and while it is hard to quantify where exactly the deviations occur, we may speculate. If these cascade thickness deviations occur in such a way as to be partially responsible for the blue shifted emission, then at most we would expect the influence of this to equate to a blue-shift about 0.28 μm. In that case, these ICLs should emit at around 4.3 μm at RT.

Other factors beyond layer thickness deviations may be responsible for this blue-shifted emission from the intended design, including variations in the interface compositions resulting from the incorporation of residual As or Sb from the growth chamber and uneven fluctuations in the beam fluxes used during growth. For

example, a study on the effect of interface bond type on the optical properties of InAs/GaSb superlattices[101] found that this SL with an InSb-like interface had a measured bandgap of 0.234 eV, corresponding to a wavelength of 5.299 μm. Those with a GaAs-like interface had a measured bandgap of 0.288 eV, corresponding to a wavelength of 4.305 μm, which is blue shifted by about 0.99 μm compared to the InSb-like interface SL, and less so for the pure InAs/GaSb SL with atomically abrupt interfaces. For the ICL, the type-II QW is formed from InAs/$Ga_{0.4}In_{0.4}Sb$, where the inclusion of In into the GaSb decreases the material bandgap somewhat. In this case, the total difference between the bandgaps of the overall SL structure with different interfaces should be smaller than in the example above. For example, a $Ga_{0.4}In_{0.4}As$ interface could be formed, which would blue shift the emission but not as dramatically as a GaAs-like interface. Also, in the study from Ref. [101], the significantly blue-shifted bandgap occurred in the SL that had an interface with unwanted As incorporation. It has been thoroughly discussed in Chapter 4 that unwanted As incorporation in the GENxplor was a significant issue for optimizing the quality and strain balance of SL structures. Therefore, it is reasonable to think that potential As incorporation into critical portions of the W-QW during growth directly contributed to the significant blue shift observed in Y061L and Y062L, which must be accounted for in future growth iterations.

Additionally, this significant blue-shift in the emission could render the refractive index contrast of the n^+-$InAs_{0.91}Sb_{0.09}$ plasmon cladding ineffective for optimally confining the optical wave, resulting in higher losses. Nevertheless, ICLs made from these wafers exhibited threshold current densities comparable to the lowest values (220-300 A/cm^2) reported for ICLs at similar wavelengths.[10, 136, 138, 160] Also, the extracted characteristic temperature T_o from these ICL wafers was between 42-48 K, which is typical for MIR semiconductor lasers based on interband transitions, and only slightly lower than state of the art GaSb-based ICLs ($\sim$50-55 K). The

successful growth of GaSb-based ICLs with the advanced waveguide structure was demonstrated on the GENxplor for the first time and provided invaluable feedback for follow up studies.

7.2 GaSb-based ICLs for shorter Mid-wavelength Operation

GaSb-based ICLs with advanced waveguides have been explored in the 3.8-6.1 μm[6, 138] range at RT, but not at wavelengths shorter than this. Here we report an investigation of GaSb-based ICLs which incorporate the advanced waveguide structure and are tailored to emit near 3.3 and 3.4 μm at RT. The continuous wave (cw) and pulsed performance of these broad area (BA) ICLs display similar performance to other GaSb-based ICLs which utilize the conventional waveguide and emit near a similar wavelength. Compared to long wavelength InAs-based ICLs, the InAs QW width is much thinner to support lasing at shorter wavelengths, resulting in a drastically increased electron-hole wavefunction overlap estimated to be 44.7% from band simulations. A band diagram for a representative GaSb-based ICL (Y082L) is shown in Fig. 7.4 , with a W-QW active region composed of AlSb/InAs/$Ga_{0.6}In_{0.4}Sb$/InAs/AlSb with layer thicknesses of 25/16.5/28/14/12 Å in the growth direction and were designed to emit at 3.30 μm at 300 K.

7.2.1 Design of Y082L and Y083L

Two GaSb-based ICL wafers were grown on the GENxplor with designs utilizing the advanced waveguide structure. Both ICL wafers have 6 cascade stages (N_c) where each W-QW active region consists of an identical layer sequence as described previously. The primary difference between the two ICL wafers stems from the variation in the SCL layer thickness. The first ICL structure (Y082L) has GaSb

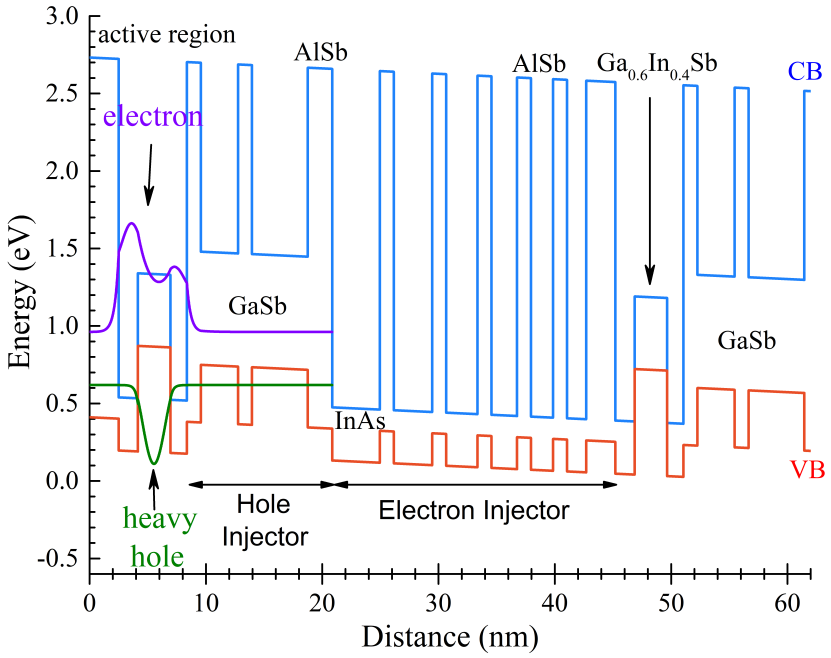

Figure 7.4: Qualitative band diagram of Y082L, a GaSb-based ICL with much thinner InAs layers in the W-QW active region in order to support shorter wavelength operation between 3.3 and 3.4 μm at RT.

SCLs doped with Te to a level of 2.7 $\times$ 10^{17} cm^{-3} each with a thickness of 2100 Å, while the second ICL structure (Y083L) incorporates the same Te-doped GaSb SCLs but with the thickness increased to 3000 Å. Both include 1 μm thick (bottom) and 0.7 μm thick (top) n^+-doped $InAs_{0.91}Sb_{0.09}$ plasmon cladding layers with a doping level of 3.2 $\times$ 10^{19} cm^{-3} and 0.75 μm (bottom and top) n-doped (1.5 $\times$ 10^{17} cm^{-3}) InAs/AlSb SL intermediate cladding layers. Fig. 7.5 shows the calculated optical modal profile and refractive index for these two ICL wafers, which also takes various connection regions into account. To calculate characteristics at RT, the waveguide simulation was generated using the designed emission wavelength at 300 K of $\lambda = 3.30$ μm for these ICLs. Several estimated parameters are shown in the figures, including the optical confinement factor in the cascade active region (Γ), the internal loss due to free-carrier absorption (α_i), the threshold gain (g_{th}), and the effective refractive index (n_{eff}) of the waveguide. Note that the estimated

optical confinement factor decreases from approximately 21.4% in Y082L to 19.9% in Y083L due to the increased thickness of the SCLs. On the other hand, the increase in the SCL thickness in Y083L leads to a reduced extension of the optical wave into the plasmon cladding, with a predicted reduction in the free-carrier absorption loss from 5.20 $cm^{-1} \rightarrow 3.65$ cm^{-1}. These two features compensate each other, resulting in a threshold gain that is only slightly reduced in Y083L compared to that in Y082L. One may observe that there is a slight asymmetry in the optical profile, which arises due to the asymmetry in the predicted refractive index values for the mid-transition regions on either side of the cascade active region. The refractive index of these thin SL layers is calculated based on a thickness weighted average, where one of the two layers has a slightly higher overall contribution of doped layers, leading to a slightly lower real part of its refractive index.

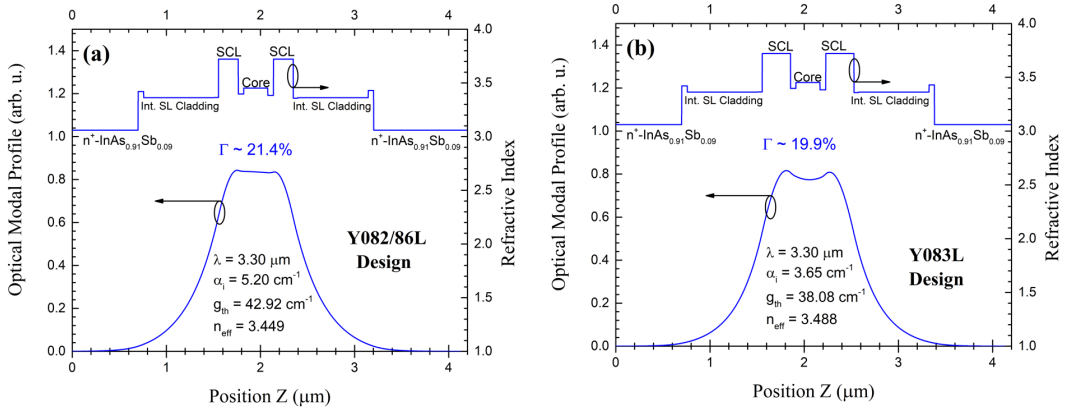

Figure 7.5: The calculated optical modal profile and refractive index for (a) Y082L and (b) Y083L. Listed in the plots are the optical confinement factor (Γ), the internal loss due to free-carrier absorption (α_i), the threshold gain (g_{th}), and the effective refractive index (n_{eff}).

7.2.2 Growth Characteristics of Y082L and Y083L

The two six-stage GaSb-based ICL wafers were grown by molecular beam epitaxy (MBE) using a Veeco GENxplor with As and Sb supplied by valved

cracking sources. In these ICL wafers, steps were taken to minimize the potential incorporation of As into unwanted layers within the W-QW active region by also implementing Sb-soaks into that crucial part of the growth. The crystalline quality of the grown ICL wafers was analyzed using x-ray diffraction (XRD) and the surface morphology was characterized by differential-interference-contrast microscopy (DIC). From the DIC images, typical oval hillock defects were observed – common to III-V ICL growth, but with little background surface roughness. The average surface defect density of Y082L was 1.4×10^4 cm^{-2}, while that of Y083L was 6.8×10^3 cm^{-2}, which are within acceptable limits for reasonable device performance.

From the XRD measurements, symmetric scans normal to the (004) planes indicate certain deviations from the intended design as shown in the representative XRD pattern in Fig. 7.6. Between both ICL wafers, an average tensile strain for the SL cladding of 0.13% in the growth direction (biaxial compressive strain) was observed, where the average substrate/SL zero-order peak separation was approximately 159 arcsec. The analysis of the XRD pattern showed that on average, the InAs/AlSb SL intermediate cladding was about 8.3% thinner than expected, while the cascade region was 13% thinner than expected, indicating a possible variance in the group III growth rates or issues during the MBE growth calibration.

To explore this, consider that the designed thickness (t_{design}) of the individual InAs and AlSb layers in the SL cladding were 26 Å and 24 Å, respectively, with a total designed number of monolayers of

$$\begin{aligned} N_{InAs}M_{InAs} = t_{design,InAs} \rightarrow N_{InAs} = \frac{t_{design,InAs}}{M_{InAs}} \approx 8.6ML \\ N_{AlSb}M_{AlSb} = t_{design,AlSb} \rightarrow N_{AlSb} = \frac{t_{design,AlSb}}{M_{AlSb}} \approx 7.8ML \end{aligned} \tag{7.1}$$

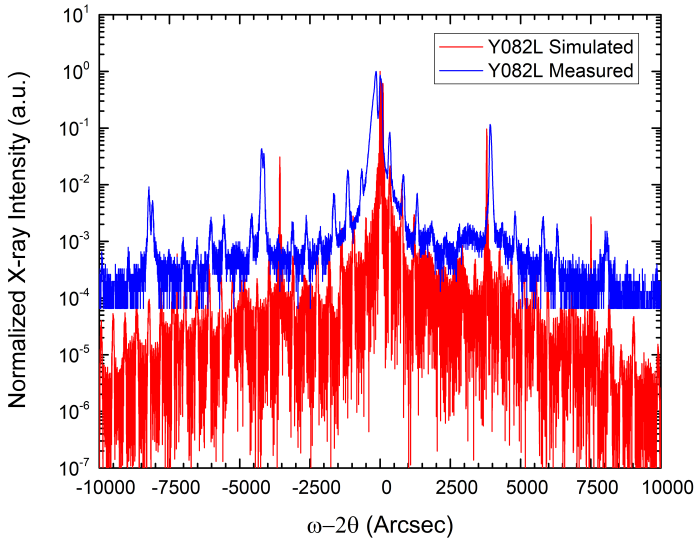

Figure 7.6: The experimentally measured XRD pattern (blue) along with the simulated pattern (red) for Y082L, which is representative of both ICL wafers grown.

where thickness of an individual monolayer M, of InAs was $M_{InAs} = 3.0292$ Å and that of AlSb was $M_{AlSb} = 3.0676$ Å. First, we can assume that the thickness deviations in the SL cladding occur uniformly throughout the entire SL. This would result in the growth of only about 7.8 ML of InAs and 7.3 ML of AlSb. This amounts to individual layer thicknesses of InAs and AlSb of about 23.5 Å and 21.7 Å in Y082L and 24.2 Å and 22.3 Å in Y083L.

However, the previous discussion lacks any physical insight and simply assumes an average deviation across all layers. A more physical description is as follows. First, consider the idea that the thickness of 1 ML of the SL should be related to the SL period (T) and the number of monolayers of the constituent layers of the SL by

$$N_{SL}M_{SL} = T \rightarrow (N_{InAs} + N_{AlSb})M_{SL} = T \rightarrow \frac{a_{SL}}{2} = \frac{T}{N_{InAs} + N_{AlSb}} \qquad (7.2)$$

where N_{SL}, M_{SL}, and a_{SL} are the number of monolayers, thickness of a single monolayer, and the lattice constant of the InAs/AlSb SL, respectively. The other terms are as defined above for Eq. 7.1. In addition, consider the idea that the sum of the individual components of the SL should also add up to the total thickness of a single period of the SL, that is to say that $T_{InAS} + T_{AlSb} = N_{InAs}M_{InAs} + N_{AlSb}M_{AlSb} = T$, which gives us two equations to work with. These may be rearranged to solve for the total number of InAs monolayers as

$$N_{InAs} = \frac{2T}{a_{SL}} - N_{AlSb} = \frac{T - N_{AlSb}M_{AlSb}}{M_{InAs}} \tag{7.3}$$

Solving Eq. 7.3 yields the number of InAs and AlSb monolayers based on experimentally measured parameters

$$\begin{aligned} N_{InAs} &= \frac{T(a_{SL} - 2M_{InAs})}{a_{SL}(M_{AlSb} - M_{InAs})} \\ N_{AlSb} &= \frac{2T}{a_{SL}} - \frac{T(a_{SL} - 2M_{InAs})}{a_{SL}(M_{AlSb} - M_{InAs})} \end{aligned} \tag{7.4}$$

Here a_{SL} is the lattice constant of the InAs/AlSb SL that is directly extracted from the measured Bragg angle of the SL 0th order peak and T is the measured period of the SL peaks from the -1 to +1 or -2 to +2 harmonic peaks.

However, by practically applying this method to the measured results for Y082L and Y083L, the consistent result is that the InAs layer thickness is about 30%-40% too thin and the AlSb is about 10% too thick. It is hard to believe that the group III growth rate calibration could be off by so much for simple binary materials. This possibly indicates an incomplete physical description or points to another underlying cause for the layer thickness deviation. Considering that the cascade region is formed, in part, from an electron injection region made up of an InAs/AlSb SL, it is likely the case that the cause of the thickness deviation in the SL intermediate cladding is the same cause for the deviation in the cascade region.

Lastly, the thickness of the n^+-$InAs_{0.91}Sb_{0.09}$ plasmon cladding should be large enough to have an intense XRD peak, allowing one to differentiate its XRD peak from the overall pattern as a whole. In this case, a direct estimation of the alloy composition may be made from the measured Bragg angle of the alloy peak based on Eq. 4.4. To estimate the position of the n^+-$InAs_{0.91}Sb_{0.09}$ XRD peak, a simulation may be generated as shown in Fig. 7.7 and then overlaid with the measured XRD data to allow for the correct assignment of the alloy peak as shown in Fig. 7.8. Using this technique it was found that the composition of the plasmon cladding was between $InAs_{0.914}Sb_{0.086}$ (if fully strained) and $InAs_{0.917}Sb_{0.083}$ (if fully relaxed) for Y082L and between $InAs_{0.92}Sb_{0.08}$ (if fully strained) and $InAs_{0.928}Sb_{0.072}$ (if fully relaxed) for Y083L.

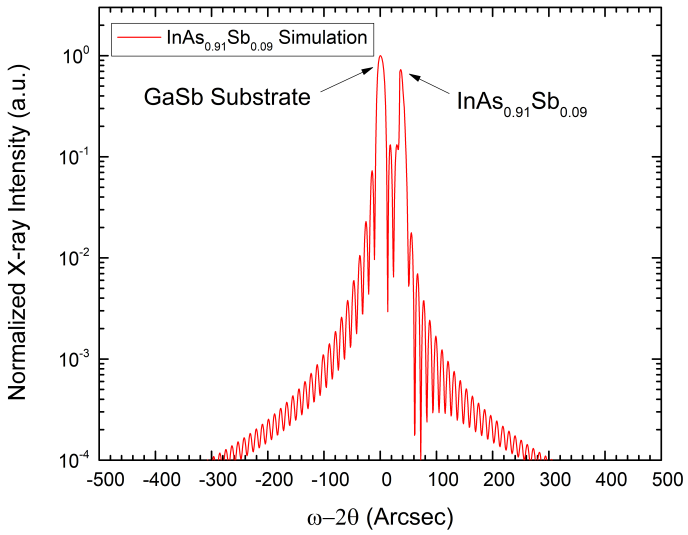

Figure 7.7: Simulated XRD pattern for a 1.7 μm thick $InAs_{0.91}Sb_{0.09}$ alloy on a GaSb substrate.

From the measured XRD pattern, the thickness of the InAs/AlSb SL consistently shows reduced thickness compared with the design, which is also qualitatively evident from the visual comparison of the measured to simulated XRD curves for Y082L and Y083L. This may result in additional leakage of the optical wave into the plasmon cladding, which may serve to increase the internal loss in the system

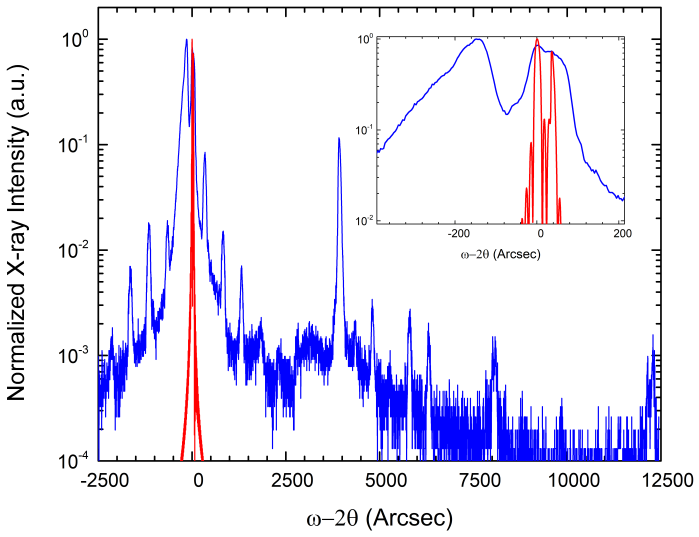

Figure 7.8: Measured XRD pattern (blue) for Y082L along with the simulated XRD pattern (red) of a 1.7 μm thick $InAs_{0.91}Sb_{0.09}$ alloy on a GaSb substrate. The inset shows a zoomed in view in the vicinity of the substrate peak, which allows for the identification of the alloy peak from the measured XRD data, and the subsequent determination of the alloy composition.

compared with the intended design. Furthermore, the thinner cascade active region will also result in the extension of the optical wave into other portions of the waveguide, which could further increase the free-carrier loss as well as increase the required threshold gain, as less of the optical wave exists within the cascade active region. The potential impact that these structural differences may have on various optical parameters such as the optical confinement factor in the cascade active region (Γ), the internal loss due to free-carrier absorption (α_i), and the threshold gain (g_{th}) may be calculated from waveguide simulations at RT. For example, using the estimated thickness deviation for the InAs/AlSb SL intermediate cladding and cascade active region for Y082L in the waveguide simulation, along with the measured emission wavelength of $\lambda = 3.28$ μm at RT, results in a decrease in the predicted optical confinement in the cascade active region to $\Gamma = 19.6\%$ and an increase in the free-carrier absorption loss from 5.20 cm^{-1} to 5.75 cm^{-1}, an increase of about 10.5%, along with an increase in the required g_{th} to 49.83 cm^{-1}.

The increased free-carrier absorption and larger threshold gain predicted by this simulation can be attributed to two factors. First, the thinner SL intermediate cladding layer allows more of the optical wave to leak into the plasmon cladding layer, resulting in an increase in the free-carrier absorption. Second, the thinner cascade active region results in a smaller overlap between optical field and the cascade active region, which reduces the optical confinement. This reduction causes a larger threshold gain in the active region to be required for lasing.

As Y083L shares similar growth deviations, comparable outcomes would be expected for that ICL wafer as well, although the thicker SCL may play a role in modifying how the optical properties change, compared to Y082L. From the waveguide simulation, along with the measured emission wavelength of $\lambda = 3.42$ μm at RT, the predicted optical confinement in the cascade active region decreases to $\Gamma = 17.6\%$, consistent with a thinner cascade active region. The estimated free-carrier loss and threshold gain both increase to $\alpha_i = 4.40$ cm^{-1}, an increase of about 20.5%, and $g_{th} = 47.26$ cm^{-1}. The greater changes in the optical parameters for ICL wafer Y083L are likely due to the more significant red-shift of the emission wavelength at RT, which may be mainly related to the increased thickness of the SCLs, but also partially related to other factors such as the mounting, fabrication, and crystal quality. This effect would bring the emission wavelength slightly closer to the plasma wavelength (λ_p), leading to slightly increased free-carrier losses.

The average thickness deviation of the cascade active region in Y082L and Y083L is more severe than the previously discussed Y061L and Y062L ICL wafers. There, the emission was blue-shifted by a large amount compared with the intended design, which could not be fully explained by considering just the thickness deviation of the cascade active region. If the thickness deviation of the cascade active region played a large role in that blue-shifted emission, then we should expect this effect to be more pronounced for Y082L and Y083L. However, this may have different

impacts on the device depending on where these thickness deviations occur. If the deviations are localized to the injection region, then it would not have a large affect the emission wavelength. However, this could still end up being problematic as the electron levels between each layer may not line up as intended, which can impede the carrier transport in the device and could manifest in a larger V_{th} required for lasing. On the other hand, if the reduced thickness is more isolated to the active region, the emission wavelength could be blue-shifted quite considerably, as previously discussed. These will be interesting features to explore in the next section, which detail the performance characteristics for Y082L and Y083L.

7.3 Initial Results for GaSb-based ICLs Operating Between 3.3-3.4 μm

Despite the structural deviations discussed in Section 7.2.2, devices made from these ICL wafers exhibited reasonable lasing performance in both cw and pulsed modes with several devices tested between both ICL wafers, Y082L and Y083L. The performance of devices from Y082L will be discussed in Section 7.3.1, while those from Y083L will be presented in Section 7.3.2. Some comparisons and discussion to Y061L and Y062L will be made in Section 7.3.3.

7.3.1 Y082L Results

The measured threshold voltage (V_{th}) and threshold current density (J_{th}) results as a function of temperature for two representative devices from the first ICL wafer, Y082LBA1-3F and Y082LBA1-3H, are shown in Fig. 7.9. Also shown are the specific thermal resistance (R_{th}) and the characteristic temperature (T_o), which were determined from the pulsed measurements based on Eq. 5.4 and 5.2, respectively. In cw mode, a representative 100-μm-wide device from the first ICL

wafer, Y082LBA1-3F, lased at 80 K with an emission wavelength of $\lambda = 2.89$ μm, a $J_{th} = 10.5$ A/cm^2, and a $V_{th} = 7.4$ V. Y082LBA1-3F went on to operate up to 242 K in cw mode, with an emission wavelength of $\lambda = 3.25$ μm and a J_{th} of 165 A/cm^2. A representative 150-μm-wide device from the first ICL wafer, Y082LBA1-3H, exhibited similar 80 K performance and operated up to a maximum cw temperature of 225 K with an emission wavelength of $\lambda = 3.21$ μm and a J_{th} of 106.9 A/cm^2. The cw operating temperature difference between the two devices is likely due to the increased thermal load in device H stemming from the wider laser ridge, which is reflected by their difference in the specific thermal resistance.

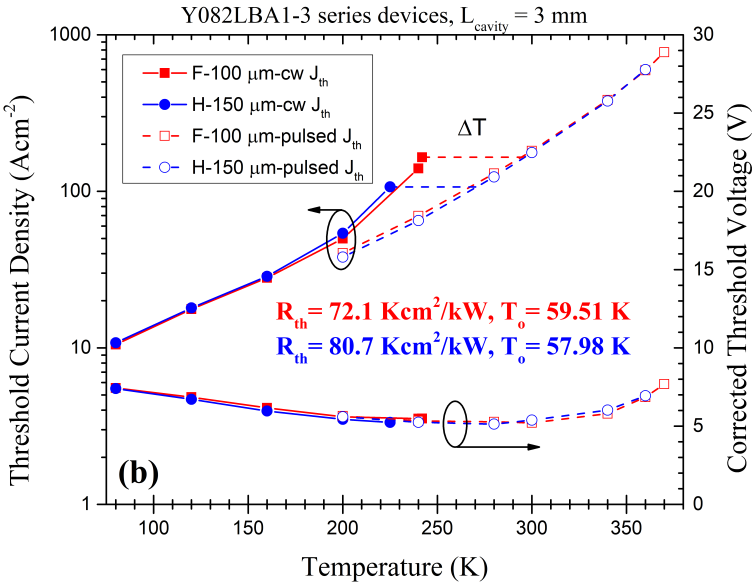

Figure 7.9: The J_{th} and V_{th} results as a function of temperature for two representative devices from ICL wafer Y082L with different laser ridge widths in both cw and pulsed modes. Included are the calculated R_{th} and T_o values.

These R_{th} values are quite large compared to GaSb-based ICLs with the conventional waveguide reported in Ref. [161], which presented R_{th} values that were around 20-45 Kcm^2/kW for ICLs with ridge widths between 100-150 μm. However, the ICLs reported in Ref. [161] had substrates that were thinned down to about 100-150 μm thick, whereas devices made from Y082L and Y083L had

unthinned substrates with thicknesses of approximately 550-600 μm, thus the heat extraction was less efficient in the latter ICLs. Also, the devices reported in Ref. [161] had cavity lengths that ranged between 0.5-1.5 mm, while those of Y082L and Y083L were 3 mm. This means that the expected J_{th} values should be smaller in the latter, which consequently leads to an increased R_{th} according to Eq. 5.4.

The cw current-voltage-light (IVL) characteristics of devices Y082LBA1-3F and Y082LBA1-3H are shown in Figs. 7.10 (a) and (b), respectively. Y082LBA1-3F reached a source-limited cw output power at 80 K of 121.5 mW/facet at an injection current of 500 mA with an extracted external quantum efficiency (EQE) of 131%, indicating the cascaded emission of photons in the ICL, and dropped to 27% at 240 K with a cw output power of 4.4 mW/facet. Y082LBA1-3H showed similar performance, with a source-limited cw output power at 80 K of 116 mW/facet and a corresponding EQE of 147%, dropping to 32% at 225 K with a cw output power of 1.9 mW/facet.

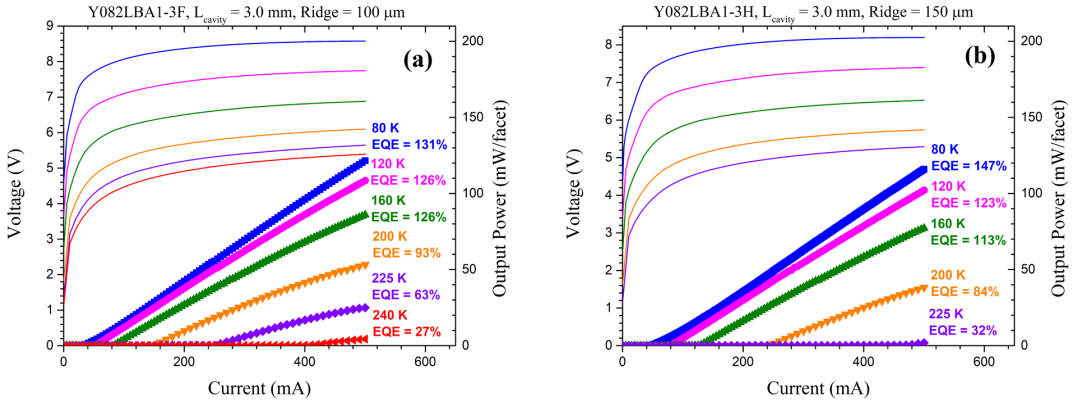

Figure 7.10: CW IVL characteristics for Y082LBA1-3F (a) and Y082LBA1-3H (b) from 80 K to their maximum operating temperatures of 240 K and 225 K, respectively. Also shown are the extracted external quantum efficiency values (EQE).

In pulsed operation, the Y082LBA1-3F and Y082LBA1-3H devices were able to lase up to 370 K with a J_{th} = 773 A/cm^2 and 360 K with a J_{th} = 600 A/cm^2, respectively, as shown in Figs. 7.11 (a) and (b). Another device with a 1.5 mm

cavity length and a 100 μm wide ridge, Y082BA1-1C, was operated up to 390 K and was then damaged due to the high pulsed current. Y082LBA1-3F lased in pulsed mode at RT with an emission wavelength of $\lambda = 3.28$ μm and a $J_{th} = 181.3$ A/cm^2, while Y082LBA1-3H lased at a similar wavelength with a $J_{th} = 176.9$ A/cm^2. This J_{th} is somewhat comparable to a 5-stage GaSb-based ICL which utilized the conventional waveguide and exhibited RT lasing at $\lambda = 3.6$ μm with a $J_{th} = 134$ A/cm^2.[160] As Ref. [160] points out, the threshold current tends to increase at even shorter wavelengths, rising above 200 A/cm^2 for devices emitting below 3.1 μm. However, the threshold voltages from devices made from Y082L were relatively high (>5 V) as illustrated in Fig. 7.9, suggesting an unsmooth carrier transport. This might be caused by substantial deviations in layer thicknesses from the design.

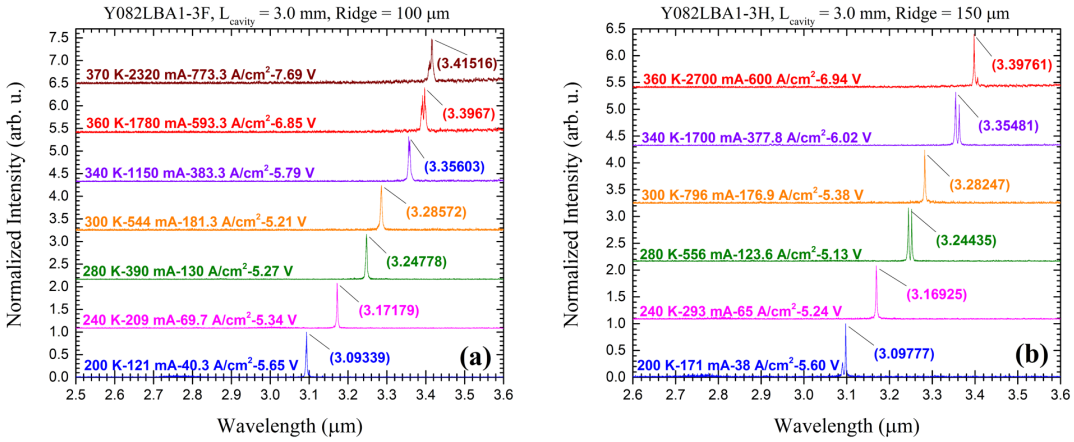

Figure 7.11: Normalized spectra under pulsed excitation for (a) Y082LBA1-3F and (b) Y082LBA1-3H. Shown in the plot are the threshold current, threshold current density, threshold voltage, and emission wavelength at each temperature step.

Nevertheless, these ICLs were able to lase in pulsed mode at high temperatures (up to 390 K) with T_o values calculated from the pulsed data between 200 K and 360 K that were close to 60 K as shown in Fig. 7.9, which is the highest among RT ICLs with similar lasing wavelengths. This offers partial validation that the advanced waveguide can lead to enhanced operation of GaSb-based ICLs emitting

at these shorter wavelengths. These preliminary results are very encouraging considering that these ICL wafers were the first growth trial after repairing and reopening the MBE system after weather related damage to the growth cells.

7.3.2 Y083L Results

Two representative devices from the second ICL wafer, Y083LBA1-3G and Y083LBA1-3E were able to lase in both cw and pulsed modes as shown in Fig. 7.12. In cw mode at 80 K, a representative 100-μm-wide device from the first ICL wafer (Y083LBA1-3G) lased at $\lambda = 3$ μm with a $J_{th} = 10.4$ A/cm^2 and a $V_{th} = 9.14$ V, which is a higher threshold voltage than that of Y082LAB1-3F. This device went on to operate up to 228 K in cw mode with an emission wavelength of $\lambda = 3.35$ μm and a $J_{th} = 120$ A/cm^2. As before, the companion device with a 150-μm-wide laser ridge (Y083LBA1-3E) exhibited similar performance at 80 K, with a $J_{th} = 11.2$ A/cm^2 and was able to lase up to 210 K in cw mode, with emission near $\lambda = 3.31$ μm and a $J_{th} = 87$ A/cm^2. From Fig. 7.12 it can be seen that the extracted R_{th} values for Y083L were superior to those from Y082L, which may indicate better mounting to the heat-sink. However, it should be noted that the R_{th} results reported for devices from Y082L were calculated at higher cw operating temperatures. For a fair comparison, consider Y082LBA1-3F at a temperature of T = 228 K (comparable to the maximum cw T for Y083LBA1-3G). In that case, the estimated specific thermal resistance is $R_{th} = 64.2$ Kcm^2/kW, much closer to the result for Y083LBA1-3G, though still slightly larger, which may be reflective of mounting and fabrication inconsistencies between the two ICL wafers.

The cw IVL characteristics of devices Y083LBA1-3G and Y083LBA1-3E are shown in Figs. 7.13 (a) and (a), respectively, where damage to the devices was avoided by limiting the injection current to 400 mA at lower temperatures.

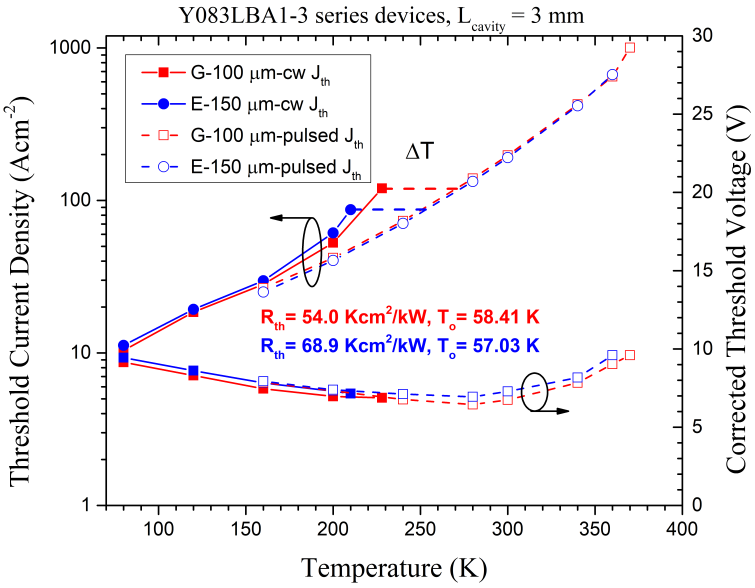

Figure 7.12: The J_{th} and V_{th} as a function of temperature for two representative devices from ICL wafer Y083L with different laser ridge widths in both cw and pulsed modes. Included are the calculated R_{th} and T_o values.

Under this restriction, Y083LBA1-3G reached a peak cw output power at 80 K of 109.1 mW/facet with an extracted external quantum efficiency (EQE) of 153%. Compared to a similar injection current for Y082LBA1-3F (96.1 mW/facet at 400 mA), the output power at 80 K from Y083LBA1-3F was about 13.5% larger. The output power dropped to 1.5 mW/facet, with an EQE of 21%, at its maximum cw operating temperature of 228 K. At a comparable cw operating temperature of 225 K, the output from Y083LBA1-3G (8.7 mW/facet) was much lower than that of Y082LAB1-3F (24.9 mW/facet) under an injection current of 500 mA. This may be due partially to the increased heating with the higher threshold voltage and the thicker SCL as it may slightly reduce the efficiency of the heat extraction from the active region. Y083LBA1-3E exhibited similar performance, with an 80 K EQE = 136% and a maximum cw output power of 90.6 mW/facet, which is again quite comparable to the equivalent output of Y082LBA1-3H (89.7 mW/facet) under a similar injection current. The output fell to 5.7 mW/facet at 210 K with an EQE =

36%. Under comparable injection currents at 200 K, the output of Y083LBA1-3E was 22.8 mW/facet while that of Y082LBA1-3H was about 68% larger at 38.2 mW/facet, again indicating reduced performance possibly due to the increased thermal load in devices from Y083L. This is also supported by comparison of both devices from Y083L at 200 K. Y083LBA1-3G showed an output of 39.4 mW/facet at 200 K, indicating the reduced performance seen in Y083LBA1-3E is associated with heating in the QW active region due to the wider laser ridge compared with Y083LBA1-3G. The variation in the EQE between devices and across ICL wafers is likely due to subtle differences in both the alignment of the power meter and each device's beam divergence.

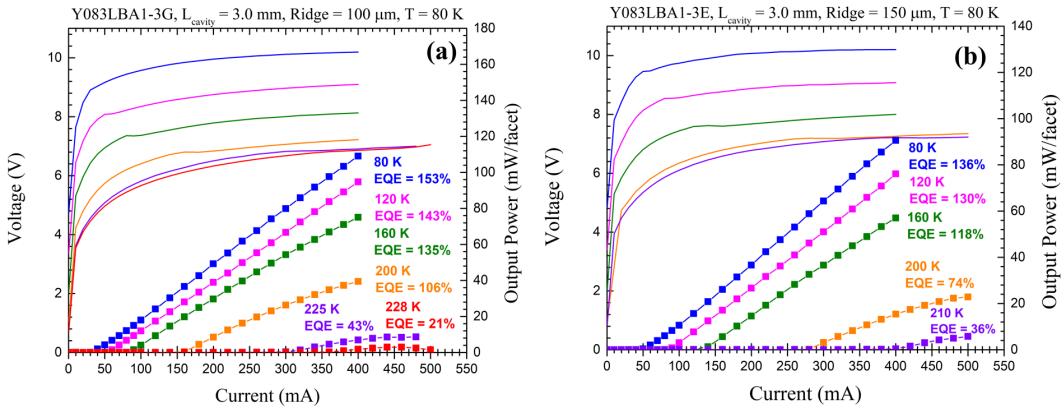

Figure 7.13: CW IVL characteristics for (a) Y083LBA1-3G and (b) Y083LBA1-3E from 80 K to their maximum operating temperatures of 228 K and 210 K, respectively. Also shown are the extracted external quantum efficiency values (EQE).

In pulsed operation devices Y083LBA1-3G and Y083LBA1-3E were able to lase up to 370 K with a J_{th} = 1003.3 A/cm^2 and 360 K with a J_{th} = 668.9 A/cm^2, respectively, as shown in Figs 7.14 (a) and (b). No device from this ICL wafer was taken to failure but considering the increased heat load with the higher threshold voltage, these devices could fail at slightly reduced temperatures compared with those made from Y082L. Y083LBA1-3G lased at RT with an emission wavelength

of $\lambda = 3.42$ μm and a slightly larger $J_{th} = 197.3$ A/cm^2 compared to Y082LBA1-3F. Y083LBA1-3E lased at a similar wavelength with a $J_{th} = 195.6$ A/cm^2.

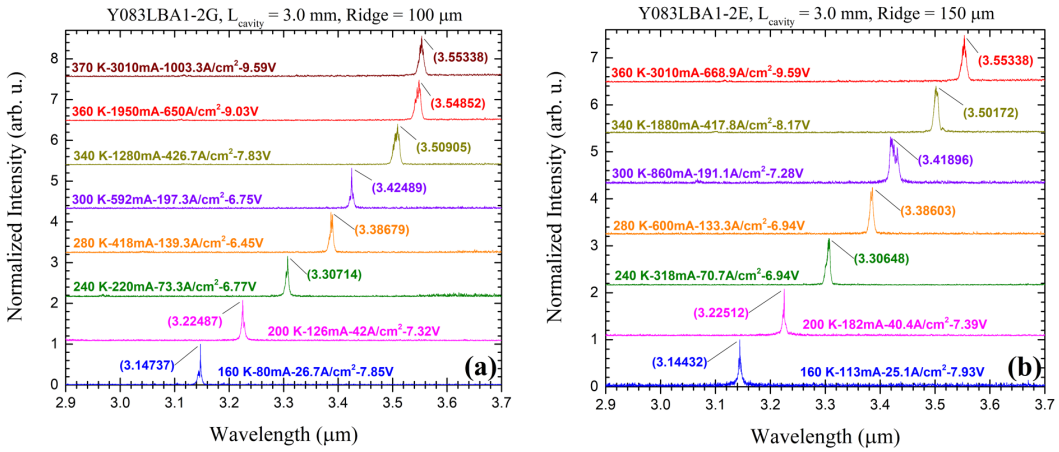

Figure 7.14: Normalized spectra under pulsed excitation for (a) Y083LBA1-3G and (b) Y083LBA1-3E. Shown in the plot are the threshold current, threshold current density, threshold voltage, and emission wavelength at each temperature step.

Devices made from Y082L and Y083L showed similar performance between 80 K and their maximum pulsed operating temperatures, with devices from Y083L generally performing slightly worse overall, which is consistent with the predicted optical results based on the waveguide simulations presented earlier. Though the increased thickness of the SCL reduces the optical confinement within the QW active region for devices from Y083L, based on simulation results in Fig. 7.5, there should be a trade-off benefit in the smaller predicted free-carrier absorption loss for devices from Y083L. This is still the case even when the effects of the thinner InAs/AlSb SL intermediate cladding and cascade portions of the device are considered in the simulation. In practice, however, the trade-off does not seem to aid the performance of devices from Y083L at elevated temperatures. This might be due to some uncertainties related to variations among the ICL structures during the MBE growth and device fabrication processes, considering that the V_{th} in devices made from Y083L were larger than that of devices from Y082L. Actually,

both ICL wafers were designed with a predicted V_{th} = 3 V at RT and considering that devices from both ICL wafers failed to hit this mark indicates at least similar issues related to the crystal quality and/or fabrication. Also, both ICL wafers were designed to emit at 3.3 μm at RT. However, devices from Y083L lased with an emission wavelength that was about 3.6% longer than the intended design at RT, which is closer to the λ_p, leading to higher free-carrier losses from the plasmon cladding. This may suggest that there were additional non-uniformities between both ICL wafers in terms of the growth of their active regions, or it may be related to the slightly poorer temperature performance in Y083L, which could result in a marginally more red-shifted emission.

7.3.3 Comparison of Y082/83L to Y061/62L

A puzzling curiosity is that even though the thickness deviation of the cascade region was more severe in devices made from ICL wafers Y082L and Y083L, their measured emission wavelengths at RT were quite close to the intended design, instead of the large blue-shift observed in Y061L and Y062L. The wavelength for Y082LBA1-3F and -3H was about 3.284 μm, while the wavelength for Y083LBA1-2G and -2E was about 3.422 μm, where an average deviation in the cascade thickness was about -14.5% and -11.7%, respectively. In Y061L, the wavelength at RT varied from 3.30-3.41 μm and for Y062L varied from 3.45-3.53 μm, where the deviation in the cascade thickness was about -6.1% and -5.8%, respectively. This may suggest that the thickness deviation in the more recently grown ICL wafers occurred away from the W-QW structure and was, therefore, less impactful to the emission wavelength.

However, both Y082L and Y083L have cascade active regions that are shorter than expected, and this effect should be manifested at least partially in the blue-shifting of the emission as it is hard to believe that such growth deviations could

be localized to only certain portions of the SL cladding. Therefore, it should be expected that there is a partial contribution to the blue-shift of the ICL emission due to the thinner cascade active region. But because of these structural deviations, there are also predicted increases in the free-carrier loss and required threshold gain for lasing, which would require an increased injection current to achieve lasing, consequently increasing the heating in the system and adding a small red-shift to the emission. Therefore, one may argue that there are two competing effects which take place that result in only a mild blue-shift in Y082L and a mild red-shift in Y083L, which may be attributed in the latter to the increased thickness of the SCL. Although there may be slightly more heating because of these effects, it should be noted that this should present as a minor contribution as the devices were tested at 300 K in pulsed mode with a relatively low duty cycle (0.5%), and thus any heating effect at RT should already be fairly limited.

More recently, it has been discovered from initial testing of newly grown ICL wafers (Y088L and Y089L), which no longer exhibit such thickness deviations, that the RT emission is roughly around 3.62 μm. This suggests that there may be some discrepancy between design and experiment and that the thickness of the InAs QWs used in the cascade active region are not designed quite right in order to achieve the desired 3.30 μm emission. If that is the case, then it may be assumed that the emission should be at around 3.60 μm, and the observed 13% thickness deviation may contribute to a blue shift of about $\lambda = 3.60 \times 0.87\% = 3.132$ μm, which is much more in line with the observed RT emission wavelength for Y082L. Additionally, there was also a major difference between the two sets of ICL wafers (Y061L/62L vs Y082L/83L) based on the MBE growth, where appropriate steps were taken in Y082L/83L to minimize the potential As incorporation into unwanted sections of the QW active region by utilizing Sb-soaks, although this is merely the first iteration of this MBE growth change and more systematic procedures

may be further developed in the future. Therefore, it may be the case that the observed blue-shift in Y061L and Y062L, beyond that suggested by the thickness deviations, could be primarily attributed to this effect.

7.4 Follow Up Study of GaSb-based ICLs Y086L and Y087L

Recently, two new GaSb-based ICL wafers were grown on the GENxplor, both with six cascade stages and identical cascade structures compared with Y082L and Y083L, except that in Y087L, two of the GaSb layers in the active region have slightly increased thicknesses. These GaSb layers form part of the hole injector QWs and this change should enable a smoother carrier transport. Also, the waveguide for Y086L and Y087L is identical to that of Y082L. Overall, this amounts to Y086L being an identical repeat of Y082L, with effort here focused on higher crystalline quality and better fabrication, forming a comparative study between devices from ICL wafers Y082L, Y086L, and Y087L. Section 7.4.1 presents the growth characteristics from this second iteration of GaSb-based ICLs with the advanced waveguide, while Section 7.4.2 discusses the potential impact of growth deviations on the various optical properties calculated from waveguide simulations. In Sections 7.4.3 and 7.4.4, the performance of devices from Y086L and Y087L is presented. Further discussions and comparisons to devices from Y082L are then elaborated upon in Section 7.4.5.

7.4.1 Growth Characteristics of Y086L and Y087L

Based on the feedback from Y082L and Y083L, two new six-stage GaSb-based ICL wafers (Y086L and Y087L) were grown by molecular beam epitaxy (MBE) using a Veeco GENxplor with As and Sb supplied by valved cracking sources.

As before, steps were taken to minimize the potential incorporation of As into unwanted layers within the W-QW active region by also implementing Sb-soaks into that crucial part of the growth. The intent of experiment was to refine the growth to reduce the thickness deviations observed in Y082L and Y083L. To characterize the effectiveness of these growth modifications, the crystalline quality of the grown ICL wafers was analyzed using x-ray diffraction (XRD) and the surface morphology was characterized by differential-interference-contrast microscopy (DIC). From the DIC images, typical oval hillock defects were observed – common to III-V ICL growth, but with little background surface roughness. The average surface defect density of Y086L was about 4.7 $\times$ 10^3 cm^{-2}, while that of Y087L was about 1 $\times$ 10^3 cm^{-2}, significantly lower than the defect density of Y086L. These newer ICL wafers had a reduced number of surface defects, however, they both exhibit a larger degree of surface roughness as shown in the DIC images in Fig. 7.15, implying a larger degree of potential relaxation than previous ICLs.

From the XRD measurements, symmetric scans normal to the (004) planes indicate that there were once again deviations in both the InAs/AlSb SL intermediate cladding and the cascade thicknesses, as shown in the representative XRD pattern in Fig. 7.16. Between both ICL wafers, an average tensile strain for the SL cladding of 0.044% in the growth direction (biaxial compressive strain) was observed, indicating an improvement in the strain balancing of the SL intermediate cladding, possibly indicating a better overall crystalline quality of these ICL wafers. The analysis of the XRD pattern showed that on average, the InAs/AlSb SL intermediate cladding was about 16.86% thicker than expected, while the cascade region was about 13.39% thicker than expected, which deviates in the opposite direction compared with Y082L and Y083L. After much discussion, it was discovered that the reason for these large growth deviations of the recent GaSb-based ICLs was due an improper use of Eq. 3.22, where the small angle approximation was being

made during growth calibration samples of the InAs/AlSb SL. This issue will be fixed in future ICL growth.

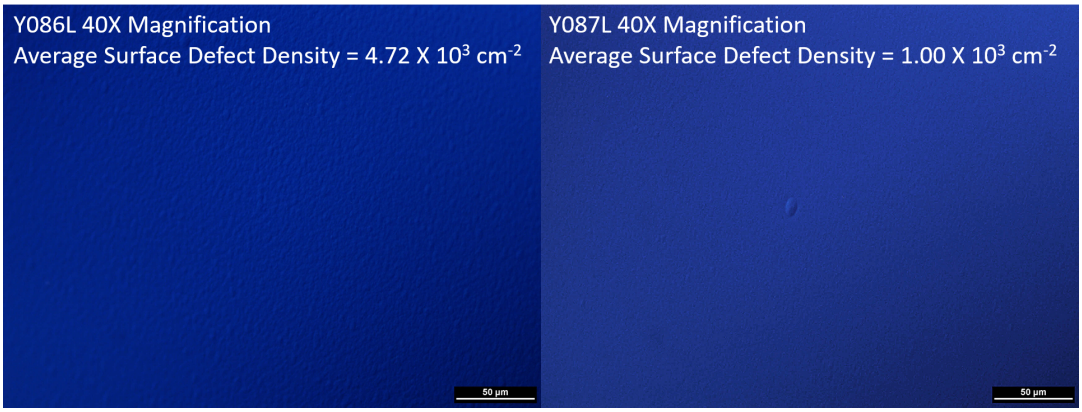

Figure 7.15: DIC images of Y086L (left) and Y087L (right) under 40× magnification. Both wafers have a similar average surface defect density as shown, which is slightly smaller than previous GaSb-based ICLs. However, the background surface roughness in both of these new ICL wafers is larger than previous ICLs.

7.4.2 Growth Impact on the Potential Operation for Y086L and Y087L

Considering that the InAs/AlSb SL intermediate cladding layer is thicker than the intended design, one can speculate as to the impact this may have on the operation of devices from these ICL wafers. First, a thicker SL cladding would lead to a larger overall thermal resistance of the device, which could potentially lead to a slightly red-shifted emission wavelength with increasing heat-sink temperature. Depending on how the cascade thickness variation occurs, the increased thickness could also lead to a red-shifted emission if the W-QW structure is affected as well. Furthermore, because the plasma effect is being exploited in the InAsSb plasmon cladding, if the optical emission wavelength of the ICL approaches the plasma wavelength (λ_p), then the real part of the refractive index will sharply decrease leading to variations in the confinement factor and free-carrier absorption loss.

Consider Fig. 7.17, which shows the calculated optical modal profile and

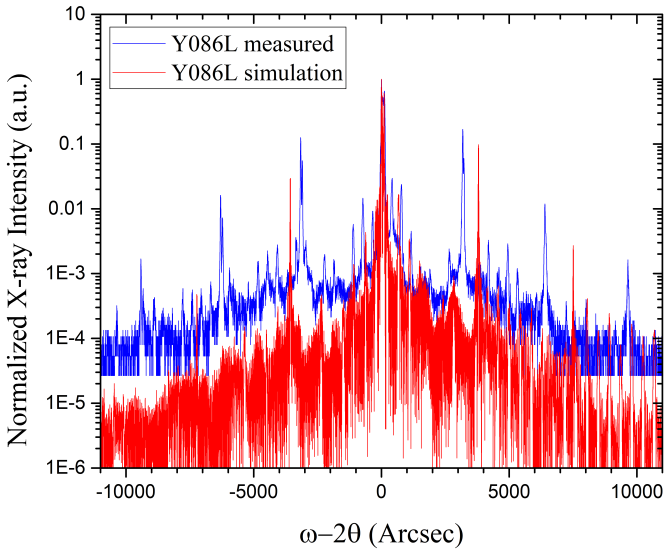

Figure 7.16: The experimentally measured XRD pattern (blue) along with the simulated pattern (red) for Y086L, which is representative of both ICL wafers grown.

refractive index for both Y082L (red) and Y086L (blue) based on the intended operating wavelength of $\lambda = 3.30$ μm, but with the associated thickness deviations in the InAs/AlSb SL intermediate cladding and the cascade active region. Shown in the plot are the calculated optical parameters for both ICL wafers, where an increase in the optical confinement of $\Gamma = 24\%$ is predicted for Y086L. The simulation also shows a decrease in both the free-carrier loss and the required threshold gain compared to Y082L of $\alpha_i = 4.19$ cm^{-1} and $g_{th} = 34.1$ cm^{-1}, respectively. In the Y086L and Y087L ICL wafers, the predicted increase in the optical confinement is qualitatively in line with a thicker cascade region as more of the optical wave may exist there. Also, the predicted decrease in the free-carrier loss is expected since the thicker SL intermediate cladding results in less of the optical wave being allowed to leak into the plasmon cladding layers, although the decrease is not as dramatic as one may expect. The differential overlap percentage indicates that the plasmon cladding layer is responsible for the largest contribution to the total

free-carrier loss in an optimized waveguide. However, there still exists free-carrier losses in other portions of the structure with a complex index of refraction, which is accounted for in the simulation.

For example, in the simulation for Y082L presented in Section 7.2.1, about 0.95% of the optical wave is contained within the plasmon cladding layer, leading to a free-carrier loss contribution of $\alpha_{i,plasmon} = 4.0$ cm^{-1}, while 19.6% of the wave is contained within the cascade active region, resulting in a free-carrier loss contribution there of $\alpha_{i,active} = 1.79$ cm^{-1}. For Y086L, about 0.44% of the optical wave overlaps with the plasmon cladding, resulting in a free-carrier loss contribution of $\alpha_{i,plasmon} = 1.85$ cm^{-1}, while 24.0% exists in the cascade active region, with a net contribution of $\alpha_{i,active} = 2.19$ cm^{-1}. These initial simulations indicate that devices from ICL wafers Y086L and Y087L may perform better as they are expected to have fewer optical losses and lower threshold gain. However, in practice the complicated interactions of these structural deviations may also lead to operating wavelength differences from the intended design, which can modify the various input parameters for the waveguide simulations and the associated discussion above. These effects will be further explored in the performance characterization of devices from Y086L and Y087L.

7.4.3 Performance Results of Y086L

Just as before, despite the structural deviations of grown ICL wafers, BA devices made from these ICL wafers exhibited reasonable lasing performance in both cw and pulsed modes with several devices tested between both ICL wafers, Y086L and Y087L. In cw mode, representative 100/150-μm-wide devices with 3-mm-long cavity lengths from the first ICL wafer, Y086LBA1-1H and Y086LBA1-1F, lased at 80 K with emission wavelengths of $\lambda = 3.36$ and 3.37 μm, respectively, and had similar threshold current densities of $J_{th} = 7$ and 6.9 A/cm^2, about 30% lower than

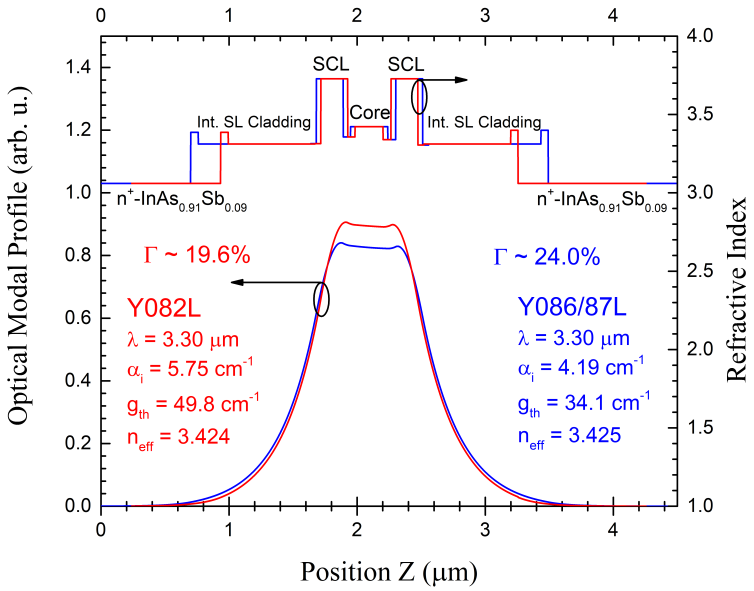

Figure 7.17: The calculated optical modal profile and refractive index for Y082L (red) and Y086L (blue) based on the intended operating wavelength, but with the structure thicknesses modified by the measured XRD results.

those from Y082L. These devices had improved threshold voltage values of V_{th} = 3.25 and 3.59 V, respectively, about 50% reduced compared to devices from Y082L, indicating possible smoother carrier transport and/or fewer non-uniformities in fabrication and crystal quality. The 2-mm-long cavity length devices from this ICL wafer (Y086LBA1-2A/B and Y086LBA1-2C) went on to operate up to 260 K and 250 K, respectively, in cw mode with emission wavelengths of λ = 3.772 and 3.767 μm, J_{th} = 152.5 and 103.3 A/cm^2, and V_{th} = 3.12 and 3.01 V, respectively, as shown in Fig. 7.18.

The cw current-voltage-light (IVL) characteristics of the two representative devices, Y086LBA1-2B and Y086LBA1-2D, are shown in Fig 7.19 (a) and (b), respectively. Y086LBA1-2B reached a peak EQE at 80 K of 210%, and subsequently dropped with increased heat-sink temperature to 42% at its maximum cw operating temperature of 260 K. Meanwhile, Y086LBA1-2D showed a peak EQE at 80 K of 234%, and subsequently decreased to 57% at 250 K. The difference in the measured

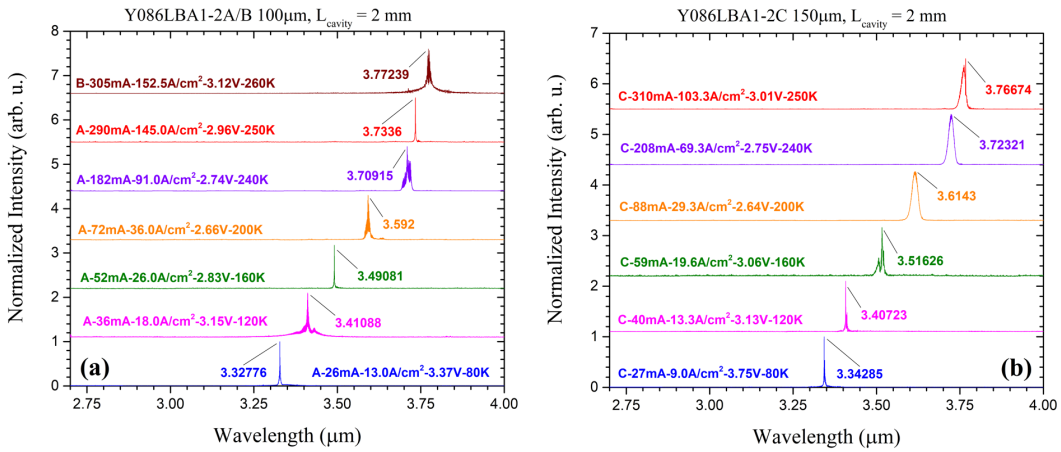

Figure 7.18: Normalized spectra under cw excitation for (left) Y086LBA1-2A/B and (right) Y086LBA1-2C. Shown in the plot are the threshold current, threshold current density, threshold voltage, and emission wavelength at each temperature step.

EQE for devices from Y086L and Y082L may be partially due to variations in alignment of the power meter but may also be related to the superior lasing characteristics for devices from Y086L as shown in Fig. 7.20.

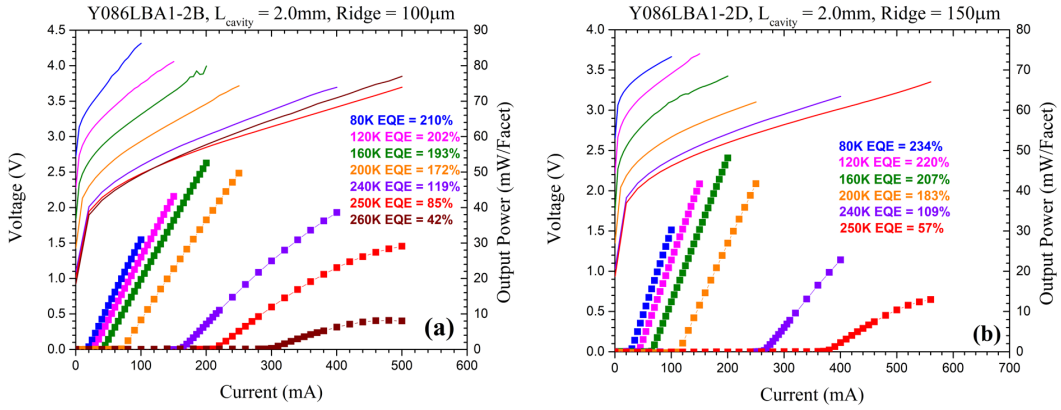

Figure 7.19: CW IVL characteristics for (a) Y086LBA1-2B and (b) Y086LBA1-2D from 80 K to their maximum operating temperatures of 260 K and 250 K, respectively. Also shown are the extracted external quantum efficiency values (EQE).

In pulsed operation, (5kHz repetition rate and 1 μs pulse width) the 3 mm cavity length devices (Y086LBA1-1H and Y086LBA1-1F) were able to lase up to 360 K and 340 K, with the results shown in Fig. 7.21. At their maximum operating

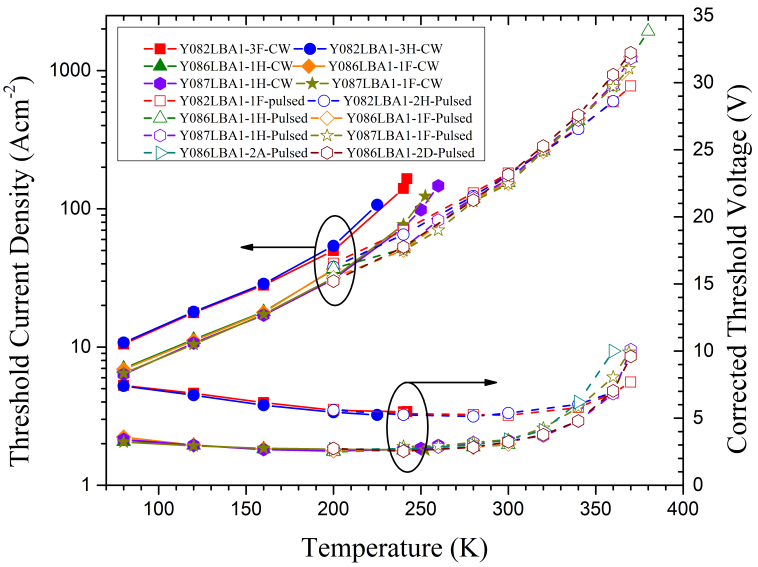

Figure 7.20: The J_{th} and V_{th} as a function of temperature for devices from ICL wafers Y082L, Y086L, and Y087L with different laser ridge widths in both cw (solid) and pulsed (dashed) modes.

temperature, these devices had emission wavelengths of 3.90 and 3.89 μm, and threshold current densities of J_{th} = 771.3 and 443.8 A/cm^2, respectively. At RT, these devices lased at 3.82 μm with nearly equal threshold current densities of J_{th} = 154.7 and 153.8 A/cm^2, respectively. This emission wavelength at RT is red-shifted somewhat severely, by about 0.5 μm from the intended design value of 3.30 μm. Their V_{th} = 3.02 and 3.06 V, respectively, leading to voltage efficiencies of about 64.4% and 63.6%. Though this is an improvement compared to devices from Y082L, it is still lower than that of close to 80% for GaSb-based ICLS with the traditional waveguide operating in this wavelength range. This indicates that there may be somewhat unsmooth carrier transport in the ICLs presented here, which may be reflective of the deviations in the layer thicknesses. However, in the ICLs from Ref. ([162]), techniques to enhance the thermal properties of the ICLs such as thinned substrates and reduced duty cycles were implemented. The pulsed operation of Y086LBA1-1H and Y086LBA1-1F could be extended slightly higher by decreasing

the duty cycle from 0.5% to 0.1% where the repetition rate was reduced to 1kHz, which reduces heating in the cascade active region. However, this repetition rate, is too close to the Fourier frequency of the FTIR, defined as $Fourier\ frequency = 2 \times optical\ velocity \times wavenumber \approx 2\ kHz$, which can cause interference in the interferogram signal, resulting in fake signals in the measured data. The optical velocity of the moving mirrors would need to be reduced by several factors which can greatly increase data acquisition time. Instead, an external InSb detector was used to conduct pulsed IVL measurements, and though the emission wavelength could not be measured in this way, it nevertheless allows for the determination of the maximum pulsed operating temperature for these BA ICLs of 380 K and 370 K, respectively.

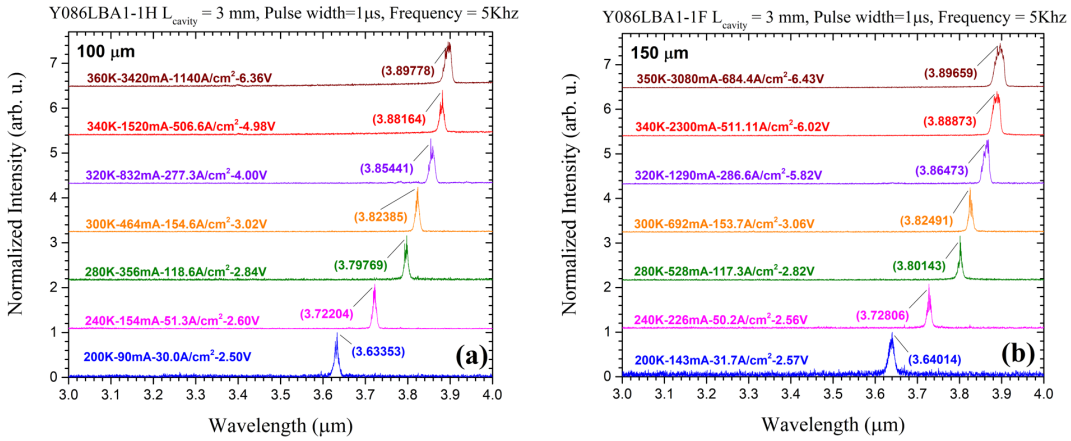

Figure 7.21: Normalized spectra under pulsed excitation for (a) Y086LBA1-1H and (b) Y086LBA1-1F. Shown in the plot are the threshold current, threshold current density, threshold voltage, and emission wavelength at each temperature step.

For devices from the Y086L ICL wafer, their T_o values ranged from 46.5-48.9 K, which are somewhat smaller than devices from Y082L. Though the performance at 80 K for devices from Y086L were superior to those from Y082L, both their J_{th} and V_{th} values exceeded that of devices from Y082L at elevated temperatures, as reflected in Fig. 7.20, which resulted in the decreased T_o values measured. This is

likely due to the red-shifted emission from the intended design at 300 K and the associated changes in the optical parameters for these ICLs, the consequences of which will be explored in Section 7.4.5, based on updated waveguide simulations.

7.4.4 Performance Results of Y087L

Compared to devices from Y086L, those from Y087L consistently showed a slightly lower cw threshold current density of about J_{th} = 6.3 and 6.4 A/cm^2, for 100-μm-wide and 150-μm-wide devices, respectively, indicating a lower Shockley-Read-Hall (SRH) recombination, consistent with the observed smaller defect density in Y087L. SRH recombination is a type of non-radiative recombination that occurs in semiconductors. In this process, an electron in the conduction band recombines with a hole in the valence band, but instead of emitting a photon, the energy is dissipated as heat. SRH recombination occurs when there are defects or impurities (sometimes called trap states) in the semiconductor material that trap electrons or holes, preventing them from participating in the normal recombination process. These devices lased with cw emission wavelengths at 80 K that were similar to those of devices from Y086L, but with slightly reduced threshold voltages of V_{th} = 3.42 and 3.22 V, respectively. Representative devices from this ICL wafer, Y087LBA1-1H (100-μm-wide) and Y087LBA1-1F (150-μm-wide), showed comparable maximum cw operating temperatures to those from Y086L of 260 K and 252.5 K, respectively. They had emission wavelengths of λ = 3.8 and 3.78 μm, J_{th} = 146.7 and 123.3 A/cm^2, and V_{th} = 2.96 and 2.62 V, respectively, as shown in Fig. 7.22. Overall, the cw lasing characteristics for devices from Y087L exhibit slightly better performance than those from Y086L, which may be reflective of the change to the GaSb layer thicknesses in the hole injector but may also be due to more uniformity in the crystal quality and/or the fabrication.

The cw current-voltage-light (IVL) characteristics of the two representative

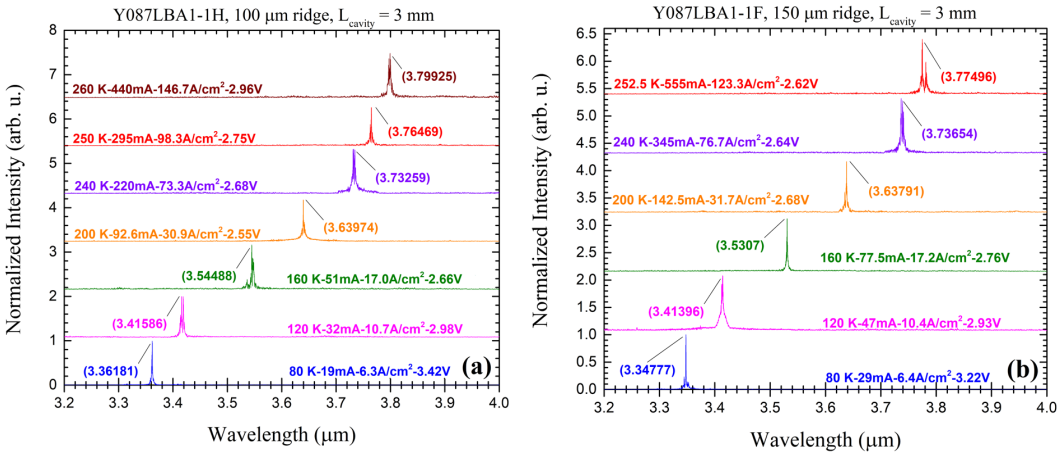

Figure 7.22: Normalized spectra under cw excitation for (a) Y087LBA1-1H and (b) Y087LBA1-1F. Shown in the plot are the threshold current, threshold current density, threshold voltage, and emission wavelength at each temperature step.

devices, Y087LBA1-1H and Y087LBA1-1F, are shown in Fig. 7.23, in which appreciable output power was observed up to 250 K for both devices. Y087LBA1-1H reached a peak EQE at 80 K of 217%, and subsequently dropped with increased heat-sink temperature to 76% at 250 K. Similarly, Y087LBA1-1F reached a peak EQE at 80 K of 219% and dropped to 59% at 250 K. Once again, the difference in the measured EQE for devices from Y087L and Y082L may be partially due to variations in alignment but may also be related to the superior lasing characteristics for devices from Y087L, similar to Y086L. Between devices from ICL wafers Y086L and Y087L, similar EQE values were observed.

In pulsed operation, (5kHz repetition rate and 1 µs pulse width) the Y087LBA1-1H and Y087LBA1-1F devices were able to lase up to 368 K and 369 K, the results of which are shown in Fig. 7.24. At their maximum operating temperature, these devices had emission wavelengths of 3.913 and 3.918 μm, and threshold current densities of J_{th} = 1120 and 1031.1 A/cm^2, respectively. At RT, these devices lased at 3.83 μm with threshold current densities of J_{th} = 162.7 and 151.1 A/cm^2, respectively. Similar to Y086L, devices from Y087L had emission wavelengths at

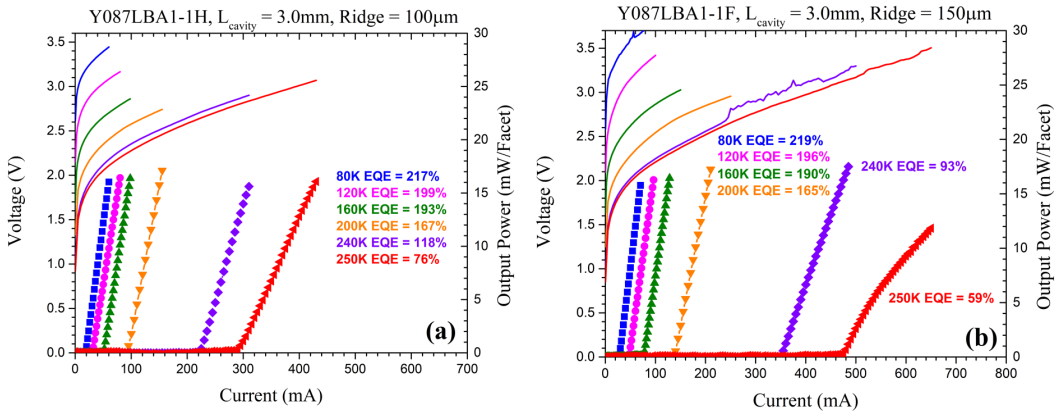

Figure 7.23: CW IVL characteristics for (a) Y087LBA1-1H and (b) Y087LBA1-1F from 80 K to 250 K, respectively. Beyond 250 K, no appreciable output power was detected in cw mode. Also shown are the extracted external quantum efficiency values (EQE).

RT that were red-shifted by a similar amount. Their threshold voltages at RT were V_{th} = 3.34 and 3.39 V, respectively, leading to voltage efficiencies reduced compared to those of Y086L, with values of 58.2% and 57.4%, respectively. This may indicate that there was possibly a slightly higher series resistance at elevated temperatures compared to that in Y086L, given that the threshold voltage was actually a little lower in devices from Y087L with a lower J_{th} at low temperatures but rose more swiftly at elevated temperatures as shown in Fig. 7.20. For devices from this ICL wafer, their T_o values ranged from 48.8-49.0 K, which are comparable to those from the Y086L ICL wafer. Similar to devices from Y086L, those from Y087L had superior performance at 80 K compared to those from Y082L. However, at elevated temperatures beyond 300 K, both their J_{th} and V_{th} values exceeded that of devices from Y082L, as reflected in Fig. 7.20 for reasons that are likely similar to those from Y086L, related to the red-shifted emission and change in the various optical properties associated with that, as discussed in Section 7.4.5.

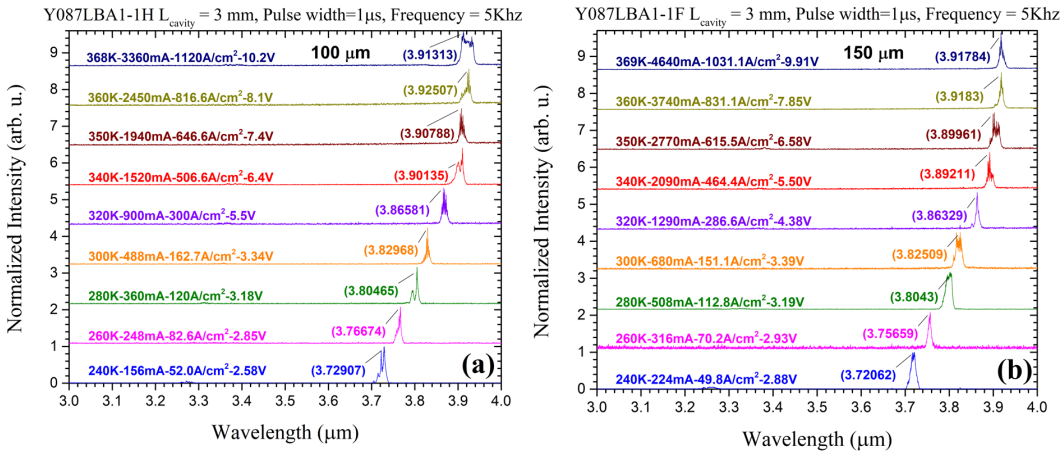

Figure 7.24: Normalized spectra under pulsed excitation for (a) Y087LBA1-1H and (b) Y087LBA1-1F. Shown in the plot are the threshold current, threshold current density, threshold voltage, and emission wavelength at each temperature step.

7.4.5 Discussion and Comparison between Y082L, Y086L, and Y087L

Compared to devices from Y082L, those from Y086L and Y087L, had thicker cascade active regions and InAs/AlSb SL intermediate cladding layers and consistently lased with superior characteristics from low to RT, but with decreased performance above that point. Though the cascade active region and the SL intermediate cladding layers were similarly deviated from the design compared to Y082L, but in the opposite direction, their lasing emission at RT varied much more significantly than those from Y082L. One consideration is that the thinner cascade active region in devices from Y082L blue-shifts the emission, while at the same time the optical losses increase due to the various factors discussed in Section 7.2.2. Thus, a competing effect occurs in devices from that ICL wafer which results in only a mild overall blue-shift at RT with emission at $\lambda = 3.28$ μm, instead of the intended $\lambda = 3.30$ μm. Conversely, in devices made from Y086L and Y087L, the emission is red-shifted due to the thicker cascade active region. This then results in the optical wave at RT being closer to the plasma wavelength for the highly doped

$InAs_{0.91}Sb_{0.09}$ plasmon cladding ($\lambda_p = 6.47$ μm at the doping level of 3.2×10^{19} cm^{-3}). If the emission wavelength of the ICL approaches the λ_p in the plasmon cladding layer, although the real part of the refractive index of the material will sharply decrease, the free-carrier absorption loss will significantly increase. At first glance, it would appear that the λ_p is far enough away from the emission wavelength of the devices from ICL wafers Y082L/86L/87L to not be impacted in terms of the increased free-carrier absorption loss. The estimated free-carrier loss in a bulk $InAs_{0.91}Sb_{0.09}$ layer at a wavelength matching that of Y082L ($\lambda = 3.28$ μm) is $\alpha_i = 427.7$ cm^{-1}, while for a wavelength matching that of Y086L/87L ($\lambda = 3.83$ μm) is 602.7 cm^{-1}, nearly 41% greater in the latter. Additionally, there are doped layers in the cascade active region and the SL intermediate cladding layers, so the free-carrier absorption loss there would also be higher with the longer lasing wavelength. Therefore, we can expect that the overall free-carrier loss in Y086L and Y087L to be greater than that in Y082L, despite less of the optical wave overlapping with the plasmon cladding layer in the latter ICLs. Taken together (the thicker cascade active region and increased optical losses) these effects compound for Y086L and Y087L, resulting in a much more dramatic shift in the RT emission wavelength and may explain why the J_{th} begins to more sharply increase in devices from Y086L and Y087L at elevated temperatures.

Indeed, the extracted optical parameters for Y086L and Y087L from the waveguide simulation using a RT emission wavelength of $\lambda = 3.82$ μm, along with the thickness deviations in the cascade active region and the SL intermediate cladding layers lead to predicted values of the various optical parameters of $\Gamma = 21.3\%$, $\alpha_i = 9.63$ cm^{-1}, and $g_{th} = 64.1$ cm^{-1}. Note that the predicted free-carrier loss is nearly 50% larger at RT than the previous estimate in Section 7.2.2, due to the red-shifted emission. With the increased emission wavelength, the overlap of

the optical wave with the plasmon cladding layers jumps from 0.49% as previously discussed to 0.66%, leading to an increase in the contribution of the free-carrier loss due to the plasmon cladding layer of $\alpha_{plasmon} = 4.03$ cm^{-1}, which is increased by nearly two times compared to the discussion in Section 7.2.2. Similarly, the contribution to the free-carrier loss due to the cascade active region is $\alpha_{active} = 2.66$ cm^{-1}, which is increased by about 30% compared to the previous discussion. In order to rectify this situation, a larger doping concentration would be needed in the plasmon cladding layer in order to further red-shift the λ_p so that the free-carrier loss contribution in the plasmon cladding could be reduced.

In summary, three nearly identical (by design) ICL wafers (Y082L, Y086L, and Y087L) with advanced waveguides were grown by molecular beam epitaxy (MBE). The advanced waveguide promises to enhance the thermal and optical properties of the ICLs and consists of the cascade active region, encapsulated by n-doped GaSb separate confinement layers (SCLs), n-doped InAs/AlSb SL intermediate cladding layers, and n$^+$-doped $InAs_{0.91}Sb_{0.09}$ plasmon cladding layers. These ICL wafers were designed to emit at $\lambda = 3.30$ μm at room temperature (RT). However, due to structural deviations which occurred during the MBE growth, the resulting emission wavelengths at RT for devices made from these ICL wafers varied between $\lambda = 3.28$ μm and 3.82 μm. These effects may be qualitatively explained based on the measured XRD patterns and the extracted optical properties of these ICLs based on waveguide simulations, which consider the shifted emission wavelengths and various structural deviations. Despite the differences compared to the intended design, unthinned broad area (BA) devices from these ICL wafers consistently lased close to 260 K in cw mode, and as high as 390 K in pulsed mode. Furthermore, devices made from these ICL wafers demonstrated RT threshold current densities as low as 151 A/cm^2 and voltage efficiencies of 64%, which are comparable with

state-of-the-art GaSb-based ICLs with traditional waveguides (134 A/cm^2 and 70%, respectively). Also, characteristic temperatures slightly smaller than (Y086L and Y087L), and even greater than (Y082L) state-of-the-art GaSb-based ICLs with the traditional waveguide were observed. These features suggest considerable potential for GaSb-based ICLs with the advanced waveguide designed to operate at shorter wavelengths.

Chapter 8

Conclusion and Future Directions

8.1 Dissertation Summary

This dissertation focused on the MBE growth of interband cascade structures mainly related to ICLs, but with some extension into ICTPVs, using III-V materials such as InAs, GaSb, AlSb, and their related alloys, as well as the optical characterization of long wavelength InAs-based and mid wavelength GaSb-based ICL devices. The ICL utilizes a multiple cascade stage design to boost the gain, per current density, in order to generate light from injected carriers with quantum efficiencies that exceed the conventional limit of unity. Chapter 1 introduced many of the laser fundamentals and developments over time which led to the modern ICL.

The overall ICL structure is built from a combination of multiple superlattice (SL) heterostructures, forming as many as hundreds of individual layers, with some of the layers having sub-nanometer thicknesses. Therefore, the growth of these devices requires atomic layer precision in thickness control in order to achieve an overall strain-balanced system where defects are minimized, leading to superior crystalline quality. MBE is a particularly well suited crystal growth technique that meets these demands, and so Chapter 2 introduced the principles of MBE growth. Additional discussions related to how the growth rate may be controlled from a careful calibration using RHEED oscillations were presented. SL structures require sufficient strain-balancing in order to have minimal defects in the larger ICL structure, and therefore a description of strain in MBE growth structures and several strain-balance methods was also introduced. The specific MBE setup used in this dissertation, the GENxplor, was discussed with emphasis placed on

how various growth related parameters are controlled like the UHV conditions and substrate temperature.

Chapter 3 covered several techniques that were used to characterize the quality of MBE grown materials, including Hall measurements, differential-interference-contrast (DIC) microscopy, and x-ray diffraction (XRD). Hall measurements provided a direct evaluation of the carrier concentration in a bulk epilayer, which allowed for the calibration of the various doping cells used. DIC microscopy was employed for the qualitative assessment of the surface morphology as well as the quantitative determination of the average surface defect density of MBE growth structures. XRD provided an invaluable tool to analyze IC growth structures as it was able to estimate several growth figures of merit such as the material quality, the growth thicknesses of bulk and SL layers, alloy compositions, and the epilayer strain.

Many of the growth studies conducted during this work were presented in Chapter 4. In order to identify where possible shortcomings existed in the growth of full IC structures, the various sub-components were grown including various alloys, the InAs/AlSb SL, and the GaSb buffer layer. The optimization of the InAsSb alloy on GaSb was first conducted for thin epilayers ($\approx$ 300 nm) and was later extended to thicker layers (> 1 μm), as required for the plasmon cladding in an ICL. The composition was determined from XRD spectra using Eq. 4.4, with subsequent growths having slightly varied As and Sb valve openings to achieve the desired composition. Later, when developing the AlAsSb alloy for the DBR, a more methodical approach was developed which involved plotting the As valve opening as a function of the As composition as measured from the XRD spectra. The data could then be fit with a power fit (Fig. 4.26) and the ideal valve opening for a desired As composition could be more accurately predicted. This alloy was successfully grown with the desired composition and several DBR structures were

then grown, which ultimately achieved the desired reflectance level of greater than 95% at the intended operating wavelength of 4 μm (Fig. 4.29). Early work on the GaSb-based ICL on the GENxplor was unsuccessful, and after much effort, it was determined to be due to the rough interface of the InAs/AlSb SL intermediate cladding layers (Fig. 4.14). This was caused by unwanted As incorporation when transitioning from InAs to AlSb growth (Fig. 4.15), creating interfacial layers of AlAsSb, and was addressed by developing an Sb-soak technique to minimize the possible thickness of the interface (Fig. 4.16). This technique was critical to the successful growth of GaSb-based ICLs on the GENxplor that were reported in Chapter 7 and was later adopted into the ICTPV growth to greatly improve the strain balance of the InAs/GaSb doped absorber.

Chapter 5 discussed some of the details related to device fabrication and the methodology for conducting optical characterization of ICLs. Many figures of merit, such as the threshold current density, threshold voltage, slope efficiency, external quantum efficiency, among many others, were introduced and discussions on how to extract the relevant parameters from measured data were presented. In order to accurately compare the measured pulsed output power between different ICL devices, and also to calculate the EQE among other parameters, a calibration was presented which related the measured results from the lock-in amplifier to the thermopile power meter. It was discovered that the resulting EQE values were source dependent, and the reason for this was attributed to the pulse shapes of the different sources used. Methods to address this issue were also investigated and presented.

ICLs have previously been well developed in the 3-6 μm range based on the traditional waveguide design using GaSb substrates. Previous efforts showed that an n^+-InAs plasmon cladding layer could replace the InAs/AlSb SL intermediate cladding in InAs-based ICLs and allowed for improved long wavelength operation,

up to 11.1 μm.[88] Also, at the same time an advanced waveguide, which placed back in a thin InAs/AlSb SL intermediate cladding layer between the InAs SCL and the plasmon cladding, could simultaneously reduce the free-carrier loss and also enhance the optical confinement within the cascade active region for InAs-based ICLs operating at 4.6 μm.[7] This advanced waveguide was implemented for the first time in InAs-based ICLs designed to emit beyond 10 μm as reported in Chapter 6. Broad area (BA) devices made from InAs-based ICL wafers with this design feature showed operation in cw mode up to 10.9 μm at 80 K with output powers of up to 32 mW/facet, the largest output power among interband lasers at this wavelength, and up to 11.5 µm at 137 K in pulsed mode, the longest emission wavelength achieved for the standard QW active region ICL. Chapter 6 also featured efforts related to the implementation of a new cascade active region, which employed $InAs_{0.5}P_{0.5}$ barriers within the QW active region and represents the first significant structural change to the cascade active region in the ICL in more than 10 years. The purpose of this experiment was to test the validity of the prediction in Ref. [8] that As and P containing barrier layers, with reduced valence band edges, could lower the electronic energy level in the InAs QWs in order to enhance the long wavelength operation of ICLs. This prediction meant that a thinner InAs layer could be used, which would enhance the electron-hole wavefunction overlap. Devices with this design change, as well as the advanced waveguide, achieved pulsed emission up to 120 K beyond 13.2 μm, which is the longest wavelength ever achieved among III-V interband lasers and first validated the prediction in Ref. [8]. Subsequent ICLs with these new design features went on to show cw operation beyond 12.4 μm, which is the first demonstration of a BA ICL operating in cw mode at such a long wavelength, and up to 150 K, beyond 13 μm in pulsed mode. These ICLs had cw output powers beyond 12 mW/facet,

comparable with and even higher than previous ICLs without $InAs_{0.5}P_{0.5}$ barriers operating at much shorter wavelengths (<10 μm).[9]

The success of the advanced waveguide for InAs-based ICLs spurred interested in adopting this design feature for GaSb-based ICLs designed to emit at shorter wavelengths. The initial results of GaSb-based ICLs with advanced waveguides were discussed in Chapter 7, with ICLs designed to emit at 4.6 μm at RT. However, these ICLs showed RT emission that was highly blue-shifted, by about 0.8 μm. This could not be fully accounted for by structural deviations in the cascade active region as measured from XRD spectra. In these early GaSb-based ICLs, Sb-soaks were used only in the InAs/AlSb SL structures, however, it was discussed that unwanted As incorporation into critical portions of the W-QW active region could potentially result in significantly blue-shifted emission. In follow up GaSb-based ICLs, Sb-soaks were implemented into virtually every layer with an As to Sb transition. Devices from the second iteration operated up to 370 K in pulsed mode, with one device taken to 390 K before it was damaged from a high injection current. A 150-μm-wide device showed RT operation at λ = 3.28 μm with a J_{th} = 176.9 A/cm^2, which is comparable to GaSb-based ICLs with the traditional waveguide, operating at 3.6 μm.[160] These ICLs were designed to emit near 3.3 μm and 3.4 μm at RT and showed only a minor blue shifted emission, despite having cascade active regions that were approximately 13% thinner than intended. It was suggested that this may be due to the fact that the SL intermediate cladding layer was also thinner than intended, which allowed more of the optical wave to leak into the InAsSb plasmon cladding, resulting in a higher overall threshold gain, requiring a larger injection current to achieve lasing, which competed against the blue-shifted emission from the cascade deviation. Nevertheless, the results of the second iteration of the GaSb-based ICLs qualitatively validated the prediction that unwanted As incorporation into the cascade active region contributed to the

blue-shifted emission observed in the initial devices. Follow up studies of a third iteration of GaSb-based ICLs with advanced waveguides and also designed to emit at 3.3 μm at RT were also presented. These ICLs had similar structural deviations in both the SL intermediate cladding as well as the cascade active region, but with the thickness deviations in the opposite direction (thicker). Devices from this latest round of testing showed improved threshold voltages and reduced threshold currents at lower heat-sink temperatures, which were predicted to be due to better crystal quality and fabrication. At RT, these devices showed emission at about λ = 3.82 μm with threshold current densities of about J_{th} = 155 A/cm^2. These ICLs showed similar temperature performance but had higher overall J_{th}'s at elevated temperatures which was due to their significantly red-shifted emission. Additionally, since the operating wavelength was closer to the plasma wavelength (λ_p) the free-carrier loss was increased in these ICLs, compared to the second iteration. The cumulative effect of this led to the increased J_{th} results at elevated temperatures and characteristic temperature (T_o) values that were reduced compared to the second iteration of device. Nonetheless, the GaSb-based ICLs with the advanced waveguide showed T_o values between 46.5-49 K, comparable to GaSb-based ICLs with the traditional waveguide. Some of the devices showed values closer to 60 K, which is the highest among RT ICLs with similar lasing wavelengths, indicating the potential for GaSb-based ICLs with the advanced waveguide.

8.2 Future Research Endeavors

There are several lines of inquiry for future research efforts. In terms of MBE growth, a more robust study of the optimization of the InAs/AlSb SL intermediate cladding should be conducted. The results presented in Chapter 4 provided a good starting point, but used only coarse adjustments to the soak time and

were developed in a sort of vacuum, without rigorous effort to also achieve high crystalline quality. Furthermore, the soak time developed from the thick SL was implemented into thin epilayer or SL transitions in other parts of the ICL, where there may not necessarily be a need for such a long soak time. Also, the nature of how the Sb soak in the GENxplor may affect the emission wavelength of ICLs should be further studied, as the results presented in Chapter 7 compete with growth deviations in other critical portions of the ICLs, which clouds the interpretation of the results where the overall influence is only qualitatively clear at this time.

While the success of the advanced waveguide and the InAsP barrier in the QW active region in InAs-based ICLs have shown tremendous promise, resulting in multiple world records for cw/pulsed emission wavelength and maximum cw output powers, the temperature performance of these ICLs is still relatively modest. Based on discussions in Chapter 6, these devices should be able to operate at higher temperatures. Further design iterations should attempt to create ideal waveguides that are optimized to the intended operating wavelength at higher temperatures. Furthermore, the role that the GaInSb hole well width plays in minimizing possible valence intersubband absorption loss should be investigated to enhance the carrier transport in these ICLs. This could be achieved by varying the thickness of that layer among several ICL structures and measuring the subsequent results. Once these ICLs begin to approach RT operation in pulsed mode, more advanced fabrication techniques should be used to enhance both the cw and pulsed performance.

For GaSb-based ICLs with the advanced waveguide, in the immediate future the issues in the growth of the cascade active region and the InAs/AlSb SL intermediate cladding need to be resolved. The devices tested and reported in Chapter 7 show great potential of the advanced waveguide, despite such large deviations in the

growth from the intended design. Once new growths are successful, focus can shift to more optimal waveguide designs based on the characterization feedback. Also, it would be interesting to explore long wavelength GaSb-based ICLs. In principle, the cascade active region between InAs-based and GaSb-based ICLs is quite similar. The main issue in extending the GaSb-based ICL to longer wavelengths is the rapid increase in thermal loss from the thicker InAs/AlSb SL cladding. The advanced waveguide has been demonstrated to improve the performance of both types of ICLs over a wide range of operating wavelengths and could be implemented in GaSb-based ICLs designed to emit at longer wavelengths. Furthermore, it would be interesting to integrate the modified barrier architecture with As/P containing compounds into the GaSb-based ICLs to further enhance their long wavelength emission. One could envision using the same ternary alloy in an initial design, although the 50/50 ratio of P:As on a GaSb substrate would contribute to a slightly higher degree of tensile biaxial strain, which may or may not be acceptable in the overall structure. For example, the lattice mismatch between $InAs_{0.5}P_{0.5}$ and InAs is about -1.57%, while for GaSb it is about -2.17%. Therefore, the P content could be slightly reduced for strain-balance considerations, while the As concentration increased. Although the valence band edge would rise slightly, it would still be below that of the AlSb barrier, which should still result in a decrease in the electronic energy level in the InAs QW. Other more novel quaternary alloys could also be explored, such as $Ga_xIn_{1-x}As_yP_{1-y}$.

References

[1] H. Ye, *Molecular Beam Epitaxy of InAs, GaSb, AlSb Structures for Interband Cascade Devices.* phdthesis, The University of Oklahoma, 2016.

[2] M. Grundmann, *The physics of semiconductors : an introduction including nanophysics and applications.* Berlin Heidelberg: Springer, 2010.

[3] S. H. Simon, *Oxford Solid State Basics.* 198 Madison Ave, New York, NY 10016, USA: Oxford University Press, 2013.

[4] J. Ayers, *Heteroepitaxy of semiconductors : theory, growth, and characterization.* Boca Raton: CRC Press, 2007.

[5] R. Q. Yang, "Research notes."

[6] Y.-Z. Lin, J. A. Massengale, W.-X. Huang, R.-Q. Yang, T. D. Mishima, and M. B. Santos, "Examination of the durability of interband cascade lasers against structural variations," *J. Infrared Millim. Waves*, vol. 39, Apr. 2020.

[7] L. Li, Y. Jiang, H. Ye, R. Q. Yang, T. D. Mishima, M. B. Santos, and M. B. Johnson, "Low-threshold InAs-based interband cascade lasers operating at high temperatures," *Applied Physics Letters*, vol. 106, p. 251102, jun 2015.

[8] R. Q. Yang, "Electronic states and interband tunneling conditions in type-II quantum well heterostructures," *Journal of Applied Physics*, vol. 127, p. 025705, jan 2020.

[9] Z. Tian, L. Li, H. Ye, R. Yang, T. Mishima, M. Santos, and M. Johnson, "InAs-based interband cascade lasers with emission wavelength at 10.4 μm," *Electronics Letters*, vol. 48, no. 2, p. 113, 2012.

[10] A. Schade and S. Höfling, "Long wavelength interband cascade lasers on GaSb substrates," in *Infrared Remote Sensing and Instrumentation XXV* (M. Strojnik and M. S. Kirk, eds.), SPIE, aug 2017.

[11] H. K. Choi, *Long-Wavelength Infrared Semiconductor Lasers.* Wiley Series in Lasers and Applications, John Wiley and Sons, Inc., 111 River Street, Hoboken, NJ 07030: Wiley, February 2005.

[12] S. S. Rassel, *Characterization and Development of Semiconductor Cascade Devices.* phdthesis, University of Oklahoma, 2018.

[13] T. Bauer, *Thermophotovoltaics.* Springer Berlin Heidelberg, 2011.

[14] T. Coutts, "A review of progress in thermophotovoltaic generation of electricity," *Renewable and Sustainable Energy Reviews*, vol. 3, pp. 77–184, jun 1999.

[15] C. Kumar and N. Patel, "Laser based in-situ and standoff detection of chemical warfare agents and explosives," in *Optically Based Biological and Chemical Detection for Defence V* (J. C. Carrano and C. J. Collins, eds.), vol. 7484, (Bellingham, Washington USA), pp. 7 – 20, International Society for Optics and Photonics, SPIE, 2009.

[16] S. Wallin, A. Pettersson, H. Östmark, and A. Hobro, "Laser-based standoff detection of explosives: a critical review," *Analytical and Bioanalytical Chemistry*, vol. 395, no. 2, pp. 259–274, 2009.

[17] J. R. Meyer, W. W. Bewley, C. L. Canedy, C. S. Kim, M. Kim, C. D. Merritt, and I. Vurgaftman, "The interband cascade laser," *Photonics*, vol. 7, no. 3, pp. 1–58, 2020.

[18] M. B. Pushkarsky, I. G. Dunayevskiy, M. Prasanna, A. G. Tsekoun, R. Go, and C. K. N. Patel, "High-sensitivity detection of tnt," *Proceedings of the National Academy of Sciences*, vol. 103, no. 52, pp. 19630–19634, 2006.

[19] M. von Edlinger, J. Scheuermann, R. Weih, L. Nähle, M. Fischer, J. Koeth, S. Höfling, and M. Kamp, "Interband cascade lasers for applications in process control and environmental monitoring," in *Light, Energy and the Environment 2015*, p. EM2A.5, Optica Publishing Group, 2015.

[20] M. Taslakov, V. Simeonov, and H. van den Bergh, "Line-of-sight data transmission system based on mid IR quantum cascade laser," in *Free-Space Laser Communication Technologies XX* (S. Mecherle, ed.), vol. 6877, (Bellingham, Washington USA), pp. 131 – 140, International Society for Optics and Photonics, SPIE, 2008.

[21] C. Bauer, U. Willer, R. Lewicki, A. Pohlkötter, A. Kosterev, D. Kosynkin, F. K. Tittel, and W. Schade, "A mid-infrared qepas sensor device for tatp detection," *Journal of Physics: Conference Series*, vol. 157, no. 1, p. 012002, 2009.

[22] M. Spearrin, C. Goldstein, C. Strand, and V. Miller, "https://www.spectraplot.com/." https://www.spectraplot.com/, Mar. 2021.

[23] C. R. Webster, P. R. Mahaffy, S. K. Atreya, G. J. Flesch, M. A. Mischna, P.-Y. Meslin, K. A. Farley, P. G. Conrad, L. E. Christensen, A. A. Pavlov, J. Martín-Torres, M.-P. Zorzano, T. H. McConnochie, T. Owen, J. L. Eigenbrode, D. P. Glavin, A. Steele, C. A. Malespin, P. D. Archer, B. Sutter, P. Coll, C. Freissinet, C. P. McKay, J. E. Moores, S. P. Schwenzer, J. C. Bridges, R. Navarro-Gonzalez, R. Gellert, and M. T. Lemmon, "Mars methane detection and variability at gale crater," *Science*, vol. 347, no. 6220, pp. 415–417, 2015.

[24] A. Einstein, "Zur quantentheorie der strahlung," *Phys. Z.*, vol. 18, p. 124, 1917.

[25] "Charles h. townes - biographical," 2005.

[26] A. L. Schawlow and C. H. Townes, "Infrared and optical masers," *Phys. Rev.*, vol. 112, pp. 1940–1949, Dec 1958.

[27] T. H. Maiman, "Stimulated optical radiation in ruby," *Nature*, vol. 187, no. 4736, pp. 493–494, 1960.

[28] R. N. Hall, G. E. Fenner, J. D. Kingsley, T. J. Soltys, and R. O. Carlson, "Coherent light emission from gaas junctions," *Phys. Rev. Lett.*, vol. 9, pp. 366–368, Nov 1962.

[29] I. Hayashi, M. B. Panish, P. W. Foy, and S. Sumski, "Junction lasers which operate continuously at room temperature," *Applied Physics Letters*, vol. 17, no. 3, pp. 109–111, 1970.

[30] J. Faist, F. Capasso, D. L. Sivco, C. Sirtori, A. L. Hutchinson, and A. Y. Cho, "Quantum cascade laser," *Science*, vol. 264, no. 5158, pp. 553–556, 1994.

[31] R. Q. Yang, "Infrared laser based on intersubband transitions in quantum wells," 7th International Conference on Superlattices, Microstructures, and Microdevices, (Banff, Canada), 7th International Conference on Superlattices, Microstructures, and Microdevices, Aug. 1994.

[32] R. Q. Yang, "Infrared laser based on intersubband transitions in quantum wells," *Superlattices and Microstructures*, vol. 17, no. 1, pp. 77–83, 1995.

[33] E. F. Schubert, *Light-Emitting Diodes*. Cambridge University Press, 2 ed., 2006.

[34] F. Zafar and A. Iqbal, "Indium phosphide nanowires and their applications in optoelectronic devices," *Proceedings of the Royal Society A: Mathematical, Physical and Engineering Sciences*, vol. 472, no. 2187, p. 20150804, 2016.

[35] S. Nakamura, M. Senoh, S. ichi Nagahama, N. Iwasa, T. Yamada, T. Matsushita, H. Kiyoku, and Y. Sugimoto, "InGaN-based multi-quantum-well-structure laser diodes," *Japanese Journal of Applied Physics*, vol. 35, pp. L74–L76, jan 1996.

[36] S. Nakamura, M. Senoh, S. Nagahama, N. Iwasa, T. Yamada, T. Matsushita, Y. Sugimoto, and H. Kiyoku, "Room-temperature continuous-wave operation of ingan multi-quantum-well structure laser diodes," *Applied Physics Letters*, vol. 69, no. 26, pp. 4056–4058, 1996.

[37] C. R. Bolognesi, J. E. Bryce, and D. H. Chow, "InAs channel heterostructure-field effect transistors with InAs/AlSb short-period superlattice barriers," *Applied Physics Letters*, vol. 69, pp. 3531–3533, dec 1996.

[38] D. Chow, H. Dunlap, W. Williamson, S. Enquist, B. Gilbert, S. Subramaniam, P.-M. Lei, and G. Bernstein, "InAs/AlSb/GaSb resonant interband tunneling diodes and au-on-InAs/AlSb-superlattice schottky diodes for logic circuits," *IEEE Electron Device Letters*, vol. 17, pp. 69–71, feb 1996.

[39] L. F. Luo, R. Beresford, and W. I. Wang, "Resonant tunneling in AlSb/InAs/AlSb double-barrier heterostructures," *Applied Physics Letters*, vol. 53, pp. 2320–2322, dec 1988.

[40] I. Vurgaftman, J. R. Meyer, F. H. Julien, and L. R. Ram-Mohan, "Design and simulation of low-threshold antimonide intersubband lasers," *Applied Physics Letters*, vol. 73, pp. 711–713, aug 1998.

[41] D. L. Smith and C. Mailhiot, "Proposal for strained type II superlattice infrared detectors," *Journal of Applied Physics*, vol. 62, pp. 2545–2548, sep 1987.

[42] R. Q. Yang and S. S. Pei, "Novel type-ii quantum cascade lasers," *Journal of Applied Physics*, vol. 79, no. 11, pp. 8197–8203, 1996.

[43] J. C. Garcia, E. Rosencher, P. Collot, N. Laurent, J. L. Guyaux, B. Vinter, and J. Nagle, "Epitaxially stacked lasers with esaki junctions: A bipolar cascade laser," *Applied Physics Letters*, vol. 71, no. 26, pp. 3752–3754, 1997.

[44] H. K. Choi, G. W. Turner, M. J. Manfra, and M. K. Connors, "175 k continuous wave operation of inassb/inalassb quantum-well diode lasers emitting at 3.5 μm," *Applied Physics Letters*, vol. 68, no. 21, pp. 2936–2938, 1996.

[45] R. Liang, T. Hosoda, G. Kipshidze, L. Shterengas, and G. Belenky, "Gasb-based diode lasers with asymmetric separate confinement heterostructure," *IEEE Photonics Technology Letters*, vol. 25, no. 10, pp. 925–928, 2013.

[46] T. Hosoda, G. Kipshidze, L. Shterengas, and G. Belenky, "Diode lasers emitting near 3.44 μm in continuous wave regime at 300 k," *Electronics Letters*, vol. 46, pp. 1455–1457(2), October 2010.

[47] G. Belenky, L. Shterengas, G. Kipshidze, and T. Hosoda, "Type-i diode lasers for spectral region above 3 μm," *IEEE Journal of Selected Topics in Quantum Electronics*, vol. 17, no. 5, pp. 1426–1434, 2011.

[48] L. Esaki and R. Tsu, "Superlattice and negative differential conductivity in semiconductors," *IBM Journal of Research and Development*, vol. 14, no. 1, pp. 61–65, 1970.

[49] R. F. Kazarinov and R. A. Suris, "Possibility of the amplification of electromagnetic waves in a semiconductor with a superlattice," *Soviet Physics-Semiconductors*, vol. 5, no. 4, p. 707, 1972.

[50] F. Wang, S. Slivken, D. H. Wu, and M. Razeghi, "Room temperature quantum cascade lasers with 22% wall plug efficiency in continuous-wave operation," *Opt. Express*, vol. 28, pp. 17532–17538, Jun 2020.

[51] J. Meyer, I. Vurgaftman, R. Yang, and L. Ram-Mohan, "Type-ii and type-i interband cascade lasers," *Electronics Letters*, vol. 32, pp. 45–46(1), January 1996.

[52] Chih-HsiangLin, R. Q.Yang, D. Zhang, S. Murry, S. Pei, A. Allerman, and S. Kurtz, "Type-ii interband quantum cascade laser at 3.8 μm," *Electronics Letters*, vol. 33, pp. 598–599(1), March 1997.

[53] R. Q. Yang, B. H. Yang, D. Zhang, C.-H. Lin, S. J. Murry, H. Wu, and S. S. Pei, "High power mid-infrared interband cascade lasers based on type-ii quantum wells," *Applied Physics Letters*, vol. 71, no. 17, pp. 2409–2411, 1997.

[54] I. Vurgaftman, J. Meyer, and L. Ram-Mohan, "Mid-ir vertical-cavity surface-emitting lasers," *IEEE Journal of Quantum Electronics*, vol. 34, no. 1, pp. 147–156, 1998.

[55] C. Felix, W. Bewley, I. Vurgaftman, J. Meyer, D. Zhang, C.-H. Lin, R. Yang, and S. Pei, "Interband cascade laser emitting >1 photon per injected electron," *IEEE Photonics Technology Letters*, vol. 9, no. 11, pp. 1433–1435, 1997.

[56] C. L. Felix, W. W. Bewley, E. H. Aifer, I. Vurgaftman, J. R. Meyer, C. H. Lin, D. Zhang, S. J. Murry, R. Q. Yang, and S. S. Pei, "Low threshold 3 μm interband cascade "w" laser," *Journal of Electronic Materials*, vol. 27, no. 2, pp. 77–80, 1998.

[57] R. Yang, J. Bradshaw, J. Bruno, J. Pham, and D. Wortman, "Mid-infrared type-ii interband cascade lasers," *IEEE Journal of Quantum Electronics*, vol. 38, no. 6, pp. 559–568, 2002.

[58] R. Q. Yang, J. L. Bradshaw, J. D. Bruno, J. T. Pham, D. E. Wortman, and R. L. Tober, "Room temperature type-ii interband cascade laser," *Applied Physics Letters*, vol. 81, no. 3, pp. 397–399, 2002.

[59] R. Q. Yang, C. J. Hill, B. Yang, and J. K. Liu, "Room-temperature type-ii interband cascade lasers near 4.1 μm," *Applied Physics Letters*, vol. 83, no. 11, pp. 2109–2111, 2003.

[60] C. J. Hill, B. Yang, and R. Q. Yang, "Low-threshold interband cascade lasers operating above room temperature," *Physica E: Low-dimensional Systems and Nanostructures*, vol. 20, no. 3, pp. 486–490, 2004. Proceedings of the 11th International Conference on Narrow Gap Semiconductors.

[61] R. Q. Yang, C. J. Hill, and B. H. Yang, "High-temperature and low-threshold midinfrared interband cascade lasers," *Applied Physics Letters*, vol. 87, no. 15, p. 151109, 2005.

[62] K. Mansour, Y. Qiu, C. Hill, A. Soibel, and R. Yang, "Mid-infrared interband cascade lasers at thermoelectric cooler temperatures," *Electronics Letters*, vol. 42, pp. 1034–1036(2), August 2006.

[63] M. Kim, C. L. Canedy, W. W. Bewley, C. S. Kim, J. R. Lindle, J. Abell, I. Vurgaftman, and J. R. Meyer, "Interband cascade laser emitting at λ=3.75 μm in continuous wave above room temperature," *Applied Physics Letters*, vol. 92, no. 19, p. 191110, 2008.

[64] A. Bauer, M. Dallner, M. Kamp, S. Höfling, L. Worschech, and A. W. B. Forchel, "Shortened injector interband cascade lasers for 3.3- to 3.6-μm emission," *Optical Engineering*, vol. 49, no. 11, pp. 1 – 6, 2010.

[65] I. Vurgaftman, W. W. Bewley, C. L. Canedy, C. S. Kim, M. Kim, C. D. Merritt, J. Abell, J. R. Lindle, and J. R. Meyer, "Rebalancing of internally generated carriers for mid-infrared interband cascade lasers with very low power consumption," *Nature Communications*, vol. 2, no. 1, p. 585, 2011.

[66] S. Subbanna, "Reflection high-energy electron diffraction oscillations during molecular-beam epitaxy growth of gallium antimonide, aluminum antimonide, and indium arsenide," *Journal of Vacuum Science and Technology B: Microelectronics and Nanometer Structures*, vol. 7, p. 289, mar 1989.

[67] C. Kittel, *Introduction to Solid State Physics*. WILEY, Nov. 2004.

[68] J. W. Matthews and A. Blakeslee, "Defects in epitaxial multilayers," *Journal of Crystal Growth*, vol. 32, pp. 265–273, Feb. 1976.

[69] N. J. Ekins-Daukes, K. Kawaguchi, and J. Zhang, "Strain-balanced criteria for multiple quantum well structures and its signature in x-ray rocking curves," *Crystal Growth & Design*, vol. 2, pp. 287–292, July 2002.

[70] B. R. Bennett, R. Magno, and N. Papanicolaou, "Controlled n-type doping of antimonides and arsenides using gate," *Journal of Crystal Growth*, vol. 251, no. 1, pp. 532–537, 2003. Proceedings of the Twelfth International Conference on Molecular Beam Epitaxy.

[71] S. E. Aleksandrov, G. A. Gavrilov, A. A. Kapralov, G. Y. Sotnikova, D. F. Chernykh, A. N. Alekseev, A. L. Dudin, I. V. Kogan, and A. P. Shkurko, "Pyrometer unit for GaAs substrate temperature control in an MBE system," *Technical Physics*, vol. 49, pp. 123–127, jan 2004.

[72] A. Bracker, M. Yang, B. Bennett, J. Culbertson, and W. Moore, "Surface reconstruction phase diagrams for InAs, AlSb, and GaSb," *Journal of Crystal Growth*, vol. 220, pp. 384–392, dec 2000.

[73] P. R, *Hall Effect Devices*. Institute of Physics Publishing, Dirac House, Temple Back, Bristol BS1 6BE, UK: IOP, 2nd ed., 2004.

[74] L. J. van der PAUW, "A method of measuring specific resistivity and hall effect of discs of arbitrary shape," in *Semiconductor Devices: Pioneering Papers*, pp. 174–182, WORLD SCIENTIFIC, mar 1991.

[75] D. K. Schroder, *Semiconductor Material and Device Characterization*. John Wiley & Sons, Inc., apr 2005.

[76] L. O. Olsson, C. B. M. Andersson, M. C. Hakansson, J. Kanski, L. Ilver, and U. O. Karlsson, "Charge accumulation at inas surfaces," *Physical Review Letters*, vol. 76, pp. 3626–3629, may 1996.

[77] P. D. Wang, S. N. Holmes, T. Le, R. A. Stradling, I. T. Ferguson, and A. G. de Oliveira, "Electrical and magneto-optical of MBE InAs on GaAs," *Semiconductor Science and Technology*, vol. 7, pp. 767–786, jun 1992.

[78] Y. G. Chai and R. Chow, "Source and elimination of oval defects on GaAs films grown by molecular beam epitaxy," *Applied Physics Letters*, vol. 38, pp. 796–798, may 1981.

[79] A. Salokatve, J. Varrio, J. Lammasniemi, H. Asonen, and M. Pessa, "Reduction of surface defects in GaAs grown by molecular beam epitaxy," *Applied Physics Letters*, vol. 51, pp. 1340–1342, oct 1987.

[80] N. J. Kadhim and D. Mukherjee, "Growth model of oval defect structures in mbe gaas layers," *Journal of Materials Science Letters*, vol. 18, no. 3, pp. 229–232, 1999.

[81] A. Szerling, K. Kosiel, A. Wojcik-Jedlinska, M. Pluska, , and M. Bugajski, "Properties and origin of oval defects in epitaxial structures grown by molecular beam epitaxy," *Optica Applicata*, vol. 35, no. 3, pp. 537–548, 2005.

[82] B. R. Bennett, B. V. Shanabrook, and E. R. Glaser, "Interface control in InAs/AlSb superlattices," *Applied Physics Letters*, vol. 65, pp. 598–600, aug 1994.

[83] R. Q. Yang, Z. Tian, J. F. Klem, T. D. Mishima, M. B. Santos, and M. B. Johnson, "Interband cascade photovoltaic devices," *Applied Physics Letters*, vol. 96, p. 063504, feb 2010.

[84] Z. Tian, R. Yang, T. Mishima, M. Santos, R. Hinkey, M. Curtis, and M. Johnson, "InAs-based interband cascade lasers near 6 μm," *Electronics Letters*, vol. 45, no. 1, p. 48, 2009.

[85] Z. Tian, R. Yang, T. Mishima, M. Santos, and M. Johnson, "Plasmon-waveguide interband cascade lasers near 7.5 μm," *IEEE Photonics Technology Letters*, vol. 21, pp. 1588–1590, nov 2009.

[86] R. T. Hinkey, Z. Tian, R. Q. Yang, T. D. Mishima, and M. B. Santos, "Reflectance spectrum of plasmon waveguide interband cascade lasers and observation of the berreman effect," *Journal of Applied Physics*, vol. 110, p. 043113, aug 2011.

[87] R. Q. Yang, L. Li, L. Zhao, Y. Jiang, Z. Tian, H. Ye, R. T. Hinkey, C. Niu, T. D. Mishima, M. B. Santos, J. C. Keay, M. B. Johnson, and K. Mansour, "Recent progress in development of InAs-based interband cascade lasers," in *SPIE Proceedings* (A. A. Belyanin and P. M. Smowton, eds.), SPIE, mar 2013.

[88] L. Li, H. Ye, Y. Jiang, R. Q. Yang, J. C. Keay, T. D. Mishima, M. B. Santos, and M. B. Johnson, "MBE-grown long-wavelength interband cascade lasers on InAs substrates," *Journal of Crystal Growth*, vol. 425, pp. 369–372, sep 2015.

[89] M. Dallner, F. Hau, S. Höfling, and M. Kamp, "InAs-based interband-cascade-lasers emitting around 7 μm with threshold current densities below 1 kA/cm2 at room temperature," *Applied Physics Letters*, vol. 106, p. 041108, jan 2015.

[90] J. Matthews and A. Blakeslee, "Defects in epitaxial multilayers," *Journal of Crystal Growth*, vol. 27, pp. 118–125, dec 1974.

[91] J. W. Matthews, "Defects associated with the accommodation of misfit between crystals," *Journal of Vacuum Science and Technology*, vol. 12, pp. 126–133, jan 1975.

[92] G. Turner, M. Manfra, H. Choi, and M. Connors, "MBE growth of high-power quantum-well diode lasers emitting at 3.5 μm," *Journal of Crystal Growth*, vol. 175-176, pp. 825–832, may 1997.

[93] M. A. Marciniak, R. L. Hengehold, Y. K. Yeo, and G. W. Turner, "Optical characterization of molecular beam epitaxially grown InAsSb nearly lattice matched to GaSb," *Journal of Applied Physics*, vol. 84, pp. 480–488, jul 1998.

[94] X. Marcadet, A. Rakovska, I. Prevot, G. Glastre, B. Vinter, and V. Berger, "MBE growth of room-temperature InAsSb mid-infrared detectors," *Journal of Crystal Growth*, vol. 227-228, pp. 609–613, jul 2001.

[95] C.-A. Chang, H. Takaoka, L. L. Chang, and L. Esaki, "Molecular beam epitaxy of AlSb," *Applied Physics Letters*, vol. 40, pp. 983–985, jun 1982.

[96] H. Ye, L. Li, R. T. Hinkey, R. Q. Yang, T. D. Mishima, J. C. Keay, M. B. Santos, and M. B. Johnson, "Mbe growth optimization of inas (001) homoepitaxy," *Journal of Vacuum Science and Technology B, Nanotechnology and Microelectronics: Materials, Processing, Measurement, and Phenomena*, vol. 31, p. 03C135, may 2013.

[97] M. E. Twigg, B. R. Bennett, B. V. Shanabrook, J. R. Waterman, J. L. Davis, and R. J. Wagner, "Interfacial roughness in InAs/GaSb superlattices," *Applied Physics Letters*, vol. 64, pp. 3476–3478, jun 1994.

[98] R. M. Feenstra, D. A. Collins, D. Z. Y. Ting, M. W. Wang, and T. C. McGill, "Interface roughness and asymmetry in InAs/GaSb superlattices studied by scanning tunneling microscopy," *Physical Review Letters*, vol. 72, pp. 2749–2752, apr 1994.

[99] Y. Ashuach, Y. Kauffmann, C. Saguy, S. Grossman, O. Klin, E. Weiss, and E. Zolotoyabko, "Quantification of atomic intermixing in short-period InAs/GaSb superlattices for infrared photodetectors," *Journal of Applied Physics*, vol. 113, p. 184305, may 2013.

[100] J. Steinshnider, M. Weimer, R. Kaspi, and G. W. Turner, "Visualizing interfacial structure at non-common-atom heterojunctions with cross-sectional scanning tunneling microscopy," *Physical Review Letters*, vol. 85, pp. 2953–2956, oct 2000.

[101] J. R. Waterman, B. V. Shanabrook, R. J. Wagner, M. J. Yang, J. L. Davis, and J. P. Omaggio, "The effect of interface bond type on the structural and optical properties of GaSb/InAs superlattices," *Semiconductor Science and Technology*, vol. 8, pp. S106–S111, jan 1993.

[102] G. Booker, P. Klipstein, M. Lakrimi, S. Lyapin, N. Mason, I. Murgatroyd, R. Nicholas, T.-Y. Seong, D. Symons, and P. Walker, "Growth of strained layer superlattices. II," *Journal of Crystal Growth*, vol. 146, pp. 495–502, jan 1995.

[103] J. Rodriguez, P. Christol, L. Cerutti, F. Chevrier, and A. Joullié, "MBE growth and characterization of type-II InAs/GaSb superlattices for mid-infrared detection," *Journal of Crystal Growth*, vol. 274, pp. 6–13, jan 2005.

[104] H. Haugan, L. Grazulis, G. Brown, K. Mahalingam, and D. Tomich, "Exploring optimum growth for high quality InAs/GaSb type-II superlattices," *Journal of Crystal Growth*, vol. 261, pp. 471–478, feb 2004.

[105] G. Tuttle, H. Kroemer, and J. H. English, "Effects of interface layer sequencing on the transport properties of InAs/AlSb quantum wells: Evidence for antisite donors at the InAs/AlSb interface," *Journal of Applied Physics*, vol. 67, pp. 3032–3037, mar 1990.

[106] J. Spitzer, A. Höpner, M. Kuball, M. Cardona, B. Jenichen, H. Neuroth, B. Brar, and H. Kroemer, "Influence of the interface composition of InAs/AlSb superlattices on their optical and structural properties," *Journal of Applied Physics*, vol. 77, pp. 811–820, jan 1995.

[107] A. Bauer, M. Dallner, A. Herrmann, T. Lehnhardt, M. Kamp, S. Höfling, L. Worschech, and A. Forchel, "Atomic scale interface engineering for strain compensated epitaxially grown InAs/AlSb superlattices," *Nanotechnology*, vol. 21, p. 455603, oct 2010.

[108] Z. Tian, Y. Jiang, L. Li, R. T. Hinkey, Z. Yin, R. Q. Yang, T. D. Mishima, M. B. Santos, and M. B. Johnson, "InAs-based mid-infrared interband cascade lasers near 5.3 μm," *IEEE Journal of Quantum Electronics*, vol. 48, pp. 915–921, jul 2012.

[109] N. L. Aung, X. Huang, W. O. Charles, N. Yao, and C. F. Gmachl, "Effect of surface defects on InGaAs/InAlAs quantum cascade mesa current–voltage characteristics," *Journal of Crystal Growth*, vol. 353, pp. 35–38, aug 2012.

[110] R. Sacks, P. Colombo, G. A. Patterson, and K. A. Stair, "Improved MBE-grown GaAs using a novel, high-capacity ga effusion cell," *Journal of Crystal Growth*, vol. 175-176, pp. 66–71, may 1997.

[111] D. G. Schlom, "Reduction of gallium-related oval defects," *Journal of Vacuum Science and Technology B: Microelectronics and Nanometer Structures*, vol. 7, p. 296, mar 1989.

[112] E. Koerperick, L. Murray, D. Norton, T. Boggess, and J. Prineas, "Optimization of MBE-grown GaSb buffer layers and surface effects of antimony stabilization flux," *Journal of Crystal Growth*, vol. 312, pp. 185–191, jan 2010.

[113] C. Vineis, C. Wang, and K. Jensen, "In-situ reflectance monitoring of GaSb substrate oxide desorption," *Journal of Crystal Growth*, vol. 225, pp. 420–425, may 2001.

[114] R. Q. Yang, Z. Tian, Z. Cai, J. F. Klem, M. B. Johnson, and H. C. Liu, "Interband-cascade infrared photodetectors with superlattice absorbers," *Journal of Applied Physics*, vol. 107, p. 054514, mar 2010.

[115] J. V. Li, R. Q. Yang, C. J. Hill, and S. L. Chuang, "Interband cascade detectors with room temperature photovoltaic operation," *Applied Physics Letters*, vol. 86, p. 101102, mar 2005.

[116] W. Haung, *Thermophotovoltaic devices and infrared photodetectors based on interband cascade structures*. PhD thesis, The University of Oklahoma, 2020.

[117] W. Huang, J. A. Massengale, Y. Lin, L. Li, R. Q. Yang, T. D. Mishima, and M. B. Santos, "Performance analysis of narrow-bandgap interband cascade thermophotovoltaic cells," *Journal of Physics D: Applied Physics*, vol. 53, p. 175104, feb 2020.

[118] W. Huang, S. S. Rassel, L. Li, J. A. Massengale, R. Q. Yang, T. D. Mishima, and M. B. Santos, "A unified figure of merit for interband and intersubband cascade devices," *Infrared Physics and Technology*, vol. 96, pp. 298–302, jan 2019.

[119] W. Huang, L. Lei, L. Li, J. A. Massengale, R. Q. Yang, T. D. Mishima, and M. B. Santos, "Enhanced collection efficiencies and performance of interband cascade structures for narrow bandgap semiconductor thermophotovoltaic devices," *Journal of Applied Physics*, vol. 124, p. 023101, jul 2018.

[120] W. Huang, L. Li, J. A. Massengale, R. Q. Yang, T. D. Mishima, and M. B. Santos, "Multistage interband cascade thermophotovoltaic devices with ≈ 0.2 eV bandgap," in *2019 IEEE 46th Photovoltaic Specialists Conference (PVSC)*, IEEE, jun 2019.

[121] W. Huang, L. Li, J. A. Massengale, R. Q. Yang, T. D. Mishima, and M. B. Santos, "Investigation of narrow bandgap interband cascade thermophotovoltaic cells," in *Physics, Simulation, and Photonic Engineering of Photovoltaic Devices VIII* (A. Freundlich, M. Sugiyama, and L. Lombez, eds.), SPIE, feb 2019.

[122] W. Huang, J. A. Massengale, Y. Lin, R. Q. Yang, T. D. Mishima, and M. B. Santos, "Resonant cavity enhanced interband cascade thermophotovoltaic cells," in *2020 47th IEEE Photovoltaic Specialists Conference (PVSC)*, IEEE, jun 2020.

[123] W. Huang and R. Q. Yang, "Limiting factors and efficiencies of narrow bandgap single-absorber and multi-stage interband cascade thermophotovoltaic cells under monochromatic light illumination," *Journal of Applied Physics*, vol. 126, p. 045714, jul 2019.

[124] R. T. Hinkey and R. Q. Yang, "Theoretical comparison of performance limits of single- and multiple-stage photovoltaic devices," *Semiconductor Science and Technology*, vol. 30, p. 015013, dec 2014.

[125] R. Q. Yang, L. Li, and Y. Jiang, "Interband cascade lasers: From original concept to practical devices," *Progress in Physics*, vol. 34, no. 169, 2014.

[126] H. Sun, *Laser Diode Basics*. Dordrecht: Springer Netherlands, 2012.

[127] C. Canedy, C. Kim, M. Kim, D. Larrabee, J. Nolde, W. Bewley, I. Vurgaftman, and J. Meyer, "High-power, narrow-ridge, mid-infrared interband cascade lasers," *Journal of Crystal Growth*, vol. 301-302, pp. 931–934, 2007. 14th International Conference on Molecular Beam Epitaxy.

[128] C. Henry, "Theory of the linewidth of semiconductor lasers," *IEEE Journal of Quantum Electronics*, vol. 18, no. 2, pp. 259–264, 1982.

[129] W. W. Bewley, C. L. Canedy, C. S. Kim, M. Kim, J. A. Nolde, D. C. Larrabee, J. R. Lindle, I. Vurgaftman, and J. R. Meyer, "Mid-infrared interband cascade lasers operating cw at thermoelectric-cooler temperatures," in *2008 Conference on Lasers and Electro-Optics and 2008 Conference on Quantum Electronics and Laser Science*, pp. 1–2, 2008.

[130] Y. Varshni, "Temperature dependence of the energy gap in semiconductors," *Physica*, vol. 34, no. 1, pp. 149–154, 1967.

[131] J. Faist, F. Capasso, C. Sirtori, D. L. Sivco, A. L. Hutchinson, and A. Y. Cho, "Continuous wave operation of a vertical transition quantum cascade laser above t=80 k," *Applied Physics Letters*, vol. 67, no. 21, pp. 3057–3059, 1995.

[132] M. Kim, W. W. Bewley, C. L. Canedy, C. S. Kim, C. D. Merritt, J. Abell, I. Vurgaftman, and J. R. Meyer, "High-power continuous-wave interband cascade lasers with 10 active stages," *Opt. Express*, vol. 23, pp. 9664–9672, Apr 2015.

[133] Y. Jiang, *High-Performance InAs-Based Interband Cascade Lasers*. phdthesis, University of Oklahoma, 2016.

[134] A. Baranov and E. Tournie, *Semiconductor Lasers Fundamentals and Applications*. Elsevier Science and Technology, 2013.

[135] J. Koeth, R. Weih, M. O. Fischer, M. Kamp, S. Höfling, J. Scheuermann, and A. Schade, "Mid infrared DFB interband cascade lasers," in *Infrared Remote Sensing and Instrumentation XXV* (M. Strojnik and M. S. Kirk, eds.), SPIE, aug 2017.

[136] R. Q. Yang, L. Li, W. Huang, S. M. S. Rassel, J. A. Gupta, A. Bezinger, X. Wu, S. G. Razavipour, and G. C. Aers, "InAs-based interband cascade lasers," *IEEE Journal of Selected Topics in Quantum Electronics*, vol. 25, pp. 1–8, nov 2019.

[137] W. L. L. T. Borca-Tasciuc, D. Achimov, "Thermal conductivity of inas/alsb superlattices," *Microscale Thermophysical Engineering*, vol. 5, pp. 225–231, jul 2001.

[138] C. L. Canedy, M. V. Warren, C. D. Merritt, W. W. Bewley, C. S. Kim, M. Kim, I. Vurgaftman, and J. R. Meyer, "Interband cascade lasers with longer wavelengths," in *SPIE Proceedings* (M. Razeghi, ed.), SPIE, jan 2017.

[139] J. A. Massengale, Y. Shen, R. Q. Yang, T. D. Mishima, and M. B. Santos, "Gasb-based interband cascade lasers with advanced waveguides operating near 3.3 and 3.4 μm," in *SPIE Proceedings*, (San Francisco, California, United States), SPIE, mar 2023.

[140] C. Sirtori, J. Faist, F. Capasso, D. L. Sivco, A. L. Hutchinson, and A. Y. Cho, "Quantum cascade laser with plasmon-enhanced waveguide operating at 8.4 μm wavelength," *Applied Physics Letters*, vol. 66, pp. 3242–3244, jun 1995.

[141] K. Ohtani and H. Ohno, "An InAs-based intersubband quantum cascade laser," *Japanese Journal of Applied Physics*, vol. 41, pp. L1279–L1280, nov 2002.

[142] K. Ohtani, K. Fujita, and H. Ohno, "Mid infrared InAs/AlGaSb superlattice quantum cascade lasers," *Applied Physics Letters*, vol. 87, p. 211113, nov 2005.

[143] R. Q. Yang and J. M. Xu, "Bound and quasibound states in leaky quantum wells," *Physical Review B*, vol. 46, pp. 6969–6974, sep 1992.

[144] I. Vurgaftman, J. R. Meyer, and L. R. Ram-Mohan, "Band parameters for III–v compound semiconductors and their alloys," *Journal of Applied Physics*, vol. 89, pp. 5815–5875, jun 2001.

[145] E. O. Kane, "Band structure of indium antimonide," *Journal of Physics and Chemistry of Solids*, vol. 1, pp. 249–261, jan 1957.

[146] A. P. Ongstad, R. Kaspi, G. C. Dente, M. L. Tilton, R. Barresi, and J. R. Chavez, "Wavelength tuning limitations in optically pumped type-II antimonide lasers," *Applied Physics Letters*, vol. 92, p. 141106, apr 2008.

[147] Y.-M. Mu and R. Q. Yang, "Theoretical investigation of mid-infrared interband cascade lasers based on type II quantum wells," *Journal of Applied Physics*, vol. 84, pp. 5357–5359, nov 1998.

[148] J. A. Massengale, Y. Shen, R. Q. Yang, S. D. Hawkins, and J. F. Klem, "Long wavelength interband cascade lasers," *Applied Physics Letters*, vol. 120, p. 091105, feb 2022.

[149] J. A. Massengale, Y. Shen, R. Q. Yang, S. D. Hawkins, and J. F. Klem, "Enhanced performance of InAs-based interband cascade lasers emitting between 10–13 μm," *Semiconductor Science and Technology*, vol. 38, p. 025009, dec 2022.

[150] L. Esaki, L. L. Chang, and E. E. Mendez, "Polytype superlattices and multi-heterojunctions," *Japanese Journal of Applied Physics*, vol. 20, p. L529, jul 1981.

[151] J. R. Meyer, C. A. Hoffman, F. J. Bartoli, and L. R. Ram-Mohan, "Type-II quantum-well lasers for the mid-wavelength infrared," *Applied Physics Letters*, vol. 67, pp. 757–759, aug 1995.

[152] S. R. White and L. J. Sham, "Electronic properties of flat-band semiconductor heterostructures," *Physical Review Letters*, vol. 47, pp. 879–882, sep 1981.

[153] R. Q. Yang and J. M. Xu, "Analysis of transmission in polytype interband tunneling heterostructures," *Journal of Applied Physics*, vol. 72, pp. 4714–4726, nov 1992.

[154] R. Yang, "Interband cascade (IC) lasers," in *Semiconductor Lasers*, pp. 487–513, Elsevier, 2013.

[155] R. A. Serway and J. S. Faughn, *College Physics (with PhysicsNow)*. Brooks Cole, 2003.

[156] R. Q. Yang and Y.-M. Mu, "Issues in mid-IR type-II interband cascade lasers," in *SPIE Proceedings* (H. K. Choi and P. S. Zory, eds.), SPIE, apr 1999.

[157] H. Knötig, J. Nauschütz, N. Opačak, S. Höfling, J. Koeth, R. Weih, and B. Schwarz, "Mitigating valence intersubband absorption in interband cascade lasers," *Laser and Photonics Reviews*, vol. 16, p. 2200156, jul 2022.

[158] J. Nauschütz, H. Knötig, R. Weih, J. Scheuermann, J. Koeth, S. Höfling, and B. Schwarz, "Pushing the room temperature continous-wave operation limit of gasb-based interband cascade lasers beyond 6 μm," 2022.

[159] J. A. Massengale, Y. Shen, R. Q. Yang, S. D. Hawkins, and J. F. Klem, "Advances in long wavelength interband cascade lasers," in *2022 28th International Semiconductor Laser Conference (ISLC)*, IEEE, oct 2022.

[160] I. Vurgaftman, R. Weih, M. Kamp, J. R. Meyer, C. L. Canedy, C. S. Kim, M. Kim, W. W. Bewley, C. D. Merritt, J. Abell, and S. Höfling, "Interband cascade lasers," *Journal of Physics D: Applied Physics*, vol. 48, p. 123001, mar 2015.

[161] R. Q. Yang, C. J. Hill, L. E. Christensen, and C. R. Webster, "Mid-IR type-II interband cascade lasers and their applications," in *SPIE Proceedings* (C.-E. Zah, Y. Luo, and S. Tsuji, eds.), SPIE, jan 2005.

[162] R. Weih, M. Kamp, and S. Höfling, "Interband cascade lasers with room temperature threshold current densities below 100 A/cm2," *Applied Physics Letters*, vol. 102, p. 231123, jun 2013.

Appendix A

List of Publications

Refereed Journal Articles

1. **J. A. Massengale**, Y. Shen, R. Q. Yang, S. D. Hawkins, and J. F. Klem, "Enhanced performance of InAs-based interband cascade lasers emitting between 10-13 μm," Semicond. Sci. Technol., **38**, 025009 (2023).

2. **J. A. Massengale**, Y. Shen, R. Q. Yang, S. D. Hawkins, and J. F. Klem, "Long wavelength interband cascade lasers," Appl. Phys. Lett. **120**, 091105 (2022).

3. Y. Lin, **J. A. Massengale**, W. Huang, R. Q. Yang, T. D. Mishima, and M. B. Santos, "Examination of the durability of interband cascade lasers against structural variations," J. Infrared Millim. Waves, **39**, 2 (2020).

4. W. Huang, **J. A. Massengale**, Y. Lin, L. Li, R. Q. Yang, T. D. Mishima, and M. B. Santos, "Performance analysis of narrow-bandgap interband cascade thermophotovoltaic cells," J. Appl. Phys. **53**, 175104 (2020).

5. W. Huang, S. M. Shazzad Rassel, L. Li, **J. A. Massengale**, R. Q. Yang, T. D. Mishima, and M. B. Santos, "A unified figure of merit for interband and intersubband cascade devices," Infrared Phys. and Tech. **96** (2019).

6. W. Huang, L. Lei, L. Li, **J. A. Massengale**, R. Q. Yang, T. D. Mishima, and M. B. Santos, "Enhanced collection efficiencies and performance of interband cascade structures for narrow bandgap semiconductor thermophotovoltaic devices," J. Appl. Phys. **124**, 023101 (2018).

7. W. Huang, L. Li, L. Lei, **J. A. Massengale**, Hao Ye, R. Q. Yang, T. D. Mishima, and M. B. Santos, "Minority Carrier Lifetime in Mid-Wavelength Interband Cascade Infrared Photodetectors," Appl. Phys. Lett. **112** 251107 (2018).

8. W. Huang, L. Li, L. Lei, **J. A. Massengale**, R. Q. Yang, T. D. Mishima, and M. B. Santos, "Electrical gain in interband cascade infrared photodetectors," J. Appl. Phys. **123**, 113104 (2018).

9. L. Lei, L. Li, W. Huang, **J. A. Massengale**, H. Ye, H. Lotfi, R. Q. Yang, T. D. Mishima, M. B. Santos, M. B. Johnson, "Resonant tunneling and multiple negative differential conductance features in long wavelength interband cascade infrared photodetectors," Appl. Phys. Lett. **111** (11), 113504 (2017).

10. W. Huang, L. Lei, L. Li, **J. A. Massengale**, R. Q. Yang, T. D. Mishima, M. B. Santos, "Current-matching versus non-current-matching in long wavelength interband cascade infrared photodetectors," J. Appl. Phys. **122** (8), 083102 (2017).

11. L. Lei, L. Li, H. Ye, H. Lotfi, R. Q. Yang, M. B. Johnson, **J. A. Massengale**, T. D. Mishima, M. B. Santos, "Long wavelength interband cascade infrared photodetectors operating at high temperatures," J. Appl. Phys. **120**, 193102 (2016).

12. E. H. Steenbergen, **J. A. Massengale**, G. Ariyawansa, Y. H. Zhang, "Evidence of carrier localization in photoluminescence spectroscopy studies of mid-wavelength infrared InAs/InAsSb type-II superlattices", Journal of Luminescence **178**, 451 (2016).

Conference Presentations and Proceedings

1. **J. A. Massengale**, Y. Shen, R. Q. Yang, T. D. Mishima, and M. B. Santos, "Progress in interband cascade lasers with advanced waveguides operating near 3.3 and 3.4 μm," Proc. SPIE 12440-17 (2023).

2. **J. A. Massengale**, Y. Shen, R. Q. Yang, S. D. Hawkins, and J. F. Klem, "Advances in Long Wavelength Interband Cascade Lasers," 28th International Semiconductor Laser Conference (ISLC), Matsue, Japan, 2022, pp. 1-2.

3. **J. A. Massengale**, Y. Shen, R. Q. Yang, S. D. Hawkins, and J. F. Klem, "Long Wavelength Interband Cascade Lasers," 15th International Conference on Mid-Infrared Optoelectronic Materials and Devices (MIOMD 2021), (2021).

4. W. Huang, **J. A. Massengale**, Y. Lin, R. Q. Yang, T. D. Mishima, and M. B. Santos, "Resonant Cavity Enhanced Interband Cascade Thermophotovoltaic Cells", 47th IEEE Photovoltaic Specialists Conference (PVSC), Calgary, AB, Canada, 2020, pp. 0825-0828, *Presenter*.

5. W. Huang, L. Li, **J. A. Massengale**, H. Ye, R. Q. Yang, T. D. Mishima, and M. B. Santos, "Multistage Interband Cascade Thermophotovoltaic Devices with 0.2 eV Bandgap", IEEE (PVSC 46), 19321634 (2019).

6. W. Huang, L. Li, **J. A. Massengale**, R. Q. Yang, T. D. Mishima, and M. B. Santos, "Investigation of narrow bandgap interband cascade thermophotovoltaic cells", Proc. SPIE 10913 (2019).

7. W. Huang, L. Li, L. Lei, **J. A. Massengale**, H. Ye, R. Q. Yang, T. D. Mishima, and M. B. Santos, "Carrier Lifetime in Mid-Infrared Type-II Superlattice Photodetectors", IEEE (IPC), 18262761 (2018).

8. R. Q. Yang, W. Huang, L. Li, L. Lei, **J. A. Massengale**, T. D. Mishima, and M. B. Santos, "Gain and resonant tunneling in interband cascade IR photodetectors", Proc. SPIE 10540 (2018).

9. R. Q. Yang, L. Li, H. Lotfi, L. Lei, Hao Ye, Yuchao Jiang, SM S. Rassel, **J. A. Massengale**, T. D. Mishima, M. B. santos, M. B. Johnson, "Recent Progress in Interband Cascade Devices," MIRSENS 4, May 2017.

10. L. Lei, L. Li, H. Ye, H. Lotfi, R. Q. Yang, M. B. Johnson, **J. A. Massengale**, T. D. Mishima, M. B. Santos, "Long wavelength interband cascade infrared photodetectors towards high temperature operation," Proc. SPIE 1011113-1 (2017).

11. E. H. Steenbergen, **J. A. Massengale**, V. M. Cowan, Z. Lin, Y. H. Zhang, C. P. Morath, "Proton radiation effects on the photoluminescence of infrared InAs/InAsSb superlattices", Proc. SPIE 8876, Aug. 2013.

12. **J. A. Massengale**, P. A. Voytas, Measuring the Thermal Fluctuations in Bulk YBCO and BSCCO, Ohio Section of the APS, **58**, 2, March 2013.

13. J. Wang, B. Ullrich, G. Brown, H. Smith, L. Grazulis, E. H. Steenbergen, **J. A. Massengale**, "Stability of lead sulfide colloidal quantum dot films on GaAs", Proc. SPIE 8634-26, Feb. 2013.